UNIVERSITY OF CAMBRIDGE
INSTITUTE OF ASTRONOMY

THE EFFECT OF BOMBARDMENT BY SMALL BODIES ON THE EVOLUTION OF ATMOSPHERES ON TERRESTRIAL BODIES

CATRIONA ALEXANDRA SINCLAIR
DARWIN COLLEGE

A dissertation submitted to the
University of Cambridge for the
Degree of Doctor of Philosophy
August 25, 2021

SUPERVISORS:
PROF. M. C. WYATT, DR. O. SHORTTLE

"She was right about that, but only by coincidence "

Terry Pratchett

Dedicated to my family

DECLARATION OF ORIGINALITY

I, Catriona Alexandra Sinclair, declare that this dissertation entitled The Effect of Bombardment by Small Bodies on the Evolution of Atmospheres on Terrestrial Bodies, solely contains work undertaken while in candidature for a research degree at this University. I confirm that this manuscript has not previously been submitted for a degree or any other qualification at this University or any other institution. This dissertation is the result of my own research and contains no outcomes from other research collaborations. The detailed analysis and written work were done exclusively by me. The length of this Thesis is within the 60,000 words limit set by the Degree Committee of Physics and Chemistry. The following parts of this Thesis have already been published in, or submitted to, academic journals:

- **Chapters 2 and 3** were adapted from the published work
  Evolution of the Earth's Atmosphere during Late Veneer Accretion
  C. A. Sinclair, M. C. Wyatt, A. Morbidelli, D. Nesvorný
  MNRAS, 499, 5334, December 2020.

- **Chapter 4** was adapted from the submitted work
  The Role of Impacts on the Atmospheres on the Moons of Outer Giants
  C. A. Sinclair, M. C. Wyatt.
  2021

The co-authors of the publications listed above only contributed indirectly to this dissertation, by their work done performing the dynamical simulations which provided the data used as model inputs in this dissertation, and by providing useful feedback on the results and writing during the drafting process of the above manuscripts.

Catriona Alexandra Sinclair
August 25, 2021

The Effect of Bombardment by Small Bodies on the Evolution of Atmospheres on Terrestrial Bodies

Catriona Alexandra Sinclair

Summary

The atmospheres of bodies in the Solar system display a great degree of diversity in their mass and composition. Impacts onto these bodies by smaller objects, such as asteroids, comets and planetesimals left over after terrestrial planet formation are evidenced by crater observations, and are an inevitable outcome of dynamical simulations of planet and moon formation. These impacts deliver mass and energy, and are capable of altering the atmosphere through erosion, volatile delivery and impact-triggered outgassing from the target body surface.

In this thesis I investigate the effect of bombardment by these small bodies on the evolution of atmospheres on planets and moons. I first provide an introduction to the processes relevant to the formation and evolution of terrestrial planets and their atmospheres in Chapter 1, with a focus on the current state of research on the role impacts have played in shaping atmospheres. I develop in Chapter 2 an analytic method through which the characteristic stalling mass (at which impact induced erosion and accretion are balanced) can be predicted, and which can be used to predict the degree of stochastic variation expected for a given atmosphere and impactor combination. I also present a numerical model for stochastic atmosphere evolution due to bombardment, incorporating prescriptions for a range of impact outcomes (fragmentation and aerial bursts, cratering events and the non-local mass loss caused by giant impacts).

These models are applied to the bombardment by asteroids, comets and left-over planetesimals on the Earth in Chapter 3 and a comparative study of the terrestrial Solar system planets (Venus and Mars) in Chapter 5, using distributions of impact velocities I calculate from the results of recent dynamical simulations. The sensitivity of these results to both the initial atmosphere conditions and the properties of the impacting populations are investigated. In Chapter 4, the numerical code and analytic predictions are also applied to cometary impacts of the atmospheres of the moons of the outer giant planets, incorporating a prescription for impact-triggered outgassing when applied to Titan. Finally in Chapter 6, I make general predictions about the influence of impacts on the atmospheres of exoplanets and hypothetical exomoons and present a simple model for the simultaneous evolution of a magma ocean and atmosphere on a terrestrial planet. The results of this dissertation are summarised in Chapter 7.

ACKNOWLEDGEMENTS

First and foremost, I am extremely grateful to my supervisor Mark, for his invaluable guidance, support and patience during my time in Cambridge. I am indebted to Ollie and his group for teaching me everything I know about rocks. I am also grateful to Josh, Jess, Seba, Amy and the rest the debris disc and white dwarf groups, for their advice and encouragement without which this thesis would not exist. I would not have considered pursuing a PhD without the encouragement of undergraduate project supervisors Giovanni and Cathie, and the support of Paul Hewitt, Max Pettini and Owen Saxton, thank you.

It has been the people at the IoA who have made my time here so special. To Jake and Adam, thanks for being the best office mates (while it was legal to be in the same room), for putting up with my mess of a desk and for providing regular distraction in the form of ABBA songs, Sainsbury's trips and coffee. None of us expected the few weeks working from home would end up being more than a year, and this is a painful way to end my PhD. However, I must thank Tom, Jeff, Jake, Steve, Matt, Andrew, Adam and Zephyr for keeping the morning coffee break going, and for putting up with my pathetic attempts at Rocket League. Tom deserves a special mention for proving that not even a global pandemic can stop the crossword, and for providing some excellent distraction in the form of impossible quizzes.

My time in Cambridge was improved immeasurably by the members of the Jitsu club and MAUL, especially Ellie, Poppy, Alice, Zack, Lilly, Gabe, Chris, Dan, Wendi and Nikki. Thank you for teaching me everything I know about falling over safely, and sometimes letting me take you down with me. The many weekend runs, good brunches and daft adventures made the last seven years the best of my life. To Caitlin, thank you for always having an excellent selection of teas, and even better advice.

I also cannot thank enough the people in Edinburgh who made lockdown bearable. My family, for letting me move back in for far longer than I originally promised, and not asking when I'll get a real job (too often). Harris, for providing an excuse to go outside and excellent distraction in the background of my zoom calls. Finally, Eilidh, Kirsty and the rest of the SIRCs for strange socially-distanced walks, hilarious video chats and excellent life advice.

Catriona Sinclair, August 25, 2021

Contents

List of Figures

List of Tables

1

Introduction

In the twenty years between the first known exoplanet, 51 Pegasi b, being discovered (Mayor & Queloz, 1995) and the detection of an Earth-like planet orbiting our closest Solar neighbour, Proxima Centauri (Anglada-Escudé et al., 2016) our understanding of planetary systems outside our own has been revolutionised. Thousands of exoplanets have been found, making use of techniques including radial velocity (e.g., Mayor et al., 2011; Fischer et al., 2016), transits (e.g., Lissauer et al., 2014; Borucki, 2016), direct imaging (e.g., Bowler, 2016; Stone et al., 2018), and microlensing (e.g., Dominik, 2010; Gaudi, 2012; Penny et al., 2019). These methods have been used in multiple exoplanet search campaigns, each focused on the detection of specific demographics of exoplanets. The search for exoplanets seeks to characterise them, understand the underlying demographics of the exoplanet population and ultimately answer the question of whether life could exist outside our own planet.

Potentially habitable Earth-like planets are challenging to detect, due to the small signal-to-noise ratios in their radial velocity and transit signals. However the discovery of Earth-like planets (Anglada-Escudé et al., 2016), and potentially habitable worlds around low-mass M dwarfs (Gillon et al., 2016) hint that the Solar system is not unique. Planetary systems appear to be extremely common, with an overall planet occurrence rate of $\gtrsim 50\%$ (Winn & Fabrycky, 2015), and show a diverse range of planet masses and orbital architectures.

It is now possible to carry out atmospheric characterisation of terrestrial planets orbiting within the habitable zone of their host star (de Wit et al., 2018). Future space missions such as PLATO and ARIEL will build on this knowledge, improving our knowledge of the occurrence rates of Earth-like planets in the habitable zones of their host stars and providing atmospheric characterisation of Neptune-mass exoplanet atmospheres (Rauer et al., 2014; Tinetti et al., 2018). Proposed missions will hopefully extend this atmospheric characterisation to Earth-like planets in the habitable zones around Sun-like stars (Kopparapu et al., 2018).

Exoplanets are expected to display a range of atmosphere masses and compositions beyond those in the Solar system, and coming missions will further our understanding of their properties (Kaltenegger & Traub, 2009; Seager, 2014; Tinetti et al., 2018; Kopparapu et al., 2018). It is therefore necessary to understand the origin and evolution of terrestrial planet atmospheres, to constrain their potential for habitability and better understand how observations of their atmospheres may inform the formation and evolution of the entire planetary system. This requires understanding of the processes that govern both atmospheric loss and growth. These mechanisms include magma ocean ingassing and outgassing (Tucker & Mukhopadhyay, 2014; Schlichting & Mukhopadhyay, 2018), photo-evaporation and hydrodynamic escape (Pepin, 1991), as well as impact-induced atmospheric erosion and volatile delivery (Shuvalov, 2009; Schlichting et al., 2015). Evidence suggests that impacts have played an important role in both the delivery of volatiles to Earth and atmospheric removal (Shuvalov et al., 2013; Pham et al., 2011; de Niem et al., 2012). Understanding how impacts affect the evolution of a planet's atmosphere requires knowledge of the dynamics of the impactors, which is dependant on the architecture and dynamical history of the entire planetary system.

This dissertation studies the role that impacts in particular have played in the evolution of thin atmospheres on small worlds. In the following section I lay out the current state of knowledge regarding terrestrial planet formation processes, our understanding of the dynamical history of the Solar system and what this means for impacts onto Earth, Venus and Mars, and the development of the most recent impact prescriptions used to study the role impacts have played in shaping atmospheres.

The mass and composition of terrestrial planet atmospheres are closely tied to the planet bulk properties, its formation history and subsequent evolution. Therefore the present day geochemical inventory of the atmospheres of Earth, Venus, Mars and other Solar system bodies gives insight into their sources, as well as the potential loss and delivery mechanisms that have acted on them over their history. These atmospheres have undergone substantial

evolution as a result of many processes acting on different spatial and temporal scales, and which act to different degrees on different bodies. The comparatively abundant observational constraints provided by the Earth make it an important test case for understanding these processes. However other atmospheres in the Solar system are substantially less altered, due to the absence of life and thus provide complementary information for understanding atmosphere evolution.

1.1 Growing a Planet

The process by which planets grow from protoplanetary discs (rotating discs of gas and dust surrounding young stars) is still not fully understood, but our understanding of planet formation has improved substantially in recent years. The existence of so many exoplanets and the evidence of planetary mass objects in protoplanetary discs clearly suggests that planet formation is both common and efficient (Blum, 2018). The details of this process will influence the types and numbers of exoplanets we observe, and so observing the structure and frequency of exoplanets and their atmospheres can help constrain planet formation processes. The occurrence rate of habitable zone Earth-like planets is estimated to be less than 0.3 per FGK star, but could be higher for planets around M dwarf stars (Hsu et al., 2019, 2020). The rings and gaps observed in a number of protoplanetary discs are interpreted as evidence of rapid planet formation (Williams & Cieza, 2011). The massive objects forming these disc sub-structures must form before the dispersal of the protoplanetary disc between $3 - 10$ Myr (Ercolano & Pascucci, 2017). Additionally, the existence of gas giant planets requires that their cores reach sufficient mass to begin runaway gas accretion within the lifetime of the disc, and terrestrial planet formation requires the formation of massive planetesimals to be complete early enough that the gas disc can damp their orbits (Morbidelli et al., 2012).

1.1.1 From dust to planetesimals

The formation of planets is broadly understood to occur in three stages. Firstly, dust forms mm−cm sized grains through collisional sticking mediated by the Van der Walls force (Birnstiel et al., 2010). Subsequent formation of km-sized planetesimals is challenging, as for grains larger than a few cm collisions become inefficient or even destructive, stalling grain growth (Blum & Wurm, 2008; Zsom et al., 2010). Furthermore, as grains grow they decouple from the gas that makes up the bulk of the protoplanetary disc and experience drag forces that cause them to migrate inwards efficiently, meaning that these grains should be removed rapidly from the disc before planets can form, the so-called radial drift problem

(Weidenschilling, 1977). Grains could overcome these barriers to planetesimal formation through fractal growth, which relies on the "stickyness" of grain monomers (Okuzumi et al., 2012), or via the streaming instability, through which clouds of pebble-sized objects undergo gravitational collapse to form km-sized objects (Rice et al., 2004; Youdin & Goodman, 2005; Johansen et al., 2007; Carrera et al., 2017). While this provides an efficient route for forming planetesimals and can reproduce the observed binary structures in the Kuiper belt (Nesvorný et al., 2019), it requires a high dust-to-gas ratio (at least in the location of the instability) and limitations on the Stokes number (Jacquet et al., 2011; Krijt et al., 2016). Which of these mechanisms is responsible for the growth of planetesimals, or indeed whether it is both or an alternative process remains the subject of debate.

1.1.2 From planetesimals to planets

Subsequent growth of planetesimals through gas drag mediated pebble accretion results in efficient formation of Moon to Mars-mass embryos (Ida & Makino, 1993). This process has been shown to be particularly efficient when pressure bumps are present in the protoplanetary disc (Chambers, 2021). Pebble accretion ceases when embryos become massive enough to dynamically stir their surroundings, decreasing their cross-section for collisional accretion (Johansen & Lacerda, 2010). The process by which these embryos become gas and ice giants is still debated, with two main theories emerging. Core accretion describes the formation of a solid core that undergoes subsequent runaway accretion of a gas envelope (Pollack et al., 1996; Rafikov, 2004; Levison et al., 2010). This mechanism predicts the existence of a sub-Saturn planet mass desert at semi-major axes below 3 au that has not yet been observed (Suzuki et al., 2018; Bennett et al., 2021). Alternatively, the gravitational instability theory describes the fragmentation and collapse of a massive protoplanetary disc to form a gas giant planet (Boss, 1997; Boley, 2009). The clumps formed through this mechanism must overcome fast migration through the disc, accretion onto the host star, and tidal destruction to form giant planets (Zhu et al., 2012). The embryos that survive beyond the lifetime of the protoplanetary disc without undergoing runaway gas accretion undergo giant collisions once the damping presence of the disc is removed, resulting in the formation of terrestrial planets (Chambers & Wetherill, 1998; Chambers, 2001). The left-over material from planet formation is then either ejected, transported onto long-term stable orbits or accreted as the "Late Veneer" (Morbidelli et al., 2018).

Exoplanetary systems show a diverse range of planet types and orbital architectures, but also many similarities to the non-planetary features seen in our own, such as exo-comets,

exo-asteroids, exo-zodiacal dust, and Kuiper belt and asteroid belt analogues (see for example Beust & Morbidelli, 1996; Wyatt, 2008; Krivov, 2010; Hughes et al., 2018; Kennedy, 2018). For this reason, greater understanding of planetary systems can be achieved through study of our own Solar system, exploiting the detailed observations that can now be made. The following section describes the current state of understanding of the dynamical evolution of the Solar system, and what this means for the formation and impact history of the terrestrial planets.

1.2 The dynamical history of the Solar system

The dynamical history of the Solar system will determine the rate and nature of impacts that occur onto the bodies in the Solar system, and so determine the relative importance of impacts on the evolution of their atmospheres. For many years, planet formation hypotheses have been unable to explain the multiple observed constraints with a self-consistent model of Solar system formation and evolution (Morbidelli et al., 2001). These constraints include the current orbits (semi-major axis, eccentricity, inclination and obliquity) of the planets; the properties of the asteroid belt, Jupiter's Trojans, the giant planets' irregular satellites; and the trans-Neptunian Objects (the Kuiper belt, scattered disc and Oort cloud). Furthermore, rock samples returned from the first Lunar missions were interpreted as evidence for an apparent spike in cratering impacts approximately 700 Myrs after planet formation, an event termed the Late Heavy Bombardment (Hartmann et al., 2000), although whether this represents a true increase in the impact flux and if so how it can be explained in a self-consistent dynamical model remains debated (Levison et al., 2001; Chambers & Lissauer, 2002; Gomes et al., 2005; Morbidelli et al., 2012, 2018).

1.2.1 The original Nice model

The Nice model (Tsiganis et al., 2005; Gomes et al., 2005; Morbidelli et al., 2005), describes the migration of the giant planets from nearly circular, compact, co-planar orbits surrounded by a primordial disc of small icy bodies, onto their present (eccentric, inclined) orbits. This is achieved in the original Nice model through inward migration of Jupiter while Saturn, Uranus and Neptune migrate outwards, until Jupiter and Saturn cross the $2:1$ mean motion resonance (MMR) resulting in a dynamical instability in the outer Solar system, eventually causing Uranus or Neptune to evolve onto Saturn-crossing orbits. Uranus and Neptune are then scattered outwards after close encounters with Saturn and Jupiter. This model can reproduce the final semi-major axes, eccentricities and inclinations of the giant planets (Tsiganis et al., 2005), and has had great success recreating many other observational constraints. These include the orbital distribution and mass of Jupiter's Trojans, in particular

the broad range of orbital inclinations, as well as their total mass (Morbidelli et al., 2005), the structure of the Kuiper belt (Gomes et al., 2005), and the irregular satellites of Saturn, Uranus and Neptune (Nesvorný et al., 2007).

1.2.2 The Grand Tack model

The initial conditions for the Nice model are provided by the "Grand Tack" model (Walsh et al., 2011), which describes the in-then-out resonant migration of Jupiter and Saturn within the gaseous protoplanetary disc. Jupiter is believed to have formed before Saturn and migrated inwards through the disc, undergoing Type II migration (Lin & Papaloizou, 1986), until Saturn formed. Resonant trapping of a lighter protoplanet can cause reversal of Type II migration, leading to outward migration of both planets. This idea has been extended, accounting for the global viscous evolution of the gaseous disc to show that Jupiter and Saturn initially both migrate inwards, with Saturn migrating more rapidly than Jupiter, eventually becoming trapped in the $3:2$ MMR (Morbidelli & Crida, 2007).

In Morbidelli & Crida (2007) the Nice model was reconsidered, using this new constraint (that the giant planets were in mutually resonant orbits as the gas disc dissipated) and found that the dynamical evolution was qualitatively similar. The capture of a Saturn mass planet into the $3:2$ MMR with a Jupiter mass planet, suggested by Morbidelli & Crida (2007), has been shown to be a common outcome of numerical simulations regardless of the initial conditions (Pierens & Nelson, 2008). The Grand Tack model proposes that Jupiter and Saturn migrate inwards until they become trapped in resonance. Once the gaps opened in the disc by the two planets overlap the inward migration reverses, and the two planets migrate outwards, still trapped in resonance. Once the gas disc dissipates, Jupiter is stalled at roughly 5.5 au, with Saturn in the $3:2$ MMR, and Uranus and Neptune also trapped in mutual resonances. This results in a compact resonant chain of almost circular, co-planar orbits, the initial conditions for the Nice model. The Grand Tack model is supported by its ability to reproduce the masses of Mars and the asteroid belt, and the observed mixing of asteroid populations (Bottke, 2015), and by the results of Pierens & Raymond (2011), who showed that the two-phase migration of Jupiter and Saturn is a robust prediction for sufficiently cool, isothermal discs.

1.2.3 Additions to the models

Despite the success of the original Nice and Grand Tack models, several observational constraints are not adequately reproduced by their combined predictions. The terrestrial planets are observed to have a low angular momentum deficit (AMD), defined as the total

angular momentum required to make the orbits perfectly circular and co-planar (Laskar, 1996), which cannot be replicated by this model. Slow crossing of secular resonances by Jupiter and Saturn is predicted to result in excessive excitation of the terrestrial planet orbits (Agnor & Lin, 2012; Brasser et al., 2009) which can cause instabilities. This constraint could be ignored if the giant planet instability occurred early, before terrestrial planet formation was complete (Kaib & Chambers, 2016).

The Nice model has been extended to include encounters between the giant planets in the "Jumping Jupiter" model (Morbidelli et al., 2010), in which Jupiter undergoes a number of scattering encounters with an ice giant, resulting in the sudden separation of Jupiter and Saturn, ending when a final encounter removes the scattering planet from Jupiter's orbit. This extension is needed to reproduce the orbital structure of the asteroid belt (in particular the Kirkwood gaps) and the observed ratio of excitation in Jupiter's eccentricity modes (Morbidelli et al., 2009). Dynamical models suggest that this occurred through several distinct scattering events, and favour an early instability, as late instabilities require extreme fine-tuning of the initial conditions (Deienno et al., 2017; de Sousa et al., 2020). A statistical study of the initial Solar system conditions by Nesvorný & Morbidelli (2012) found that it is challenging to reproduce the present day Solar system conditions with only four giant planets, as encounters between the planets during the instability were extremely violent (often resulting in ejection of at least one ice giant) when the planets were initially on compact, resonant orbits. To resolve this issue, they propose that there was at least one additional ice giant, which was ejected by Jupiter during the instability. The jumping-Jupiter model is also capable of recreating the orbital distributions of the known Jupiter Trojans as well as the observed asymmetry between populations in the two Lagrange points (Nesvorný et al., 2013).

A further problem that must be resolved in any model of Solar system evolution is the low rate of terrestrial planet survival in the Nesvorný & Morbidelli (2012) simulations, and the low AMD of the terrestrial planets. There have been two potential solutions to this problem proposed. Firstly, that there was initially another planet in the inner Solar system, located between Mercury and Venus, and a collision between this planet and Mercury reduced the AMD. Such a violent collision, capable of stripping the mantle of a proto-Mercury and ejecting the additional planet, is also invoked to explain why Mercury is similar in appearance to the core of a planetesimal (Asphaug & Reufer, 2014). Secondly, that the instability occurred early, before terrestrial planet formation was complete, and therefore when the inner Solar system architecture could have been different to its present state (Nesvorný & Morbidelli, 2012). The early instability hypothesis has accumulated support in recent years, as it can explain several key issues with the original Nice model beyond the terrestrial planet constraints (Nesvorný,

2018). An early instability would not only avoid the fine-tuning of the initial conditions required by the original Nice model (Gomes et al., 2005; Deienno et al., 2017) but also explain the small size of Mars compared to the other terrestrial planets (Clement et al., 2018).

1.2.4 The end of giant impacts

The rapid migration of the giant planets causes a period of intense bombardment onto the terrestrial planets. The giant impacts that characterise the final phase of terrestrial planet growth from Mars-size embryos to proto-planets eventually end. The final such impact onto Mars has been proposed as the origin of the Martian crustal dichotomy, the $4 - 8$ km elevation difference between the Northern Highlands and the Southern Lowlands (Marinova et al., 2008). For the Earth, the last giant impact (generally accepted as the last impact that caused global surface melting and mixing of surface melt with the core) is believed to be the Moon-forming impact. While it is widely accepted that the origin of the Moon was an impact between the proto-Earth and a smaller object (sometimes called "Theia"), the precise details of the collision remain debated (Canup, 2004; Ćuk et al., 2016; Lock et al., 2018). The stable isotope ratios are the same between the Moon and the Earth, implying vigorous mixing of material after a violent impact (Wiechert et al., 2001; Young et al., 2016), however the Moon appears depleted in volatiles relative to the Earth (Wolf & Anders, 1980). One explanation for this depletion is the formation of a "Synestia" (a short-lived, molten, doughnut-shaped object) produced after a fast-spinning proto-Earth was impacted by a Mars-sized embryo (Lock et al., 2018). Alternatively, the Moon and Earth may have formed together after the collision of two larger embryos (Canup, 2012).

1.2.5 Continued accretion of a Late Veneer

Regardless of the precise mechanism through which the Moon formed, the final differentiation of the Earth's core occurred afterwards, with all the highly siderophile elements (HSEs) sequestered into the metallic core. Due to their high affinity for metals, HSEs are preferentially sequestered into the core of an object as it differentiates. Consequently, excess HSEs measured in the crust of a body are believed to record the amount of material accreted since core formation.

HSEs provide a mechanism through which to constrain the subsequent bombardment of the Earth and Moon after this final giant impact, since direct evidence of early impacts on Earth in the form of craters does not exist due to crustal processing by tectonic activity, with the oldest known impact crater only 2.2 Gyr old (Erickson et al., 2020). HSE abundances in the mantles

of the Earth, Moon and Mars are all in chondritic proportions, which supports the argument that their higher than expected abundances are due to delivery in a "Late Veneer" rather than inefficient core formation[1]. Mantle HSE measurements imply that approximately (0.5 ± 0.2) %wt. of Earth's mass (3×10^{22} kg) was delivered in the Late Veneer, and approximately 0.025% wt of the Moon's mass (2×10^{19} kg) was delivered in the same manner (Day et al., 2007; Day & Walker, 2015; Day et al., 2016). These estimates are supported by Tungsten isotope measurements (Willbold et al., 2015; Touboul et al., 2015). Both the Tungsten and HSE measurements imply that the Earth accreted around 10^3 times the mass that the Moon accreted, despite having a gravitational cross-section only 20 times larger.

There have been several explanations proposed to resolve this discrepancy. Bottke et al. (2010) suggest that the size distribution of the objects that delivered the Late Veneer was dominated by the largest objects, and accretion was therefore a stochastic process, statistically favouring impacts with the Earth rather than the Moon (Brasser et al., 2016). Genda et al. (2017) extend this, proposing that a single giant impactor (*Moneta*) delivered the entire terrestrial HSE budget. Alternatively, a size distribution dominated by small bodies proposed by Schlichting et al. (2012) invokes the difference in gravitational focusing between the Earth and the Moon to explain the discrepancy. Finally, the geochemical history of the Moon may have been more complex than previously assumed (Morbidelli et al., 2018), and the discrepancy between the Earth and Lunar HSE abundances may be explained through a combination of lower than expected impactor retention for the Moon (Zhu et al., 2019) and sulfide segregation of HSEs into the core during the end of the Lunar magma ocean crystallisation and mantle overturn (Elkins-Tanton et al., 2011; Rubie et al., 2016).

This accretion tail scenario is discussed in detail in Morbidelli et al. (2018), and has been a major recent advance in the field, successfully explaining both the HSE constraints on the Earth and the Moon and the Lunar cratering record within the context of the most recent numerical simulations of the fluxes of comets, asteroids and left-over planetesimals. In the accretion tail scenario the impact rate onto the terrestrial planets has been declining since terrestrial planet formation concluded, and this is favoured over invoking a spike in impact rates around 3.9 Gya[2], known as the Lunar terminal cataclysm (Morbidelli et al., 2018). The lower Lunar abundance of HSEs therefore reflects a later onset of accumulation in the mantle due to later Lunar mantle solidification at $100 - 150$ Myr after formation (Elkins-Tanton et al., 2011).

[1] As they are present in the mantle in amounts that are similar relative to the abundances measured in CI-chondrites, rather than following trends in solubility

[2] Gya = Giga-year ago, using the geosciences convention of counting backwards in time

Estimates of the corresponding Late Veneer masses on Venus and Mars are less well constrained. No direct isotopic measurements of the surface of Venus have been made, and so the only estimates for the mass of material accreted after core formation come from dynamical simulations of the impacting material. These imply the accretion of 0.8% wt. in dry chondritic material (Gillmann et al., 2020). For Mars, the measured HSE excesses result in estimates that range from 0.25% wt. (Brandon et al., 2012; Taylor, 2013; Marchi, 2020) to 1.4% wt. (Brasser et al., 2016), in a volatile-poor Late Veneer. This variation is due to alternative hypotheses regarding the impact chronology and the core formation scenarios (Righter et al., 2015).

1.3 Atmospheric evolution processes

Growth of a terrestrial planet atmosphere can occur through accretion of primordial gases from the pre-stellar nebula, mantle outgassing from magma oceans, volcanic outgassing, or delivery by impactors, while the atmosphere may be lost as a result of escape to space, impacts during the final stages of planet formation, or mantle ingassing. In the following section, I briefly describe these processes and how observations constrain their influence on the Earth's atmosphere.

1.3.1 Escape processes

Atmosphere escape processes are typically divided into thermal and non-thermal processes. The thermal escape processes depend on the upper atmosphere temperature, which is controlled by the location of the planet and the host star's extreme and X-ray UV (EUV-XUV) flux. Thermal atmosphere mass loss is typically split into Jeans escape (whereby individual particles in hot atmospheres are accelerated above the planet escape velocity) and hydrodynamic escape (when bulk loss of the atmosphere occurs due to thermal acceleration). Hydrodynamic escape of light atmosphere components can "drag" heavier elements or isotopes with it (Gronoff et al., 2020). These two regimes represent opposite ends of a continuum of atmosphere mass loss, with hydrodynamic escape favoured when the thermal velocity is high relative to the planet escape velocity (Volkov et al., 2011).

Non-thermal mechanisms are many and complicated, but in essence involve the acceleration of particles in the atmosphere above the planet escape velocity. The acceleration can be caused by solar radiation, through processes including photo-chemical escape, ion pickup or sputtering, charge exchange, and ion outflow. Other ion escape can occur through plasma instabilities lofting ions upwards before they can be picked up by the solar wind (Gronoff et al., 2020).

These non-thermal mechanisms are most important when the solar radiation is energetic, early in the Sun's evolution, and so are neglected in this dissertation.

1.3.2 Earth's atmosphere

The relative abundance of observational measurements for the Earth provide a unique opportunity to apply observational constraints to models for the evolution of terrestrial planet atmospheres. Each of the potential atmosphere evolution processes listed above should leave observable traces in the geochemistry of the atmosphere and solid Earth. Observational constraints include volatile concentrations, isotopic ratios and elemental ratios, for both the Earth's reservoirs and Solar system bodies. Absolute concentrations are challenging to measure (since mantle concentrations must be estimated from partially devolatilised basalt samples), and so volatile ratios (C/H, C/S, C/N, etc.) are extremely important for comparison between Earth and Solar system body measurements, as are the abundances and isotopic ratios of noble gases. Simple mass fractionation arguments predict that heavy noble gases should be less depleted and less fractionated in the atmosphere. However xenon is both more depleted and more fractionated that krypton, a lighter noble gas, this is known as the "missing xenon" paradox. Interpretation of these signatures is further complicated due to the substantial evolution of the atmosphere, in particular due to the presence of a biosphere, something that appears unique to Earth. The origin and evolution of Earth's atmosphere is a topic that is far from resolved (see for example Chyba, 1990; Elkins-Tanton et al., 2011; Halliday, 2013; Marty et al., 2016; Zahnle et al., 2020). A brief (and non-exhaustive) summary of the constraints and their interpretation in relation to three mechanisms relevant to atmospheric evolution (hydrodynamic escape, mantle outgassing and impacts) are described in the following sections.

1.3.3 Hydrodynamic escape

It has been proposed that the proto-Earth accreted a hot hydrogen-dominated atmosphere of Solar-composition nebular gas during formation (Hayashi et al., 1979; Ikoma & Genda, 2006) that was lost through hydrodynamic escape (Pepin, 1991; Dauphas, 2003), and the present day abundances and isotope ratios of the elements are a result of subsequent mantle outgassing and projectile delivery. This has been invoked by Pepin (1991) to explain the "missing xenon" paradox, through the preferential loss of light xenon isotopes via hydrodynamic escape. The previous existence of a primary atmosphere is also supported by observations of helium and neon with solar isotope ratios in the Earth's interior (Harper & Jacobsen, 1996). However there are arguments against significant retention of a primary atmosphere.

Firstly, the abundances of noble gases appear more similar to those seen in carbonaceous meteorites than to the Sun (Zahnle et al., 2007), suggesting an alternative source. Furthermore, hydrodynamic escape should result in isotopic fractionation, as lighter isotopes are preferentially removed with the escaping bulk H_2, leaving behind an atmosphere enriched in heavy isotopes relative to the mantle. This prediction fits the data for neon on Earth, with isotopically lighter neon present in the mantle compared to the atmosphere (Ozima & Podosek, 2002). However the mantle is enriched in heavy isotopes of other noble gases including krypton (Holland et al., 2009), contradicting this. Finally, the isotope compositions of H, C, N and Cl preserved in the mantle are chondritic (Marty, 2012; Halliday, 2013; Sharp & Draper, 2013), which would require hydrodynamic H_2 loss to cease at precisely the point when these compositions were reached for each element, a different time for each different element, which is very unlikely (Schlichting & Mukhopadhyay, 2018). This leads to the conclusion that hydrodynamic escape of a primordial atmosphere alone cannot explain all the observations of Earth's atmosphere, but should not be discarded entirely as it can explain some.

1.3.4 Mantle outgassing and ingassing

Mantle outgassing describes the process by which volatiles are released from the mantle. Violent impacts during the giant impact phase of planet formation are believed to result in global magma oceans on Earth (Elkins-Tanton, 2012). Plume mantle sources and mid-ocean ridge basalts (MORBs) both sample the Earth's mantle, with the plume sources sampling the deeper and thus less processed mantle reservoirs relative to the MORB sources. Measurements of the noble gasses helium and neon are of particular relevance because they are not recycled back into the mantle and so should preserve signatures of the ancient magma ocean (Porcelli et al., 2001). The $^3He/^{22}Ne$ ratio of the plume sources is approximately $2-3$, while the MORBs have an even higher ratio of ~ 10. Helium is more soluble than neon in the mantle by roughly a factor of 2, a phenomenon invoked by Honda & McDougall (1998) to explain the MORB measurements. This difference in solubilities means that magma ocean outgassing is capable of increasing the $^3He/^{22}Ne$ ratio, and therefore the difference between the plume and MORB sources implies a difference in the outgassing history of the deep and shallow mantle reservoirs.

Ingassing (dissolution of volatile elements from the atmosphere into the magma ocean) could have the same impact on the $^3He/^{22}Ne$ ratio, and the importance of this mechanism is supported by observations of Solar-wind-like neon isotopic ratios in the Kola plume (Yokochi & Marty, 2004). However, $^3He/^{22}Ne$ ratios in the plume and MORB sources are both

super-Solar, an observation that cannot be explained solely by ingassing (Schlichting & Mukhopadhyay, 2018), nor by mantle outgassing associated with long term tectonic cycling. It can however be explained through a series of giant impact-induced magma ocean phases which undergo ingassing and associated episodes of atmosphere loss (Tucker & Mukhopadhyay, 2014), or alternatively through crystallisation of a basal magma ocean (Coltice et al., 2011). The loss of the existing, equilibriated atmosphere is necessary for the $^{3}He/^{22}Ne$ ratio to be changed by an episode of magma ocean outgassing, but this is a natural consequence if these magma oceans are created by giant impacts (Schlichting et al., 2015). The difference in solubilities of helium and neon means that a single episode of outgassing could at most enrich the mantle in helium by a factor of two, and therefore the higher MORB $^{3}He/^{22}Ne$ ratio implies that multiple magma oceans and associated atmosphere loss episodes occurred (Schlichting & Mukhopadhyay, 2018).

The prediction for multiple giant impacts capable of forming magma oceans is supported by dynamical simulations, implying (as discussed in §1.1) that the final stages of terrestrial planet formation are characterised by violent collisions between planetary embryos (Chambers & Wetherill, 1998; Chambers, 2001). At the end of the giant impact stage, after the Moon-forming impact, the majority of the mantle was molten (Canup, 2004). As the planet cools and the magma ocean solidifies, volatiles can be degassed into the atmosphere, resulting in the formation of a secondary atmosphere, dominated by H_2O , CO, CO_2 and H_2 (Thompson et al., 2021). Noble gas concentrations should be fractionated in magma oceans, due to their differing solubilities. However, the mantle and atmosphere have non-radiogenic ratios of neon and krypton (Holland et al., 2009) with the atmosphere enriched in ^{22}Ne relative to the mantle (Marty, 2012) and depleted in ^{84}Kr (Halliday, 2013). This cannot be explained through either outgassing, or a combination of outgassing and hydrodynamic loss (Schlichting & Mukhopadhyay, 2018), and therefore another process must be affecting the mantle composition, potentially the effect of impacts onto the Earth. The giant impact phase begins at a time when the total mass contained in the planetesimals is comparable to the total mass contained in the protoplanets, and impacts by these planetesimals continue throughout the giant impact phase and beyond (Morbidelli et al., 2018).

1.3.5 Impacts

Despite the chondritic isotope ratios of many individual volatile elements (H, C, N and Cl) in the mantle, the relative abundances of these volatiles in the Earth's atmosphere are not chondritic (Marty, 2012; Halliday, 2013). In combination with the fact that impacts are an inevitable consequence of Solar system formation models, these observations have been used

to argue for the significance of impact-induced atmospheric evolution. Impacts result in the delivery of mass and energy to the atmosphere, and thus can both erode existing atmospheres and deliver volatiles that replenish the atmosphere (Zahnle et al., 1992; Shuvalov, 2009; Schlichting et al., 2015). Furthermore, impacts are also capable of melting the surface of a target body, releasing previously trapped volatiles in a process known as impact-triggered outgassing (Artemieva & Lunine, 2005; Kraus et al., 2011).

Impacts can be studied in lab-based experiments, using high-speed photography to study small impacts in detail, for example in Housen & Holsapple (2011). Theoretical predictions have also been made, for example the vapour plume expansion model of Zel'dovich & Raizer (1967) and more recently in Schlichting et al. (2015) and Yalinewich & Schlichting (2019). Detailed hydrodynamic simulations of atmosphere loss and delivery have been carried out by, among others, Svetsov (2007), Shuvalov (2009) and Shuvalov et al. (2014). More recently, prescriptions for the outcome of larger impacts based on numerical smoothed particle hydrodynamic (SPH) simulations have been derived by Kegerreis et al. (2020a), Kegerreis et al. (2020b) and Denman et al. (2020).

Different methods for studying impacts probe different impact regimes. Impactors that are large enough to penetrate through the atmosphere to reach the ground intact but that are not so massive that they cause global distortion of the target can be modelled as point source explosions on the surface and are referred to as *cratering* impacts (Svetsov, 2007; Shuvalov, 2009). *Giant* impacts are those massive enough relative to the target to cause global effects, by eroding the target or by causing a shock wave to propagate through the target, resulting in atmosphere loss from the antipode (Schlichting et al., 2015; Denman et al., 2020). Objects that impact a bare target can deliver volatiles, resulting in the growth of an atmosphere from an initially atmosphere-less planet in the *airless limit* (Shuvalov, 2009; Cataldi et al., 2017). Conversely, impactors in particularly dense atmospheres may break up in flight due to aerodynamic stresses, undergoing *fragmentation* (where the impactor splits into multiple parts that impact the surface) or *aerial bursts* (where the impactor is completely destroyed in the atmosphere and does not reach the surface), delivering more energy to regions of the atmosphere at higher altitudes. A detailed explanation of varied impactor prescriptions that are included in this dissertation is given in Chapter 2.

1.4 Impact atmosphere studies

Comparative studies of the evolution of Solar system atmospheres as a result of impacts were first conducted for the outer moons Titan, Ganymede and Callisto, by both Zahnle et al. (1992) and Griffith & Zahnle (1995) using a relatively simple "snowplough" impact prescription. Within this framework impactors above critical mass and velocity values are assumed to remove the entire atmosphere mass above the tangent plane at the impact site, while impactors below these values are assumed to contribute their entire volatile content to the atmosphere. The results of these two studies are similar, finding that impacts result in overall growth of an atmosphere on Titan and erosion towards a small atmosphere mass on Ganymede and Callisto. Significant stochastic variation was observed in Griffith & Zahnle (1995) due to the inclusion of a Monte-Carlo impactor sampling approach.

In Pham et al. (2011) the authors attempted to explain the differences between the present day atmospheres of Earth, Venus and Mars through asteroid and comet impacts, concluding that impacts could erode Mars' atmosphere but deliver volatiles to Venus and Earth. In de Niem et al. (2012) the inherent stochasticity of impact sizes and velocities during a period of heavy bombardment was studied on Earth and Mars by implementing prescriptions for atmospheric erosion and impactor accretion based on the results of Svetsov (2000). They considered the effect of varying the impactor compositions (through the ratio of asteroid- to comet-like impactors) and the initial atmospheric pressure, finding that impacts by such populations should result in atmospheric growth for both Earth and Mars.

More recently, the prescription from Shuvalov (2009) was used in Marounina et al. (2015) to investigate the evolution of Titan's atmosphere during a proposed late heavy bombardment scenario. The results from this study suggest that impacts cause significant atmospheric erosion on Titan. The inclusion by Marounina et al. (2015) of a prescription for impact-triggered outgassing using the prescriptions from Kraus et al. (2011) and Sekine et al. (2011) can cause the release of a significant mass of volatiles into the atmosphere, resulting in atmospheric growth. Impact-triggered outgassing, and its relevance to the terrestrial planets and icy moons, is discussed in §2.1.5.

The effect of impacts on exoplanet atmospheres was studied for the first time in Kral et al. (2018), which investigated volatile delivery and atmosphere erosion of the primordial atmospheres of the TRAPPIST-1 planets by comets. In Wyatt et al. (2019), an analytical model for the evolution of an atmosphere due to impacts that can both remove atmosphere mass and deliver volatiles, based on the prescription of Shuvalov (2009), was developed. This model

quantifies how the growth or loss of an atmosphere depends sensitively on the assumptions made about the impact velocity, and the composition and size distribution of the impactors. Furthermore, the initial atmosphere mass was also found to be an important factor in determining the atmospheric evolution resulting from impacts, with the same impactor population theoretically capable of causing growth of an small atmosphere and erosion of an large atmosphere (Wyatt et al., 2019). This can lead to an equilibrium solution, whereby the atmosphere mass is maintained at a constant value by impacts, as discussed in Schlichting et al. (2015). When applied to the Earth, the results of Wyatt et al. (2019) showed that either growth or loss were possible.

Most recently, in Sakuraba et al. (2019) the evolution of the atmospheres of Earth, Venus and Mars were considered using a numerical model based on the results of Svetsov (2000) and Svetsov (2007) to parameterise impactor accretion and Shuvalov (2009) to parameterise atmosphere mass loss. This work aimed to explain the cause of a significant gap between the abundances of nitrogen and the noble gases in the current atmospheres of all three terrestrial planets through element partitioning, which is believed to vary between the planets due to their differing geochemical processes (runaway greenhouse effects on Venus, the carbon-silicate cycle and the presence of oceans on the Earth and the formation of water and CO_2 ice on Mars). Impacts by a single population of relatively volatile-rich impactors result in atmosphere growth from atmosphere masses similar to their present day values on these planets, although the most massive initial atmospheres on Venus are depleted, resulting in convergence towards an atmosphere pressure of approximately 50 bar.

As described in §1.2, dynamical models of the Solar system predict an extended accretion tail of impacts that continue for 100s of millions of years after terrestrial planet formation is complete. These previous investigations of the evolution of the terrestrial planet's atmosphere have not considered the new model for the impact history of the Earth presented in Nesvorný et al. (2017a), Nesvorný et al. (2017b) and Morbidelli et al. (2018), assuming that the impact rate onto the terrestrial planets has been declining since planet formation concluded.

In order to understand the evolution of the atmospheres of Mars, the Earth, Venus and the outer moons as a result of impacts, it is necessary to understand both the properties of the impactors (their size, composition, impact flux, and velocity relative to the target body), which may vary over time, and the effect of each impact on the atmosphere. Within the context of the Solar system, these impactors can be categorised into three populations:

- Comets: icy bodies originating from the Trans-Neptunian disc;

- Asteroids: rocky volatile-rich objects originating from the asteroid belt;
- Planetesimals left-over from the terrestrial planet region after terrestrial planet formation (hereafter referred to as left-over planetesimals): which are rocky and very volatile-poor due to their formation location in the hot inner region on the protoplanetary disc.

The latter of these populations is believed, based on isotopic constraints (Gillmann et al., 2020), to make up the bulk of the material impacting the Earth and Mars (and therefore Venus also), but have not previously been studied in the context of their effect on the atmospheres of the terrestrial planets. This dissertation addresses these questions, using the most recent dynamical models to investigate the evolution of the terrestrial planet atmospheres due to impacts by these bodies. These populations are described in detail in §3.1 in the context of their application to the Earth, and §5.1.1 for Venus and Mars, where I discuss the assumptions made regarding their properties including impact fluxes, size distributions and compositions.

1.5 Atmosphere evolution on Venus and Mars

Despite the relative similarity of Venus, Earth and Mars' formation conditions, these terrestrial planets display extreme atmosphere diversity. How they acquired their current atmospheres, and what the conditions may have been like in the past are still open questions.

1.5.1 Current atmosphere states

Venus currently has a massive, hot atmosphere, with a surface temperature of 740 K and surface pressure of 93 bar. The mass budget is dominated by carbon dioxide (96.5%), with a 3.5% contribution from nitrogen, three times the budget in the Earth's atmosphere. There are further trace amounts of other species such sulfur dioxide in the form of optically thick clouds, argon, water vapour and carbon monoxide (Basilevsky & Head, 2000; Bertaux et al., 2007). Unlike the Earth, Venus has no intrinsic magnetic field, but the upper ionised layers of the atmosphere provide an induced magnetosphere that protects the lower atmosphere from the Solar magnetic field. Lighter gases, such as water, are continuously lost from the atmosphere along the induced magnetotail as a result of the solar wind (Svedhem et al., 2007).

Mars currently has a thin, cool atmosphere, less than 1% of the present day mass of Earth's atmosphere, composed predominantly of carbon dioxide, with smaller amounts of nitrogen and argon, as well as trace water vapour, and other noble gases (Mahaffy et al., 2013). The surface pressure shows seasonal variability of up to 25% due to the condensation of CO_2

during the Martian winter (Sindoni et al., 2011; Trainer et al., 2019). The N_2 budget is enriched in heavier ^{15}N, suggesting that mass-selective escape processes have been significant, supported by evidence that Mars is also enriched in ^{38}Ar relative to ^{36}Ar. Mars also seems to be enriched in ^{40}Ar, produced by the radioactive decay of ^{40}K, which cannot be explained by mass-selective loss processes. This observation provides evidence that impact erosion was significant during the early history of Mars, removing a significant portion of the primordial atmosphere (which contained primordial ^{36}Ar), leaving the ^{40}Ar excess to be produced by the later decay of ^{40}Kr.

1.5.2 Formation and evolution models

Some have argued that Venus may have been habitable early in its history. Depending on the initial conditions assumed for the orbit, volatile content and rotation rate of Venus, models have suggested that the surface of Venus could cool sufficiently to condense a liquid water ocean underneath clouds. This would allow a climate similar to the Archean Earth to persist for up to 2 Gyr before increasing Solar radiation triggered a runaway greenhouse phase (Kasting & Harman, 2013; Way et al., 2016; Salvador et al., 2017; Way & Del Genio, 2020). There are issues with this, in particular the removal of O_2 (produced by dissociation of a liquid water ocean by the solar wind) through hydrodynamic escape after such a long time period (Lichtenegger et al., 2016). Furthermore, the orbital distance of Venus is close to a critical value at which the condensation time of an early outgassed steam atmosphere above a magma ocean can increase from a few Myr (as is believed to be the case for Earth) to $\sim$ 100 Myr, long enough for the planet to become desiccated by hydrodynamic escape (Hamano et al., 2013; Massol et al., 2016). It may therefore be more likely that there was never a liquid ocean on Venus and instead water was removed early through hydrodynamic escape, triggering the solidification of the Venusian magma ocean (Gillmann et al., 2009; Elkins-Tanton, 2012). In this scenario, CO_2 is produced by outgassing from a magma ocean, volcanism, and exogenous delivery through impacts (Lichtenegger et al., 2016). Oxygen can be incorporated into the hot crust, oxidising the upper mantle (Gillmann et al., 2009). Mixing of this oxidised surface material with reduced N_2-rich material in the deep interior of Venus would cause increased N_2 outgassing, potentially explaining the high nitrogen mass in Venus' atmosphere in comparison to the Earth (Lichtenegger et al., 2016). It is not certain whether plate tectonics ever existed on Venus (O'Neill et al., 2007; Noack et al., 2012). Water in the lithosphere is believed to be important for plate tectonics, therefore a desiccated Venus may not have been able to support plate tectonics (Solomatov, 2004). Without plate tectonics, CO_2 cannot be subducted into the mantle, and in combination with volcanic outgassing, will accumulate in the atmosphere. The carbonate-silicate cycle maintains a stable surface

temperature on Earth, but requires liquid surface water to operate. The absence of this feedback loop on Venus allows the runaway greenhouse effect to occur, with increasing CO_2 driving increased atmosphere temperature, producing the atmosphere seen today.

The origin and evolution of Mars' atmosphere continues to be debated. Evidence for liquid surface water is provided by valley networks, which are common on equatorial Noachian ($4.25- \sim 3.5$ Gya) terrain (but rare on younger surfaces), as these imply the presence of a hydro-logical cycle that persists for at least 10^6 to 10^7 years (Mangold et al., 2004; Hoke et al., 2011). Further evidence comes from crater lakes, which are a natural outcome of valley formation on cratered surfaces and can provide information about the water cycle. The high number of closed lakes in comparison to lacustrine features (open basins formed when flow rates are high enough to overflow closed lakes) on Mars disfavours both periodic catastrophic flooding and a very wet early climate (Barnhart et al., 2009). The Martian rover Curiosity found evidence for in situ fluvial erosion at Gale crater, but chemical analysis suggest low aqueous alteration of the minerals, implying that the eroding flows were short in duration. Finally, Fe and Mg-rich phyllosilicates (clays) are common on Noachian terrains, requiring the existence of water if they formed on the surface, although arguments have been made for subsurface formation in water-poor geothermally-heated regions, followed by transport to the surface via erosion (Williams et al., 2013). Carbonates should be formed efficiently on a warm and wet planet with a basaltic crust and CO_2-rich atmosphere, and thus the low abundance of carbonates implies that early Mars was either very dry or only warm episodically (Pollack et al., 1987; Niles et al., 2013).

Climate models of Mars in a Late Noachian Icy Highlands model find that several hundreds of metres of water ice could have existed as glaciers in the highlands. Transient top-down melting of these glaciers could provide a large reservoir of melt water capable of forming the observed geological features (Fastook & Head, 2015). Comparisons of this cold and icy scenario to a warm and wet climate using 3D general circulation models in Wordsworth et al. (2015) found that high solar flux or artificial greenhouse warming is required to maintain the warm, wet climate. Episodic melting in the cold and icy case, driven by the combined effects of impacts, seasonal forcing and volcanoes, can successfully recreate the distribution of valley networks, which is not the case for warmer climate (Wordsworth et al., 2015; Palumbo et al., 2018). More recent models provide further evidence for episodic heating of an otherwise cold and icy climate causing periods of flooding through glacial melting, rather than prolonged Earth-like conditions (Boatwright & Head, 2021; Wordsworth et al., 2021).

1.6 Atmosphere evolution on moons of the gas giants

Much like the terrestrial planets, the moons of the giant planets in our Solar system display a large degree of variation among their bulk properties and atmospheres. I consider the evolution of atmospheres on these moons as a result of impacts in Chapter 4. The three largest Jovian moons - Ganymede, Callisto and Europa - are diverse in terms of their mass and inferred internal structures, but are similar in terms of the low atmospheric pressures estimated on their surfaces. Saturn's moon Titan is similar in size to Ganymede and Callisto, but is unique for being the only moon to possess a substantial atmosphere. This atmosphere is composed mainly of nitrogen with a smaller methane component and has a surface pressure of 1.5 bar (Strobel, 1982; Coustenis, 2005). Neptune's largest moon Triton is close in size to Europa, yet has a tenuous nitrogen atmosphere and a surface layer of frozen nitrogen while Europa is essentially bare (Ingersoll, 1990; Hall et al., 1995; Ruiz, 2003).

Moons orbiting planets outside our own Solar system (exo-moons) are yet to be detected, despite likely existing. This is due to the significant difficulties in extracting the faint signal and distinguishing between an exo-moon and other effects such as further unseen planets or starspots. Models suggest that in-situ formation of such a moon (approximately Neptune-sized orbiting a super-Jovian planet) is plausible (Moraes & Vieira Neto, 2020). Transit timing variations (TTVs) are one promising avenue, however distinguishing exo-moon signatures from the effect of other unseen planets remains challenging (Kipping, 2009; Heller et al., 2016). Transit duration variations are potentially a less ambiguous detection method, and apparent planetary transit radius variations may provide further means of detecting exo-moons using combined KEPLER, PLATO and TESS data (Awiphan & Kerins, 2013; Heller et al., 2016; Rodenbeck et al., 2020).

While multiple candidate exo-moons have been proposed (Fox & Wiegert, 2021), these have been disputed (Kipping, 2020). The most promising candidate remains an earlier discovery, Kepler 1625b-i, although even this has not be unambiguously determined to be an exo-moon (Teachey & Kipping, 2018). As observational capabilities improve it will be possible to detect and even characterise exo-moons. Exo-moons remain a promising possibility when considering habitable environments outside out own Solar system (Lammer et al., 2014). For this reason it is important to understand the processes that will influence their atmospheres and thus their potential to host life. The potential for impacts to shape the atmospheres of exo-moons is explored in §6.2 in Chapter 6. The processes determining atmosphere evolution on exo-moons are similar to those that act on planetary atmospheres, described in §1.3.2, but can be complicated by interactions between the planet and the moon. This is particularly

complex if the moon resides inside the magnetic field of the planet. Furthermore, small icy bodies can store significant volatile masses in their crust which can be released by impact-triggered outgassing. Indeed, the potential outgassed origin of Titan's atmosphere proposed by Marounina et al. (2015) is supported by the measured D-H ratio and excess CH_4 in comparison to CO, which suggest that cometary volatiles are not the likely direct source of the atmospheric material on Titan (Coustenis, 2005).

1.7 Outline

In this thesis I investigate the effect of bombardment by small bodies on the evolution of atmospheres on planets and moons. In Chapter 2 I describe the prescription used to parameterise the effect of a range of impact outcomes (fragmentation, aerial bursts, cratering events and non-local mass loss caused by giant impacts) and present an analytic method through which the characteristic stalling mass (at which impact-induced erosion and accretion are balanced) can be predicted. I also describe the numerical model for stochastic atmosphere evolution due to bombardment, incorporating prescriptions for a range of impact outcomes that I have developed. In Chapter 3 I describe the application of the code to the evolution of Earth's atmosphere due to bombardment by asteroids, comets and left-over planetesimals, using distributions of impact velocities I calculate from the results of recent dynamical simulations. In Chapter 4, the analytic model and code are applied to cometary impacts of the atmospheres of the moons of the outer giant planets, incorporating a prescription for impact-triggered outgassing when applied to Titan. This chapter also includes a description of the timescales involved with atmosphere evolution as a result of impacts, which can be used to predict the degree of stochastic variation expected for a given atmosphere and impactor combination. The sensitivity of these results to both the initial atmosphere conditions and the properties of the impacting populations are investigated. In Chapter 5, these models are applied to the atmosphere evolution of Venus and Mars using the same framework as for the consideration of Earth's atmosphere. Finally in Chapter 6, I make general predictions about the influence of impacts on the atmospheres of exoplanets and hypothetical exo-moons and discuss directions for future work. My conclusions are presented in Chapter 7.

2

A statistical code of stochastic bombardment to model the evolution of an atmosphere

The outcome on the atmosphere of an impact will depend on the impactor energy, whether the impactor reaches the surface intact, and if so whether it causes global effects. The effect of impacts on planetary atmospheres was first studied in Melosh & Vickery (1989), Vickery & Melosh (1990) and Ahrens (1993) using the vapour plume expansion model of Zel'dovich & Raizer (1967). This was extended to consider the atmosphere evolution during an extended period of bombardment in Zahnle et al. (1992), with giant impacts studied in Genda & Abe (2003). Detailed simulations of atmosphere loss and delivery have been carried out by Svetsov (2007) and Shuvalov (2009) considering a range of impactor parameters including density, velocity and impact angle. A theoretical framework within which to understand these simulation results was given in Schlichting et al. (2015). The fragmentation of impactors in the atmosphere, leading to aerial bursts was studied in Shuvalov & Trubetskaya (2007) and first applied to the Earth in Shuvalov et al. (2013) with an prescription for the kind of impact (cratering, fragmenting or aerial burst) presented in Shuvalov et al. (2014).

Further atmospheric effects resulting from impacts have also been investigated. Schlichting et al. (2015) studied non-local mass loss caused by giant impacts on planet atmospheres, extending their predictions to high-velocity giant impacts in Yalinewich & Schlichting (2019).

More recently, prescriptions modelling the outcome of giant impacts based on SPH simulations were derived by Kegerreis et al. (2020b) Kegerreis et al. (2020a) and Denman et al. (2020), which I discus and compare to those of Schlichting et al. (2015) in §2.1.2. While most of these studies are primarily focused on Earth-like atmospheres there have been a smaller number of investigations into the effect of impacts on less dense atmospheres on smaller targets (Thébault & Augereau, 2007; Cataldi et al., 2017, for example), relevant for Mars and the moons of the giant planets.

The numerical code developed in this dissertation combines multiple prescriptions for the outcome of an impact in an attempt to cover as much of the parameter space spanned by potential impactors as possible. Cratering impacts are described by the prescriptions presented in Shuvalov (2009), and were incorporated into the analytic model described in Wyatt et al. (2019). Large impactors, that can cause additional non-local atmosphere loss through global ground motion, are described in Schlichting et al. (2015) and their inclusion is discussed in §2.1.2. The combination of the cratering and giant impact prescriptions used in the first iteration of my numerical code, applied to the Earth in Chapter 3 is described in §2.1.3. The extrapolation of these prescriptions into the regime where the atmosphere mass becomes very small, the "airless limit", is discussed in §2.1.4.

The inclusion of a specific prescription for impact-triggered outgassing from water ice, relevant for the study of Titan's massive atmosphere in Chapter 4 is discussed in §2.1.5. The extrapolation of the Shuvalov (2009) cratering prescription to parameters beyond the scope of the initial simulations should be done with caution, as if impactors do not reach the ground and cause a cratering event then different physical processes determine the outcome. Impacts of this kind, where the impactors may be slowed sufficiently to cause aerial bursts or fragment during their flight are described in §2.1.6.

The method by which an analytic prediction for the behaviour of an atmosphere under bombardment by a given population of impactors is presented in §2.3. This allows the determination of both the qualitative behaviour of the atmosphere and the calculation of an analytic "stalling mass", the atmosphere mass at which mass gain and loss rates are equal and the atmosphere mass evolution stalls.

The first iteration of the numerical code developed to study the stochastic evolution of an atmosphere, used to study the Earth in Chapter 3 is presented in §2.2. The validation and testing of this version is described in §2.4. The inclusion of impact-triggered outgassing into

the code for use in the study of the moons in Chapter 4 is discussed in §2.5.2. The second version of the code, used to study Venus and Mars in Chapter §5 is described in §2.5.3. This includes the addition of the impactor fragmentation and aerial burst prescriptions and the modification of the code to use a pre-calculated grid of atmosphere mass loss and impactor mass accretion values. The testing of this version of the code is described in §2.6.

2.1 Prescriptions

2.1.1 Cratering impacts

The analytic prescriptions from Shuvalov (2009) are fits to the angle-averaged results from simulations of impactors with a range of sizes ($D = 1 - 30$ km), impact velocities ($v_{\rm imp} = 10 - 70$ km s^{-1}) and densities ($\rho_{\rm imp}$), undergoing cratering impacts on an Earth-like planet. The atmosphere mass changes resulting from an impact are presented in terms of a single parameter, the erosional efficiency (η). This is a function of the impactor properties (D, $\rho_{\rm imp}$ and $v_{\rm imp}$) and target (planet or moon) properties (escape velocity $v_{\rm esc}$, density $\rho_{\rm targ}$, atmosphere scale height H, and atmosphere density at the base of the atmosphere ρ_0) through

$$\eta = \left(\frac{D}{H}\right)^3 \left[\left(\frac{v_{\rm imp}}{v_{\rm esc}}\right)^2 - 1\right]\left[\frac{\rho_{\rm imp}\rho_{\rm targ}}{\rho_0(\rho_{\rm imp} + \rho_{\rm targ})}\right]. \tag{2.1}$$

Assuming an isothermal, ideal atmosphere at temperature

$$T = 278 L_*^{0.25} a_{\rm targ}^{-0.5} {\rm K}, \tag{2.2}$$

where L_* is the host star luminosity in units of $\rm L_\odot$ and $a_{\rm targ}$ is the planet semi-major axis in au, the atmosphere scale height is

$$H = 0.73 \times 10^6 L_*^{0.25} a_{\rm targ}^{-0.5} M_{\rm targ}^{-1/3} \rho_{\rm targ}^{-2/3} \mu^{-1} {\rm m}, \tag{2.3}$$

where $\rho_{\rm targ}$ is in g cm^{-3} and $M_{\rm targ}$ is the target mass in $\rm M_\oplus$. This can be combined with equation 2.1, further assuming that $H \ll R_{\rm targ}$, the total atmosphere mass is approximately

$$m \equiv \delta M_{\rm targ} \approx 4\pi R_{\rm targ}^2 H\ \rho_0, \tag{2.4}$$

to give the expression for η used in Wyatt et al. (2019)

$$\eta = 0.5 \times 10^{-18} L_*^{-0.5} a_{\rm targ} M_{\rm targ}^{1/3} \rho_{\rm targ}^{5/3} \delta^{-1} \mu^2 D^3 \frac{\left[\left(\frac{v_{\rm imp}}{v_{\rm esc}}\right)^2 - 1\right]}{\left(1 + \frac{\rho_{\rm targ}}{\rho_{\rm imp}}\right)}. \tag{2.5}$$

The prescription from Shuvalov (2009) for cratering impacts gives the fractional atmosphere mass lost due to a single impact by a body with mass $m_{\rm imp} = \frac{\pi}{6}\rho_{\rm imp}D^3$ to be

$$\frac{m_{\rm atmloss}}{m_{\rm imp}} = \left[\left(\frac{v_{\rm imp}}{v_{\rm esc}}\right)^2 - 1\right]\chi_{\rm a}(\eta), \tag{2.6}$$

where

$$\begin{aligned}\log\big(\chi_{\rm a}(\eta)\big) = &-6.375 + 5.239\big(\log(\eta)\big) - 2.121\big(\log(\eta)\big)^2 \\ &+ 0.397\big(\log(\eta)\big)^3 - 0.037\big(\log(\eta)\big)^4 + 0.0013\big(\log(\eta)\big)^5.\end{aligned} \tag{2.7}$$

The prescription for atmosphere loss given by equation 2.7 is not appropriate for large values of η (the most energetic impactors). The simulations performed in Shuvalov (2009) cover up to $\eta \sim 10^6 - 10^7$. Naively applying the prescription for atmosphere mass loss above results in absolute atmospheric mass loss values that decrease with increasing impactor mass for values of $\eta > 10^{6.3}$. This is not physically realistic, so I modify the prescription for χ_a for values of $\eta > 10^6$. This modification takes the form of a power-law, fit to $\chi_a(10^4 \leqslant \eta \leqslant 10^6)$, applied to $\eta > 10^6$ with a correction to avoid a discontinuity in χ_a at $\eta = 10^6$

$$\log\big(\chi_a(\eta > 10^6)\big) = -0.6438\eta + 0.4746. \tag{2.8}$$

This results in absolute atmosphere mass losses that increase with impactor mass up to the polar cap limit, in line with the theoretical framework presented in Schlichting et al. (2015). The polar cap limit arises from the constraint that the maximum atmosphere mass that can be ejected by a single cratering impact cannot be greater than the mass of the atmosphere contained in the polar cap above the impact site

$$m_{\rm max} = m_{\rm cap} = 2\pi\rho_0 H^2 R_{\rm targ}. \tag{2.9}$$

This is incorporated into the prescription given by equation 2.6 as an upper bound on $m_{\rm atmloss}$.

The fractional impactor mass accreted by the target due to a single impact is given by

$$\frac{m_{\rm impacc}}{m_{\rm imp}} = \begin{cases} 1 & \eta \leqslant 10, \\ 1 - \chi_{\rm pr}(\eta) & 10 \leqslant \eta < 1000, \\ 1 - \chi_{\rm pr}(\eta = 1000) & 1000 < \eta, \end{cases} \tag{2.10}$$

where

$$\chi_{\rm pr}(\eta) = \min\left[0.07\left(\frac{\rho_{\rm targ}}{\rho_{\rm imp}}\right)\left(\frac{v_{\rm imp}}{v_{\rm esc}}\right)\Big(\log(\eta) - 1\Big), 1\right]. \tag{2.11}$$

2.1.2 Giant impacts

For the most energetic impactors, the prescription for atmosphere loss given by equation 2.6 is not a physically complete description, as violent impacts can cause a shock wave to propagate through the target, causing non-local atmosphere loss by accelerating regions of the atmosphere on the antipode beyond the escape velocity. A prescription for this effect is given by Schlichting et al. (2015) (for an isothermal atmosphere)

$$\frac{m_{\rm atmloss,GI}}{m_{\rm imp}} = \delta \frac{v_{\rm imp}}{v_{\rm esc}} \left[0.4 + 1.4x - 0.8x^2 \right], \tag{2.12}$$

where $x \equiv \left(\frac{v_{\rm imp}}{v_{\rm esc}}\right)\left(\frac{m_{\rm imp}}{M_{\rm targ}}\right)$.

2.1.3 Full prescription

Fig. 2.1 shows the values of $\frac{m_{\rm atmloss}}{m_{\rm imp}}$ (including the polar cap limit and giant impact induced losses described above) and $\frac{m_{\rm impacc}}{m_{\rm imp}}$ as a function of impactor size and ratio of impact velocity to target velocity (velocity ratio) for three atmosphere masses (with $\mu = 29$) and two impactor densities. The locations in parameter space of the simulations performed in Shuvalov (2009) are also shown, illustrating the regions of parameter space where these results are constrained by simulations and where the outcome has been extrapolated. The impactor and target densities used in Shuvalov (2009) are not identical to those used here, so these locations are approximate. While the fractional atmosphere mass loss is small for both the smallest and largest impactors, the absolute atmosphere mass loss increases monotonically with impactor size.

Considering first the mass loss prescription (right panels). The middle row (Earth-like atmosphere mass) shows that objects with $D \sim 10 - 100$ km are most efficient at atmosphere removal. Comparison with the top row shows that these most efficient objects become larger as the atmosphere mass increases. The figures also show where the polar cap limit applies, illustrating that this is relevant only for the largest objects ($D > 100$ km for an Earth-like atmosphere mass), however the impactor size at which it becomes relevant decreases as the atmosphere mass decreases. The effect of non-local atmosphere mass loss caused by the largest impactors is visible only for the most massive atmosphere ($\delta = 8.5 \times 10^{-6}$).

Considering next the fractional impactor mass accretion prescription (left panels), this is constant for impactors larger than ~ 1 km. For low density, comet-like, impactors (density $\rho_{\rm imp} = 0.9$ g cm^{-3}) the largest impactors results in no accretion of impactor material by the

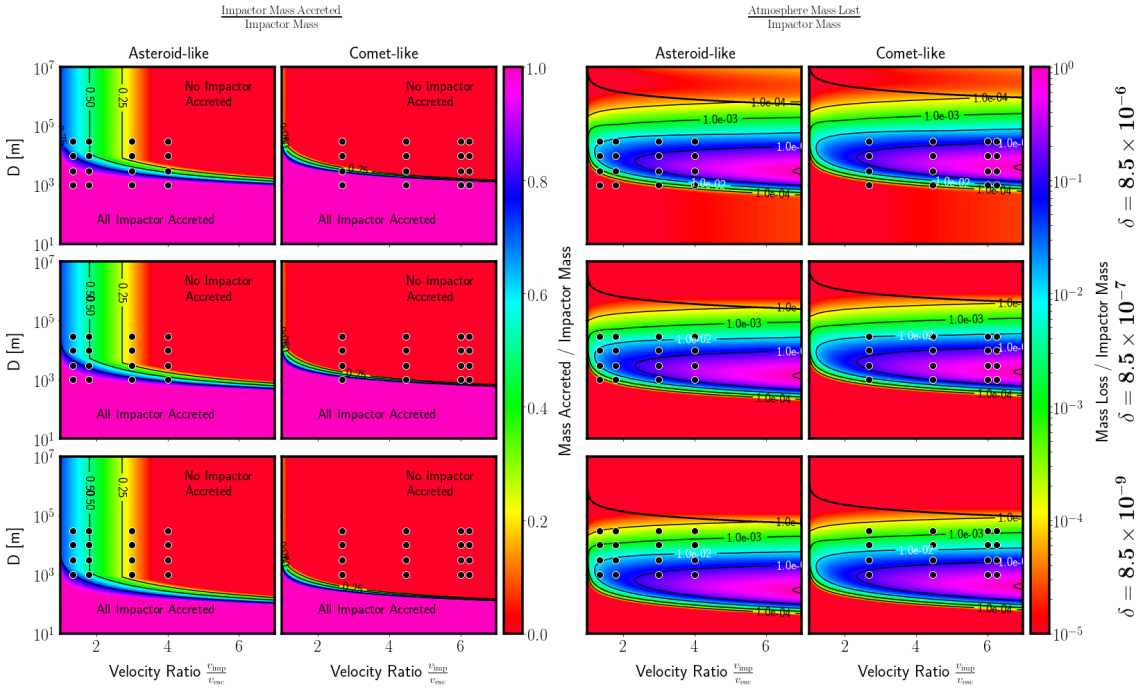

Figure 2.1: The prescription used to calculate the change in atmosphere mass, as a function of impactor size D and the ratio of impact velocity to target escape velocity $\left(\frac{v_{\rm imp}}{v_{\rm esc}}\right)$. The left columns show the fractional mass accreted $\left(\frac{m_{\rm impacc}}{m_{\rm imp}}\right)$ and the right columns show the fractional atmosphere mass loss $\left(\frac{m_{\rm atmloss}}{m_{\rm imp}}\right)$, including both the polar cap limit (thick black line) and the effect of large impacts (seen most clearly for large, fast, asteroid-like impactors in the most massive atmosphere). The first and third columns show these values for asteroid-like impactors ($\rho_{\rm imp} = 2.8$ g cm^{-3}) and the second and fourth columns show comet-like impactors ($\rho_{\rm imp} = 0.9$ g cm^{-3}). The locations of the simulations on which these prescriptions are based are shown by filled black circles. These values were calculated assuming an Earth-like planet ($\rho_{\rm targ} = 5.5$ g cm^{-3}, $a_{\rm targ} = 1$ au, $M_{\rm targ} = 1$ M$_\oplus$) orbiting a Sun-like star. The atmosphere is assumed to have $\mu = 29$, and shown for three different masses, corresponding to 0.01, 1 and 10 times the present day value ($\delta_\oplus = 0.85 \times 10^{-6}$).

target. For higher density, asteroid-like, impactors (with density $\rho_{\rm imp} = 2.8$ g cm^{-3}) this is the case only for impact velocities above ~ 40 km s^{-1}, with a non-zero fraction of the impactor mass accreted for slower impactors.

2.1.4 Low atmosphere mass effects

Airless limit

Special consideration must be given to the behaviour of the atmosphere in the "airless limit", where the atmosphere is negligible in comparison to the impact induced vapour plume. This is relevant when impacts deplete the atmosphere, but also when considering the potential for atmospheric growth on an initially bare rock. I adopt the approach used in Shuvalov (2009), whereby this limit is defined to apply for impacts with $\eta > 1000$. This occurs for the largest and fastest impactors, and extends to cover a larger portion of the impacting population as the atmosphere mass decreases. In this limit, the fractional impactor mass retained in a collision depends only on the impactor density and velocity ratio, as illustrated in equation 2.11 and Fig. 2.1.

While there are a number of prescriptions available (see, e.g. Thébault & Augereau, 2007; Svetsov, 2007; Zhu et al., 2019) I test the validity of the Shuvalov (2009) airless limit prescription through comparison to the prescription from Cataldi et al. (2017) (their equations 3, 4 and 5), which is based on the experimentally calibrated ejecta model from Housen & Holsapple (2011). A comparison between these prescriptions is shown in Fig. 2.2, which illustrates that the qualitative trends in fractional impactor mass retained with impactor size and velocity ratio are the same for both prescriptions. Both prescriptions predict that at low atmosphere masses, the fractional impactor mass retained is independent of impactor mass and depends only on impact velocity. In the extreme case of an initially bare rock target, this prescription allows growth of the atmosphere, with the efficiency depending on the density and velocity of the impacts. However, the velocity at which the impactor mass accreted by the target becomes zero is lower for the Cataldi et al. (2017) prescription, meaning that either the Cataldi et al. (2017) prescription underestimates the amount of material accreted, or the Shuvalov (2009) prescription overestimates it. The Housen & Holsapple (2011) models do not distinguish between target and impactor material, and are also based on low-velocity, low-mass experimental data. Thus, for the impacts that are considered in this dissertation, where the impactor sizes and velocities span a large range, the Shuvalov (2009) prescriptions are the most applicable, and so I adopt them for the remainder.

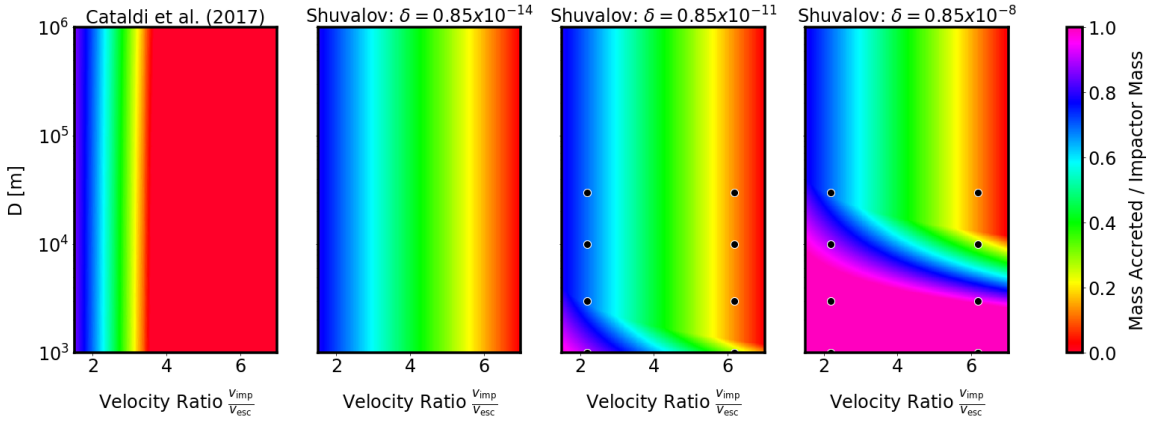

Figure 2.2: Comparison of the predicted fractional mass retained after an impact from the Shuvalov (2009) and Cataldi et al. (2017) expressions, shown as a function of impactor size (D) and ratio of impactor velocity to target escape velocity ($\frac{v_{\rm imp}}{v_{\rm esc}}$) for an Earth-like planet. The Cataldi et al. (2017) prescription assumes no atmosphere, while for the Shuvalov (2009) prescription the results are shown for various different atmosphere masses. Black filled circles show the locations in $(\delta, D, v_{\rm imp})$ parameter space for which simulation or experimental data was obtained.

The lower atmosphere mass limit

It is important when interpreting the results in the low atmosphere mass regime to quantify the point at which the atmosphere ceases to behave as a fluid, particularly when considering the extremely low atmosphere masses relevant to the outer moons studied in Chapter §4. This does not address the validity of the prescriptions, however the impactor accretion in the airless limit was compared in to the atmosphere-less simulation results from Cataldi et al. (2017) in §2.1.4 and found to be in qualitative agreement. The fluid approximation holds when the mean free path, $\lambda = (\sqrt{2}n\sigma)^{-1}$ (the number density of particles, n, and the collisional cross-section of the particles, σ) of a molecule or atom in the atmosphere is less than the typical length scale of the atmosphere. The atmosphere scale height defined by equation 2.3, is independent of the atmosphere pressure and a good choice for this length scale.

Equating these length scales gives a lower limit for the number density of $n_{\rm lim} = (\sqrt{2}\sigma H)^{-1}$, and therefore a lower limit on the surface pressure of $P_{\rm surf\ lim} = n_{\rm lim}kT$. Assuming an ideal gas, and provided that $m_{\rm atm}/M_{\rm tar} \ll 1$, the atmosphere mass is related to the atmosphere scale height, the target radius, $R_{\rm tar}$, and the surface atmosphere density, ρ_0, by equation 2.4. Combining this equation with the surface pressure limit gives the following limit:

$$m_{\rm atm\,lim} \approx \frac{4\pi\mu m_{\rm H} R_{\rm tar}^2}{\sqrt{2}\sigma}. \tag{2.13}$$

This limit depends only on the atmosphere composition (through μ and σ) and the target body radius. For the Earth, which has a nitrogen-dominated atmosphere with $\mu = 28$ and

$\sigma_{N_2} = 0.43$ nm^2, this limit is approximately 7×10^{-18} M$_\oplus$. The limit is within an order of magnitude of the fluid limit calculated for Venus (8×10^{-18} M$_\oplus$) and Mars (2×10^{-18} M$_\oplus$), which both have CO_2-dominated atmospheres ($\mu = 44$ and $\sigma_{CO_2} = 0.52$ nm^2).

For the moons of the outer giants, their smaller radii results in a lower fluid limit. Oxygen (with $\mu = 32$ and $\sigma_{O_2} = 0.4$ nm^2) makes up the bulk of the atmospheres of Europa, Ganymede and Callisto (discussed in detail in §4.1), while Triton and Titan have nitrogen-dominated atmospheres. The estimated fluid limits for these bodies are lowest for Triton, at $\sim 3 \times 10^{-22}$ M$_\oplus$ due mainly to its small size, and highest for the largest moon considered in Chapter 4 Ganymede, at $\sim 1.43 \times 10^{-21}$ M$_\oplus$. This limit is just above the estimated mass for Europa's atmosphere, which is sometimes considered as a collisionless exosphere rather than a true fluid atmosphere.

Below these limits the atmosphere can no longer be treated as a fluid and the prescriptions for impact induced atmosphere mass loss are no longer applicable. Therefore the behaviour of the atmosphere cannot reliable predicted below $\sim 10^{-20}$ M$_\oplus$. This limit is discussed in relation to the application of the analytic prescription and numerical code to the outer moons in in Chapter 4 .

2.1.5 Impact-triggered outgassing

To calculate the volatile contribution as a result of impact-triggered outgassing (relevant for the study of Titan) I adopt the prescription from Kraus et al. (2011). This gives the relative mass of melted and vaporised target (moon) material ($m_{\mathrm{m+v}}$) for impacts into icy surfaces,

$$\begin{aligned}\log_{10}\left(\frac{m_{\mathrm{m+v}}}{m_{\mathrm{imp}}}\right) &= -0.53 + 0.0017T + 0.7\log_{10}(\sin\theta) \\ &\quad - 0.46\phi + \frac{3}{2}\Big(0.554 + 0.07\phi\Big)\log_{10}\left(\frac{v_{\mathrm{surf}}^2}{E_m(\phi)}\right),\end{aligned} \tag{2.14}$$

where v_{surf} is the velocity of the impactor at the target surface, T is atmospheric temperature, ϕ surface porosity, θ impact angle and E_m the specific enthalpy of ice. When including this prescription I assume that $\phi = 20$ %, $\theta = \frac{\pi}{4}$ and $T = 100$ K (appropriate for Titan), and therefore the enthalpy is $E_m(\phi, T) = 7.85 \times 10^5$ J kg^{-1} (Kraus et al., 2011). Impacts with velocities below 8 km s^{-1} are predicted to produce no melting and thus contribute zero outgassed volatiles.

This prescription assumes impacts onto a surface with no atmosphere, therefore I also include,

following Marounina et al. (2015), the expression for atmospheric drag from Svetsov (2007) to account for the deceleration of the impactor. This expression converts the impact velocity $v_{\rm imp}$ into a surface velocity $v_{\rm surf} = f v_{\rm imp}$, where

$$f = \exp\left[\frac{-\rho_0}{\rho_{\rm imp}}\left(\frac{1}{2}\frac{2H}{D} + \frac{4}{3}\left(\frac{2H}{D}\right)^2\sqrt{\frac{\rho_0}{\rho_{\rm imp}}} + 2\left(\frac{2H}{D}\right)^3\frac{\rho_0}{\rho_{\rm imp}}\right)\right]. \tag{2.15}$$

This results in decreased relative melted mass through both the dependence of $m_{\rm m+v}$ on $v_{\rm surf}$ in eq. 2.14 and the loss of melting from any impactors with $v_{\rm imp} \geqslant 8$ km s $^{-1}$ but $v_{\rm surf} < 8$ km s $^{-1}$. The reduction in outgassing as a result of atmosphere drag becomes important only above relatively high atmosphere masses, comparable to Titan's current atmosphere.

Combining the two expressions above allows calculation of the relative surface melt mass, which combined with the impactor mass ($m_{\rm imp}$) and initial surface volatile fraction ($x_{\rm v,targ}$) gives the outgassed volatile mass

$$m_{\rm outgas} = \begin{cases} m_{\rm imp}\left(\frac{m_{\rm m+v}}{m_{\rm imp}}\right)x_{\rm v,targ} & v_{\rm surf} \geqslant 8{\rm km\ s^{-1}}, \\ 0 & v_{\rm surf} < 8{\rm km\ s^{-1}}. \end{cases} \tag{2.16}$$

In order to account for the depletion of volatiles in the crust over time as a result of impact-triggered outgassing I apply two limiting values to the outgassing prescription based on the available mass of volatiles in the crust. This first is a cap on the total mass of volatiles that a single impactor can release,

$$m_{\rm out,cap} = 2\pi\rho_{\rm surf}D^2(R_{\rm targ} - D)x_{\rm v,targ}. \tag{2.17}$$

This limit is analogous to the polar cap limit for atmosphere mass loss given by eq. 2.9 in that it limits the volume of the surface that can be vapourised to be less than the volume contained above the tangent plane, assuming the impactors penetrate to a depth of D. This cap applies only to the largest ($D >\sim 100$ km) impactors, limiting their volatile contribution to $\sim 10^{-8}$) $M_\oplus$ for a Titan-size moon, assuming a water ice ($\rho_{\rm surf} = 1$ g cm^{-3}) crust containing 1% volatiles (Waite et al., 2009; Alibert & Mousis, 2007). I also limit the total mass of volatiles contained in the crust available to be released by impacts. This limit is explored in detail in the study of the outer moons presented in §4.6, but for the nominal case it is assumed that impacts can release at most the volatiles contained within a 20 km thick water ice crust. The application of this limit is equivalent to allowing the surface volatile fraction, $x_{\rm v,targ}$ to evolve in time, but is computationally more efficient and also allows the investigation the effect of

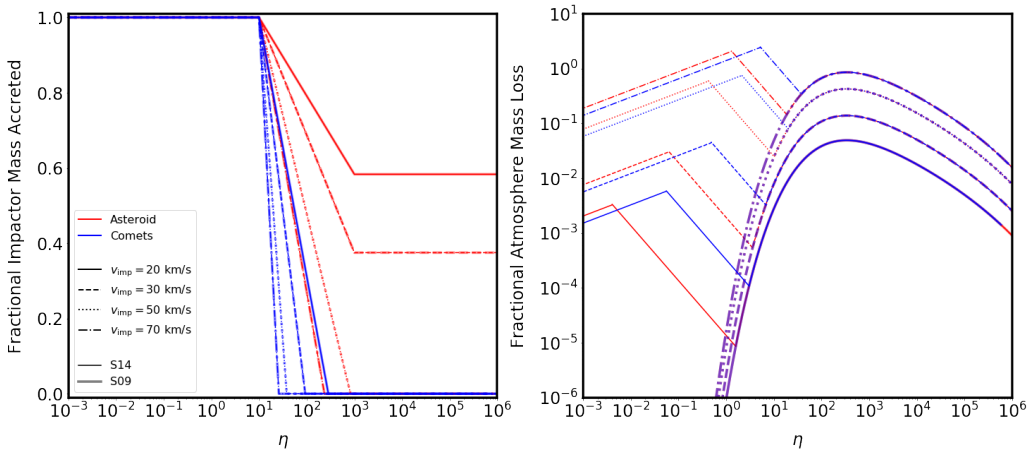

Figure 2.3: The predicted fractional atmosphere mass loss (left panel) and impactor mass accreted (right panel) for impacts onto an Earth-like planet as a function of erosional efficiency (η). These are calculated using my modified version of the Shuvalov (2009) and Shuvalov et al. (2014) prescriptions, including the corrections discussed in the text for calculation of the atmosphere density and the updated interpolation method in the fragmentation regime. The original Shuvalov (2009) cratering only prescription is shown by transparent thicker lines, in comparison to the Shuvalov et al. (2014) prescription including aerial bursts and fragmentation, which is shown by opaque thinner lines. The results for asteroid-like impactors are shown in red and comet-like impactors in blue, with the line style illustrating the impact velocity.

varying the volatile fraction or depth of the crust by changing only a single parameter. This limits the total volatile mass limit that can physically be released by impact-triggered outgassing to be $\sim 1.6 \times 10^{-6}$ $M_{\oplus}$ for Titan.

The predicted behaviour of the atmosphere undergoing atmospheric erosion and delivery due to impacts and impact-triggered outgassing is discussed in §4.6.

2.1.6 Aerial bursts and impactor fragmentation

In hot, dense atmospheres, such as those investigated in Chapter 5, it is no longer reasonable to assume that the majority of impactors reach the surface intact. Instead, a significant fraction of impactors are expected to undergo either complete disruption in the atmosphere (an aerial burst) or break up into fragments that then impact the surface (fragmentation). For this reason, the impact prescriptions described above must be extended to account for these effects.

Fragmentation and aerial burst heights

To characterise the effect of aerial bursts and fragmentation I make use of the prescriptions from Shuvalov et al. (2014), who performed numerical simulations of impacts into hot dense atmospheres, extending the work done in Shuvalov (2009). These prescriptions are based on

two key parameters, $H_{1/2}$, the height at which the projectile velocity it reduced by half due to drag (where aerial bursts are considered to occur) and $H_{\rm fr}$, the height at which fragmentation occurs. Impacts with negative values for both $H_{1/2}$ and $H_{\rm fr}$ are cratering in nature (they reach the ground intact). Impacts with $H_{\rm fr} > 0$ but $H_{1/2} < 0$ fragment in the atmosphere, while whose with $H_{1/2}$ and $H_{\rm fr}$ both positive undergo aerial bursts. The fits given for these two values are:

$$H_{1/2} = -A_{1/2} H \ln \left(\frac{B_{1/2} D}{2H} \sqrt{\frac{\rho_{\rm imp}}{\rho_0}} \right), \tag{2.18}$$

and

$$H_{\rm fr} = -A_{\rm fr} H \ln \left(\frac{B_{\rm fr} D}{2H} \sqrt{\frac{\rho_{\rm imp}}{\rho_0}} \right), \tag{2.19}$$

where H is the atmosphere scale height, D the impactor size, $\rho_{\rm imp}$ the impactor density and ρ_0 the surface density of the atmosphere. The scale factors given are $A_{1/2} = A_{\rm fr} = 1.4$ and $B_{1/2} = 5.5$, $B_{\rm fr} = 3.5$.

Values are given in Shuvalov et al. (2014) for the values of the erosional efficiency parameter (η), numerical and predicted values of $H_{\rm f}$ and $H_{1/2}$, numerical fractional atmosphere and projectile mass loss ($\frac{m_{\rm a}}{m_{\rm imp}}$ and $\frac{m_{\rm p}}{m_{\rm imp}}$) and the predicted atmosphere mass loss from Shuvalov (2009) for thirteen combinations of impactor and atmosphere parameters. These can be used to test the application of their prescriptions to my model, excluding two values as they have different values for $\frac{m_{\rm a}}{m_{\rm imp}}$ between two tables.

While my assumed ideal, isothermal atmosphere model correctly recreates the atmosphere scale height and erosional efficiency values from Shuvalov et al. (2014), and thus my values for the cratering only atmosphere mass loss predictions are in agreement, attempting to recreate the given values for the fragmentation and half heights $(H_{1/2})$ and $(H_{\rm fr})$ is less successful, likely due to differences in our calculation of the surface atmosphere density (ρ_0).[1] I correct for this by using alternative values A and B calculated based on linear regression of equations 2.19 and 2.18 with $y = \frac{H_x}{H}$ and $x = \ln \frac{D}{2H} \sqrt{\frac{\rho_{\rm imp}}{\rho_0}}$. This gives values for $A_{\rm fr}$ and $A_{1/2}$ that agree with the given value of 1.4, but alternative values of $B_{\rm fr} = 1.24$ and $B_{1/2} = 1.97$, rather than the Shuvalov et al. (2014) values of $B_{1/2} = 5.5$ and $B_{\rm fr} = 3.5$.

[1] No values for this are given in Shuvalov et al. (2014) and so this hypothesis cannot be directly tested

Atmosphere mass loss

Using the values of η, $H_{\rm fr}$ and $H_{1/2}$ derived above the atmosphere mass loss values can be calculated using the prescription from Shuvalov et al. (2014). Cratering impacts (when $H_{1/2}, H_{\rm fr} < 0$) are assumed to follow the prescription described in §2.1.1, given by equation 2.6. The atmosphere mass loss due to aerial bursts (when $H_{1/2}, H_{\rm fr} > 0$) is

$$\left(\frac{m_{\rm atmloss}}{m_{\rm imp}}\right)_{\rm ab} = 5.5 \times 10^{-3}(v_{\rm imp} - v_*)^2\sqrt{\rho_{\rm imp}}\left(\frac{D}{H}\right), \tag{2.20}$$

where $\rho_{\rm imp}$ is in g cm^{-3}, velocities in km s^{-1} and distances in km, and

$$v_* = 15 + 0.2H. \tag{2.21}$$

In between these two regimes (when $H_{1/2} < 0$ but $H_{\rm fr} > 0$), the impactor undergoes fragmentation and the atmosphere mass loss is interpolated between the two regimes

$$\ln\left(\frac{m_{\rm atmloss}}{m_{\rm imp}}\right)_{fr} = \ln\left(\frac{m_{\rm atmloss}}{m_{\rm imp}}\right)_{\rm cr} + \left[\ln\left(\frac{m_{\rm atmloss}}{m_{\rm imp}}\right)_{\rm ab} - \ln\left(\frac{m_{\rm atmloss}}{m_{\rm imp}}\right)_{\rm cr}\right] \times \frac{H_{\rm fr}}{H_{\rm fr} - H_{1/2}}. \tag{2.22}$$

According to Shuvalov et al. (2014) this prescription should predict absolute atmosphere mass loss that increases monotonically with impactor mass (although there should be two peaks in the relative atmosphere mass loss per impactor mass - representing most efficient cratering and aerial burst sizes). I find however, that this is not the case, with the interpolation in the fragmenting regime predicting an absolute atmosphere mass loss that decreased with increasing impactor mass in some cases. I correct for this using the following process. If the calculated *absolute* atmosphere mass loss increases with impactor size across the full size distribution then this value, from equations 2.6, 2.20 and 2.22, is used unchanged. If this is not the case, then I apply an alternative interpolation regime by first calculating three atmosphere loss values: the maximum value of the cratering mass loss ($m_{\rm a\ max}$), the value of the aerial burst mass loss calculated for the largest object that undergoes aerial bursts[2] ($m_{\rm a\ AB}$) and the value of the fragmentation mass loss calculated for the largest object that undergoes fragmentation[3] ($m_{\rm a\ fr}$). There are two possible reasons why the atmosphere mass loss may fail to increase monotonically with impactor mass. Firstly, the maximum aerial burst absolute mass loss may be larger than the maximum cratering mass loss ($m_{\rm a\ AB\ max} > m_{\rm a\ max}$), in which case I assume that the absolute atmosphere mass loss for the range of impactor sizes between the most efficient cratering impact and the size at which the aerial burst absolute

[2]which is equal to the value of the fragmentation mass loss calculated for the smallest object that undergoes fragmentation

[3]which is equal to the value of the cratering mass loss calculated for the smallest object that undergoes a purely cratering impact

mass loss is equal to this maximum cratering mass loss is constant and equal to the maximum cratering mass loss.

Secondly, the maximum aerial burst absolute mass loss is smaller than the maximum cratering mass loss, but the fragmentation absolute mass loss decreases at some point as the impactor size increases. In this case, I abandon the Shuvalov et al. (2014) fragmentation mass loss (equation 2.22), and assume that the mass loss calculated for impactors below the fragmentation-aerial burst ($H_{\rm half} = 0$) transition follows the aerial burst prescription, while that above is assumed to follow the cratering prescription. A fill value for the absolute mass loss in the intermediate region, is calculated as

$$m_{\rm fill} = 10^{\frac{1}{2}\left(\log_{10}(m_{\rm a\ AB})+\log_{10}(m_{\rm a\ fr})\right)}, \tag{2.23}$$

where $m_{\rm a\ AB}$ is the aerial burst absolute mass loss at the aerial burst-fragmentation transition, and $m_{\rm a\ fr}$ is the cratering absolute mass loss at the fragmentation-cratering transition.[4] The fill value is then used to fill between the points on the aerial burst and cratering mass loss curves where it intersects. This is an approximation, and results in a slight shifting of which impactors are assumed to undergo aerial bursts relative to fragmentation. However, this updated prescriptions recreates the Shuvalov et al. (2014) simulation results, as shown in Fig. 2.3.

Impactor mass accretion

Shuvalov et al. (2014) do not offer an updated fit for the mass of the projectile that is lost (primarily along the wake) during an impact into a hot and dense atmosphere, instead stating that the fit provided by Shuvalov (2009) (equation 2.10) is sufficient. They do however state that all impactor mass in impacts that undergo aerial bursts should be accreted, rather than simply following the cratering prescription from Shuvalov (2009), which is in agreement with their own numerical simulation results[5]. I find that the Shuvalov (2009) prescription agrees with these qualitative descriptions for low energy impacts, but under-predicts the fractional impactor mass retained for more energetic impacts. I therefore modify my model such that all impactors assumed to undergo aerial bursts ($H_{1/2}, H_{\rm fr} > 0$) are entirely accreted. I do not interpolate between the cratering and aerial burst prescription here, and so in some cases this will lead to a discontinuity in fractional impactor mass accretion with impactor size. While this is nonphysical, when averaging over impactor sizes and velocities it is not important and so in the interests of computational efficiency an interpolation is not attempted.

[4] If the size distribution does not cover either or both of these transitions, the mass is taken as the absolute mass loss caused by the smallest impactor size

[5] with the caveat that there are only four simulations in this regime

2.2 The statistical code of stochastic bombardment

2.2.1 Overview

I have developed a statistical code of stochastic bombardment to model the evolution of the atmosphere of a terrestrial target body (planet or moon) as it undergoes impacts. The code is designed to be modular, with the choice of impactor populations, prescription for the outcome of a given impact, and initial system parameters able to be independently specified. In the following explanation it is assumed that given the atmosphere, target and impactor properties, it is possible to calculate two properties:

1. the atmosphere mass removed by each impactor relative to the impactor mass $\frac{m_{\rm atmloss}}{m_{\rm imp}}$,
2. the impactor mass fraction retained after an impact $\frac{m_{\rm impacc}}{m_{\rm imp}}$.

The operation of the code does not depend on the method used to calculate these values. The method used is discussed in §2.1, and in principle the code can be applied using any combination of the cratering, fragmenting and aerial bursts, outgassing and giant impact prescriptions. The choice of prescription used depends on the nature of the atmosphere and impactors, and is discussed for application to the Earth, the outer moons of the Giant planets, and Venus and Mars in Chapters 3, 4 and 5 respectively. Given specified impactor populations, the code will evolve the atmosphere through time, tracking the total atmosphere mass, target mass and atmosphere composition (through the fraction of the total mass that has been delivered by each impactor population). The mean molecular weight (MMW) is calculated from the impactor properties and atmosphere mass fractions.

2.2.2 Inputs

The code takes as inputs a series of parameters describing the initial conditions of the target and its atmosphere, and the population of impactors. For the target body (whether this is a planet or a moon), the mass ($M_{\rm targ}$), and bulk density ($\rho_{\rm targ}$) must be given. Furthermore either the temperature of the atmosphere $T_{\rm atm}$ must be given, or the semi-major axis ($a_{\rm targ}$) of the target and luminosity (L_*) of the host star must be provided, through which the atmosphere temperature can be calculated assuming radiative equilibrium. Finally, the initial atmosphere is described in terms of its mass (m_0), and bulk MMW (μ_0).

It is possible to specify any number of impactor populations, each characterised by an associated bulk density, volatile fraction, composition, size distribution, impact flux and

distribution of impact velocities. The bulk density (ρ_k), volatile fraction ($x_{\mathrm{v},k}$) and MMW (μ_k) of the k-th impactor population are given as single numbers.
Both the size and impact velocity distributions can be time dependent. The size distribution is specified as the number fraction of impactors, in N_{size} log-spaced size bins between a minimum (D_{min}) and maximum size (D_{max}). The number fraction of objects in the i-th size bin, with size D_i (and mass $m_{\mathrm{imp}}(D_i, \rho_k)$), at time t, is written here as $f_{\mathrm{N},i,k}(t)$. The impact velocity distribution is specified in a similar manner. The velocity bins are log-spaced between a minimum (v_{min}) and maximum (v_{max}) velocity, with N_{vel} bins in total. The number fraction of objects in the j-th velocity bin, with velocity v_j at time t is written here as $f_{\mathrm{v},j,k}(t)$. The final input is $R_k(t)$, the total impactor flux rate of the k-th impactor population of all impactor masses as a function of time.

2.2.3 Method

Due to the range in impactor parameters that are considered throughout this dissertation (size, velocity, composition) it is not computationally feasible to update the atmosphere properties separately for each individual impactor. Instead, discrete time steps are considered, within which the code starts from knowledge of the atmosphere and target properties in the previous time-step (at time t), as well as the impactor properties introduced above. In order to reduce computation time, the code makes use of an adaptive time step, discussed further in §2.4.1.

For each time step (Δt), the code calculates the effect of each impactor population in the following manner. The number of impactors $N_{i,j,k}$(t) with size D_i, velocity v_j in the k-th population is drawn from a Poisson distribution, with the parameter λ (average number of impacts per time interval)

$$\lambda_{i,j,k} = R_k(t)\ f_{\mathrm{N}\ i,k}(t)\ f_{\mathrm{v}\ j,k}(t)\ \Delta t. \tag{2.24}$$

For use in this version of the numerical code, the values of $\left(\frac{m_{\mathrm{atmloss}}}{m_{\mathrm{imp}}}\right)_{i,j,k}$ and $\left(\frac{m_{\mathrm{impacc}}}{m_{\mathrm{imp}}}\right)_{i,j,k}$ are calculated using the following approach:

1. The effect of cratering impacts is accounted for using the chosen prescription (see §2.1.1).
2. The atmosphere mass loss caused by a single impactor is bounded from above by the polar cap mass (equation 2.9).
3. The effects of non-cratering impacts are included (see §2.1.2).

The total atmosphere mass loss caused by all impactors in that population is then calculated by summing over the size and velocity bins,

$$m_{\mathrm{atmloss},k} = \sum_{i=1}^{N_{\mathrm{size}}} \sum_{j=1}^{N_{\mathrm{vel}}} \left[N_{i,j,k}(t) m_{\mathrm{imp}}(D_i, \rho_k) \left(\frac{m_{\mathrm{atmloss}}}{m_{\mathrm{imp}}} \right)_{i,j,k} \right]. \tag{2.25}$$

The total mass of impactor material accreted is then calculated in a similar fashion,

$$m_{\mathrm{impacc},k} = \sum_{i=1}^{N_{\mathrm{size}}} \sum_{j=1}^{N_{\mathrm{vel}}} \left[N_{i,j,k}(t) m_{\mathrm{imp}}(D_i, \rho_k) \left(\frac{m_{\mathrm{impacc}}}{m_{\mathrm{imp}}} \right)_{i,j,k} \right]. \tag{2.26}$$

The volatile content $x_{\mathrm{v},k}$ is defined such that it corresponds to the volatiles that will end up in the atmosphere, so it is then used to calculate the mass that is accreted as a solid onto the target mass, and the mass that is added to the atmosphere. With all these values calculated, the target mass can then be updated for the next time step as

$$M_{\mathrm{targ}}(t + \Delta t) = M_{\mathrm{targ}}(t) + \sum_{k=1}^{N_{\mathrm{comp}}} \Big[m_{\mathrm{impacc},k} \big(1 - x_{\mathrm{v},k}\big) \Big]. \tag{2.27}$$

The atmosphere mass is then calculated in a two step process. On the assumption that atmospheric mass removal occurs before the volatiles delivered are released, the total atmospheric mass loss is calculated from the sum of the contribution by each impactor type, and used to calculate the intermediate atmospheric mass

$$m_{\mathrm{mid}} = m(t) - \sum_{k=1}^{N_{\mathrm{comp}}} \big(m_{\mathrm{atmloss},k} \big). \tag{2.28}$$

If this value is negative a time step warning flag is raised, since this is nonphysical, and as discussed in §2.4.1 typically only occurs if the atmosphere mass is particularly low or the impactors are particularly extreme in their mass or velocity. If this is the case, then m_{mid} is set to be zero[6]. The new atmosphere mass is then calculated from the sum of the masses of volatiles delivered by each impactor type as

$$m(t + \Delta t) = m_{\mathrm{mid}} + \sum_{k=1}^{N_{\mathrm{comp}}} \Big[m_{\mathrm{impacc},k}\, x_{\mathrm{v},k} \Big]. \tag{2.29}$$

For comparison with the analytic models of Wyatt et al. (2019), the code also records the value

[6]For numerical reasons it is actually set to an arbitrarily small number, typically 10^{-55} $\mathrm{M}_{\oplus}$

of $f_{\rm v}$, the ratio of atmosphere mass gain and mass loss rates

$$f_{\rm v}(t) = \frac{\dot{m}^{+}}{\dot{m}^{-}} = \frac{\sum_{k=1}^{N_{\rm comp}} \left[m_{{\rm impacc},k}\ x_{{\rm v},k} \right]}{\min\left(\sum_{k=1}^{N_{\rm comp}} \left[m_{{\rm atmloss},k} \right],\ m(t) \right)}. \tag{2.30}$$

This comparison is discussed further in §2.4.4. The change in μ due to the impacts in that time-step are calculated, through

$$\mu(t + \Delta t) = \frac{\left(m_{\rm mid}\mu(t) + \sum_{k=1}^{N_{\rm comp}} \left[m_{{\rm impacc},k}\ x_{{\rm v},k}\ \mu_{{\rm imp},k} \right] \right)}{m(t + \Delta t)}. \tag{2.31}$$

The code tracks the atmosphere mass at each time that has been delivered by each impactor population $(m_k(t))$, which is calculated through

$$m_k(t + \Delta t) = \left(m_k(t) - f_k(t) \sum_{k=1}^{N_{\rm comp}} \left[m_{{\rm atmloss},k} \right] + m_{{\rm impacc},k}\ x_{{\rm v},k} \right). \tag{2.32}$$

This is used to calculate the corresponding atmosphere mass fraction $f_k(t) \equiv \frac{m_k(t)}{m(t)}$.

2.2.4 Outputs

At the determined output checkpoints (typically 10^4 yr intervals), the time, atmosphere mass, target mass, atmosphere MMW, value of $f_{\rm v}$, and fraction of the atmosphere (by mass) that has been delivered by each impactor population are recorded. At the end of the simulation, the number of "giant impacts" is recorded, as is a flag specifying if the atmosphere mass ever reached a negative value (and so needed to be reset to the atmosphere mass floor described in §2.2.3). The total mass of *impacting* and *accreted* material for each population is also recorded, allowing the accretional efficiency of each population and the delivered mass of any non-volatile components such as water to be calculated. This is described in detail in §3.3.3 for water delivery to the Earth.

2.3 Analytic predictions

2.3.1 Stalling mass and behaviour

The prescriptions described in §2.1 for the effect of a single impact can be combined with distributions of the impactor properties to predict the combined effect of a population of impactors, without running the full numerical code. This is done by summing the individual

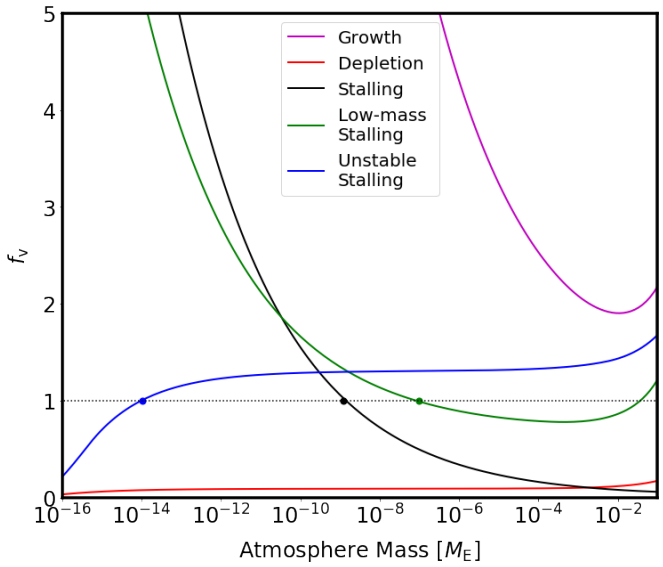

Figure 2.4: Five examples of the behaviour of f_v as a function of atmosphere mass, illustrating the different ways the atmosphere can (or cannot) stall as described in the text.

contributions of a number of impactors assumed to arrive simultaneously, neglecting the stochastic nature of impacts and time evolution of the atmosphere and target properties. This assumption means that while overall trends in atmosphere evolution can be predicted, it is not possible to predict the precise time-dependent behaviour of the atmosphere. The importance of considering the timescales for atmosphere evolution and the effect that this has on the stochastic behaviour of an atmosphere is discussed in relation to its application to the outer moons in §4.3.2 and to Venus and Mars in §5.3.3.

Considering the same distributions of impactor properties as described for use in the numerical code in §2.2, and the prescriptions for relative atmosphere mass loss impactor mass retention given by equations 2.6 and 2.10, the total atmosphere mass loss caused by all impactors can be calculated by summing over the size and velocity bins, to give the expressions in equations 2.25 and 2.26.

These values can be used to calculate the ratio of atmosphere mass gain to mass loss rates,

$$f_v = \frac{m_{\text{impacc}} x_v}{m_{\text{atmloss}}}. \tag{2.33}$$

An alternative expression, including the effect of impact-triggered outgassing is given by,

$$f_{v,\text{outgas}} = \frac{m_{\text{impacc}} x_v + m_{\text{outgas tot}}}{m_{\text{atmloss}}}, \tag{2.34}$$

where

$$m_{\text{outgas tot}} = \sum_{i=1}^{N_{\text{size}}} \sum_{j=1}^{N_{\text{vel}}} \left[N_{i,j}(t) m_{\text{imp}}(D_i, \rho) \left(\frac{m_{\text{outgas}}}{m_{\text{imp}}} \right)_{i,j} \right]. \tag{2.35}$$

The value of f_{v} determines whether an atmosphere will grow (when f_{v} is greater than one and the rate of volatile delivery exceeds the rate of atmosphere erosion) or whether it will deplete (when f_{v} is less than one) (Wyatt et al., 2019). It therefore follows that atmospheres should remain unchanged in mass if $f_{\text{v}} = 1$. This equilibrium atmosphere mass can be either stable or unstable, depending the exact dependence of f_{v} on atmosphere mass.

If f_{v} increases with increasing atmosphere mass (the gradient is positive) a small perturbation below the equilibrium leads to a value of $f_{\text{v}} < 1$ and thus runaway depletion, equally, a small perturbation above the equilibrium mass leads to a value of $f_{\text{v}} > 1$ and thus to runaway growth. This phenomenon is labelled as "unstable" stalling for the rest of this dissertation. Conversely, if f_{v} decreases with increasing atmosphere mass then small perturbations away from the equilibrium will be corrected. This behaviour gives rise to the phenomenon of a characteristic "stable" stalling mass for a given population of impactors.

The precise behaviour of f_{v} as a function of atmosphere mass is a complex function of multiple impactor and target properties, but can be broadly grouped into five qualitative categories of behaviour:

- **Growth** $f_{\text{v}} > 1$ for all atmosphere masses, so the atmosphere grows forever and no stable stalling mass exists
- **Depletion** $f_{\text{v}} < 1$ for all atmosphere masses, so the atmosphere depletes forever and no stable stalling mass exists
- **Stable Stalling** f_{v} decreases with increasing atmosphere mass, crossing one a single time at the stable stalling mass
- **Unstable Equilibrium** f_{v} increases with increasing atmosphere mass, crossing one once (where the atmosphere mass does not change but is unstable to small perturbations, which can result in either runaway growth or runaway depletion)
- **Conditional Stalling** f_{v} is equal to one for multiple atmosphere masses, displaying one or more stable stalling masses and unstable equilibria. In this case the atmosphere can undergo runaway growth, runaway depletion or stalling behaviour depending on the initial atmosphere mass

These five behaviours are illustrated in Fig. 2.4. Which of these profiles occurs depends on both the impactor and target properties, and is not trivial to predict, but in general increased impactor volatile fraction, slower impact velocities, a greater number of large impactors and decreased atmosphere scale heights all result in higher atmosphere growth.

2.3.2 Growing from a bare rock

In the case of runaway depletion, it is sensible to consider if a stalling mass might exist beyond the lowest atmosphere mass considered in the calculation of $f_{\rm v}$. It is possible to distinguish between atmospheres that stall at a very low atmosphere mass and those that undergo true "runaway depletion". Runaway depletion occurs when the numerator in the calculation of $f_{\rm v}$ (atmosphere mass gain rate) is zero, and so no matter how small the value of the denominator (atmosphere mass loss rate) becomes $f_{\rm v}$ remains finite and zero. This can occur because as $m \to 0$, for all impactor sizes and velocities, $\eta \to \infty$ due to the m^{-1} term in equation 2.5. In this case, if the impactor properties are such that the value of the projectile accretion fraction in the "airless limit" $\left(1 - \chi_{\rm pr}(\eta > 10^3)\right)$ is zero (as is the case for low-density or very fast imapctors) then no impactor material is retained in any collision.

For a stalling mass to exist the fractional impactor mass accreted in the airless limit regime must be non-zero. This occurs if the impactor is sufficiently slow and dense. Specifically, since the minimum impact velocity is the target escape velocity, this requires that

$$\begin{aligned} \chi_{\rm pr}(\eta = 10^3) &< 1 \\ 0.07 \frac{\rho_{\rm targ}}{\rho_{\rm imp}} \frac{v_{\rm imp}}{v_{\rm esc}} \left(\log\left(10^3\right) - 1 \right) &< 1 \\ 0.14 \frac{v_{\rm imp}}{v_{\rm esc}} &< \frac{\rho_{\rm imp}}{\rho_{\rm targ}} \\ \rho_{\rm imp} &> 0.14 \rho_{\rm targ} \approx 0.77 {\rm g\ cm}^{-3}. \end{aligned} \tag{2.36}$$

Any combination of impactor properties that violates this will result in zero atmosphere growth even at the smallest atmosphere mass.

In reality, the behaviour of an atmosphere at very low mass will be determined by the effect of individual impacts rather than the cumulative effect of the entire distribution. A realistic population of impactors will have a distribution of impact velocities, and so some will be capable of delivering volatiles to the atmosphere while other will erode any volatiles present, resulting in transient low mass atmospheres.

Table 2.1: The properties of the four planets used in the tests of the updated impact prescription described in the text. Hot Earth is similar to the planet used in the original simulations of Shuvalov et al. (2014).

Planet	**Mass** $[M_\oplus]$	**Radius** $[R_\oplus]$	**Density** $(\rho_{\rm targ})$ [g cm^{-3}]	**Temperature** [K]	**Scale Height** (H) [km]
Venus	0.815	0.949	5.24	321	9.6
Earth	1.000	1.000	5.51	278	7.5
Hot Earth	1.000	1.000	5.51	1500	40.7
Mars	0.1075	0.531	3.93	221	15.8

Table 2.2: The densities, volatile fractions, and relative velocities of the four impactor types used in the tests of the updated impact prescription described in the text, chosen to most closely match those used in Shuvalov et al. (2014)

Population	**Density** $\rho_{\rm imp}$ [g cm^{-3}]	**Volatile Fraction** $x_{\rm v}$	**Relative Velocity Ratio** $\xi = \frac{v_{\rm rel}}{v_{\rm targ}}$
Left-over Planetesimal	3.5	0.00035	0.5
S-Type Asteroid	3.4	0.0046	0.3
S-Type Asteroid[1]	3.3	0.02	0.3
C-Type Asteroid	2.0	0.105	0.3
Comet	0.9	0.2	1.0

2.3.3 Predicted influence of the aerial burst and impactor fragmentation prescription

The potential effect of including the aerial burst and impactor fragmentation prescription described in §2.1.6 in addition to the cratering prescription described in §2.1.3 on the atmosphere mass behaviour for Venus, Earth and Mars can be considered using the analytic prediction described above. The current properties of these planets are assumed, as well as the addition of a "hot Earth" case for comparison with the simulation results in Shuvalov et al. (2014) (an Earth-like planet with a 1500 K atmosphere). The properties of these test planet cases are described in Table 2.1, and the four simplified impactor populations used for testing are described in Table 2.2. These are based on the impactor types (comets, C- and S-type asteroids and left-over planetesimals) that are believed to have made up the material bombarding the terrestrial planets, discussed in detail for the Earth in §3.1 and for Venus and Mars in §5.1.1. The impactors are assumed to follow a simple differential power-law size distribution with $\alpha = 3.5$ for the asteroids and left-over planetesimals and $\alpha = 3.1$ for the comets, between $D_{\rm min} = 1$ m and $D_{\rm max} = 1000$ km.

The atmosphere mass loss calculated using equations 2.6, 2.20 and 2.22 as a function of

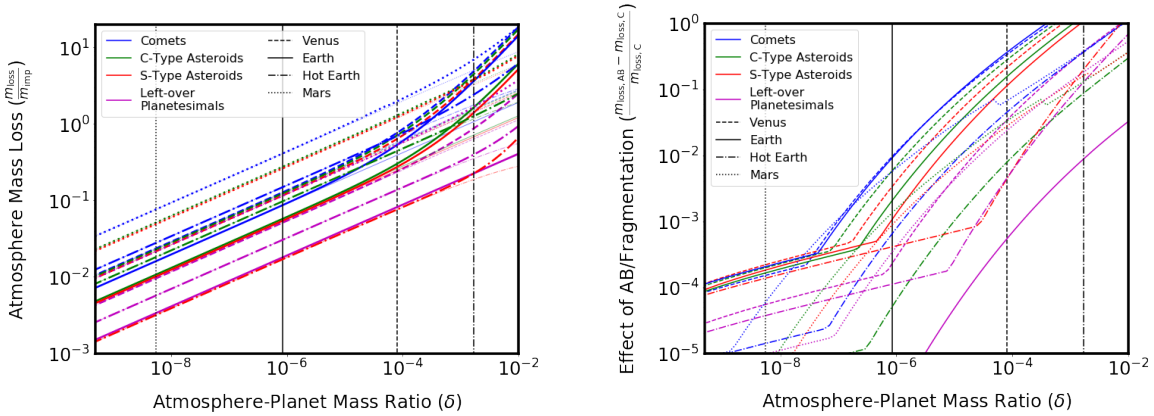

(a) (b)

Figure 2.5: The predicted fractional atmosphere mass loss as a function of atmosphere-to-planet mass ratio, comparing the cratering only (thin lines) and combined cratering and aerial bursts (thick lines) predictions is shown in panel (a). The assumed planet properties are shown by the line style and the impactor type assumed by the line colour. The difference in atmosphere mass loss caused by including the effects of aerial bursts and fragmentation is illustrated in panel (b).

atmosphere mass is shown for these sixteen combinations in Fig. 2.5. The cratering only, and cratering combined with new aerial bursts and fragmentation predictions are shown in the top panel by different line style, while the difference between the two predictions is shown in the bottom. As can be seen, this difference (integrated over all impactor sizes) is less than 1% for Earth-like or smaller ($< 10^{-6}$ $M_{\oplus}$) atmospheres, but becomes significant for much more massive and hotter atmospheres.

2.4 Validation and testing

Before the code can be applied it must be tested. This first requires choosing appropriate values for the time step and number of size and velocity bins. These are discussed in §2.4.1, 2.4.2 before I outline a set of test simulations for which there is an analytical solution in §2.4.3 that are used to validate the code and these choices in §2.4.4.

2.4.1 Time step size choice

Due to the number of impactors considered, it is not computationally feasible to consider individually every single impactor, particularly since most are small and therefore cause negligible atmosphere mass change. However, combining the effects of too many impactors arriving in a single time step could result in a loss of detail in the resulting evolution. Therefore the code incorporates an adaptive time step. In order to avoid artificially selecting against the largest impactors, which will by definition cause a significant change in the

atmosphere, the time step is pre-calculated neglecting the stochastic nature of the impacts. A maximum fraction atmosphere mass change limit is specified ϵ (referred to later as the accuracy) and used to calculate the time step length through

$$\Delta t = \epsilon \frac{m}{\dot{m}} \quad \text{where} \quad \dot{m} = \frac{m(t+\delta t) - m(t)}{\delta t}, \tag{2.37}$$

using equations 2.24 to 2.29, modifying the impactor sampling such that it is not stochastic, and therefore the number of impactors of each size is not necessarily a whole number. This calculated value is then bounded from above by a maximum value, set by the time interval of the time dependent impactor properties, and from below by a minimum value of 1 yr in order to prevent the code from failing to run.

The choice of the value for the parameter ϵ is a balance of computation time and accuracy. It must be small enough that the relative change in atmosphere mass remains less than 0.1, when the stochastic nature of the impacts is included, and the atmosphere mass never becomes negative. This is tested in §2.4.4. I choose a value of $\epsilon = 10^{-4}$ as this keeps the relative deviation between the atmosphere masses calculated by the numerical code and the analytic solution < 0.01 % for all but the lowest atmosphere masses.

2.4.2 Bin number choice

The number of impactor size bins used is determined such that the values of $f_{\rm v}$ (the ratio of atmosphere growth to loss) and $t_0 = \frac{m_0}{\dot{m}^-}$ (the time it would take the atmosphere to be completely depleted in the absence of any volatile delivery) calculated analytically (through the integrals given in equations $9 - 11$ of Wyatt et al., 2019) agree with those calculated using the code, ignoring the stochastic nature of impacts. The resulting convergence of $f_{\rm v}$, for a range of impactor compositions and velocities, is well fit by a power-law

$$\frac{f_{\rm v} - f_{\rm v,analytic}}{f_{\rm v,analytic}} \approx 7.5\ N_{\rm bins}^{-2}, \tag{2.38}$$

with the convergence of t_0 following a similar relation. I therefore choose a value of $N_{\rm bins} = 500$, to achieve convergence better than 1 in 10^4, giving a fractional bin spacing of $\frac{D_{i+1} - D_i}{D_i} \approx 0.03$.

The number of velocity bins is chosen to balance computational cost with capturing the full range and detail of the distribution of impact velocities. These bins are logarithmically spaced between the minimum possible impact velocity (the escape velocity of the Earth, 11.2 km s^{-1})

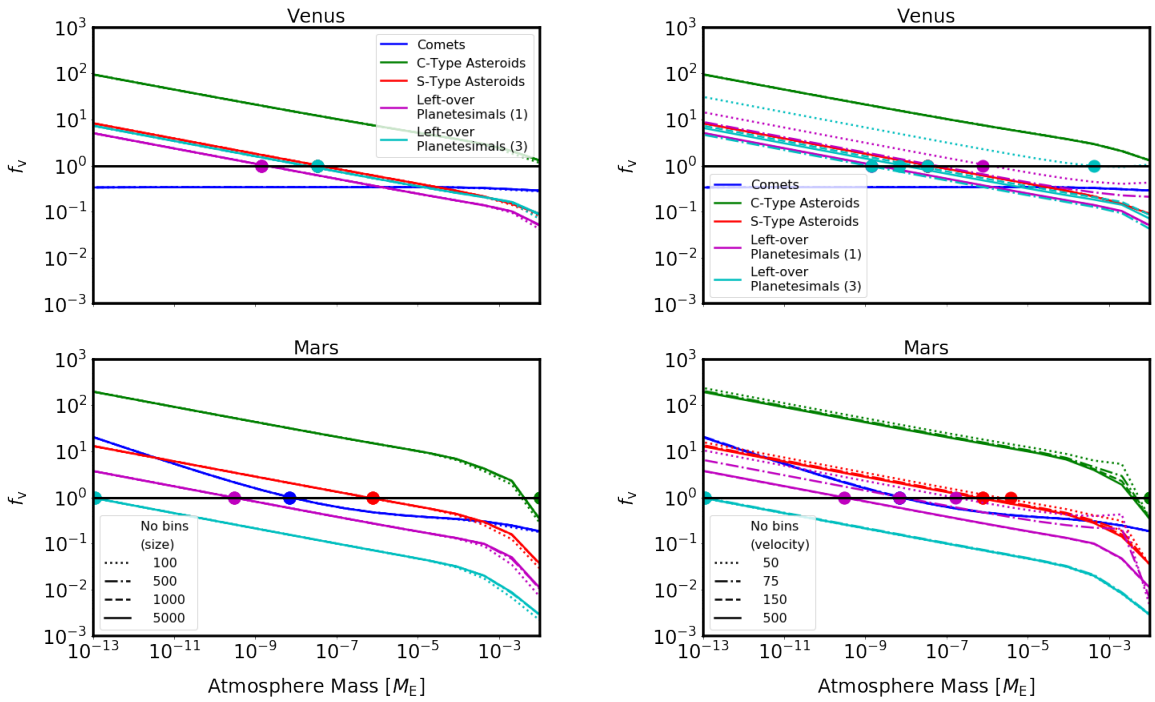

(a) (b)

Figure 2.6: Convergence testing results for the number of bins used in when specifying the distribution of impactor properties. In column (a) the number of impactor size bins is varied, and a single impactor velocity is assumed, while in column (b) the number of velocity bins covering the distribution for each population is varied and 1000 impactor size bins are used. Each test population has the nominal composition and constant impact rate with time. Two planetesimal velocity distributions are shown to capture the potential variation in impact velocity distribution (specifically the number of slow impactors, which are critical for determining how much impactor delivery occurs). In all cases the size distribution is a single power-law between 1m and 1000km. The results for Venus are shown in the top panels and Mars in the bottom panels.

and the maximum impact velocity (which depends on the population being considered). I use $N_{\rm vel} = 50$ and a maximum impact velocity of 85 km s^{-1}, which gives a factor of $\frac{v_{j+1}-v_j}{v_j} \approx 0.04$ difference between bins. For further discussion of the impact velocity distributions applied to the Earth, see §3.1.1.

When applying the code to Venus and Mars I use the same method, but due to the higher impact velocities for these planets relative to their escape velocities these choices must be revised. Results of convergence testing, using the analytic prediction for $f_{\rm v}(m_0)$ are shown in Fig. 2.6a, from which it can be seen that convergence is reached at $N_{\rm size} = 500$ bins, unchanged from the Earth. For the number of velocity bins, convergence requires a greater number of velocity bins than 50, due to the greater span in impact velocities. For this reason I chose to use 150 velocity bins, which achieves convergence in all cases. The distribution is extended to a maximum impact velocity of 15 $v_{\rm esc}$ and I use $N_{\rm vel} = 150$ velocity bins, maintaining the fractional bin spacing of ~ 0.04.

2.4.3 Test simulations and the analytic solution

In order to test the numerical code, I construct four test impactor populations that result in a range of atmospheric outcomes. For all tests I consider an Earth-like planet and initial atmosphere ($m_0 = 0.85 \times 10^{-6}$ M$_\oplus$, $\mu = 29$). I consider different impactor compositions, each characterised in terms of a bulk density (ρ_{imp}), and volatile fraction $(x_{\rm v})$. I also assign MMWs (μ_k) to each of the different impactor populations, based on realistic values for the Solar system bodies these test populations most closely resemble. For a full discussion of these values, see §3.1.4. The total mass contained in the impactor population is assumed to be $M_{\rm tot} = 0.01$ M$_\oplus$, and a single size distribution, with $D_{\rm min} = 1$ m, $D_{\rm max} = 1000$ km and $\alpha = 3.5$ is adopted. The typical velocity of each impactor population relative to the target velocity is given by $v_{\rm rel} = \xi v_{\rm targ}$ which is then converted into an impact velocity (accounting for gravitational focusing)

$$v_{\rm imp}(\xi) = \sqrt{v_{\rm esc}^2 + \left(\xi v_{\rm targ}\right)^2}. \tag{2.39}$$

These test impactor properties, labelled by the outcome they have on the atmosphere, are shown in Table 2.3. For all populations, the value of $f_{{\rm v}\,j,k}(t)$ (number of impactors in each velocity bin) is constant in time, and non-zero only in the bin corresponding to $v_{\rm imp}$.

For each test population, I calculate, using equations $9 - 11$ in Wyatt et al. (2019), the values of $f_{\rm v}$ and t_0. These values combined with the initial atmosphere mass m_0, allow the analytic solution to the atmosphere mass as a function of time derived in Wyatt et al. (2019) to be

Table 2.3: The densities, volatile fractions, MMWs and relative velocities of the four impactor types used in the numerical code to specify the distribution of impactor properties used in the code tests. The value of $f_{\rm v}$, the ratio of atmosphere mass gain to mass loss rates, is also shown for each population, calculated as described in the text.

Outcome	**Density** $\rho_{\rm imp}$ [g cm^{-3}]	**Volatile Fraction** $x_{\rm v}$	**Mean Molecular Weight** μ	**Relative Velocity Ratio** $\xi = \frac{v_{\rm rel}}{v_{\rm targ}}$	**Mass Gain / Loss Ratio** $f_{\rm v}$
Depletion	3.5	10^{-4}	15	0.5	0.027
stalling	2.8	0.02	26	1.0	0.70
constant	2.8	0.02	26	0.9	1.03
Growth	2.8	0.02	26	0.3	12.8

calculated as

$$\frac{m}{m_0} = \left[1 + \left(\frac{\alpha - 1}{3}\right)\left(f_{\rm v} - 1\right)\frac{t}{t_0}\right]^{\left(\frac{3}{\alpha - 1}\right)}. \tag{2.40}$$

The calculated values of $f_{\rm v}$ are shown also in Table 2.3.

2.4.4 Comparison to the analytic model

I first test the simplest implementation of the numerical code, which calculates the atmosphere mass evolution using only the cratering prescriptions (using equations 2.10 and 2.6), ignoring the polar cap limit and giant impact effects as these are not included in the analytic solution (given by equation 2.40). Furthermore, the stochastic nature of the impacts is ignored in this implementation of the code (meaning that it is possible for a fraction of an impactor to arrive in a given time step), and the planet mass and atmospheric composition do not evolve. In all tests 500 size bins, 50 velocity bins and an accuracy of $\epsilon = 10^{-4}$ are used, with minimum and maximum time step sizes of 1 yr and 10^4 yrs respectively. The resulting atmosphere mass evolution is shown in Fig. 2.7a, which shows general trends in growth or loss for each test population in agreement with the predictions made using Fig. 3 in Wyatt et al. (2019).

The deviation of the numerical code result from the analytic solution is shown in Fig. 2.7b. It is largest for the cases where the atmosphere depletes but is significant even for the "growth" population. This arises from the fact that the values of $f_{\rm v}$ and t_0 depend on atmosphere mass, and so change over time. This results in atmosphere masses for the "growth" population that are lower than the analytic solution. Furthermore, this plot reveals that the "constant" and "stalling" populations demonstrate the stable stalling phenomenon described in §2.3.1. In the case of the "constant" population the value of $f_{\rm v}$ is initially very close to one, and so the rates of atmosphere mass gain and mass loss are roughly equal resulting in very little change in the atmosphere mass. For the "stalling" population, this phenomenon can be understood by

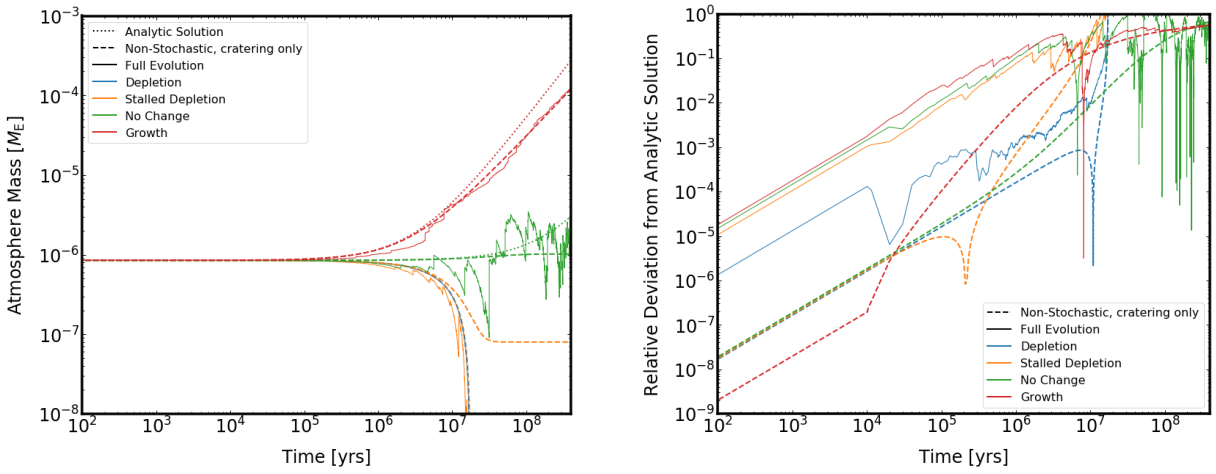

(a) (b)

Figure 2.7: Comparison of the atmosphere mass calculated using the analytical solution (shown by dotted lines) to the results of the cratering-only implementation of the code (dashed lines) and the full implementation including stochasticity, time evolution of the target properties and large impacts (solid lines). Panel (a) shows atmosphere mass as a function of time, and (b) shows the relative deviation of the atmosphere mass calculated by the numerical code from the analytical solution. Results are shown for the four test impactor populations described in Table 2.3, assuming in all cases an $\alpha = 3.5$ size distribution, $D_{\rm max} = 1000$ km and $M_{\rm tot} = 0.01$ $M_\oplus$ for the impactors, and an initially Earth-like atmosphere.

considering the change in the rate of atmosphere mass gain to mass loss ($f_{\rm v}$) as a function of time. For this impactor population, the value of $f_{\rm v}$ is initially less than one, predicting atmosphere loss, but as the atmosphere mass decreases $f_{\rm v}$ increases until it reaches one and the atmosphere mass loss and mass gain rates are equal resulting in stalled atmosphere evolution.

I also consider the inclusion of effects not accounted for by the analytic solution, namely the stochastic nature of impacts, the time evolution of the target mass ($M_{\rm targ}$) and MMW, (μ), the polar cap limit, and non-local large impact induced mass loss. Stochasticity is relevant primarily for the largest impactors, since the total numbers of these objects are typically less than the number of time steps taken by the code. The atmosphere evolution resulting from including these effects is shown in Fig. 2.7a. The general trends in atmosphere mass are similar, but the evolution is less smooth with time. This can be seen also in the relative deviation of the code results from the analytic solution shown in Fig. 2.7b. The stochastic effects dominate, but the inclusion of the large impact effects does result in lower atmosphere masses, through slower atmospheric growth or more rapid atmospheric loss. The difference due to time evolution of the target properties is small, because the change in target mass is small and the atmosphere composition has only a minor influence on the atmosphere mass change prescriptions (a more detailed discussion of these dependencies is given in §2.6.1). The

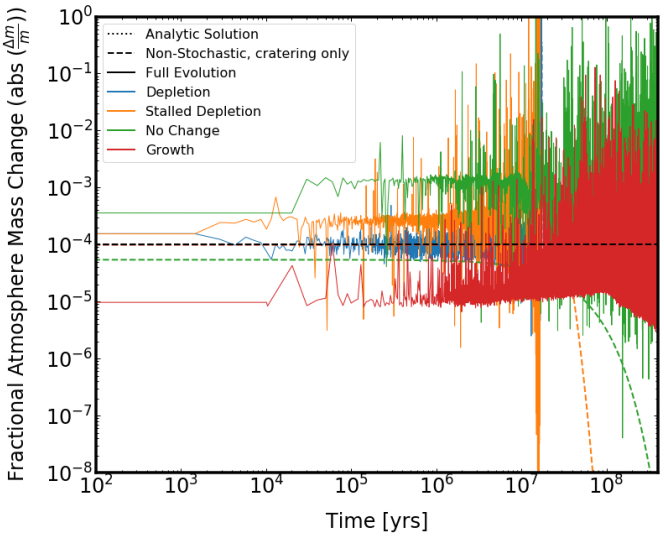

Figure 2.8: The fractional atmosphere mass change as a function of time, for the four impactor populations considered in Fig. 2.7. This limit is constant when the stochastic nature of impacts is ignored, but varies significantly between time steps when the stochasticity is included. The chosen value for the limit (10^{-4}) is shown as a black dashed line for reference.

details of the atmosphere evolution resulting from these effects is not captured by the analytic solution alone, and so motivates the development of this numerical model.

The fractional atmosphere change $\left(\frac{\Delta m}{m}\right)$ in each time step is shown in Fig. 2.8. The adaptive time step keeps this less than the accuracy limit ($\varepsilon = 10^{-4}$) when stochasticity is not included until the atmosphere mass becomes very small (at which point the time step lower limit is reached). Including stochasticity results in it varying by orders of magnitude between subsequent single time steps, both above and below the specified limit. In all runs it remains less than 100 % unless the atmosphere mass becomes very small, and so is is not necessary to decrease the chosen value of the accuracy.

2.5 Application of the numerical code

2.5.1 The Earth

The code described in §2.2 is applied to the Earth in Chapter 3. To parameterise the effect of an impact the Shuvalov (2009) cratering prescription and Schlichting et al. (2015) giant impact prescriptions are used. Based on the fluid fluid limit predictions made in §2.1.4 I apply a lower atmosphere mass limit of 10^{-18} $M_{\oplus}$.

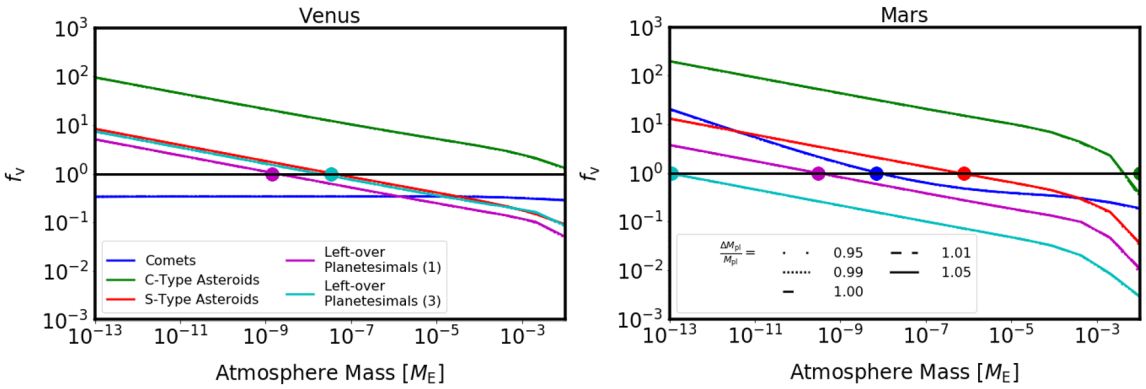

Figure 2.9: The ratio of atmosphere mass gain to mass loss rates (f_v) as a function of atmosphere mass for five representative populations of impactors onto Venus (top panel) and Mars (bottom panel). The effect of changing the planet mass by 1 and 5% is shown.

2.5.2 The outer moons of the gas giants

In Chapter 4, I apply the numerical code and analytic predictions to the study of five of the moons of the gas giants: Ganymede, Callisto, Europa, Titan and Triton. In the results presented in §4.4, which does not include the contribution of impact-triggered outgassing, the Shuvalov (2009) cratering prescription and Schlichting et al. (2015) giant impact prescriptions are used. Based on the fluid limit predictions made in §2.1.4, the behaviour of the atmospheres of these bodies cannot accurately be predicted below around 10^{-20} $M_\oplus$. A lower atmosphere mass limit of 10^{-19} $M_\oplus$ is adopted, below which the atmosphere mass is assumed to be negligible. The inclusion of the airless limit prescription, described in §2.1.4, means that below a limiting atmosphere mass (dependent on the specific properties of the system) the prescription for impactor accretion is unchanged. In §4.6.2, I also make use of a version of the code modified to include the contribution of impact-triggered outgassing to the atmosphere, using equation 2.35.

2.5.3 Venus and Mars

In order to apply the numerical code to the evolution of atmospheres on Venus and Mars in Chapter 5 two modifications are made: including the prescriptions for aerial bursts and impactor fragmentation described in §2.1.6, and implementing a lookup version of the code to improve computational efficiency. As described in §2.2.3, the code calculates the change in atmosphere mass by considering the net effect of all impacts arriving in each time step (which is adapted on the fly to keep the relative non-stochastic atmosphere mass change below a specified accuracy) simultaneously. The updated prescription described in equations 2.6, 2.10, 2.20 and 2.22 is significantly more complex to calculate, as the distribution of impactor sizes arriving at each velocity for each population must be interpolated in the fragmenting regime.

For this reason, running the code at the required accuracy becomes computationally prohibitive very quickly. I therefore developed an alternative version of the evolution module to pre-calculate the atmosphere mass loss and impactor mass accretion values that have previously been calculated on the fly. These prescriptions are calculated for each size and velocity bin for each impactor, but also depend on the target mass, atmosphere mass and atmosphere MMW - properties that will evolve over the course of the simulation - and so this grid must be calculated for multiple values of these parameters. These calculations can be simplified by taking advantage of the fact that the atmosphere mass loss and impactor mass accretion prescriptions are only weakly dependent on the target mass and that in the application of the code to Venus and Mars the planet mass is not expected to change by more than $\sim 1\%$, and so the planet mass can be treated as constant.

2.6 Testing of the second numerical code version

I test this new implementation of the code in a similar manner as in §2.4.3. First the assumption that the planet mass can be treated as constant is tested, before the number of atmosphere mass and atmosphere MMW bins required for the results to converge is determined. Finally I consider how the inclusion of the fragmentation and aerial burst prescriptions changes conclusions made for the evolution of Earth's atmosphere (because the results presented in Chapter 3 are calculated without them).

2.6.1 Planet mass change testing

The dependence of $f_{\rm v}$ on the atmosphere mass (which can be used to predict the behaviour of the atmosphere as a result of a given impactor population) is shown in Fig. 2.9 for five populations considered in the following testing. These have the nominal compositions and size distributions assumed for impacts onto Venus and Mars, and a single velocity calculated as the weighted average from the velocity distributions for these planets. This plot shows that even a relatively extreme 5% change in the target mass has negligible effect on the predicted value of $f_{\rm v}$ for a given atmosphere mass. Given that the fractional masses of impacting material (total mass relative to the planet mass) are at most 2% in the extreme cases considered for both Venus and Mars, and that the likely accretion efficiency (based on the results found for the Earth) is around 66%, changes in the planet mass sufficient to alter the atmosphere mass prescription values are not likely. I therefore pre-calculate the atmosphere mass loss and impactor mass accretion values assuming a constant value of the planet mass equal to the present day values for Venus and Mars. The evolution of the planet mass due to accretion of the impacting material is still tracked by the code.

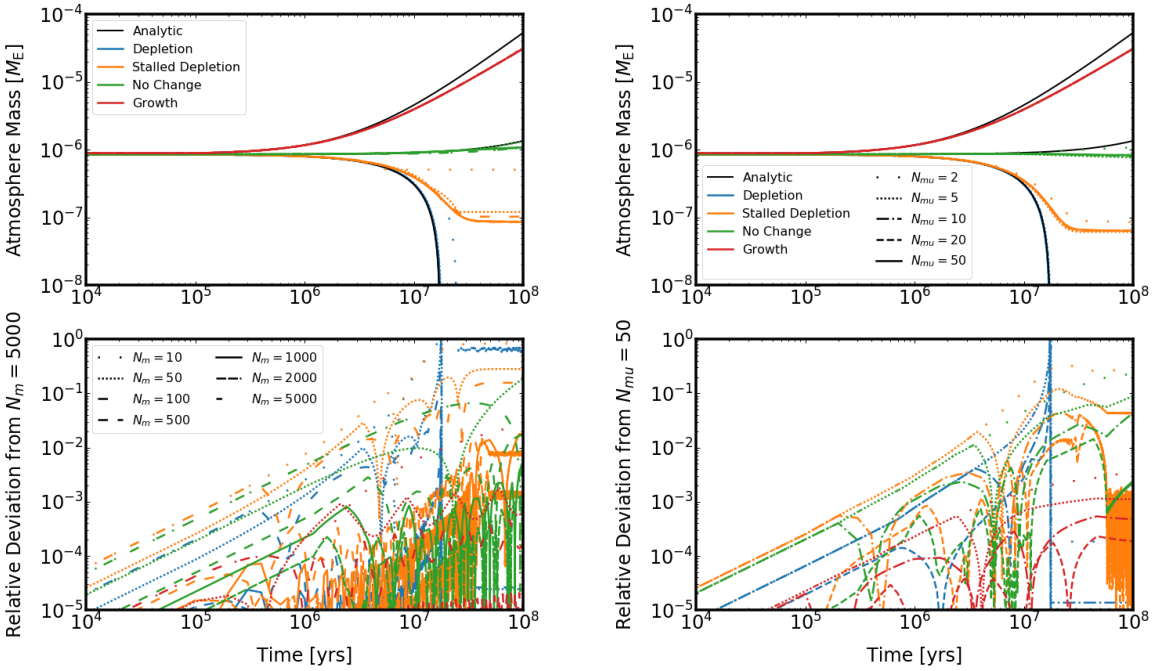

Figure 2.10: Convergence testing results for the number of bins used in the lookup table. In column (a) the number of atmosphere mass bins is varied, and the impactor MMW is kept equal to the atmosphere value, while in column (b) the number of atmosphere MMW bins is varied and 1000 atmosphere mass bins are used. Each test population has a single impact velocity and constant impact rate with time. The top panels show the atmosphere mass as a function of time, with the analytic solution shown in black for comparison. The bottom panels show the relative deviation of the numerical results from the results corresponding to the run for that population with the most number of bins.

2.6.2 Number of pre-calculation bins

To determine the number of atmosphere mass bins required to accurately implement the pre-calculation method I perform convergence testing using a non-stochastic implementation of the code. A constant atmosphere MMW is used, and four test populations demonstrating different atmosphere outcomes ("growth", "constant", "stalling", and "depletion") are considered for an initially Earth-like atmosphere, whose properties are summarised in Table 2.2. The results shown calculated using a range of number of atmosphere mass bins, log-spaced between 10^{-18} $M_\oplus$ and 10^{-3} $M_\oplus$ are shown in Fig. 2.10a. The atmosphere evolution converges for $N_m \geqslant 500$, which keeps the relative change in atmosphere mass below 1%. This corresponds to a maximum fractional bin spacing of 0.07, used in future application of the code.

The number of atmosphere MMW bins needed is tested in the same manner, using N_μ bins spaced linearly between 10 and 46. These results are shown in Fig. 2.10b. In this case

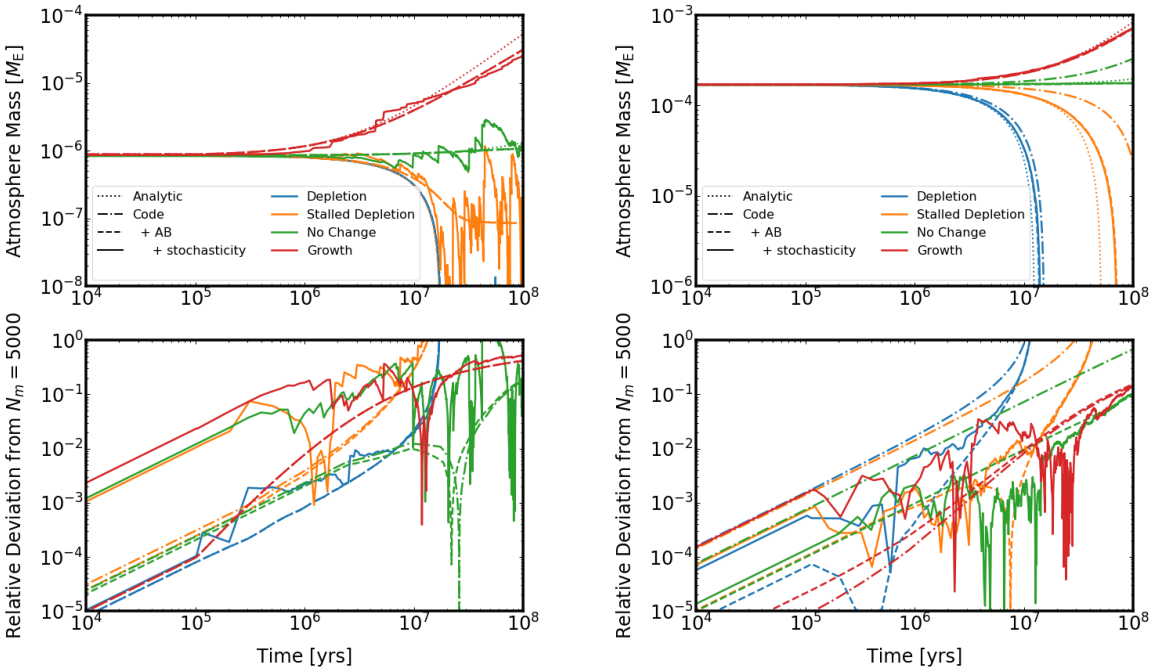

Figure 2.11: Code testing results for the new pre-calculation method included in the code with the aerial burst and fragmentation prescriptions included. Both figures show the difference between the analytic, non-stochastic and stochastic versions of the code, with the non-stochastic standard S09 prescription shown also. Column (a) shows the results for an Earth-like, cool, atmosphere while column (b) shows the results for a much more massive, hot atmosphere similar to present day Venus. The top panels show the atmosphere mass as a function of time, calculated using 1000 atmosphere mass bins and 5 μ bins. The bottom panels shows the relative deviation from the analytic solution.

convergence at $< 1\%$ is achieved for $N_\mu = 20$, giving a maximum fractional bin spacing of 0.7. This value is used in all further applications of the code.

2.6.3 Testing of the pre-calculation method

Finally, I test the code in comparison to the analytic solution from Wyatt et al. (2019). To do this I use 500 size bins, 1000 atmosphere mass bins, constant atmosphere MMW (equal to the impactor MMW) and the impactor populations from Table 2.2. These populations represent a dry, fast, enstatite chondrite-like impactor that rapidly strips the atmosphere, and three asteroid-like impactors at different velocities. In each case a total impactor population mass of 0.0025 $M_\oplus$ is assumed. The analytic solution is compared to a non-stochastic pre-calculated version of the code (with only the cratering prescription), a non-stochastic code including the updated aerial burst and fragmentation prescription, then a full stochastic implementation of the code. The analytic prediction calculates an atmosphere mass evolution with time assuming a constant value of f_v for each impactor population (also shown in Table 2.2) and so

does not recreate the characteristic stalling behaviour as this relies on $f_{\rm v}$ evolving towards one.

The results for a cool Earth-like atmosphere ($m_0 = 0.85 \times 10^{-6}$ M$_\oplus$, $T_{\rm atm} = 278$K) are shown in Fig. 2.11a. This illustrates the inaccuracy of the analytic solution due to the change in $f_{\rm v}$ as the atmosphere mass changes and demonstrates that stochastic variation is significant, particularly at lower atmosphere masses. There is little difference between the non-stochastic code results with and without the aerial burst and fragmentation prescription, as expected for a cool and thin atmosphere, for which this prescription is not relevant.

To test the effect that the new prescription has on a more appropriate atmosphere I repeat these tests on a hot, massive atmosphere ($P_{\rm surf} = 200$ bar, $T = 800$ K), constructing four new test populations that produce the same quantitative results ("depletion", "stalling", "constant" and "growth") but are different in terms of composition and velocity, which are also shown in Table 2.2. These populations also assume a significantly more massive total impacting population mass (5% $M_\oplus$) to produce an observable change in a more massive atmosphere. The results of these tests are shown in Fig. 2.11b. From these results it can be seen that the inclusion of the aerial burst and fragmentation prescription results in greater atmosphere mass loss and lower final atmosphere masses when compared to the previous prescription, as expected. At this high atmosphere mass, with the larger impacting population, stochastic effects are less noticeable.

2.7 Alternative large impact prescription

The largest impacts considered in this dissertation, in the accretion tail scenario, are not the "giant impacts" associated with planet formation (Chambers, 2001). For this reason, I use a relatively simple (and thus fast to calculate in the code) prescription for the non-local atmosphere mass loss caused by large impactors, based on the work of Schlichting et al. (2015) and described in §2.1.2, and assume that the Shuvalov (2009) prescription for impactor mass accretion can be extrapolated into the *airless limit* for large impacts. Truly giant impacts, where the impactor and target masses are comparable, can cause substantial erosion of the target atmosphere and target body itself and have effects predicted by hydro-code simulations that are more complicated than those captured by the Schlichting et al. (2015) prescription. If the size distribution of impactors considered by the code is extended beyond objects with diameters of ~ 1000 km (Vesta-sized) to Mars-sized embryos (3000 km) then the treatment of the largest impactors must be reconsidered.

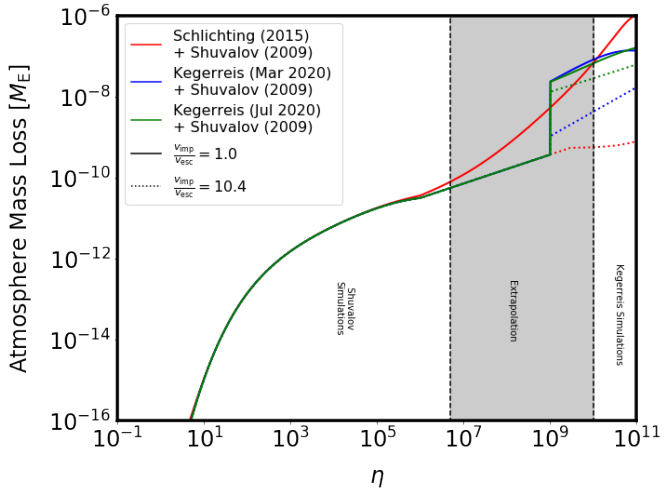

Figure 2.12: The predicted fractional atmosphere mass loss after an impact, as a function of the erosional efficiency parameter η. The values calculated by the combined cratering and Schlichting et al. (2015) prescription used in the majority of this dissertation is shown in red, and the alternative combined cratering and Kegerreis et al. (2020b) prescription (assuming a $45\,\mathrm{deg}$ impact angle) is shown in blue, while the updated Kegerreis et al. (2020a) prescription is shown in green. All values are calculated for an Earth-like atmosphere and C-type asteroid-like impactors. In order to display the large values of η at which these prescriptions diverge, the predicted atmosphere mass loss for impactors with sizes $D = 1 - 10^7$ m, and two extremes of impact velocity, are calculated and shown by different line styles. The range of values for η corresponding to the cratering simulations, and the Kegerreis et al. (2020b) SPH simulations are shown, as is the (shaded) region between the two in which the cratering prescription is extrapolated.

The combination of the Shuvalov (2009) cratering and the Schlichting et al. (2015) giant impact prescriptions described in §2.1 is not the only available method for parameterising the atmosphere loss caused by impacts. As an alternative to the Schlichting et al. (2015) giant impact atmosphere mass loss prescription, I consider in the following section two prescriptions from Kegerreis et al. (2020b,a) and Denman et al. (2020), and as an alternative to the Shuvalov (2009) impactor accretion prescription I consider the prescription from Denman et al. (2020).

2.7.1 Kegerreis (2020) prescriptions

The prescription from Kegerreis et al. (2020b), a fit to the results of 3D SPH simulations, parameterises atmosphere loss as a function of specific impact energy

$$Q = \left(1 - b\right)^2 \frac{1}{2} \frac{m_{\mathrm{imp}}(M_{\mathrm{targ}} + m)}{(m_{\mathrm{imp}} + M_{\mathrm{targ}} + m)^2} v_{\mathrm{imp}}^2, \tag{2.41}$$

where variation in the impact angle (θ) is accounted for through the impact parameter $b = \sin(\theta)$. This energy scales similarly with impactor properties as the erosional efficiency η. The fractional atmosphere mass loss per impactor mass is

$$\frac{m_{\rm atmloss}}{m_{\rm imp}} = \frac{m}{m_{\rm imp}} \times 3.2 \times 10^{-5} \left(\frac{Q}{\rm Jkg^{-1}} \right)^{0.604}. \tag{2.42}$$

To use this prescription for my model of the Earth requires significant extrapolation in impactor size and atmosphere mass. The Kegerreis et al. (2020b) simulations consider only a single impactor mass and composition (the canonical Moon-forming impactor). The range of atmosphere masses considered is much higher than those in my models, from $10^{-2.5} - 10^{-1}$ $\rm M_{\oplus}$. Furthermore, the atmosphere in their simulations is assumed to be hotter than I consider, which should to lead to a higher atmosphere mass loss estimates. To investigate the effect of using this prescription I construct an impact prescription, incorporating a switch from the combined cratering and Schlichting et al. (2015) prescription to the Kegerreis et al. (2020b) prescription for impacts with $\eta > 10^9$ (chosen as this value lies between the maximum η considered in Shuvalov (2009) and the estimated minimum η considered in Kegerreis et al. (2020b)). The atmosphere mass loss predicted by the two prescriptions considered is shown in Fig. 2.12, from which it can be seen that the Kegerreis et al. (2020b) prescription does predict higher mass loss for both the most and least energetic impactors, for a range of impact velocities. The approximate locations covered by the two sets of simulation results are shown, while the region of parameter space in which the results must be extrapolated is highlighted.

In a subsequent paper, (Kegerreis et al., 2020a) extended their earlier work to consider different impactor-target mass ratios and presented an updated prescription for the fractional atmosphere mass loss. This is parameterised in a different way, no longer using the specific incident energy, instead, the atmosphere mass loss per impactor mass is now

$$\frac{m_{\rm atmloss}}{m_{\rm imp}} = \frac{m}{m_{\rm imp}} \times 0.64 Y^{0.65}, \tag{2.43}$$

where

$$Y = \left[\left(\frac{v_{\rm imp}}{v_{\rm esc}} \right)^2 \left(\frac{m_{\rm imp}}{m_{\rm imp} + + m_{\rm targ}} \right)^{0.5} \left(\frac{\rho_{\rm imp}}{\rho_{\rm targ}} \right)^{0.5} f_M(b) \right], \tag{2.44}$$

and $f_M(b)$ accounts for the impact parameter through:

$$f_M = \frac{\rho_{\rm targ} V_{\rm targ}^{\rm cap} + \rho_{\rm imp} V_{\rm imp}^{\rm cap}}{\rho_{\rm targ} V_{\rm targ} + \rho_{\rm imp} V_{\rm imp}} \tag{2.45}$$

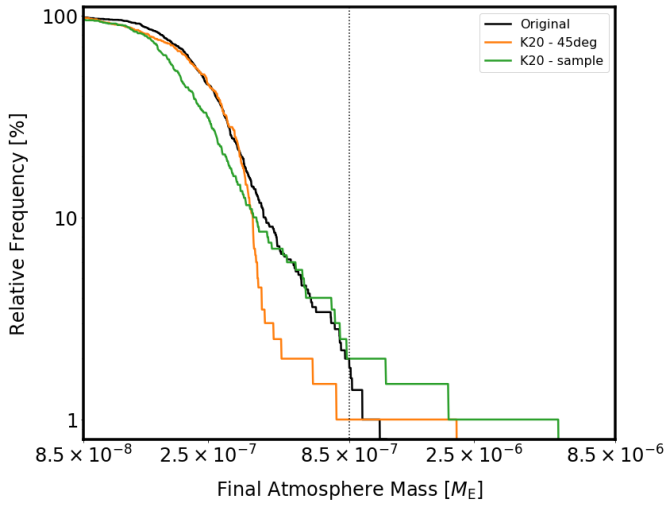

Figure 2.13: The distribution of final atmosphere masses calculated for the nominal atmosphere and impactor populations comparing the combined cratering and Schlichting et al. (2015) prescription (our earlier nominal case), and the Kegerreis et al. (2020b) prescription (both randomly sampled impact angles and an assumed impact angle of $45\,\mathrm{deg}$). The Schlichting et al. (2015) prescription includes the results of 500 runs, while the two Kegerreis et al. (2020b) prescriptions include 200 runs each.

and the cap volume $V^{\mathrm{cap}}_{\mathrm{imp,targ}} = \frac{\pi}{3} d^2 \left(3R_{\mathrm{imp,targ}} - d\right)$ depends on the parameter $d = (R_{\mathrm{targ}} + R_{\mathrm{imp}})(1 - b)$.

This is shown in comparison to the (Schlichting et al., 2015), and Kegerreis et al. (2020b) prescriptions in Fig. 2.12.

To further investigate the dependence of the results for the Earth presented in Chapter 3 on the assumptions made about the giant impact prescriptions I consider replacing the Schlichting et al. (2015) large impact prescription with the prescription from Kegerreis et al. (2020b) in the numerical code. The Shuvalov (2009) prescriptions assume $45\,\mathrm{deg}$ as the most likely impact angle, while Schlichting et al. (2015) assume head-on collisions. Due to the strong dependence of the Kegerreis et al. (2020b) predicted atmosphere loss on θ, I consider both a constant impact angle of $45\,\mathrm{deg}$ and sampling the impact angle for each impactor randomly from a uniform distribution. The results from the numerical code are illustrated in Fig. 2.13, as the relative frequency of the final atmosphere masses obtained in the reference case for the Earth (presented in §3.2.5) compared to the results for the same initial conditions and impactor populations, but implementing the Kegerreis et al. (2020b) prescription.

In general the final atmospheres mass distribution are similar, with median percentage changes in the final atmosphere mass of -72.0, -71.2 and -76.9 % for the Schlichting et al.

(2015), Kegerreis et al. (2020b) ($45\,\mathrm{deg}$) and Kegerreis et al. (2020b) (sampled angle) prescriptions respectively. Kruskal-Wallis H Tests show that the Kegerreis et al. (2020b) ($45\,\mathrm{deg}$) results are not statistically different from the combined cratering and Schlichting et al. (2015) prescription, (with p-value $p = 0.153$), however the Kegerreis et al. (2020b) (sampled angle) results are ($p = 2.3 \times 10^{-5}$). These results, using randomly sampled impact angles, result in cases of greater atmospheric loss and also of more extreme large atmosphere masses than the $45\,\mathrm{deg}$ case. This is likely due to the non-linear dependence of the atmosphere mass loss on impact angle (see equations 2.41 and 2.42). The higher number of low final atmosphere masses in the Kegerreis et al. (2020b) prescription runs in general agrees with the prediction made in §2.1.2, that this prescription might overestimate the atmosphere mass loss by the largest impactors due to the higher atmospheric temperatures used in their simulations.

2.7.2 Denman (2020) prescriptions

A further alternative prescription for the parameterisation of giant impacts is given by Denman et al. (2020), in which a series of SPH simulations for large impactors onto planets with thick atmospheres were performed, and this work provides a procedure for calculating the atmosphere mass loss as well as the core and mantle mass of the largest remnant, which is assumed to be the final, post-collision mass for comparison with the other prescriptions used in this dissertation. Importantly, this paper showed that a single impact cannot remove the entire atmosphere mass without causing significant target erosion, an effect that is not accounted for in the Schlichting et al. (2015) giant impact. This parameterisation is done in terms of the specific incident energy of the impactor, equation 2.41 assuming $b = 0$ (head on collisions).

Following equations 21 to 26 in Denman et al. (2020) allows the calculation of the atmosphere mass loss and largest remnant mass (M_{LR}) as a function of the impactor and target properties. The fractional impact mass accreted can be calculated from the mass of the largest remnant as

$$\frac{m_{\mathrm{imp,acc}}}{m_{\mathrm{imp}}} = \frac{\left(\frac{M_{\mathrm{LR}}}{M_{\mathrm{targ}}+m_{\mathrm{imp}}}\right) \times (M_{\mathrm{targ}} + m_{\mathrm{imp}}) - M_{\mathrm{targ}}}{m_{\mathrm{imp}}}. \tag{2.46}$$

This prescription for impactor mass accretion agrees qualitatively with the Shuvalov (2009) prescription, but Shuvalov (2009) underestimates the accreted impactor mass and does not account for erosion of the planet by the fastest, largest impactors. In both cases slow impactors result in accretion of most of their mass onto the planet, while fast impactors contribute no mass according to the Shuvalov (2009) cratering prescription, and can cause net mass loss through erosion of the target according to the Denman et al. (2020) prescription.

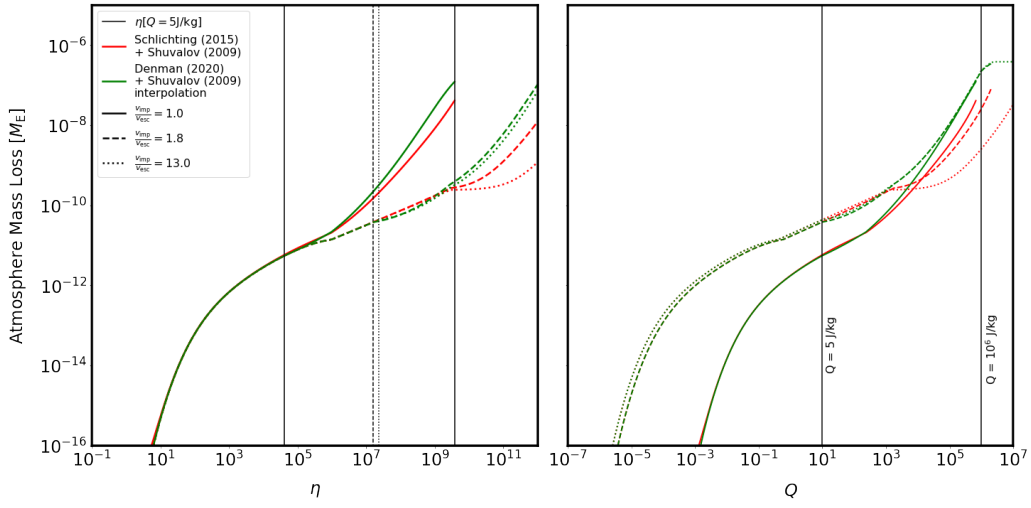

(a)

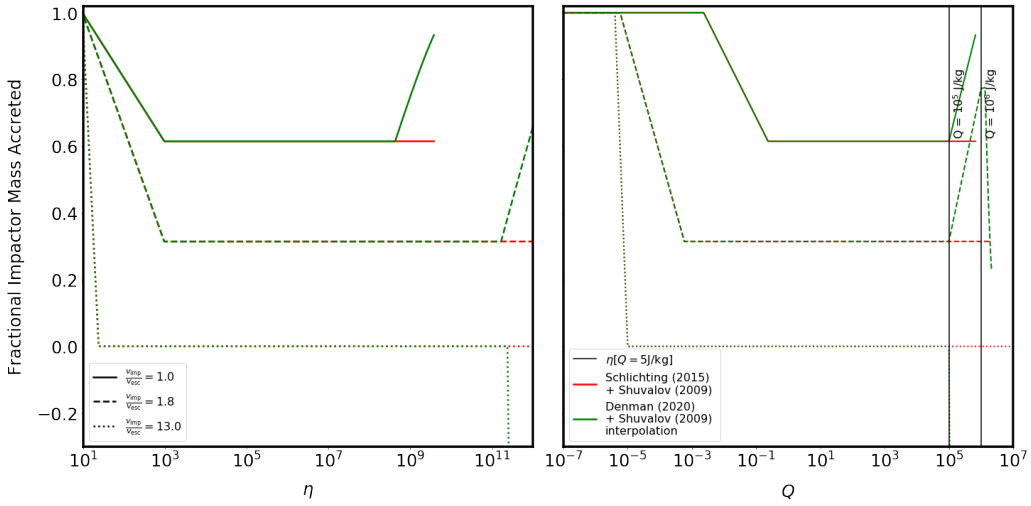

(b)

Figure 2.14: The top panels show the predicted absolute atmosphere mass loss from an Earth-like planet, as a function of erosional efficiency (η) in the left panel and specific impact energy (Q) in the right panel. The bottom panels show the predicted fractional impactor mass accreted as functions of the same parameters. The Schlichting et al. (2015) prescription for large impact effects are shown by red lines, while the Denman et al. (2020) prescriptions are shown in green. Three representative values for the velocity ratio are shown by different line styles. The limits used to specify the different interpolation regimes are shown by vertical black lines. These are single values of Q, but correspond to different values of η for different impactor velocities.

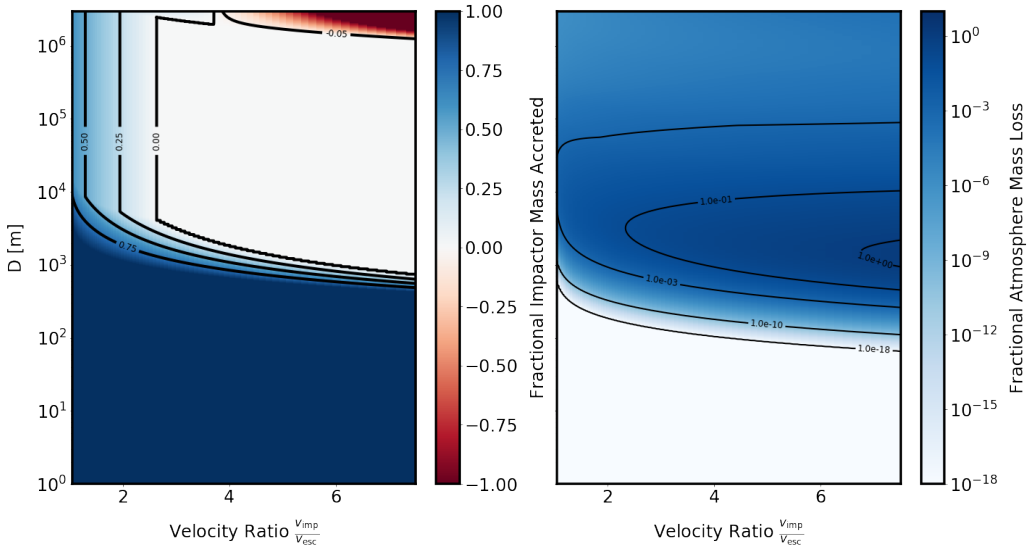

Figure 2.15: The fractional impactor mass accreted (left panel) and the fractional atmosphere mass loss (right panel) calculated using the interpolation regime described in the text as a function of the ratio of impact velocity to planet escape velocity and impactor size.

These two prescriptions can be combined to implement a modified impact prescription for atmosphere mass loss and impactor mass accretion including the potential for target mass erosion. To construct a prescription that is appropriate for a larger range of impactor sizes I interpolate, dividing the impacts into three regimes depending on their specific impact energy (Q):

1. $Q < Q_{\rm lim,Sh09}$ where the Shuvalov (2009) prescription is used unchanged;
2. $Q_{\rm lim,Sh09} < Q < Q_{\rm lim,D20}$ where the Shuvalov (2009) and Denman et al. (2020) prescriptions are interpolated;
3. $Q < Q_{\rm lim,D20}$ where the Denman et al. (2020) prescription is used unchanged.

For the atmosphere mass loss, the specific impact energy values adopted as the limits on these regimes, $Q_{\rm lim,Sh09,loss} = 10 {\rm J/kg}$ and $Q_{\rm lim,D20} 10^6 {\rm J/kg}$, are chosen to be roughly equal to the most and least energetic impacts considered in Shuvalov (2009) and Denman et al. (2020) simulations respectively. Between these limits the atmosphere mass loss is interpolated logarithmically in Q. For the impactor mass retention, a higher lower limit is chosen, as the phenomena important for the Denman et al. (2020) results (catastrophic disruption of the target, and increased accretion efficiency due to the gravitational contribution by the projectile) are relevant only for the most massive, energetic impactors. In this case, the lower limit on Q is set to be $Q_{\rm lim,Sh09,loss} = 10^5 {\rm J/kg}$. Between these limits the change in target mass is interpolated linearly in $\log(Q)$. The predicted atmosphere mass loss as a function of both

erosional efficiency and specific impact energy is shown in Fig. 2.14a, for three values of the impact velocity ratio and an Earth-like planet. In each case, the values of η, Q and atmosphere mass loss are calculated for an asteroid-like impactor composition, up to a maximum impactor size of $10,000$ km (larger than anything considered in this dissertation but shown for illustrative purposes).

The predicted fractional impactor mass retention as a function of η and Q is shown in Fig. 2.14b. For the slower, most massive impactors, an increase in accretional efficiency at large sizes can be seen, due to the increase in the mutual escape velocity of the planet and impactor system, favouring retention of more material after the impact. For the extreme case of a very high velocity impact, the largest impactors result in total disruption of the planet, with the Denman et al. (2020) prescription following the catastrophic disruption scaling from Leinhardt & Stewart (2012) (assuming the mass of the largest post-collision remnant represents the final planet mass), and so significant mass loss from the planet is predicted.

These results are summarised for asteroid-like impactor properties onto an Earth-like planet, in the 2D plots shown in Fig. 2.15. These show the fractional atmosphere mass loss and impactor mass accretion as a function of both impactor size and ratio of the impact velocity to the planet escape velocity. From this it can be seen that noticeable planet mass loss occurs only for impactors more massive than those considered previously (when the adopted prescription did not account for any target erosion), requiring $D > 1000$ km. Given the quantitative agreement between the relatively simple Shuvalov (2009) and Schlichting et al. (2015) prescriptions and the more complex Kegerreis et al. (2020b,a); Denman et al. (2020) simulation results it is considered acceptable to use the Shuvalov (2009) and Schlichting et al. (2015) in the rest of this dissertation.

2.8 Summary

To summarise, this chapter presents the methodology on which the rest of this dissertation is based, by:

- Presenting the prescriptions used to describe the effect of an impact on the atmosphere of a range of impact regimes and discussing alternatives;
- Describing the numerical code used to model the stochastic evolution of an atmosphere undergoing bombardment, and the process used to validate it;
- Deriving an analytic prediction for the atmosphere stalling mass.

3

The evolution of Earth's atmosphere

In this chapter I apply the numerical code described in §2.2 in chapter 2 to the evolution of the Earth's atmosphere as it undergoes bombardment following the Moon-forming impact. The enstatite chondrite-like composition of the Late Veneer implies that the mass of impacting objects is dominated by the population of planetesimals left-over after terrestrial planet formation, however impacts by comets and asteroids are also predicted by dynamical models. The impact prescription used in the code in this chapter consists of the combined Shuvalov (2009) cratering (see §2.1.1) and Schlichting et al. (2015) giant impact (see §2.1.2) prescriptions described in §2.1.3.

I first describe the impactor populations considered, calculating realistic impact velocity distributions based on the results of dynamical simulations of the early history of the Solar system (within the framework of the Nice and Grand Tack models) in §3.1. In §3.2 the results from the code are presented, first for individual impactor populations in isolation to investigate the effect of changing the assumed impactor properties. I consider a representative evolution of the Earth's atmosphere undergoing bombardment by all impactor populations simultaneously in §3.2.5 and investigate the effect of varying the atmosphere initial conditions in §3.2.6. Finally in §3.3 I discuss these results, considering the phenomenon of atmospheric convergence, quantifying the predicted water delivery to the Earth and comparing my results

to previous studies. I also briefly discuss potential alternative atmosphere evolution mechanisms, and propose directions for future work. My conclusions are presented in §3.4.

3.1 Assumed impactor and planet properties

In order to accurately constrain the evolutionary history of Earth's atmosphere due to impacts, it is necessary to know the number of objects of different sizes that impact the Earth as a function of time, the velocities they arrive with and their composition. The effect of three distinct populations of impactors are considered: left-over planetesimals, comets and asteroids. In the following sections I discuss the choices made regarding their properties.

3.1.1 Impact velocities and probabilities

For all impactor populations I use results from the following N-body dynamical simulations to calculate the flux of impactors in each velocity bin.

Asteroids: Nesvorný & Morbidelli (2012) performed simulations of the giant planet instability, evolving five giants initially in mutual MMR, with a disk of left-over planetesimals located beyond the outermost planet. Within these simulations, a series of encounters between Jupiter and Saturn and the fifth giant planet results in discrete, step-like, evolution of the semi-major axes of Jupiter and Saturn, and ejection of the fifth planet. The simulations most successful at recreating the current Solar system architecture were extended in Nesvorný et al. (2013) and Nesvorný et al. (2017a), from which I calculate the asteroid impactor fluxes. These simulations successfully reproduce the orbital distributions of main belt asteroids and current impact fluxes. In the case I adopt from Nesvorný et al. (2017a) (their CASE1B), the orbits of the inner planets and $50,000$ asteroids are integrated over the lifetime of the Solar system, using the CASE1 results from Nesvorný et al. (2013) to determine the orbits of the giant planets during and after the instability (which is assumed to occur early, at $t \approx 5.7$ Myr). The terrestrial planets are assumed to have an initial AMD slightly lower than the present value and the initial distribution of asteroids is weighted by a Gaussian distribution in inclination and eccentricity.

Comets: To calculate the number of impacts by comets onto the Earth, the results from CASE2 in Nesvorný et al. (2017b) are used. These simulations follow the evolution of test particles originating from the trans-Neptunian disk, using artificial force terms to recreate the planetary migration and instability from Nesvorný & Morbidelli (2012). This approximation of the

planetary migration is not identical to that assumed for the asteroids, but is similar, therefore using these two cases together here is acceptable.

For both the asteroid and comet data, time zero in the dynamical simulations does not correspond to the start time of the simulations performed in this chapter (the Moon-forming impact). While the timing of the giant planet instability relative to the Moon-forming impact is not certain, I assume in this dissertation an early instability (Clement et al., 2018, 2019) and thus use data from $t > 50$ Myr in the dynamical simulations.

Left-over planetesimals: The simulations of terrestrial planet formation from Walsh et al. (2011) are used as the starting conditions for the simulations of left-over planetesimals performed by Morbidelli et al. (2018), which cloned the orbital distributions of planetesimals surviving at 30 and 50 Myr (approximately when the planets stabilise), for two different simulations, and consider two different initial terrestrial planet configurations (their current orbits, and circular coplanar orbits). The orbits of the planets and 2000 left-over planetesimals in each of these eight configurations are then integrated for 500 Myr. Seven of these configurations are considered (with the one not used randomly excluded), allowing the uncertainties in the models to be accounted for. For the nominal case a single configuration is considered, called here case 1, which corresponds to one of the cases cloned at 30 Myr, with the terrestrial planets on their current orbits.

The simulations described above give the orbital elements (semi-major axis, eccentricity and inclination) of each particle in the Earth-crossing region, and the Earth. The Earth was not included in the simulations concerning the comets, so I interpolate the values from the asteroid data for my calculations. For each particle the number of impacts in each velocity bin at each time ($R_k(t) \times f_{\mathrm{v},j,k}(t)$ in §2.2.2) is calculated using the method described in Wyatt et al. (2010). This represents each particle as a population of particles with random mean longitude, argument of pericentre and longitude of ascending node and does likewise for the Earth, before a total of at least $N_{\mathrm{part}} = 10^5$ particles are chosen from the overlapping region of these two populations. In the cases where the Earth has zero eccentricity and inclination, its torus is artificially set to have a width of 3 Hill radii[1]. The collision rates and relative velocities between each pair of closest neighbours are calculated and summed (using the relevant weighting) over the orbit to give the probability distribution as a function of relative velocity. The calculated probability distributions (i.e. the probability of a particle on a given orbit colliding with the Earth at a particular velocity) have irregular shapes, often with multiple peaks, that cannot be properly represented by a single average value. This motivates the

[1]Increased to 5 Hill radii if 3 gives zero probability

inclusion in the code presented in §2.2 of a distribution from which the impact velocities are drawn.

Since the number of particles in the Earth-crossing region is smaller at late times I combine time-steps such that there are at least $N_{\min} = 50$ particles contributing to each velocity distribution. This choice reflects a balance between retaining the variation in impact velocities resulting from different dynamical histories and avoiding velocity distributions that are inaccurate due to sampling only a small number of particles. The number of comets in the Earth-crossing region declines very rapidly (due to ejection through close encounters with Jupiter) and so it is necessary to combine the velocity distributions for all comets into a single distribution. To avoid the unrealistic scenario of a constant (extremely low) impact rate onto the Earth by comets for the entire time period, I impose an artificial exponential decay for the impactor flux rate. This decay is assumed to have a half life of 10 Myr, based on an approximate fit to the time dependency of the total impact probability. While this is a simplification, the final results we obtain are insensitive to the precise impact times in comparison to the variation introduced by other effects considered.

The distributions calculated using the above method are shown as mass accretion rates ($\frac{R_k(t)}{\int R_k(t)\mathrm{d}t} \times f_{\mathrm{v},j,k}(t) \times M_{\mathrm{tot}\ k}$, using the total mass estimates described in §3.1.3) in Fig. 3.1, illustrating the irregular distributions at each time step. The results are shown for each of the three impactor populations, using the nominal left-over planetesimal dynamics. The left-over planetesimals are in general slower, and more heavily skewed towards the slowest collisions (at escape velocity), while the asteroid and comet populations both contribute impactors with velocities up to 6 times the escape velocity. The mass accreted from the left-over planetesimal population is significantly higher than the other two populations. The effect of combining multiple time steps to have a minimum of 50 particles contributing to each distribution is most pronounced at late times, when the original simulations contain fewer particles.

The calculated values of $\frac{R_k(t)}{\int R_k(t)\mathrm{d}t} M_{\mathrm{tot}\ k}$ and $f_{\mathrm{v},j,k}$ for the different impactor populations are shown in Fig. 3.2. The left-over planetesimal cases are labelled as case 1 to case 7. A spike in impact probability is seen at around 270 Myr for two cases (3 and 4), due to left-over planetesimals trapped in MMRs with the Earth. These bodies are phase-protected from collisions with the Earth, but they give a non-zero collision probability in my code because resonant protection is not accounted for. Eventually these bodies leave the resonance by chaotic diffusion, then quickly disappear under the effects of planetary encounters. The effect of these spikes is seen in the atmosphere evolution profiles shown in §3.2.4, but they do not have a significant effect on the final atmosphere masses when compared to the other cases.

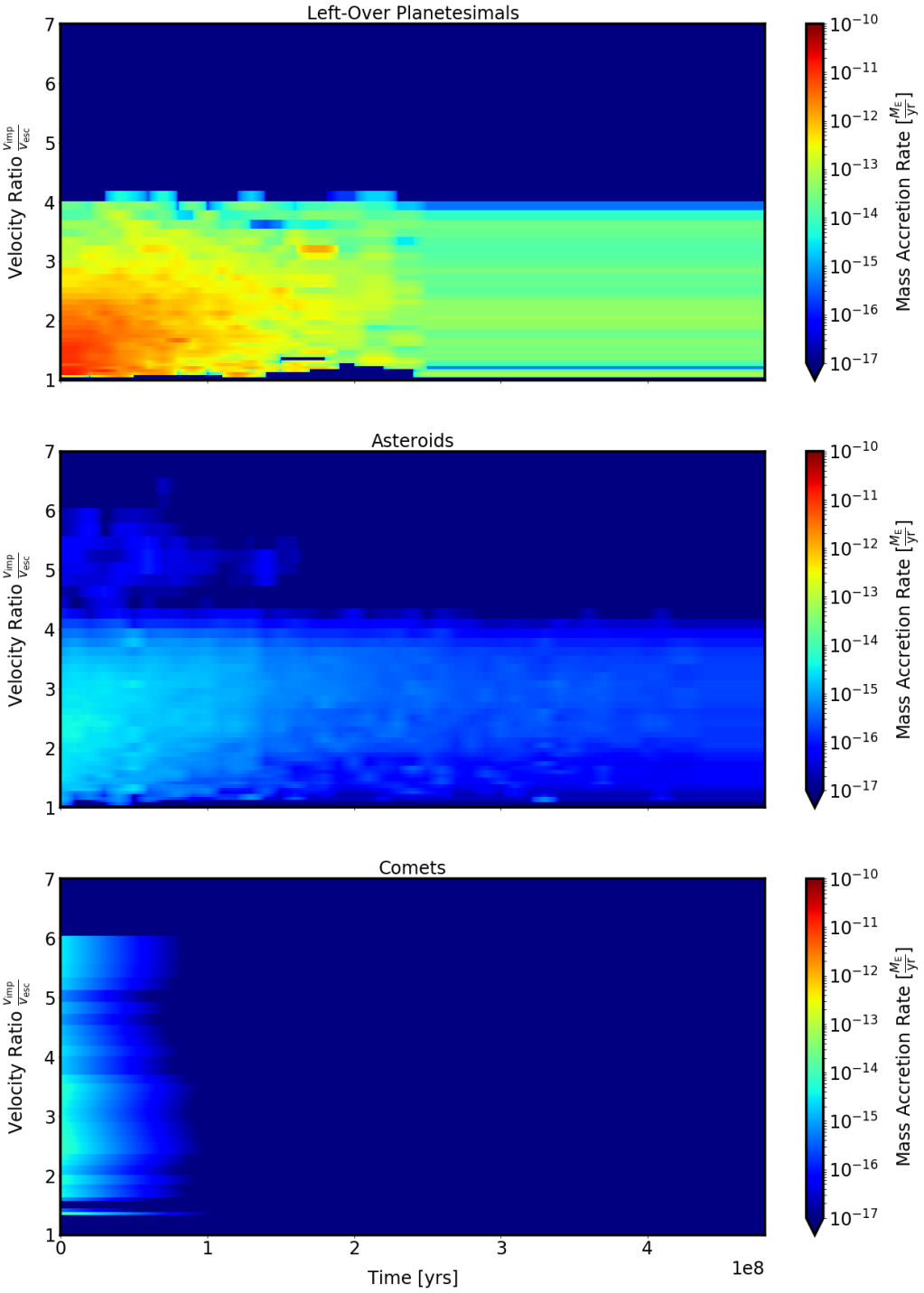

Figure 3.1: An illustration of the distribution of mass accretion rate in time and velocity ($\frac{R_k(t)}{\int R_k(t)\mathrm{d}t} f_{\mathrm{v}j,k}(t) M_{\mathrm{tot}\ k}$) for each of the three impactor populations: left-over planetesimals (top), asteroids (middle) and comets (bottom). This presentation allows the total mass accreted from three populations as a function of time or velocity to be visualised through summing over the other axis. These plots show the distribution after multiple time steps have been combined (if necessary). For comets, the total number of particles used to calculate the distribution is small, meaning that all the velocity distributions are combined. I therefore impose an artificial exponential decay with a half life of 10 Myr.

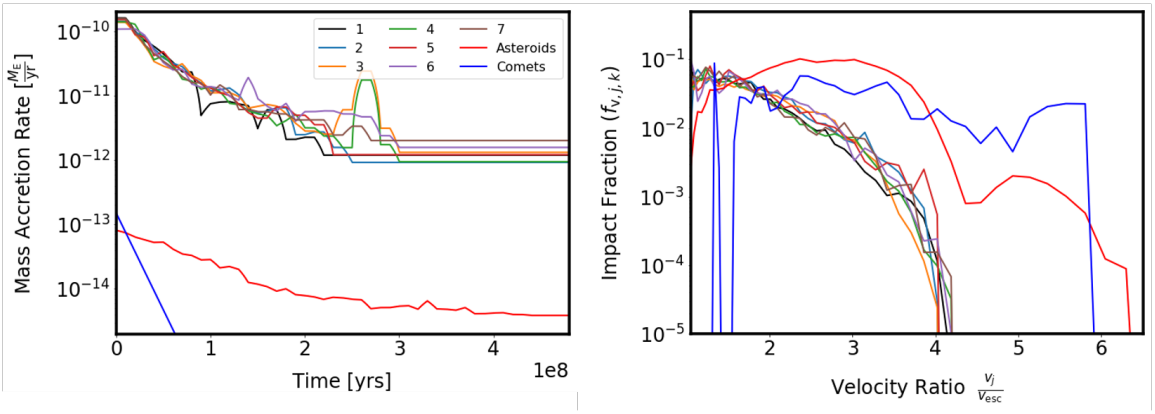

Figure 3.2: The mass accretion rate ($\frac{R_k(t)}{\int R_k(t)\mathrm{d}t} M_{\mathrm{tot}\ k}$) and impact fraction as a function of velocity ($f_{\mathrm{v},j,k}$) calculated for the different impactor populations are shown in the left and right panels respectively.

3.1.2 Size distribution

The distribution of impactor sizes at the time of the impacts cannot directly be measured, and so must be inferred from observational signatures. I assume a size frequency distribution (SFD) that is the same as the present day main belt asteroids, from Bottke et al. (2005), for the left-over planetesimal and asteroid populations, supported by observations that the impactor size distribution inferred from the Lunar craters matches that expected from the main belt asteroids (Strom et al., 2005). For the comets I assume a shallower size distribution similar to that for the primordial trans-Neptunian disk from Nesvorný et al. (2018). The upper limit of the size distribution is chosen to be $D_{\mathrm{max}} = 1000$ km, approximately equal to the size of the largest object in the asteroid belt. The lower limit is set to be 1 m, and objects between this size and the minimum size given in Bottke et al. (2005) (1 km) or Nesvorný et al. (2018) (100 m) are assumed to have a collisional SFD with an $\alpha = 3.5$ power-law (Dohnanyi, 1969). These SFDs are shown in Fig. 3.3. The largest objects contribute the majority of the total mass in the distribution derived from the main belt asteroid SFD, while the comet mass is dominated by ~ 100 km bodies.

The lower size limit of $D_{\mathrm{min}} = 1$ m is chosen to balance the computational costs of including increasing large numbers of increasingly small impactors with their influence on the results. Small impactors typically have a negligible influence on the atmosphere as they remove very little atmosphere mass and contain only a fraction of the total population mass. For fixed impactor and planet properties, equation 2.5 shows that the erosional efficiency depends on atmosphere mass as $\eta \propto m^{-1}$ and thus as the atmosphere mass decreases the value of $\eta(D_{\mathrm{min}})$ increases. The lower size limit is found not to affect the predicted atmosphere evolution provided that the minimum value of the erosional efficiency is $\eta(D_{\mathrm{min}}) < 0.1$ (Wyatt et al.,

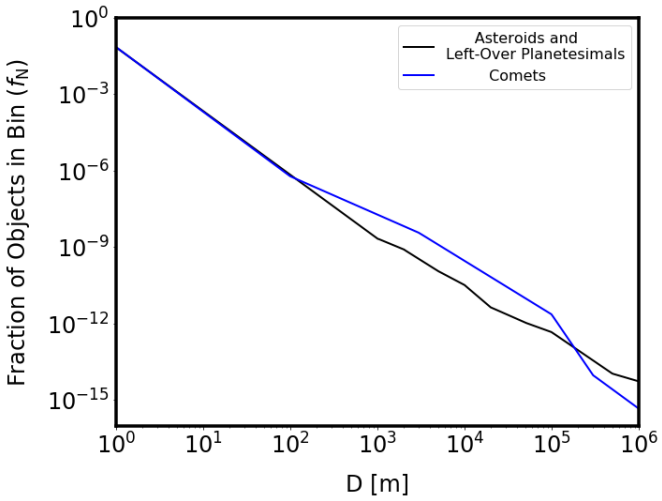

Figure 3.3: The number of objects in each size bin, shown as a black line for the asteroids and left-over planetesimals (based on the asteroid belt size frequency distribution) as a black line, and for the comets (based on the distribution from Nesvorný et al. (2018)) as a blue line.

2019). For the range of impactor and planet properties considered in this chapter this limit is reached at an atmosphere mass of $\sim 10^{-13}$ $M_\oplus$, significantly smaller than the typical atmosphere masses discussed here.

3.1.3 Total impacting mass

The total number of impactors sampled by the code from each population over all velocity and size bins is normalised by the total mass that *impacts* the planet over the course of the simulation ($M_{\mathrm{tot},k}$),

$$M_{\mathrm{tot},k} \equiv \int \sum_{i}^{N_{\mathrm{size}}} \sum_{j}^{N_{\mathrm{vel}}} R_k(t) f_{\mathrm{N},i,k}(t) f_{\mathrm{v},j,k}(t) \frac{\pi}{6} \rho_k D_i^3 \, \mathrm{d}t. \tag{3.1}$$

This is not the same as the total mass *accreted* by the planet as this accreted mass depends on the atmosphere mass and composition (see equation 2.10), which it is not possible to predict in advance. The choices for these masses are made using different approaches for each of the three populations.

Asteroids: For the asteroid population, I make use of the result from Nesvorný et al. (2017a) that 177 asteroids with size $D > 10$ km are expected to impact the Earth over the full 4.5 Gyr span of their simulations. Using the exponential fit given by their equation 1, 76 impacts are predicted to occur during the time period I consider. Assuming a weighted average density of the two asteroid types (described in detail in §3.1.4) this corresponds to a total mass of

asteroids of $M_{\rm tot,\ ast} = 3.94 \times 10^{-6}$ M$_\oplus$, which I adopt as the nominal value.

Comets: For comets, the population is normalised using the capture fraction of the Jupiter Trojans from the simulations of Nesvorný et al. (2013), $f_{\rm capt} = 5 \times 10^{-7}$ (Nesvorný et al., 2018). The calculation of the intrinsic collision probability described in §3.1.1 gives that the total probability per comet initially in the disk (after 50 Myr) is $P_{\rm tot,c} = 1.08 \times 10^{-7}$. Comparing these two numbers, the mass in the comet population is thus a fraction $n = \frac{P_{\rm tot,c}}{f_{\rm capt}}$ of the total mass estimated for the Trojans, $M_{\rm Trojans} = (0.3 \pm 0.19) \times 10^{-10}$ M$_\odot$. This gives $M_{\rm tot,c} = 2.2 \times 10^{-6}$ M$_\oplus$, which is taken as the nominal value.

Left-over planetesimals: The population of left-over planetesimals has no present day population that can be used to normalise it, and so a different approach is required. I instead normalise this population using the Late Veneer mass (the total mass accreted by the Earth since core formation ended, discussed in §1.2) as an observational constraint. It is implied by isotopic constraints that most of this mass came from left-over planetesimals rather than asteroids and comets. Normalising in this way not be done directly, as the accreted mass depends on the evolutionary history of the atmosphere, which in turn depends on the total impacting mass.

To calculate the correct normalisation mass, i.e. the total mass contained in the objects that *impact* the Earth that will result in accretion of a mass approximately equal to the Late Veneer mass I therefore use an iterative approach, making a first guess of $M_{\rm tot,\ plan} = 0.01$ M$_\oplus$, using the code to calculate the accreted mass. The estimate of $M_{\rm tot}$ is then updated, and this process is repeated until the accreted mass (averaged over several runs to account for stochastic effects) is in agreement with the Late Veneer mass, (0.005 ± 0.002) M$_\oplus$ (Warren et al., 1999; Walker, 2009). In all cases a total mass estimate of $M_{\rm tot,plan} = 0.0075$ M$_\oplus$ is found to produce an acceptable range of total accreted masses.

For the comets and asteroids, the uncertainty in their total masses introduced by uncertainties in the values used to calculate them is quantified above, but this is very small in comparison to the total mass of left-over planetesimals. Instead, I investigate increasing the total mass for these two populations by a factor of ten in §3.2.2 and §3.2.1 when these populations are considered in isolation.

Table 3.1: The densities and volatile fractions of the four impactor populations used in the numerical code are shown here, both as the parameters describing a linear trend and as nominal values. The estimated MMW of the volatiles released is also shown.

Impactor Type	Minimum $\rho_{\rm imp}$ [g cm^{-3}]	Maximum $\rho_{\rm imp}$ [g cm^{-3}]	A	B	Nominal $\rho_{\rm imp}$ [g cm^{-3}]	Nominal $x_{\rm v}$	μ
Comet	0.6	1.2	-0.5	0.65	0.9	0.2	38
Carbonaceous / C type	1.5	2.5	-0.19	0.485	2.0	0.105	39
Ordinary / S type	2.5	4.0	-0.006	0.025	3.4	0.005	13
Enstatite	3.0	4.5	-0.0003	0.0014	3.5	0.00035	15

3.1.4 Composition

Within the numerical code, impactor composition is defined by a bulk density, volatile fraction, and mean molecular weight (MMW). The volatile fraction refers specifically to the mass fraction of the impactor that is outgassed into the atmosphere after the impact. Water is not included in this value, on the grounds that it is expected to be in the liquid phase on the surface of planets in the habitable zone (Zahnle et al., 2007). This outgassed mass fraction has an associated MMW (μ_k), that depends on the ratios of different species present. I adopt for each impactor population an approximate representative range for the density and volatile fraction, and assume a linear relation ($x_{\rm v} = A\rho_{\rm imp} + B$) between these two parameters in order to avoid adding a further free parameter. For each population, the extrema and centre of these ranges are used to construct three potential compositions: "wet" (lower density, more volatile-rich), "nominal" and "dry" (higher density, more volatile-poor). The value of μ_k for the mass outgassed by each impactor population is approximated from the molecular abundances in the literature, and assumed to be constant. These parameters are summarised in Table 3.1 and Fig. 3.4, and their choice justified below.

Asteroids: The asteroids are split into two sub-populations, corresponding to ordinary chondrites and carbonaceous chondrites in terms of their composition. The S-type asteroid and ordinary chondrite meteorite labels are used interchangeably (as are the C(+B)-type and carbonaceous chondrite labels), to allow necessary constraints to be placed on the impactor properties. This is imprecise, but until there are better observational constraints on the composition of small Solar system bodies it is necessary to combine data from meteorites and asteroids.

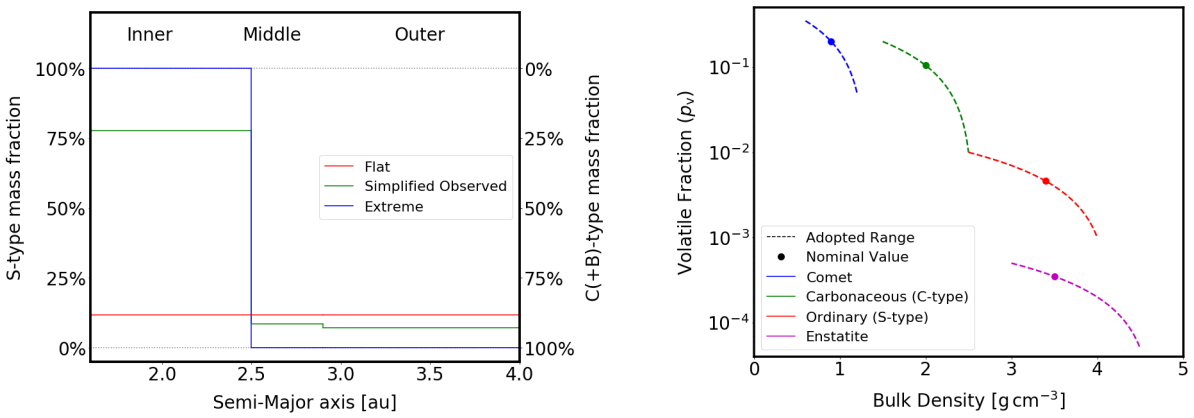

(a) (b)

Figure 3.4: Panel (a) shows the S-type fraction as a function of initial semi-major axis for the three different approaches used to describe the asteroid-like impactor population. The nominal case, a simplified version of the DeMeo (2014) distribution, is shown in green. Panel (b) shows the range (shown by a dashed line) and nominal values (filled circle) of volatile fraction and bulk density of the different impactor populations.

- The C-type asteroid/carbonaceous chondrite-like sub-population is relatively volatile-rich. These objects have the bulk of their outgassed volatile content in carbon dioxide, with lesser amounts of hydrogen, carbon monoxide, hydrogen sulfide and sulfates; as well as trace methane, nitrogen and ammonia (Schaefer & Fegley, 2010; Sephton, 2002). This results in a relatively high $\mu \sim 39$. I adopt a density range spanning $1.5 - 2.5$ g cm^{-3}, and a volatile range spanning $0.01 - 0.2$, giving the values of m and c in Table 3.1 (Carry, 2012).

- The S-type asteroid/ordinary chondrite-like sub-population is comparatively volatile-poor. These objects have the bulk of their outgassed volatile content in carbon monoxide and hydrogen, with lesser amounts of carbon dioxide, methane, hydrogen sulfide, nitrogen and ammonia, and trace amounts of sulfur dioxide (Schaefer & Fegley, 2010). This results in a estimate of $\mu \sim 13$. I assume the density spans $2.5 - 4$ g cm^{-3}, and the volatile range spans $0.001 - 0.01$ (Carry, 2012).

These two populations are distinguished using their initial semi-major axes (a_0), to calculate two separate distributions of $R_k(t)$ and $f_{\mathrm{v},j,k}(t)$. To investigate the relative importance of this separation I consider three different distributions. First, a flat distribution, with no dependence on a_0, splitting the total mass such that $\sim 11.7\%$ of the total mass is in S-type asteroids and the rest is in C(+B) types (DeMeo, 2014). Second, a simplified extrapolation of the taxonomic distribution presented in Table 6 of DeMeo (2014). Considering S-type to represent one population, and combined C and B-types to represent the other, the mass ratio of S : (B+C) is calculated for the inner ($1.6 - 2.5$ au), middle ($2.5 - 2.9$ au) and outer ($2.9 - 4.0$ au) zones of the asteroid belt. Third, an extreme distribution, where it is assumed

that all objects with $a_0 < a_{\rm lim}$ are S-type (ordinary chondrite-like) and all objects with $a_0 > a_{\rm lim}$ are assumed to be C-type (carbonaceous chondrite-like). $a_{\rm lim} = 2.5$ au is calculated such that the total mass in each sub-population is consistent with the other cases. These are illustrated in the upper plot in Fig. 3.4. The second case is treated as the nominal case when other effects are investigated.

Comets: For the comet population, the majority of the volatiles are assumed to be in carbon monoxide, and carbon dioxide, with a small fraction in methane, hydrogen sulfide, ammonia, ethane, methanol, formaldehyde, and hydrogen cyanide (Mumma & Charnley, 2011; Rubin et al., 2019). This allows the estimation of the value of $\mu \sim 38$. To avoid unnecessary complications, noting from Table 3 in Mumma & Charnley (2011) that the range in cometary abundances of single species is typically at least an order of magnitude, I adopt lower and upper bounds on the volatile fraction of $0.05 < x_{\rm v} < 0.35$, with a most likely value of $x_{\rm v} = 0.2$. This gives a range of densities spanning $0.6 - 1.2$ g cm^{-3}.

Left-over planetesimals: For the left-over planetesimals, I assume a very volatile-poor enstatite chondrite-like composition. The majority of the material outgassed by this material is in hydrogen and CO, with smaller amounts in carbon dioxide, nitrogen, methane, hydrogen sulfide and ammonia, with trace amounts of other gases (Schaefer & Fegley, 2010). This gives an estimate of $\mu \sim 15$. I assume the density spans $3 - 4.5$ g cm^{-3}, and the volatile range spans $5 \times 10^{-5} - 5 \times 10^{-4}$ (Carry, 2012).

3.1.5 Initial planet and atmosphere conditions

My simulations start after the final giant (Moon-forming) impact, after which accreted material cannot be sequestered into the core, and so is recorded in the mantle as an excess of HSEs. This accreted Late Veneer is estimated to have a mass of (0.005 ± 0.002) M$_\oplus$ (Warren et al., 1999; Walker, 2009). I therefore assume that the Earth starts in the simulations with a mass of 0.995 M$_\oplus$. This allows it to reach roughly the current value of 1 M$_\oplus$ having accreted the Late Veneer mass. This assumes that all the Late Veneer material is delivered in the span of the simulation, which covers 500 Myr, with negligible material accreted after this time. This is a reasonable approximation, as this period is considered to be the tail end of a period of heavy bombardment, which decreases monotonically over time (Morbidelli et al., 2018).

The Earth is assumed to have constant bulk density ($\rho_{\rm pl} = 5.5$ g cm^{-3}), and to be on its current

orbit ($a_{\rm pl} = 1$ au). To calculate the atmosphere temperature I adopt a profile for the Sun's luminosity from Bahcall et al. (2001), which increases from approximately $0.7 - 0.75$ $L_\odot$ over the 500 Myr covered by the dynamical data. The assumption that the Earth's atmosphere is isothermal is a simplification, and indeed an adiabatic atmosphere is possibly a more likely scenario in the time immediately following the Moon-forming impact. However it is a necessary assumption in order to make use of the Shuvalov (2009) prescription. The Schlichting et al. (2015) giant impact prescription has an alternate form for adiabatic atmospheres, which takes the same form as equation 2.12 but with slightly different coefficients. This suggests that there would be a small but non-zero difference in the predicted atmospheric evolution if a non-isothermal atmosphere was considered.

The mass and composition of the early Earth's atmosphere is not well constrained by observations, but is thought to be broadly similar to the present day (dominated by nitrogen with smaller amounts of carbon dioxide and water) (Kasting, 1993). Nitrogen and argon isotope observations have been used to constrain the surface partial pressure of nitrogen to be $pN_2 < 1.5$ bar before 3 Gya (Marty et al., 2013), and more recent models suggest that pN_2 was low in the past (Lammer et al., 2018). Unlike the current atmosphere, the oxygen content was very low before ~ 2.5 Gya (Bekker et al., 2004).

I consider a range of values for the initial atmosphere mass, spanning $m_0 = (0.85 \times 10^{-8} - 0.85 \times 10^{-5})$ $M_\oplus$, corresponding to $0.01 - 10$ times the present value. I also consider a range of atmosphere compositions, from $\mu_0 = 2.3$ (representing a primordial hydrogen-dominated atmosphere) to 45 (representing a denser, carbon dioxide-dominated atmosphere), the effect of which is discussed in §3.2.6. The nominal values adopted when varying other parameters are $m_0 = 0.85 \times 10^{-6}$ $M_\oplus$ and $\mu = 29$, describing the present day atmosphere.

Impactor	Case	Final Change in Atmosphere Mass			Final Impactor Fraction		
		Median [%]	Minimum [%]	Maximum [%]	Median [%]	Minimum [%]	Maximum [%]
Asteroid	Wet	0.60	−0.25	788.76	0.97	0.23	88.77
Asteroid	Nominal	0.86	−0.18	149.01	1.21	0.20	59.96
Asteroid	Dry	−0.11	−0.35	103.91	0.22	0.02	51.07
Asteroid	Massive	32.00	2.51	710.33	26.66	5.80	87.83
Comet	Wet	−2.60	−2.73	−2.48	0.74	0.73	0.74
Comet	Nominal	−2.51	−2.61	−2.40	0.46	0.45	0.46
Comet	Dry	−2.49	−2.67	0.46	0.23	0.15	3.17
Comet	Massive	−24.1	−24.5	−23.9	4.75	4.73	4.76
Planetesimal	Wet	−50.4	−79.4	−16.4	94.54	92.43	97.36
Planetesimal	Nominal	−75.3	−94.7	−47.4	94.94	91.46	98.10
Planetesimal	Int-1	−85.9	−99.2	−58.2	96.12	92.32	99.98
Planetesimal	Int-2	−95.4	−99.98	−79.3	99.12	94.72	100.00
Planetesimal	Int-3[1]	−99.0	−100.0	−84.3	100.00	97.41	–
Planetesimal	Int-4[1]	−100.0	−100.0	−96.9	–	98.67	–
Planetesimal	Int-5[1]	−100.0	−100.0	−99.1	–	97.17	–
Planetesimal	Dry[1]	−100.0	−100.0	−100.0	–	–	–
Planetesimal	1	−71.9	−92.0	−37.2	95.00	91.96	98.13
Planetesimal	2	−96.0	−99.9	−80.3	99.94	97.96	100.00
Planetesimal	3	−77.7	−93.8	−36.3	99.47	95.96	99.998
Planetesimal	4	−74.6	−93.2	−56.0	94.97	91.73	98.07
Planetesimal	5	−95.3	−99.9	−78.1	99.83	97.75	100.00
Planetesimal	6	−92.6	−99.5	−70.1	99.81	98.52	100.00
Planetesimal	7	−88.0	−99.7	−69.4	97.87	93.50	99.98

Table 3.2: The final fractional change in atmosphere mass (relative to the initial mass of 0.85×10^{-6} $M_\oplus$) and fraction of the final atmosphere mass delivered by the impactor population (impactor fraction), both shown as median, minimum and maximum values, for the 100 runs of the code for each individual impactor population considered. For the asteroids, the results for the three spatial initial distributions of C- and S-types are shown combined, and the impactor fractions are shown as $(f_{\mathrm{S-type}}, f_{\mathrm{C-type}})$.
[1] These atmospheres were in some cases completely depleted by the arrival of the "dry" left-over planetesimals, so no meaningful final atmosphere impactor fraction can be given.

3.2 Results

I first consider the individual effect of each impactor population, which allows the result of the assumptions made regarding the impactor composition and uncertainties in the dynamics of the left-over planetesimals to be investigated in isolation. These individual results can then be used to predict the effect on the atmosphere if the estimates made for the total population masses were varied significantly. In all cases, the code was run a total of 100 times with identical initial conditions. Table 3.2 summarises the results, showing the median and range of the final change in atmosphere mass, final MMW and fraction of the atmosphere delivered by each impactor population. Further results, including the total mass *accreted* by the Earth for each population and a discussion of the inferred water delivery, are shown in Table 3.4 in §3.3.3.

3.2.1 Asteroids

The effect of asteroid impacts on the evolution of Earth's atmosphere is considered first, varying both the composition of the asteroids and the spatial distribution of the C- and S-type asteroids. Three compositions ("wet", "nominal" and "dry") and three spatial distributions of the C- and S-type asteroids ("flat", "observed" and "extreme"), described in §3.1.4, are considered, as is the effect of increasing the total impacting mass by a factor of ten, giving ten separate cases, each of which was run 100 times.

The evolution of the atmosphere mass through time is shown in Fig. 3.5a, from which it can clearly be seen that the effect of single stochastically sampled events can result in a wide variety of final atmosphere masses. A relative frequency plot of the final atmosphere masses for each case is shown in Fig. 3.5b, which also shows the effect of considering only composition (combining the results from the three spatial distributions of the asteroid types). This presentation is motivated by the observation that the distribution of final atmosphere masses is very similar between the "flat", "observed" and "extreme" asteroid distributions considered. This is not surprising, as the asteroid impact rates calculated in §3.1.1 appear to show little dependence on the spatial distributions of the asteroid types. Thus, in the following, this effect will be neglected, and only the combined results will be considered to investigate the dependence of the results on the composition and total mass of the asteroid population.

The average value and range for both the final atmosphere mass and fraction of the atmosphere delivered by the two asteroid types are summarised in Table 3.2. The "nominal" and "wet" asteroids result most typically in atmospheric growth, with similar final median

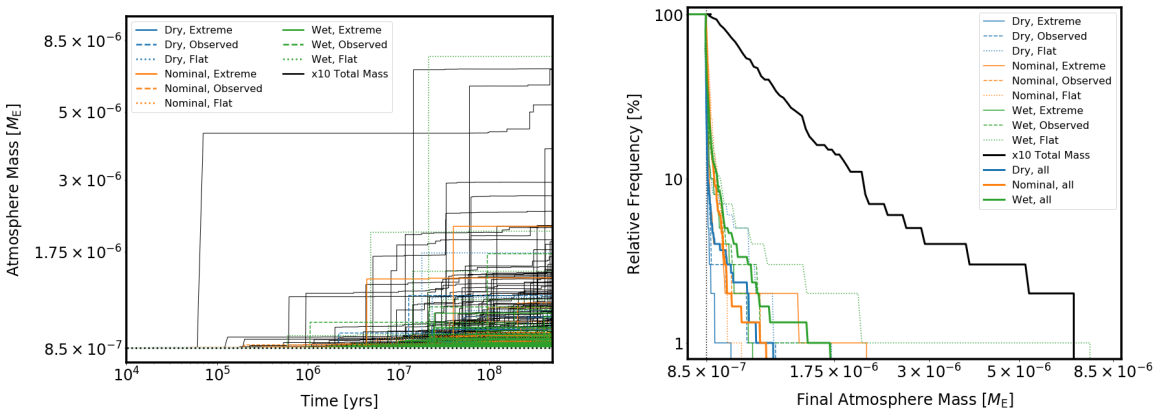

(a) (b)

Figure 3.5: The results considering the nominal atmosphere evolved under impacts by the ten different asteroid populations considered. Panel (a) shows the total atmosphere mass as a function of time, and panel (b) shows the corresponding relative frequency (percentage of runs with masses greater than the x-axis value) of the final atmosphere masses. These results are produced by running the numerical code 100 times each, considering three impactor compositions ("wet" "nominal" and "dry", shown by lines of different colours), three potential spatial distributions of the C- and S-type asteroids are also considered ("flat", "observed" and "extreme", shown by different line styles), as well as the effect of increasing the mass of the "nominal" population by a factor of ten.

atmosphere mass growth for both populations (percentage changes of 0.86% and 0.60% respectively from the initial atmosphere mass of 0.85×10^{-6} $M_\oplus$), however the volatile-rich "wet" population produces a larger range of final values than the "nominal" population. The "dry" asteroids on average result in slight atmosphere loss of -0.11%, however some runs produce an atmosphere mass percentage increase of up to 104%, more than doubling the atmosphere mass.

The extremely high final atmosphere masses that occur in some runs are the result of the stochastic arrival of large, slow asteroids that deliver a substantial portion of their mass in volatiles to the atmosphere. This can be understood by considering the maximum mass of volatiles that can be delivered by a single impactor. Equations 2.5 to 2.11 give the impactor mass accreted, and therefore the volatile mass delivered by a single impact,

$$M_{\text{max v}} = \frac{\pi}{6}\rho_{\text{imp}} D^3 \, x_{\text{v}} \, (1 - \chi_{\text{pr}}). \tag{3.2}$$

For the nominal total population mass considered, there are $\sim$ 0.019 asteroids with $D > 500$ km, meaning that impactors larger than this size are expected to occur in only a few $\%$ of the 100 runs in each case. The largest, slowest impactor possible ($D = 1000$ km, $\frac{v_{\text{imp}}}{v_{\text{esc}}} = 1.01$, could deliver $\sim$ 75% of its mass (according to Fig. 3.2), corresponding to a maximum volatile delivery of $M_{\text{max v}} \approx 16 \; m_0$, comparable to the largest increases in

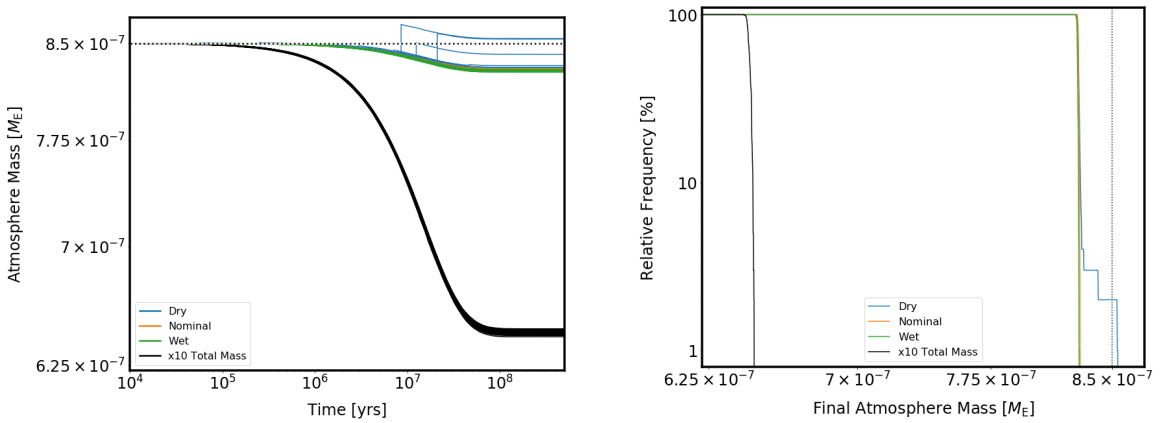

(a) (b)

Figure 3.6: The results considering the nominal atmosphere evolved under impacts by the comet population in isolation. Panel (a) shows the total atmosphere mass as a function of time, and panel (b) shows the corresponding relative frequency (percentage of runs with masses greater than the x-axis value) of the final atmosphere masses. These results are produced by running the numerical code 100 times each, considering three impactor compositions ("wet" "nominal" and "dry"), as well as the effect of increasing the mass of the "nominal" population by a factor of ten.

atmosphere mass seen in Fig. 3.5a.

The "dry" impactors also produce less of the particularly extreme final atmosphere masses seen for the "wet" and "nominal" results. This results from the decreased volatile fraction of these impactors, meaning that the largest possible single delivery of volatiles is smaller, and so stochastic sampling of the same velocity and size of impactors results in a smaller delivery of volatiles to the atmosphere in comparison to the "wet" and "nominal" cases. Increasing the total impactor mass by a factor of ten, results in greater atmosphere growth, with a median final atmosphere change of 32%, and a greater number of stochastic outliers, since the larger total mass makes the sampling of the largest impactors more probable.

3.2.2 Comets

I now consider the effect on the Earth's atmosphere caused by the population of comets alone, for which the total atmosphere mass as a function of time is shown in Fig. 3.6a. A relative frequency plot of the final atmosphere masses is shown in Fig. 3.6b. From these plots it can be seen that the "wet" and "nominal" comets result in atmospheric erosion, with median percentage total mass decreases of 2.6-2.5$\%$. This erosion is larger by a factor of ~ 10 when the total impacting mass increases by a factor of ten. Counter-intuitively, the "drier" impactors result in general in slightly less atmospheric erosion, and in some cases in stochastic atmospheric growth.

To understand this effect, consider again the maximum volatile mass that could be delivered by a single large object. From Fig. 2.1 it can be seen that the impactor mass accreted is largest for the lowest velocity impactors, $\frac{v_{\rm imp}}{v_{\rm esc}} \sim 1.3$ for the slowest comet considered here. While for the nominal composition, total population mass and size distribution it is predicted that there are ~ 0.033 objects with $D > 250$ km (therefore large cometary impacts are expected in ~ 3 of the 100 runs), equation 2.11 predicts that even the slowest comets (with $\frac{v_{\rm imp}}{v_{\rm esc}} = 1.3$, as can be seen from Fig. 3.2) result in zero accreted mass for impactors larger than ~ 10 km. Therefore only the smallest cometary impactors contribute material to the atmosphere, and these objects are both so numerous that their arrival is not stochastic in nature and so small that they cannot individually deliver a mass of volatiles comparable to the atmosphere mass, meaning that no stochastic large jumps in atmosphere mass occur. However, in the case of the "dry" comets, their density is high enough that they behave more like the asteroids shown in Fig. 2.1, with a non-zero fraction of the largest objects accreted if it impacts with a slow enough velocity. A 250 km diameter "dry" comet contains 8.2×10^{-8} $\rm M_{\oplus}$ in volatiles, comparable to $\sim 10\%$ of the initial atmosphere mass. An impact by such an object, if the sampled impact velocity is low and thus a non-zero fraction of the impactor mass can be accreted, can explain the few runs that show stochastic increases in atmosphere mass.

3.2.3 Comparison to previous results

The results presented above for the effect of comets and asteroids on the atmosphere are in contrast to those predicted by the previous study performed by de Niem et al. (2012), which also considered asteroids and comets using a stochastic approach. I therefore address the discrepancies briefly here before presenting the results for the left-over planetesimals. For a detailed comparison of the results presented above to those previously published, see §3.3.4. While both my results and de Niem et al. (2012) find atmospheric growth as a result of asteroid impacts, the cometary impactors here result in atmospheric erosion in contrast to the significant growth predicted by de Niem et al. (2012). This difference in behaviour is due to differences in my impact prescriptions and my assumed velocity distribution for the comets.

Firstly, the modified implementation of the model from Svetsov (2010) used by de Niem et al. (2012) is similar to the Shuvalov (2009) prescription, but does predict the accretion of a small but non-zero fraction of the largest cometary impactor mass. This is contrast to the Shuvalov (2009) prescription adopted in this chapter, which predicts that comets are less efficient at delivering material to the atmospheres. Increasing the density of the comet population assumed in this chapter results in some fraction of the largest impactor's mass being accreted, switching the results from atmospheric erosion to growth.

Secondly, the velocity distributions adopted by de Niem et al. (2012) for their asteroid and comet populations contains a larger number of the slowest impactors. As was discussed in de Niem et al. (2012), the slowest impactors can have a disproportionately large effect on atmospheric evolution, since they are in general less efficient at removing atmosphere mass whilst also being more efficient at delivering volatiles. I therefore would expect both more atmosphere erosion and less atmosphere growth for my distribution of velocities, as is observed.

3.2.4 Left-over planetesimals

Objects impacting the Earth after the Moon-forming impact are constrained by the Late Veneer to be dominated by enstatite chondrite-like left-over planetesimals and so this population is likely the most significant in terms of atmosphere evolution. I consider variation in both the composition and dynamics of the left-over planetesimals below.

Dynamics

Considering first the variation in impactor dynamics, Fig. 3.7a shows the results assuming the "nominal" composition and comparing the median atmosphere masses at each time for the seven dynamical cases described in §3.1.1, corresponding to different initial conditions assumed for the simulations in Morbidelli et al. (2018). From this plot it can be seen that for each population the atmospheres on average follow a distinct evolutionary track. The distribution of final atmosphere masses for the different populations shown in Fig. 3.7b illustrates the stochastic variation in the final atmosphere masses. This variation is also apparent from the range of final atmosphere mass changes summarised in Table 3.2.

The different cases, corresponding to different impactor dynamics, all result in atmospheric erosion. The atmosphere mass loss differs between runs, with the median final atmosphere mass varying between 4 and 38% of the initial value for cases 2 and 1 respectively. No atmospheres in these cases are completely stripped, but do end up less than 0.1% of the initial value in one or two runs for cases 2 and 5. These cases correspond to two different AMDs with a 30 Myr cloning time in the Walsh et al. (2011) simulations from which the left-over planetesimal orbits are taken. From these results it would seem that the assumptions made about the total AMD of the terrestrial planets has a smaller effect on the evolution of the atmosphere mass than the assumptions made about the timescale for terrestrial planet formation and the initial orbits of the terrestrial planets.

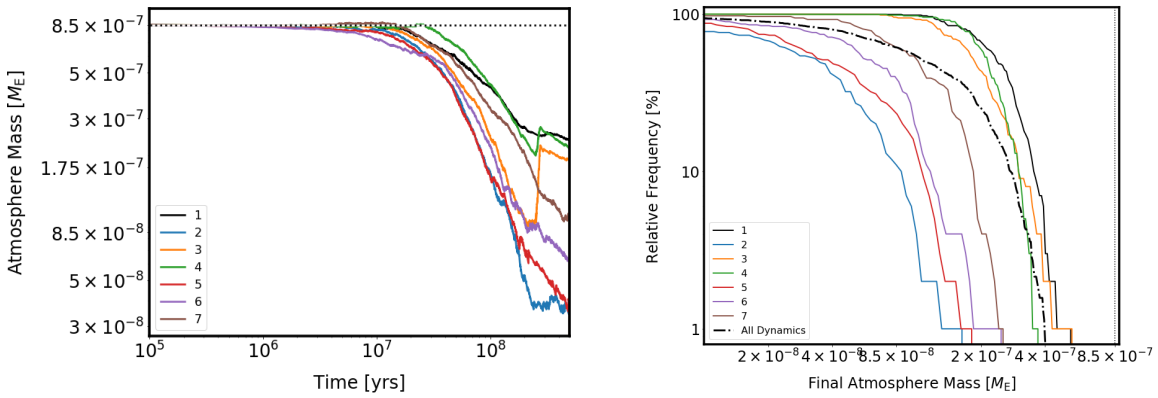

(a) (b)

Figure 3.7: The results considering the nominal atmosphere evolved under impacts by the populations of left-over planetesimals with different dynamics. Panel (a) shows the median total atmosphere mass as a function of time, and panel (b) shows the corresponding relative frequency (percentage of runs with masses greater than the x-axis value) of the final atmosphere masses. These results are produced by running the numerical code 100 times each. The seven different cases for the planetesimal dynamics are shown as lines of different colours and all assumed to have the nominal composition.

The key factor determining the final atmosphere mass is the number of particularly slow impactors sampled by the code. The seven different velocity distributions shown in Fig. 3.2 look similar, but in fact differ in the number of very slow impactors that they predict. Using the analytical model of Wyatt et al. (2019), for impactors with an $\alpha = 3.5$ power-law size distribution and the nominal left-over planetesimal composition, it is possible to predict the value of f_v (the ratio of atmosphere growth to erosion) as a function of impact velocity. As noted in Wyatt et al. (2019), this transition can be very sharp, and for the toy model here it is predicted that velocities greater than $v_{imp} \approx 1.06 v_{esc}$ should result in atmosphere erosion, while slower velocities result in growth. The behaviour of the population described in §3.1 is more complicated than this toy model, but in general it is expected that sampling from distributions with more of the slowest (atmosphere growing) impactors should result in higher final atmosphere masses. This is demonstrated in Fig. 3.8, which illustrates the dependence of the relative change in median final atmosphere mass for each of the seven populations on the fraction of impactors with velocity below this limit. As predicted, cases with fewer slow impactors end with smaller final atmosphere masses, as the impacts in general tend to be more eroding. The average final composition of these atmospheres, summarised in Table 3.2, varies slightly depending on the degree of atmospheric erosion. Comparing the different cases, the median final impactor-derived atmosphere fraction varies between 95.0% for case 1 (which resulted in the least atmospheric erosion) and 99.9% for case 2 (which resulted in the largest atmospheric erosion).

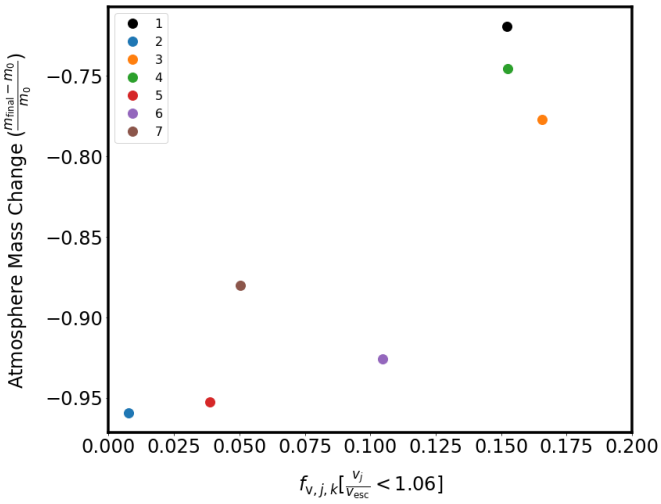

Figure 3.8: The median relative change in final atmosphere mass change as a function of the fraction of impactors with velocities below the value predicted (by a simplified analytic model) for the transition from atmospheric growth to erosion.

Label	$\rho_{\rm imp}$ [g cm^{-3}]	$x_{\rm v}$
Wet	3.0	5×10^{-4}
Nominal	3.5	3.5×10^{-4}
Int-1	3.75	2.75×10^{-4}
Int-2	4.0	2×10^{-4}
Int-3	4.125	1.675×10^{-4}
Int-4	4.25	1.25×10^{-4}
Int-5	4.375	0.875×10^{-4}
Dry	4.5	0.5×10^{-4}
C-Type	2.0	0.105

Table 3.3: The label, bulk density and volatile fraction adopted for the three original and five extra compositions considered for the populations of left-over planetesimals.

Composition

I investigate the composition of the left-over planetesimal population in more detail than for the other two impactor populations due to the sensitivity of the final atmosphere mass to the assumed composition, which can be seen in Fig. 3.9a. This is achieved using nine populations: "wet", "nominal", "dry", and five further intermediate values between "nominal" and "dry" (assumed to follow the linear relation between density and volatile content described in §3.1.4) and finally an extreme case similar to C-type asteroids. These properties are summarised in Table 3.3.

Fig. 3.9a shows the median atmosphere mass as a function of time, which depends strongly

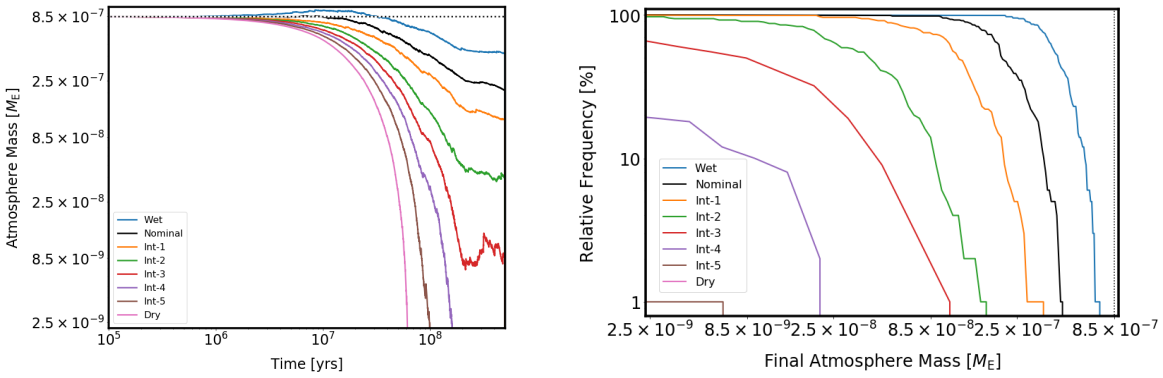

(a) (b)

Figure 3.9: The results considering the nominal atmosphere evolved under impacts by the populations of left-over planetesimals with different assumed compositions. Panel (a) shows the median total atmosphere mass as a function of time, and panel (b) shows the corresponding relative frequency (percentage of runs with masses greater than the x-axis value) of the final atmosphere masses. These results are produced by running the numerical code 100 times each. The eight different left-over planetesimal compositions considered are shown as lines of different colours, and all assumed to have the nominal (case 1) dynamics.

on the assumed impactor composition. The distribution of final atmosphere masses for the different populations is shown in Fig. 3.9b, and the median value and range of the final change in atmosphere mass are given in Table 3.2. There is an obvious lack of any large stochastic increases in atmosphere mass, such as those seen for the asteroid and "dry" comet populations. This can again be explained by considering the maximum mass of volatiles that could be delivered by a single impactor. In this case, there are ~ 20 objects with $D > 500$ km, and so "large" impacts are expected to occur in all runs of the code. With the nominal parameters, the maximum mass of volatiles delivered by the slowest, largest impactor possible (with $\frac{v_{\rm imp}}{v_{\rm esc}} = 1.01$ and $D = 1000$ km) is $M_{\rm max\ v} = 0.099\ m_0$. This also explains the observed decrease in absolute magnitude of variation in the final atmosphere mass about the median value as the volatile content of the impactors is reduced, because the largest, slowest impactors will contain comparatively less volatiles, and so the stochastic effect of single impacts will be smaller in this case.

As the volatile content of the impactors is decreased the median final atmosphere mass decreases. Two transitions in the distribution of final atmosphere masses occur. Firstly, between "Int-2" and "Int-3" some fraction of the simulations result in loss of the majority of the atmosphere mass.[2] Secondly, between "Int-5" and "dry" no atmospheres survive the length of the simulation (and in the case of "Int-5" this represents only one out of the 100

[2]In order to prevent an unreasonably long computation time, the code is halted once the atmosphere mass reaches 10^{-15} $M_\oplus$. This results in an under-estimation of the total solid mass accreted in these runs, but test runs of individual cases do not suggest that the atmosphere is capable of recovering from this level of atmosphere loss and thus this approach does not affect the estimation of the minimum volatile content required for atmosphere survival

runs). This total stripping occurs most rapidly for the "dry" population, with a median time for depletion of ~ 64 Myr.

These transitions are explained by the very low volatile content assumed for these impactors, as the population cannot deliver sufficient volatiles to balance the atmosphere mass they remove upon impact. The minimum volatile content for all the atmospheres to survive (albeit at typically 5% of the original atmosphere mass) is that of "Int-2" ($x_{\mathrm{v}} = 0.02\%$). Cases "Int-3", "Int-4" and "Int-5" result in total atmosphere loss in some runs, implying that a volatile content greater than $x_{\mathrm{v}} = 0.01675\%$ (corresponding to "Int-3") is required to guarantee that the atmosphere is not entirely stripped.

Increasing the volatile content of the impactors to a level comparable to the C-type asteroids results in significant atmosphere growth, with a median final atmosphere mass of approximately $300 - 480\ m_0$. If the Late Veneer mass was predominantly delivered by this kind of impactor, as opposed to drier enstatite chondrite-like material, I would therefore predict a final atmosphere mass orders of magnitude greater than the present day value.

The average final composition of these atmospheres, summarised in Table 3.2, is also determined by the impactor composition. In general, as the volatile content of the impactor population decreases, the final atmosphere mass decreases, and the proportion of the final atmosphere mass delivered by the left-over planetesimals increases. A smaller range of final proportions is also observed for the "drier" impactors, as a result of the smaller range of final atmosphere masses noted above.

3.2.5 Representative evolution

In order to investigate the effects of stochasticity on the atmosphere evolution, the code is run with the nominal values for all parameters described in the previous section for a total of 500 iterations, including all three impactor populations. The resulting atmospheric evolution is shown in Fig. 3.10a. A relative frequency plot of the final atmosphere masses for these 500 runs is shown in Fig. 3.10b. From this it can be seen that the majority of runs follow a very similar profile, with the atmosphere mass increasing very slightly to a maximum value by $1 - 50$ Myr, then decreasing steadily over the remainder of the simulation. The median final atmosphere mass ($\pm 95\%$ confidence intervals) is $(0.238^{+0.543}_{-0.150} \times 10^{-6})\ \mathrm{M}_{\oplus}$. This represents a loss of $\sim 72\%$ of the atmosphere mass.

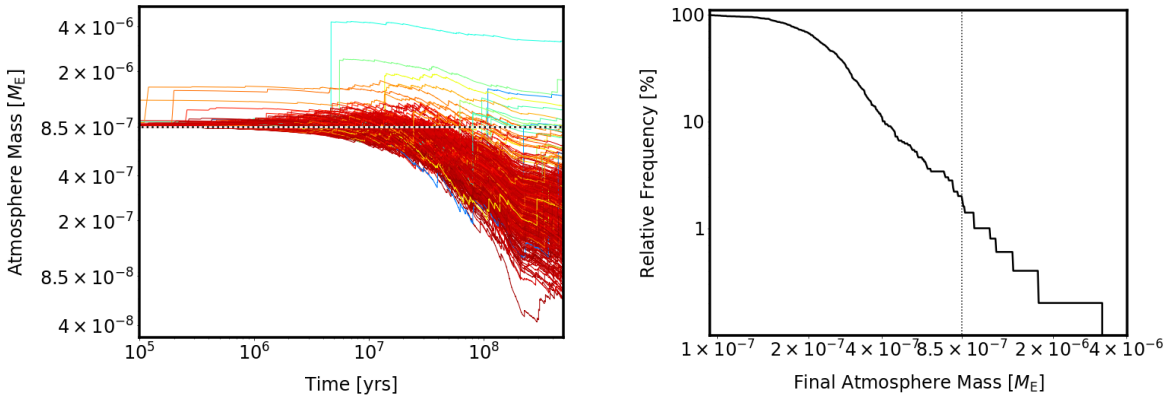

(a) (b)

Figure 3.10: The results produced for 500 iterations of the numerical code considering the evolution of an Earth-like atmosphere and planet, impacted by populations of comets, asteroids and left-over planetesimals. Panel (a) shows the total atmosphere mass as a function of time, and panel (b) shows the corresponding relative frequency (percentage of runs with masses greater than the x-axis value) of the final atmosphere masses. The colour of the line in panel (a) reflects the composition of the final atmosphere, with bluer lines representing more asteroid-dominated atmospheres and redder lines more planetesimal-dominated. The impactor populations' dynamics, size distribution, total mass and composition are set by the nominal values of the free parameters.

The median atmosphere mass as a function of time for these runs is shown in Fig. 3.11, along with the median contribution to the atmosphere from the different impactor populations (assuming the "nominal" values for their compositions) over time. From this it can be seen that the "typical" results all end up with left-over planetesimal dominated atmospheres. The median ($\pm 95\%$ confidence intervals) compositions of the final atmospheres are $(93.8^{+2.7}_{-3.6})\%$ left-over planetesimal, $(0.685^{+0.370}_{-0.481})\%$ C-type asteroidal, $(0.0692^{+0.0.0412}_{-0.0.0364})\%$ cometary, and $(0.004^{+0.323}_{-0.003})\%$ S-type asteroidal. From this it is possible to conclude that approximately three quarters of the original primary atmosphere is lost, and replaced with mainly volatiles delivered by the left-over planetesimals, with small, variable contributions from C- and S-type asteroids, and a small but less variable contribution from comets. The cometary contribution is consistent with the conclusion that cometary material made up $< 0.5\%$ of the late accretion mass inferred from observations of the atmospheric noble gas budget (Marty et al., 2016; Schlichting & Mukhopadhyay, 2018).

Xenon is of particular interest, since atmospheric xenon is depleted relative to both chondritic xenon and atmospheric krypton, and is also more enriched in its heavy isotopes than any potential source. This combination of constraints is impossible to achieve through models of atmospheric escape, giving rise to the so-called "Xenon Paradox". One potential explanation to this paradox is the delivery of $\sim 22\%$ of the Earth's atmospheric Xe by cometary material (Marty et al., 2017). While only $\sim 0.07\%$ of the final atmosphere mass is typically made up of

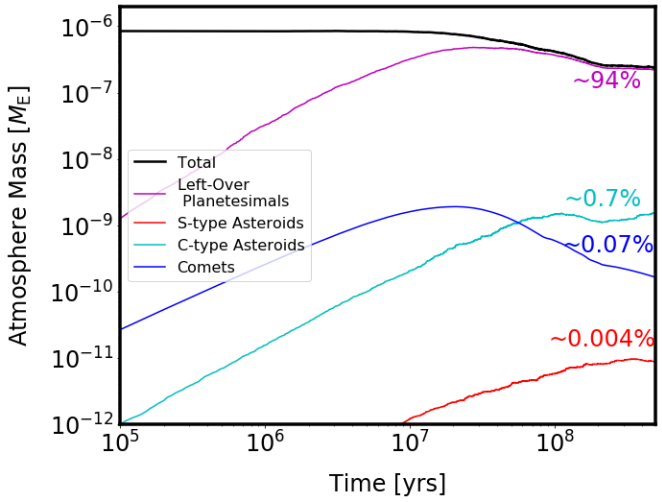

Figure 3.11: The median total atmospheric mass as a function of time for the average evolution of the 500 code runs using the nominal impactor parameters. The median proportion of the atmosphere mass that has been delivered by each of the different impactor populations at each time is shown also.

material delivered by comets, this is not necessarily in conflict with the above statement. Comets are disproportionately enriched in xenon relative to both carbon and hydrogen compared to other Solar system bodies (Halliday, 2013). It is therefore possible that a small amount of cometary material could contribute significantly to the atmosphere's overall xenon inventory. A detailed investigation of the elemental abundances and isotope ratios of the Earth's atmosphere is left for future study.

The fractional contribution of each source (primary, left-over planetesimals, both asteroid types and comets) to the final atmosphere mass for each of the 500 runs is shown in Fig. 3.12. The majority of runs result in the planetesimal-dominated atmospheres discussed above. However, the effects of random, rare impacts sampled stochastically by the code cannot be ignored, and are illustrated here by the $1.4\% \approx 7/500$ of runs that produce high final atmosphere masses. These correspond to the bars in Fig. 3.12 where the final atmosphere is dominated by volatiles delivered by C-type asteroids. These atmospheres are heavily influenced by single impacts by large asteroids, with final atmosphere masses of up to 3.2×10^{-6} $M_\oplus$. These large asteroids are slow, sampled from the top left hand corner of the asteroid-like plots in Fig. 2.1, and result in modest atmosphere mass loss but contribute a significant fraction of their volatiles to the atmosphere. As discussed in §3.2.1, a large, slow C-type impactor can deliver a mass of $\sim 10^{-6}$ $M_\oplus$ of volatiles in a single impact and so could cause these deviations from the typical final atmosphere mass. These impactors would have a mass of $\sim 2 \times 10^{-5}$ $M_\oplus$, larger than the total mass estimated for the combined population of C-type asteroids by a factor of ~ 6, meaning that these kinds of impactors should be sampled

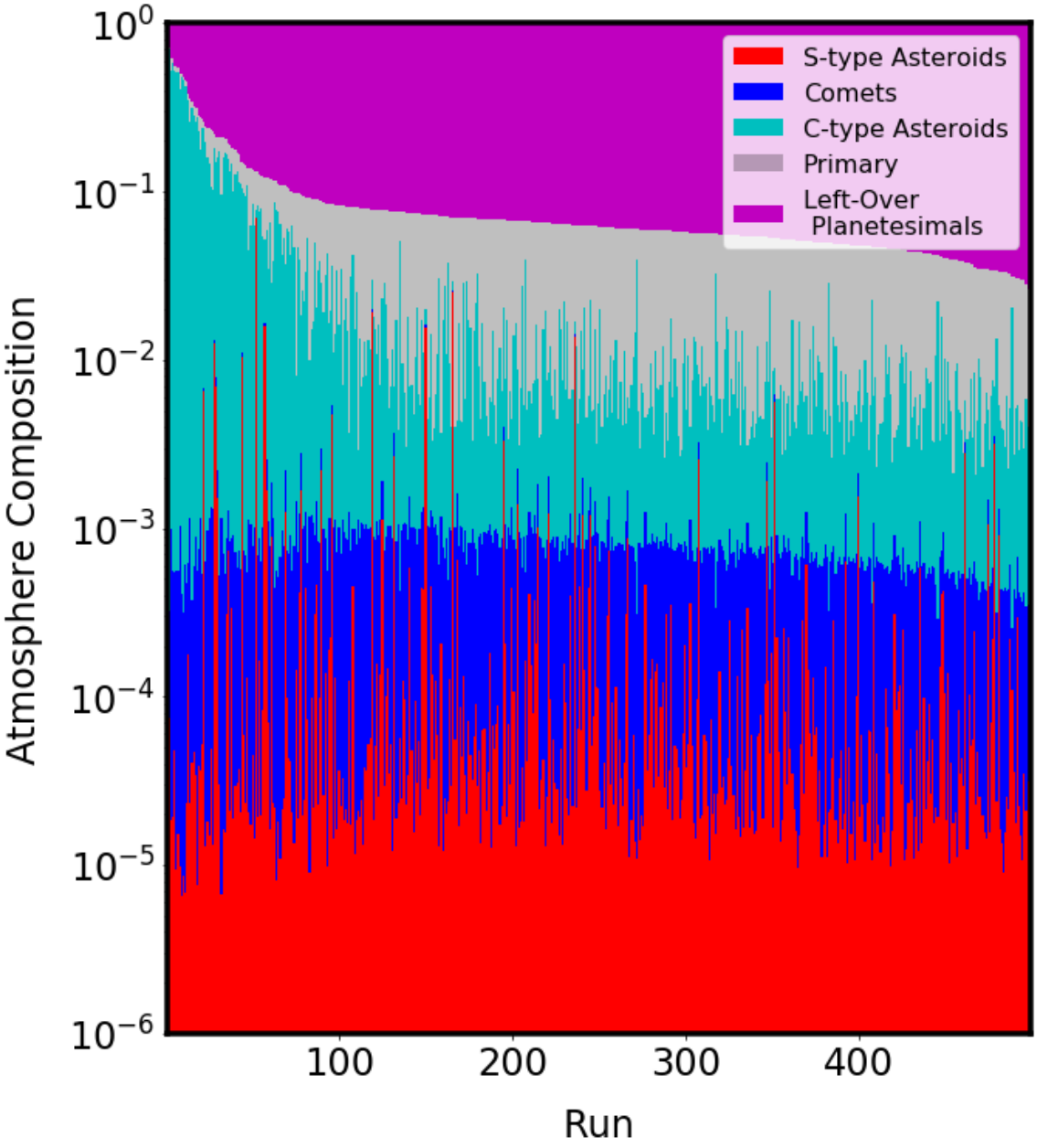

Figure 3.12: The fractional source of the final atmosphere resulting from the 500 runs shown in Fig. 3.10a, in order of increasing planetesimal portion, shown on a log scale. The majority of runs result in atmospheres that are dominated by the volatiles delivered by the left-over planetesimals, with a smaller portion due to residual primary atmosphere, followed by C-type asteroids, comets and finally S-type asteroids. A small fraction of the runs show unusually large final atmosphere masses, and are dominated by the volatiles delivered by single large C-type asteroid impacts, or in two cases, an S-type asteroid impact.

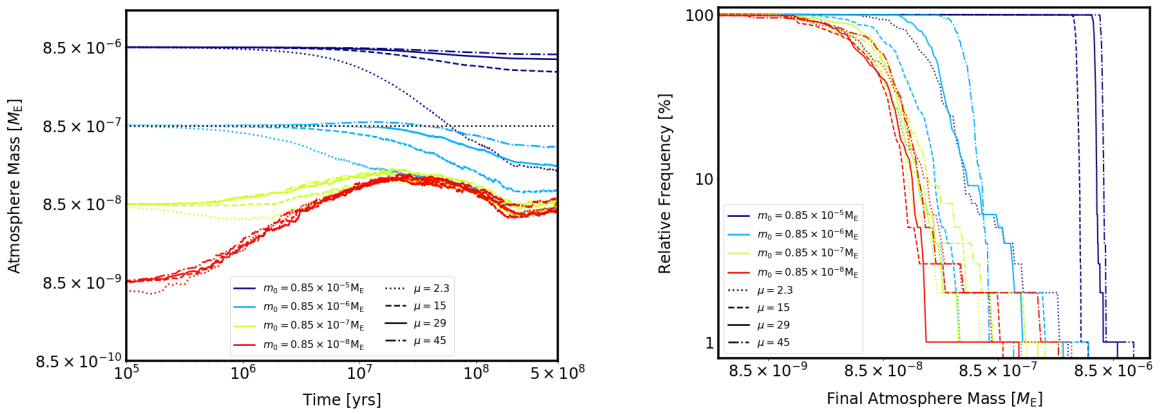

(a) (b)

Figure 3.13: The results produced considering the evolution of sixteen different initial atmospheres, run 100 times each, under bombardment by the nominal populations of comets, asteroids and left-over planetesimals. Panel (a) shows the median total atmosphere mass as a function of time, and panel (b) shows the relative frequency (percentage of runs with masses greater than the x-axis value) of the final atmosphere masses. The initial atmosphere mass is indicated by the line colour, with the μ_0 shown by the line style.

by the code very rarely. This behaviour is not likely to be representative of the evolution of our own atmosphere, as isotopic analysis suggests that the Late Veneer was delivered by enstatite chondrite-like material, not carbonaceous chondrites. However there has been recent work suggesting that it is possible that the Late Veneer could consist a combination of carbonaceous and non-carbonaceous material (Hopp et al., 2020).

3.2.6 Initial conditions

I now investigate how the choice of initial atmospheric mass and MMW affects the atmosphere evolution by considering four initial atmosphere masses, spanning four orders of magnitude from $m_0 = (0.85 \times 10^{-8} - 0.85 \times 10^{-5})$ $M_\oplus$, and four different initial atmosphere compositions, with $\mu_0 = 2.3$, 15, 29 and 45, giving sixteen different initial configurations. All other parameters for the impactor populations are kept at the nominal values. The median evolution of these initial atmospheres by the four impactor populations described in §3.1 for these different initial conditions are shown in Fig. 3.13a.

The stochastic effects are more pronounced for smaller initial atmospheres, as a fraction of the total atmosphere mass can be delivered by a relatively smaller impactor. This results in a greater relative range of final atmosphere masses for these populations, shown in the distributions of final atmosphere masses in Fig. 3.13b. Fig. 3.14, which shows the initial and final locations of all the atmospheres considered, and the median final values of each set of initial conditions in atmosphere mass-MMW space.

From this it can be seen that in general the initially low mass atmospheres ($m_0 = 0.85 \times 10^{-8}$ $M_\oplus$) undergo growth, tending towards the same final condition regardless of their starting composition, with median final masses between $(6.6 - 9.9) \times 10^{-8}$ $M_\oplus$. The atmospheres that start with a mass 10% of the present day value undergo relatively minor changes in atmosphere mass, with median final masses between $(7.9 - 9.5) \times 10^{-8}$ $M_\oplus$, but all tend towards a common composition dominated by the material delivered by the left-over planetesimals. The atmospheres that start with the present day mass in general deplete, with the primordial ($\mu_0 = 2.3$) case having a median final atmosphere within the range reached by the low initial atmosphere masses. The median final atmosphere mass in this case increases with increasing μ_0, from 7.4×10^{-8} $M_\oplus$ to 4.6×10^{-5} $M_\oplus$. For the largest initial atmospheres (ten times the present atmosphere mass), the final atmosphere mass depends strongly on the composition, with a higher μ_0 resulting in a higher final atmosphere mass (6.9×10^{-6} $M_\oplus$ for $\mu_0 = 45$ compared to 4.1×10^{-6} $M_\oplus$ for $\mu_0 = 15$). This effect is most pronounced for the primordial composition, which depletes to a level similar to that reached by the initially less massive atmospheres (2.3×10^{-7} $M_\oplus$). These results suggest that atmospheres with lower μ_0 are easier to remove through impacts, and that the properties of the final atmosphere can be determined entirely by the impactor population if that population is capable of completely replacing the initial atmosphere.

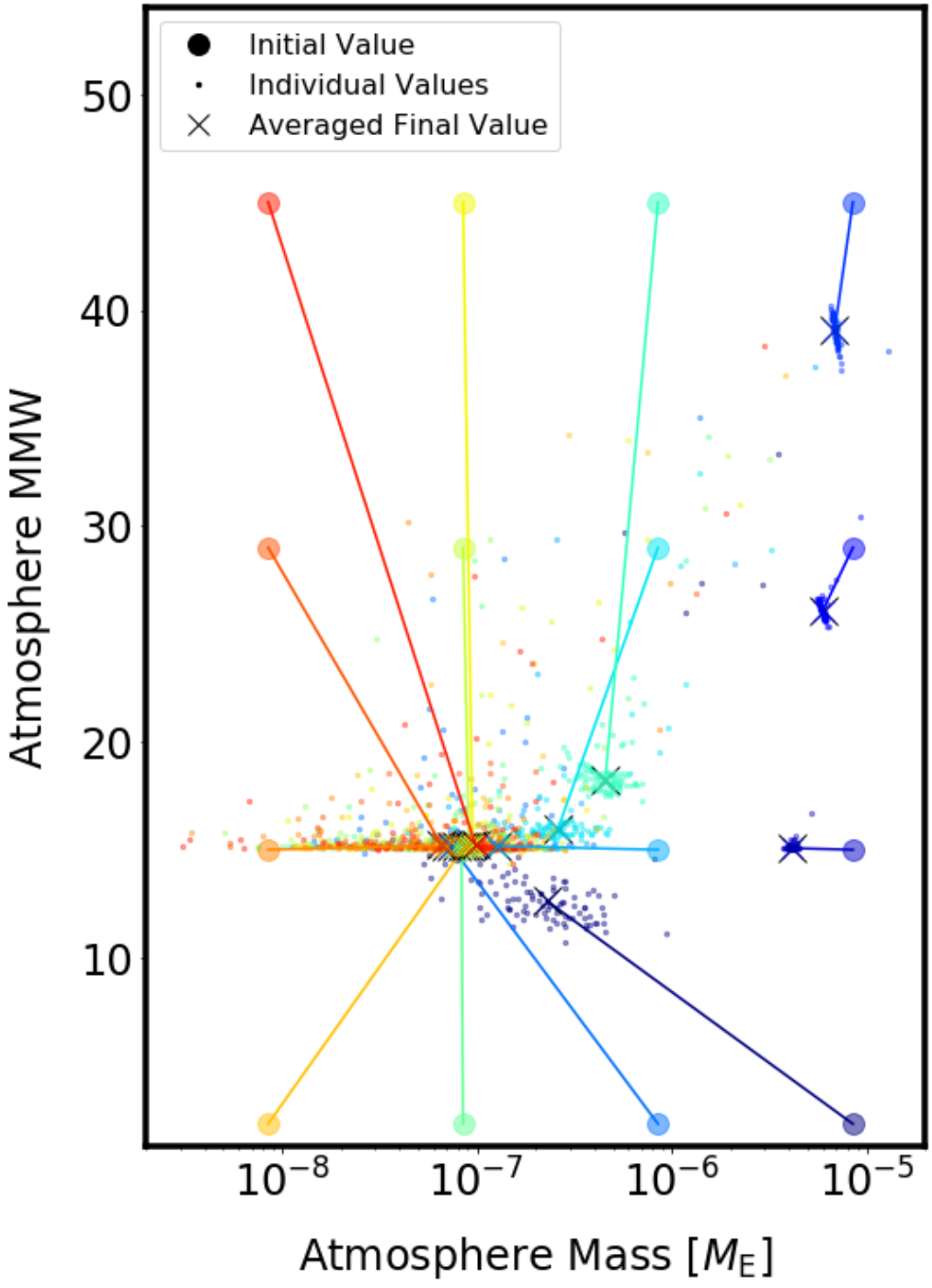

Figure 3.14: The change in the atmosphere mass and MMW over the course of the simulations for the sixteen different initial atmosphere conditions. The initial conditions are shown as filled circles of different colours. The final values are shown as crosses at the median location, with the final values shown in dots of the same colour.

3.3 Discussion

3.3.1 Variation in the impactor population parameters

The results of §3.2.2, 3.2.1 and 3.2.4 can be used to consider how changing the assumptions made about the populations of comets, asteroids and left-over planetesimals might affect my conclusions. Consider the average evolution of the atmosphere in the representative case, which results in approximately half the original atmosphere mass being lost, with a final atmosphere composition dominated by the material delivered by the left-over planetesimals.

If the population of comets was much more massive, or was "wetter" (lower density and higher volatile content) significant change in the atmosphere evolution would not necessarily be expected, however if they were "drier", the final atmosphere would be expected to occasionally end with high masses dominated by material delivered by a comet. These atmospheres would be analogous to the rare large final atmosphere masses that are seen in the representative case due to the stochastic sampling of a large, slow, asteroid.

If the asteroid population was much more massive, the results presented in §3.2.1 predict that the final atmosphere mass would be higher, with the delivery of asteroid material potentially able to negate the atmospheric loss caused by the left-over planetesimals. In this case that the final atmosphere would be dominated by asteroidal material, with the C- and S-type fractions in proportion to their total mass ratio (around $8.6 : 1$). In general a "wetter" population of asteroids would be expected to result in a larger final atmosphere mass, and in an increase in the occurrence of stochastic large impacts leading to a wider range of final atmosphere masses.

A drier population of left-over planetesimals would be expected to strip the entire atmosphere mass very efficiently, within 75 Myr, while a "wetter" population would be expected to cause less erosion than the "nominal" case, as discussed in §3.2.4. The dynamics of the left-over planetesimals appears to be a less important parameter, however the results presented in §3.2.4 suggest that variation in the median final atmosphere mass of $\sim 25\%$ is possible (comparable to variation between a volatile content of $x_{\mathrm{v}} = 0.02\%$ and 0.035%).

3.3.2 Atmospheric convergence

The convergence of the final atmosphere towards a mass and bulk MMW determined only by the properties of the impactor populations regardless of the initial atmospheric conditions, as shown in §3.2.6, is interesting. The stalling of an atmosphere at a particular mass is a

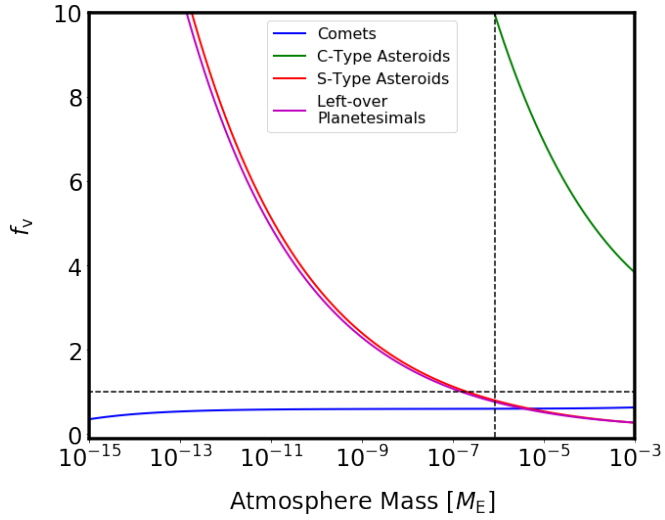

Figure 3.15: The ratio of atmosphere growth to loss as a function of atmosphere mass calculated according to equation 2.30, averaged over the distribution of impact velocities for each population, and assuming simplified properties representative of each of the four impactor populations. The line $f_v = 1$, where the atmosphere mass should remain constant, is shown by a horizontal dashed black line. The current atmosphere mass of the Earth is shown by a vertical dashed black line.

phenomena that was predicted first by Schlichting et al. (2015). The results presented in §3.2 can be understood using the formalism of the analytical model of Wyatt et al. (2019). The behaviour of f_v (the ratio of atmosphere growth to loss as a function of atmosphere mass) as a function of atmosphere, and thus the method by which the qualitative atmosphere behaviour can be predicted and the stable stalling mass (if it exists) can be estimated is discussed in detail in §2.3.1.

The impactor populations I have considered in this chapter are significantly more complicated in their properties than those of the analytical model, but simplifications can be made in order to investigate the stalling effect. Adopting the nominal impactor compositions and total masses, and considering each population in isolation, assuming an $\alpha = 3.1$ power-law for the differential size distribution of the comet population, and an $\alpha = 3.5$ power-law for the other populations, it is possible to calculate f_v averaged over the distribution of impact velocities given by $f_{v,j,k}$ using equation 2.33. This is shown for the four impactor populations in Fig. 3.15.

From this it can be seen that, in agreement with the results presented in §3.2.2, the analytic model predicts atmospheric loss ($f_v < 1$) as a result of cometary impacts. The results for asteroids are also in line with what is observed in the numerical results, with the dominant C-type population predicting atmospheric growth. Impacts by the left-over planetesimals are

predicted to result in atmospheric loss, as was found using the code. Due to the significantly higher mass of impacting left-over planetesimals in comparison to the other populations, the atmospheric evolution and thus the predicted stalling mass are expected to be dominated by the effect of this population. Fig. 3.15 would imply that planetesimal impacts should result in an atmosphere that stalls at a mass of approximately 1.5×10^{-7} $M_{\oplus}$, consistent with what was found for this nominal population using the code.

The observed convergence might imply that it is not possible to constrain the initial conditions of the Earth's atmosphere in the period before the accretion of the Late Veneer. However, while there may be no signature of the initial atmospheric mass and composition in the final mass and composition it remains to be seen whether more detailed isotopic signatures (for example in the $^{15}N/^{14}N$ ratios, or in the noble gases) might be capable of distinguishing between different initial scenarios. This relies on data regarding the isotopic signatures of the volatiles contained within the different impactor populations, which are not currently well constrained for all isotopes in all impactors, but is an interesting avenue of research.

While it is not possible to infer precisely the initial conditions for the Earth's atmosphere, the results of §3.2.6 can be used to place some speculative limits on the initial atmosphere of the Earth. While it might be expected that the atmosphere will grow slightly after the end of this period of bombardment due to outgassing, it is unlikely that significant atmospheric loss occurred after this time. Therefore it is possible to conclude that an atmosphere larger than 10 times the present mass is unlikely to have been present on Earth after the Moon-forming impact, unless such an atmosphere had a primordial composition, and was therefore easier to remove via impacts.

3.3.3 Water delivery

The results of §3.2.1, 3.2.2 and 3.2.4 can be further analysed to estimate the approximate amount of water delivered to Earth by each population. Using these results rather than the combined results from §3.2.5 allows the investigation of how changing the assumptions made regarding the impactor composition and dynamics affects the predictions for the water delivery. This is a simplification, but comparing the nominal single impactor results to the individual contributions to the representative case with all populations considered, no significant difference in the water mass delivered by each population is found.

Water has so far been excluded from the atmosphere volatile inventory tracked, as is it

assumed to be in liquid form at the atmosphere temperatures considered and so will not contribute to the atmosphere. However it is possible to estimate the water delivered by combining estimates for the average bulk water content of the different impactor populations with the results for the amount of solid impactor material accreted by the Earth. I adopt approximate water fractions H_2O $(\mathrm{wt.}\%)$ for the nominal populations of comets, asteroids (combining C- and S-types), and left-over planetesimals of 50% (Mumma & Charnley, 2011), 10% and 0.01% respectively (Barnes et al., 2016). The water fraction is assumed to be constant between the "wet", "nominal" and "dry" compositions, to avoid additional complexity, with the caveat that the masses calculated are rough estimates.

The results are shown in Table 3.4, from which it can be seen that the impactor accretion values from the results of the simulations predict that for the typical outcomes the largest contributors are the left-over planetesimals, which deliver around 0.2% of an ocean mass of water ($M_{\mathrm{ocean}} = 2.3 \times 10^{-4}$ $\mathrm{M}_{\oplus}$). This prediction is roughly constant between different assumptions about the planetesimal properties, but could vary if the water content of the left-over planetesimals is substantially different from the assumed value. If instead the left-over planetesimals had a composition more similar to C-type asteroids, they could deliver at least an ocean mass of water to Earth, however as discussed in §3.2.4 this would result in an unrealistically large final atmosphere mass. Higher levels of water delivery (up to $0.04\ M_{\mathrm{ocean}}$) are possible in the extreme cases where single large asteroids impact the Earth.

The total water content of the Earth is uncertain, with estimates of between $(0.25 - 4)\ M_{\mathrm{ocean}}$ water potentially present in the mantle (Ahrens, 1989; Jambon & Zimmermann, 1990; Bolfan-Casanova et al., 2003), and up to $5\ M_{\mathrm{ocean}}$ water present in the core (Wu et al., 2018). The origin of this water is also not well understood, it may have been accreted during the early stages of planet formation (Drake & Campins, 2006), or been delivered by the Moon-forming impactor (Budde et al., 2019). The fraction of Earth's water delivered by comets is still uncertain, but there is evidence that it is at most 10% (Dauphas et al., 2000), supporting the predictions made based on my results. To exceed this limit would require either a much more massive comet population, or an even drier composition (with density > 1.2 g cm^{-3} and volatile fraction $x_{\mathrm{v}} < 0.05$, recalling the non-intuitive result of §3.2.2), or some combination of the two factors.

Impactor	Case	H_2O (wt.%)	Impactor Mass Accreted [$M_\oplus$]			Water Delivered [M_{ocean}]		
		(bulk estimate)	Median	Minimum	Maximum	Median	Minimum	Maximum
Asteroid	Wet	10	6.27×10^{-8}	1.17×10^{-8}	3.35×10^{-5}	2.72×10^{-5}	5.09×10^{-6}	1.46×10^{-2}
Asteroid	Nominal	10	1.28×10^{-7}	1.88×10^{-8}	1.21×10^{-5}	5.56×10^{-5}	8.16×10^{-6}	5.27×10^{-3}
Asteroid	Dry	10	2.18×10^{-7}	2.73×10^{-8}	8.86×10^{-5}	9.46×10^{-5}	1.18×10^{-5}	3.85×10^{-2}
Asteroid	Massive	10	3.76×10^{-6}	6.67×10^{-7}	6.15×10^{-5}	1.64×10^{-3}	2.90×10^{-4}	2.67×10^{-2}
Comet	Wet	50	1.77×10^{-8}	1.75×10^{-8}	1.78×10^{-8}	3.85×10^{-5}	3.81×10^{-5}	3.88×10^{-5}
Comet	Nominal	50	1.92×10^{-8}	1.90×10^{-8}	1.95×10^{-8}	4.18×10^{-5}	4.13×10^{-5}	4.24×10^{-5}
Comet	Dry	50	3.86×10^{-8}	2.58×10^{-8}	5.49×10^{-7}	8.39×10^{-5}	5.61×10^{-5}	1.19×10^{-3}
Comet	Massive	50	1.81×10^{-7}	1.80×10^{-7}	1.81×10^{-7}	3.93×10^{-4}	3.91×10^{-4}	3.94×10^{-4}
Planetesimal	Wet	0.01	4.65×10^{-3}	3.46×10^{-3}	5.71×10^{-3}	2.02×10^{-3}	1.50×10^{-3}	2.48×10^{-3}
Planetesimal	Nominal	0.01	4.97×10^{-3}	3.45×10^{-3}	6.61×10^{-3}	2.16×10^{-3}	1.50×10^{-3}	2.87×10^{-3}
Planetesimal	Int-1	0.01	5.16×10^{-3}	3.38×10^{-3}	6.79×10^{-3}	2.25×10^{-3}	1.47×10^{-3}	2.95×10^{-3}
Planetesimal	Int-2	0.01	5.27×10^{-3}	4.15×10^{-3}	7.40×10^{-3}	2.29×10^{-3}	1.81×10^{-3}	3.22×10^{-3}
Planetesimal	Int-3[1]	0.01	5.18×10^{-3}	3.55×10^{-3}	7.80×10^{-3}	2.25×10^{-3}	1.54×10^{-3}	3.39×10^{-3}
Planetesimal	Int-4[1]	0.01	4.97×10^{-3}	3.56×10^{-3}	7.43×10^{-3}	2.16×10^{-3}	1.55×10^{-3}	3.23×10^{-3}
Planetesimal	Int-5[1]	0.01	4.73×10^{-3}	3.55×10^{-3}	7.53×10^{-3}	2.06×10^{-3}	1.55×10^{-3}	3.27×10^{-3}
Planetesimal	Dry[1]	0.01	4.15×10^{-3}	3.01×10^{-3}	5.85×10^{-3}	1.81×10^{-3}	1.31×10^{-3}	2.54×10^{-3}
Planetesimal	1	0.01	5.08×10^{-3}	3.95×10^{-3}	6.48×10^{-3}	2.21×10^{-3}	1.72×10^{-3}	2.82×10^{-3}
Planetesimal	2	0.01	4.94×10^{-3}	3.87×10^{-3}	6.31×10^{-3}	2.15×10^{-3}	1.68×10^{-3}	2.74×10^{-3}
Planetesimal	3	0.01	4.85×10^{-3}	3.79×10^{-3}	6.44×10^{-3}	2.11×10^{-3}	1.65×10^{-3}	2.80×10^{-3}
Planetesimal	4	0.01	4.95×10^{-3}	3.75×10^{-3}	6.49×10^{-3}	2.15×10^{-3}	1.63×10^{-3}	2.82×10^{-3}
Planetesimal	5	0.01	4.79×10^{-3}	3.23×10^{-3}	6.13×10^{-3}	2.08×10^{-3}	1.41×10^{-3}	2.66×10^{-3}
Planetesimal	6	0.01	4.82×10^{-3}	3.79×10^{-3}	6.44×10^{-3}	2.10×10^{-3}	1.65×10^{-3}	2.80×10^{-3}
Planetesimal	7	0.01	4.89×10^{-3}	3.56×10^{-3}	6.14×10^{-3}	2.13×10^{-3}	1.55×10^{-3}	2.67×10^{-3}
ALL	Reference	–	5.00×10^{-3}	3.68×10^{-3}	7.46×10^{-3}	2.32×10^{-3}	1.68×10^{-3}	2.11×10^{-2}

Table 3.4: The final change in planet mass and calculated water mass delivered by the impactor population, both shown as median values and ranges, for the 100 runs of the code for each individual impactor population considered. For the asteroids, the results for the three initial distributions of C- and S-types are shown combined, and the impactor fractions are shown as (f_{S-type}, f_{C-type}). Note [1] These atmospheres were in some cases completely depleted and so the code halted early, in which case the final solid mass accreted (and therefore water delivered) is underestimated. The final line shows the water mass delivered by all four population in the reference case.

3.3.4 Comparison with previous studies

My conclusions regarding the potential evolution of Earth's atmosphere can be compared to those of Pham et al. (2011), de Niem et al. (2012) and Wyatt et al. (2019). Each of these papers adopted different impact prescriptions, and assumed different properties for the impactor populations. Combined with the different methods of calculating the atmospheric evolution over time these result in different predictions for the evolution of Earth's atmosphere during accretion of the Late Veneer. Here I briefly summarise the approach, assumptions and results for each paper and discuss how my approach has led to sometimes significantly different conclusions.

Pham et al. (2011)

Pham et al. (2011) investigated the different evolutionary pathways that the atmospheres of Earth, Venus and Mars may have taken as a result of impacts. The effect of bombardment on the three planets was considered using a simplified prescription for atmosphere mass loss, by dividing impactors into two categories: those that are too small to have any effect on the atmosphere, and those that are massive enough to completely remove the entire atmosphere mass contained in the polar cap ($m_{\rm cap}$, the same as equation 2.9). They assume an exponential decay in impacts from $t_0 = 4.6$ Gya, assuming that a fixed fraction of the impactors are fast enough to cause the loss of the polar cap mass. To calculate the mass of volatiles delivered in an impact they assume a parameterisation in terms of the planet mass, volatile fraction and vaporisation factors for each impactor population. They consider only asteroids and comets, and calibrate the impact fluxes using the Lunar crater record, estimating a ratio of $0.82 : 0.18$ asteroid to comet for the Earth.

Pham et al. (2011) find that impacts onto Earth result in the atmosphere mass remaining approximately constant through time. Considering the results of §3.2.1 and 3.2.2, the results of my nominal simulations predict that asteroids should result in atmospheric growth, while comets result in loss. The assumptions I make regarding the impactor populations (discussed in §3.1.3) predict that there should be a marginally higher mass of impacting asteroidal material than cometary material, however the total impacting mass is dominated by the left-over planetesimals. If I assume instead that the Late Veneer was delivered by a combination of asteroids and comets only, it is possible that the mass estimates for these two populations would be more similar to those of Pham et al. (2011) and my estimates for the total final atmosphere mass of the Earth might be in agreement. I have demonstrated that the dynamics of the impacting population can have a significant effect on the final atmosphere

mass, making the difference between growth or loss, an effect that is not accounted for in Pham et al. (2011).

de Niem et al. (2012)

The work performed in de Niem et al. (2012) provides an opportunity to consider how the recent advances in the understanding of the dynamical history of the Solar system affect predictions made regarding the evolution of Earth's atmosphere. de Niem et al. (2012) used a similar approach to simulating atmosphere evolution as was adopted in this chapter, stochastically sampling from distributions of impactor sizes and velocities. However, as discussed in §3.2.3, they use a different impact prescription: a modified implementation of the model from Svetsov (2000) in comparison to the combination of Shuvalov (2009) and Schlichting et al. (2015) adopted in this chapter. As was shown in §2.7, the choice of impact prescription can have an effect on the atmospheric evolution predicted, however as shown in Fig. 2 of de Niem et al. (2012), the Svetsov (2000) and Shuvalov (2009) prescriptions predict broadly similar eroded atmosphere masses. The difference in predicted impactor mass accreted is also small, however as discussed in §3.2.3 this can cause a noticeable difference in the mass accretion predicted for large, low density impactors.

As in Pham et al. (2011), de Niem et al. (2012) do not consider the effect of left-over planetesimals on the atmosphere, instead taking data from simulations of an older iteration of the Nice model (Gomes et al., 2005; Morbidelli et al., 2010) then investigating a range of asteroid to comet ratios to specify the composition of the impacting population. Their distributions of velocities appear similar to the distributions calculated in §3.1.1 for the left-over planetesimals, particularly in regards to the lack of impactors with $v_{\rm imp} > 4v_{\rm esc}$. This is in contrast to the predicted faster asteroid and comet distributions calculated in §3.1.1, and de Niem et al. (2012) furthermore do not consider the time evolution of the impact velocity distributions. The total mass that they estimate to impact the Earth (3.3×10^{-5} $\rm M_{\oplus}$) is higher than the estimate for the total mass contained in the cometary and asteroid impactors combined made in §3.1.3 (6.1×10^{-6} $\rm M_{\oplus}$), but this neglects the significant mass contained in the left-over planetesimals.

I can compare my results to those of de Niem et al. (2012) using the results of §3.2.1 and 3.2.2. Their assumed comet compositions lie between my "nominal" and "dry" comet populations, while their asteroids are most similar to my "dry" asteroids. §3.2.2 would therefore imply that, if the impactors were entirely cometary, I might predict modest atmospheric loss while this scenario results in the largest atmosphere growth in de Niem et al. (2012). This

discrepancy is discussed in §3.2.3, and arises from a combination of the difference in the impactor prescriptions and the on average higher velocities sampled by my distribution in comparison to that used in de Niem et al. (2012). For the asteroids, the results presented in this chapter predict modest atmosphere growth, although if the mass of this population is increased (as needed to match the total impacting mass in de Niem et al. (2012)) I could conceivably recreate their results. Despite these similarities, the inclusion of the population of left-over planetesimals in my model results in significantly different overall conclusions. The difference in our predictions highlights the importance of revisiting this topic in light of the advances in the understanding of the bombardment history experienced by Earth.

Wyatt et al. (2019)

In Wyatt et al. (2019), the analytical model uses the same Shuvalov (2009) cratering impact prescription used in this chapter, albeit without the Schlichting et al. (2015) giant impact prescription. This model assumes a simple power-law size distribution, a single impactor population and a single impact velocity, and neglects stochasticity. The conclusions from Wyatt et al. (2019) predicts growth of the Earth's atmosphere for asteroid-like impactors, but loss for comet-like impactors, in agreement with my results. This paper highlighted the sensitivity of the predictions regarding atmosphere evolution to the impactor properties, in particular the velocities. Within a plausible range of impactor velocities, the Wyatt et al. (2019) model can predict significant atmosphere growth for slower impacts but loss for faster impacts, but cannot account for the variation in impactor velocities within a single impactor population, which I have found in §3.2.4 causes significant variation in the calculated final atmosphere masses. Furthermore, I have shown that the stochastic delivery of volatiles by the largest impactors can result in significant deviation of the atmosphere mass from the "typical" evolution.

3.3.5 Alternative atmospheric evolutionary mechanisms

This chapter has focused on the role impacts play in the evolution of Earth's atmosphere, neglecting a number of other effects. This is motivated by the fact that I consider only a short period of Earth's history during which the impact rate was high, and the effect of impacts is expected to dominate the atmospheric evolution. However, other processes can and do influence the atmosphere; prior atmospheric evolution would have determined the atmospheric properties at the onset of the period of bombardment, while processes that occur after the end of the simulation might further alter the atmosphere, influencing how the results presented in this chapter should be interpreted.

Initial atmospheric conditions

As discussed in §3.2.6, the initial conditions for my simulations (the atmosphere that remains once the final episode of core-mantle differentiation following the Moon-forming impact has occurred) are not well constrained by observations. It has been proposed (Pepin, 1991; Dauphas, 2003) that the proto-Earth had a Solar-composition atmosphere that was lost through hydrodynamic escape driven by extreme-UV flux from the active young Sun. Hydrodynamic atmosphere loss results in fractionation of elemental isotopes, as lighter isotopes are preferentially removed with the escaping hydrogen leaving behind an atmosphere enriched in heavier isotopes relative to the mantle. At the present time, the narrative on this mostly considers the possibility that an initially large atmosphere was lost hydrodynamically and subsequently a secondary atmosphere was replenished by outgassing, for more detail see §1.3.2. This is inconclusive because while He and Ne observations agree with such a possibility (Harper & Jacobsen, 1996; Ozima & Podosek, 2002), Kr does not (Holland et al., 2009). Furthermore, to recreate the chondritic isotope compositions of H, C, N and Cl in the mantle (Marty, 2012; Halliday, 2013; Sharp & Draper, 2013) requires fine tuning of the hydrodynamic loss of hydrogen which is an unlikely scenario (Schlichting & Mukhopadhyay, 2018).

A further process that will have played a significant role in determining the initial conditions for my simulations are the violent large impacts predicted by dynamical simulations (Chambers & Wetherill, 1998; Chambers, 2001) during later stages of planet formation leading up to the Moon-forming impact. These impacts are believed to result in substantial atmosphere loss (Schlichting & Mukhopadhyay, 2018) and global magma oceans on Earth (Elkins-Tanton, 2012), which should undergo ingassing and outgassing. Outgassing of a secondary atmosphere during solidification of a magma ocean is expected to result in noble gas concentrations in the magma oceans that are fractionated according to their differing solubilities. As discussed in §1.3.2 the $^{3}He/^{22}Ne$ ratios observed in plume mantle sources and mid-ocean ridge basalts are used to argue for a series of global magma oceans and associated atmosphere mass loss. Furthermore, the mantle and atmosphere ratios of Ne and Kr cannot be explained through either outgassing, or a combination of outgassing and hydrodynamic loss (Schlichting & Mukhopadhyay, 2018). This leaves open the possibility that a different process has further affected the atmosphere evolution, and means I am free to consider a wide range of potential initial conditions for my simulations.

The results from §3.2.6 suggest that impacts are capable of removing an atmosphere with primordial composition and mass up to 10 times more massive than the present day

atmosphere. Impact driven atmosphere loss would have a different isotopic signature than either hydrodynamic loss or mantle-atmosphere exchange, since it results in bulk loss of the atmosphere. Thus it might be possible to reconcile an initially high atmosphere mass with these isotopic signatures through a combination of hydrodynamic escape, ingassing, outgassing and impacts. It is also important to note that the cratering impact prescription does not include the effect of impactor fragmentation or aerial bursts, which would increase the erosional efficiency of impactors in a hot atmosphere (Shuvalov et al., 2014). As discussed in §2.3.3 the influence of these additional prescriptions is negligible for Earth's current atmosphere as considered in this study, but could contribute to the removal of an initially more massive atmosphere. These effects combined could potentially effectively strip a large atmosphere, replacing it with a secondary outgassed atmosphere. More work needs to be done to understand the combined effect of these processes, and to predict what kind of secondary atmosphere would result particularly in regards to the isotopic signatures that would result from such a scenario.

Impact-triggered outgassing

My prescription for the effect of an impact on the atmosphere neglects a potentially significant effect, that of impact-triggered outgassing from the rocky surface. The motivation for this is firstly to avoid introducing a number of unconstrained free parameters into the model and secondly because the focus of this chapter is the effect of impacts on the atmosphere mass directly.

The consideration of impact-triggered outgassing from the icy surface of Titan is considered in chapter 4. A sufficiently energetic impact will deliver enough energy to melt a portion of the planet's surface, from which trapped volatiles can be released into the atmosphere (through outgassing). The mass of volatiles released in this manner depends not only on the impact history, but also the volatile content of the mantle, and the properties of the planet that determine the volume of melt produced. The work of Schlichting et al. (2017) showed that impact-triggered outgassing can completely negate impact driven atmosphere mass, leading to significant atmosphere growth, and so this is a mechanism worth addressing in more detail.

Using a simplified toy model, it is possible estimate the mass of the Earth that would be melted as a result of impacts by the left-over planetesimals (ignoring the other populations). An analytic expression for the volume of melt on a planet with radius $R_{\rm pl}$ and volume $V_{\rm pl}$

produced by an impactor with radius $R_{\rm imp}$ is given by Reese & Solomatov (2006),

$$V_m = \frac{1}{2} V_{\rm pl} \Big(\frac{r_m}{R_{\rm pl}} \Big)^3 \Big(1 - \frac{3}{8} \frac{r_m}{R_{\rm pl}} \Big), \tag{3.3}$$

where

$$\left(\frac{r_m}{R_{\rm pl}} \right)^3 = 2 \Big(\frac{v_{\rm imp}}{v_{\rm imp}^{Pm}} \Big)^{3/2} \Big(\frac{R_{\rm imp}}{R_{\rm pl}} \Big)^3. \tag{3.4}$$

For dunite to melt entirely at 1 bar, the value of the critical impact velocity $(v_{\rm imp}^{Pm})$ is estimated to be 7 km s^{-1} (Reese & Solomatov, 2006). This gives a predicted fractional melt mass (or melting efficiency) of

$$\frac{M_m}{M_{\rm imp}} = \frac{\rho_{\rm pl}}{\rho_{\rm imp}} \Big(\frac{v_{\rm imp}}{7 \text{ km s}^{-1}} \Big)^{3/2}. \tag{3.5}$$

For the left-over planetesimals (neglecting the $(1 - \frac{3}{8} \frac{r_m}{R_{\rm pl}})$ factor since this is ≈ 1 for even the largest impactors considered here), the weighted average of the velocity distribution suggests a typical melting efficiency of ~ 6, allowing an estimate of the total melt mass to be calculated. Assuming a bulk mantle volatile content in the range $0.01 - 0.15\%$ (Schlichting et al., 2017), assuming that all volatiles in the melt are outgassed, this delivers a total volatile mass of $\sim 0.5 - 7 \times 10^{-5}$ M$_\oplus$ to the atmosphere. This calculated mass is insensitive to whether the entire population of left-over planetesimals is used or only impactors above a certain size are considered. This is $5 - 80$ times the current atmosphere mass, and could be significantly more massive than both the predicted atmospheric erosion by left-over planetesimal impacts as well as the total mass of volatiles contained in the entire impacting population of left-over planetesimals (2.6×10^{-6} M$_\oplus$).

This estimated outgassed mass is an upper limit, because it assumes that each impactor melts a unique portion of the planet. It would be more reasonable to assume that impactors arriving late in the time period will remelt material that has already been melted (and outgassed the volatiles it contains) at least once. Despite this, impact-triggered outgassing could overwhelm the atmospheric depletion that my results show as well as significantly alter the composition predicted for the final atmosphere. However detailed inclusion of its effects is left for a different study.

Implications for life

My results suggest that at the end of the simulations ($\sim$ 4 Gya) the atmosphere is predominantly composed of material delivered by the left-over planetesimals, assumed to be primarily hydrogen and carbon monoxide, with smaller contributions from carbon dioxide, nitrogen, methane, hydrogen sulfide and ammonia. A highly reduced atmosphere (methane,

hydrogen and ammonia dominated) may be necessary for the emergence of life, however this contradicts geological evidence that the Earth's mantle has always been oxidised (carbon dioxide, water and nitrogen-dominated). Zahnle et al. (2020) propose that this disagreement could be resolved if the Late Veneer was sufficiently reducing, which is the case for dry enstatite chondrite-like impactors. However their arguments require that the Late Veneer must be delivered in a small number of massive impacts that are capable of vaporising the ocean in order to provide the high H_2 pressures needed to favour methane and ammonia production over carbon dioxide and nitrogen.

For the size distribution adopted in this chapter the creation of a highly reducing atmosphere in their models would require either the extraction of extra reducing power from the Earth's mantle or the existence of as yet unknown catalysts. However Zahnle et al. (2020) did not consider atmospheric erosion or volatile delivery resulting from impacts, and thus the prediction made in this chapter for an atmosphere dominated by volatiles delivered by the left-over planetesimals could create a transient highly reducing atmosphere without the need for massive ocean-vaporising impacts, potentially providing conditions conducive for the production of pre-biotic molecules without requiring impacts so violent they would wipe out any extant life.

Subsequent atmospheric evolution

The atmosphere during and immediately after the relatively intense period of bombardment considered in my simulations is unlikely to be in thermo-chemical equilibrium, and so would be expected to continue to evolve over time. Some molecular species delivered by the impactor populations will be destroyed through photo-dissociation on various timescales, altering the chemistry of the atmospheres. Outgassing, driven by volcanism, that occurs between the end of the simulations and the present day is likely to further alter the atmosphere composition. Other processes, such as the carbon-silicate cycle are known to act as feedback loops, stabilising the Earth's climate over millions of years (Walker et al., 1981). Furthermore, the emergence of life and the presence of a biosphere on Earth has significantly impacted the atmosphere, most noticeably through the Great Oxidation Event around 2.2 Gya (Lyons et al., 2014). As a consequence of these effects, the fact that the final atmosphere compositions that I predict do not match the present day composition of the Earth's atmosphere is not necessarily a cause for concern.

3.4 Conclusions

In this chapter I have investigated the evolution of Earth's atmosphere due to impacts in the period of time after the Moon-forming impact. To do this I have constructed three populations of impactors: comets, asteroids and left-over planetesimals, calculating the distribution of impact velocities and impact fluxes from the results of dynamical simulations of the Solar system (Nesvorný et al., 2013, 2017a; Morbidelli et al., 2018). Considering the effect on Earth's atmosphere of each of these populations individually, I have found that comets in general cause the atmosphere to deplete, and this loss is greater for more massive populations or lower density impactors. If the comets are assumed to be denser they can in some cases result in growth due to the stochastic arrival of large, slow objects. In contrast, asteroids cause atmospheric growth, and the final atmosphere mass in general increases as the assumed volatile content of the asteroids increases. Increasing the total impacting mass increases the number of stochastically sampled large, slow impactors resulting more often in very large final atmosphere masses. Compared to the other individual populations, the stochastic effects are most obvious for the asteroid population due to the fact that for the initial atmosphere mass and impactor sizes assumed, large (and therefore stochastic) asteroid impacts only ever lead to growth. Since large comets and left-over planetesimals deliver almost no volatiles (due to their low accretion efficiency and low volatile content respectively) only large asteroids are capable both of contributing a substantial portion of their mass to the planet, and releasing a significant fraction of that mass into the atmosphere. The left-over planetesimals always result in atmospheric erosion with the final atmosphere mass decreasing as the volatile content of the impactors is decreased, until the entire atmosphere is stripped rapidly for sufficiently "dry" impactors. Considering plausible variation in the impactor dynamics I have found that this can cause typical atmosphere mass loss to vary between -72% and -96%.

Investigating the combined effect of all three populations, the results emphasise the importance of considering stochastic events, as the relatively rare arrival of a single large impactor can have significant effects on the atmosphere mass and composition. For identical starting conditions a wide range of outcomes is possible, with variation introduced through the uncertainty in the impactor dynamics and compositions. The results from the nominal case show modest atmospheric loss, with a median final atmosphere mass of 0.24×10^{-6} $\mathrm{M}_{\oplus}$. The sampling of a large, slow asteroid can result in significantly higher final atmosphere masses than the median value. I have found that the final atmosphere is in general dominated by material delivered by the left-over planetesimals, with a smaller primary component and even smaller contributions from asteroids and comets, consistent with observational constraints.

The initial mass and composition assumed for the Earth's atmosphere makes relatively little difference to the final outcome, however it is possible to rule out an initial atmosphere mass significantly greater than the present mass as the material delivered in the Late Veneer is not capable of sufficient erosion. The exception to this would be if the initially massive atmosphere was primordial, as atmospheres with lower μ_0 are easier to remove.

To summarise, the most important takeaway points from this chapter are:

- For the impactor properties and impact prescriptions I assume, asteroids result in atmosphere growth while comets and left-over planetesimals result in atmosphere erosion;
- The dominant population of left-over planetesimals results in evolution that converges towards an atmosphere mass slightly lower than the current value;
- These conclusions are sensitive to the assumed impactor composition and the dynamics of the left-over planetesimals.

4

The role of impacts on the atmospheres on the moons of outer giants

The Jovian moons Ganymede, Callisto, and Europa, Saturn's moon Titan and Netpune's moon Triton display a large degree of variation among their properties, which offer clues to their different formation and evolutionary histories. The processes acting on these moons are numerous, but of particular interest is the effect of bombardment of their atmosphere as such impacts are an inevitable consequence of Solar system formation models and are evidenced by the extensive cratering seen on their surfaces (see for example Strom & Croft, 1993; Korycansky & Zahnle, 2005; Mah & Brasser, 2019; Bell, 2020). In this chapter I investigate the comparative effect of impacts on these moons, to attempt to understand the diversity of the atmospheres on these moons. This is motivated by the fact that the methods used to parameterise the effect of an impact have improved since previous studies regarding atmospheric evolution of the moons of the giant planets (Zahnle et al., 1992; Griffith & Zahnle, 1995; Marounina et al., 2015, in, for example). Furthermore, variation in the impactor properties has not been considered systematically in previous comparative studies.

I use the analytic model derived in §2.3.1 to investigate of the quantitative atmosphere behaviour, the stable atmosphere "stalling" mass and the timescale of the evolution. The properties assumed for the outer moons and the nominal impacting population of comets are

described in §4.1 and §4.2 respectively. Firstly I assume the Shuvalov (2009) cratering and Schlichting et al. (2015) giant impact prescriptions described in §2.1.1 and §2.1.2, the results for which are presented in §4.3. The role of the largest impactor size in setting the stalling mass and the degree of stochastic variability expected in the atmosphere evolution is also discussed. In §4.4 I compare the analytic predictions to the results of the numerical code presented in §2.2. The sensitivity of these predictions to the impactor properties (density, volatile content, size distribution and dynamics) is investigated in §4.5. The effect of including a prescription for impact-triggered outgassing using the method described in §2.1.5 on the atmospheric evolution is then investigated in §4.6. My results are discussed in §4.7 and my conclusions presented in §4.8.

4.1 The outer satellites

The properties of the five moons I investigate (excluding Io due to the substantial volcanic outgassing and influence of Jupiter's magnetic field which make impacts less significant) are summarised in Table 4.1. Atmosphere temperatures and scale heights are shown both as observed values and estimates based on radiative equilibrium. The effect of the difference between these values on the predicted atmosphere evolution is explored in §4.5.5.

When there is no observational atmosphere mass value in the literature to compare to my results I estimate an upper limit from the observed surface pressure, or column density ($n_{\rm col} = H\frac{P_{\rm surf}}{kT}$), limits through,

$$m_{\rm atm} = \frac{3R_{\rm tar}P_{\rm surf}}{G\rho_{\rm tar}} = \frac{3R_{\rm tar}n_{\rm col}kT}{G\rho_{\rm tar}H}. \tag{4.1}$$

For Europa, Ganymede and Callisto, the column densities are taken from the literature, while for Titan and Triton I use surface pressure estimates. In the following I describe the internal structure of these moons, and describe the observations used to estimate the atmosphere mass.

BODY	Mass [$M_\oplus$]	Density [g cm^{-3}]	Separation [$\times 10^6$ km]	Semi-Major Axis [au]	Atmosphere Mass [$M_\oplus$]	Atmosphere MMW	Temperature [K]	Scale Height [km]
Europa	0.00804	3.01	671.1	5.20	$(0.66 - 3.84) \times 10^{-18}$	32	120 (90)	23.5 (17.7)
Ganymede	0.0248	1.94	1070.4	5.20	$(0.23 - 4.05) \times 10^{-18}$	32	120 (100)	21.6 (18.1)
Callisto	0.0180	1.83	1882.7	5.20	$7.2 \times 10^{-18} - 3.6 \times 10^{-16}$	44	120 (130)	18.2 (19.8)
Titan	0.0225	1.88	1221.9	9.58	1.51×10^{-6}	20	88 (90)	26.9 (27.4)
Triton	0.0036	2.06	355.0	30.07	$(0.69 - 1.14) \times 10^{-11}$	28	50 (40)	18.8 (15.1)

Table 4.1: Properties of the moons of the outer giant planets considered in this Chapter. Separation is the orbital distance of the moon to the host planet, and semi-major axis is the value of the host planet. Two atmosphere temperatures and scale heights are shown. The non-bracketed value is that estimated assuming radiative equilibrium with incident stellar flux, neglecting potential tidal heating forces. The bracketed value is the best estimate from current observations, with the caveat that Triton is warming as Netpune's orbit takes it closer to the sun.

Ganymede, the largest Jovian moon, consists of an iron core, with a water-ice and silicate mantle and potentially a subsurface internal ocean (Sohl et al., 2002). It is the largest object in the Solar system without a substantial atmosphere. Voyager constrained the surface pressure to $< 25 \times 10^{-12}$ bar (Broadfoot et al., 1981), likely composed of O_2, as evidenced by HST observations of atomic oxygen air-glow and spectroscopic detection of ozone and O_2 (Hall et al., 1998). The observed O_2 column density is $(0.3 - 5) \times 10^{14}$ cm^{-2} (Hall et al., 1998; Feldman et al., 2000), while the H_2 density is < 10 % of this value and so ignored in the following calculation (Feldman et al., 2000). This column density, combined with the scale height and surface temperature from Table 4.1, gives an estimated surface pressure of $(0.02 - 0.40)$ μPa. The corresponding atmosphere mass limits are shown in table 4.1.

Callisto is the next largest Jovian moon, with a relatively low density, evidence for a silicate core and a subsurface ocean (Anderson et al., 2001). The surface is ancient and heavily cratered, with no evidence for tectonic or volcanic activity. The extremely thin CO_2 atmosphere (~ 0.75 μbar) has a column density of 8×10^{14} cm^{-2} (Carlson, 1999). However, the presence of a strong ionosphere implies a substantial molecular oxygen component, with column density potentially as high as 4×10^{16} cm^{-2} (Liang et al., 2005; Cunningham et al., 2015). This results in an estimated surface pressure of 0.73 μPa (36 μPa with the oxygen component).

Europa is the smallest of Jupiter's Galilean moons, with a silicate rock composition, a water-ice crust and potentially a metallic core (Kivelson et al., 2002). The surface is covered in cracks with few craters, which may be due to a subsurface water ocean, evidenced by water vapour plumes. Europa's oxygen-dominated atmosphere is extremely thin, with a O_2 column density of $(2.4 - 14) \times 10^{14}$ cm^{-2} (Hall et al., 1998). This is frequently considered to be a collisionless exosphere[1] rather than a true atmosphere (Hall et al., 1995; Johnson et al., 2002). The estimated surface pressure is $(0.17 - 0.98)$ μPa, and the corresponding atmosphere mass estimate is close to the fluid limit derived in §2.1.4.

Titan has a massive atmosphere composed of 94% N_2, 5.6% CH_3, 0.1% H_2 and trace hydrocarbons (Catling & Kasting, 2017). The estimated surface pressure on Titan is 1.47×10^5 Pa (McKinnon & Kirk, 2014), giving a total mass estimate of 1.51×10^{-6} $M_\oplus$.

Triton has a substantial rock and metal core, an icy mantle and crust and a tenuous nitrogen atmosphere, believed to contain trace amounts of carbon monoxide and methane. The inferred

[1] gravitationally bound material that does not behave as a fluid

atmospheric pressure has increased from $(14 - 40)$ Pa between 1989 (Tyler et al., 1989) and 2009 (Lellouch et al., 2010), potentially consistent with the vapour pressure of nitrogen as the atmosphere temperature increases from 38 to 50 K (Grundy & Stansberry, 2000). This change in the surface pressure and the implications for my conclusions are explored in detail in §4.7. I assume a surface pressure range of $(14 - 19)$ Pa.

4.2 The nominal impactor population

Impacts onto the outer moons are expected be dominated by objects from the trans-Neptunian disk, as they are the only population of small bodies with an origin exterior to the giant planets. In the following results I therefore consider a nominal comet-like impactor population with properties as described below. This allows detailed investigation of the typical atmospheric stalling mass and its nature, and to isolate the effect of timescales on these values. This nominal population is also used to investigate the stochastic nature of impacts using the numerical code. Later I consider the dependence of these predictions on the assumed composition, size and velocity distributions of the impactors.

4.2.1 Composition

The nominal impactor population is assumed to have a single homogeneous composition, specified by three parameters: bulk density $(\rho_{\rm imp})$, volatile fraction $(x_{\rm v})$ and MMW of the delivered volatiles $(\mu_{\rm imp})$.

The predicted atmosphere mass evolution is only weakly dependent on μ and so if the atmosphere is replaced by delivered material and μ changes, the predicted atmosphere mass evolution is only slightly altered. Therefore I do not consider the effect of variation in this parameter, and assume a constant value of $\mu_{\rm imp} = 32$ (Griffith & Zahnle, 1995). Comets display a wide degree of observed compositional diversity, with densities estimated between $0.3 - 1.2$ g cm^{-3}, and so in §4.5.2 a range of bulk densities spanning $0.5 - 2.5$ g cm^{-3} is considered (Festou et al., 2004). When considering the effect of variation in other parameters, $\rho_{\rm imp} = 1.0$ g cm^{-3} is assumed.

In the nominal case an estimated volatile fraction for comets of 10% (Griffith & Zahnle, 1995) is adopted. In reality the volatile content of the impactors is likely more complicated, and so a range of potential volatile fractions from $2 - 50\%$ is investigated in §4.5.2. The volatile fraction is not simply a property of the comet in isolation, as the species that contribute mass to the

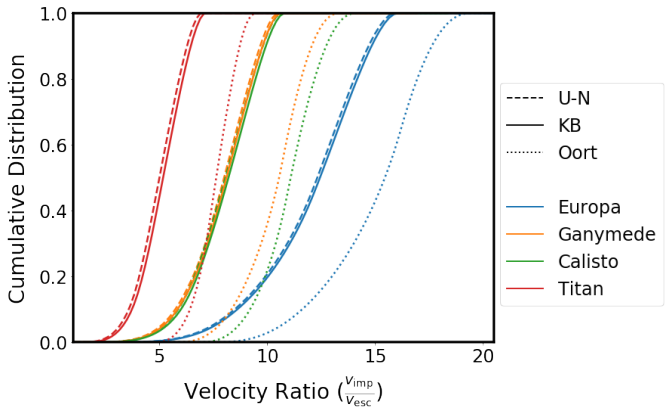

Figure 4.1: The results of the Zahnle et al. (1992) method of calculation for three different source populations. Objects from the Oort cloud ($a = 20000$ au, $i = 0 - 180\,\mathrm{deg}$ isotropic), Kuiper belt (the nominal population, $a = 50$, $0 < i < 10\,\mathrm{deg}$) and Uranus-Netpune planetesimals ($a = 25$, $0 < i < 10\,\mathrm{deg}$) are shown by different line styles. Each distribution is shown as a ratio of impact velocity to the escape velocity of the moon.

atmosphere depend on the atmospheric temperature. For example Triton is substantially cooler than the atmospheres of Jupiter's moons. While I do not directly investigate this possibility here, a different volatile fraction may be more appropriate for Triton and Titan in comparison to Europa, Ganymede and Callisto.

4.2.2 Velocity distribution

The effect of an impact on the atmosphere is sensitive to the impact velocity, and thus the choice of how to specify the distribution of impact velocities is important.

I follow the approach of Zahnle et al. (1992) to construct distributions of impact velocities based on dynamical arguments, as follows. The comets are assumed to be on orbits specified by a single semi-major axis, pericentres distributed uniformly between $p_{\min}$ to $p_{\max}$ and inclinations distributed isotropically between $i = 0 - i_{\max}$. The heliocentric distributions are thus $n(a, p, i)\,\mathrm{d}a\,\mathrm{d}p\,\mathrm{d}i \propto \sin(i)\,\mathrm{d}a\,\mathrm{d}p\,\mathrm{d}i$. The relative velocity (at infinity) between a comet and a planet with orbital velocity v_{tar} is

$$\begin{aligned} v_\infty^2 &= \xi^2 v_{\mathrm{tar}}^2 \\ &= v_{\mathrm{tar}}^2 \left(3 - \frac{a_{\mathrm{tar}}}{a} - 2\cos(i) \sqrt{\frac{p}{a_{\mathrm{tar}}} \left(2 - \frac{p}{a}\right)} \right). \end{aligned} \tag{4.2}$$

The impact parameter (b) onto a satellite with orbital velocity v_{sat} is $bv_\infty = rv_{\mathrm{t}}$, where v_{t} is the tangential velocity of the comet at a distance r from the satellite. The maximum impact

parameter (when $r = a_{\rm sat}$ and $v_t = v = \sqrt{v_\infty^2 + 2v_{\rm sat}^2}$) is

$$b_{\rm max} = r\frac{v_{\rm t}}{v_\infty} = a_{\rm sat}\sqrt{1 + 2\frac{v_{\rm sat}^2}{v_\infty^2}}. \tag{4.3}$$

The impact parameter is assumed to be distributed uniformly between 0 and $b_{\rm max}$ and the relative inclination between the comet and the satellite plane (i') is assumed to be isotropic such than $\cos(i')$ is uniformly distributed between 0 and 1. In the coordinate system centred on the planet, the satellite and comet have velocities of $\mathbf{v}_{\rm sat} = (0, v_{\rm sat}, 0)$ and $\mathbf{v}_{\rm com} = (v_{\rm r}, v_{\rm t}\cos(i'), v_{\rm t}\sin(i'))$ respectively. Their relative velocity is therefore

$$v_{\rm rel}^2 = |\mathbf{v}_{\rm sat} - \mathbf{v}_{\rm com}| = v_\infty^2 + 3v_{\rm sat}^2 - 2v_{\rm t}v_{\rm sat}\cos(i'). \tag{4.4}$$

The impact velocity (including gravitational focusing) is thus

$$v_{\rm imp}^2 = v_{\rm rel}^2 + v_{\rm esc}^2 = v_\infty^2 + 3v_{\rm sat}^2 - 2v_{\rm t}v_{\rm sat}\cos(i') + v_{\rm esc}^2. \tag{4.5}$$

According to Zahnle et al. (1992), following Shoemaker & Wolfe (1982) gives the collision probability for each comet to be proportional to

$$P_{\rm col} \propto \left(1 + 2\frac{v_{\rm sat}^2}{v_\infty^2}\right)\left(1 + \frac{v_{\rm esc}}{v_\infty^2 + 2v_{\rm sat}^2}\right)\frac{\xi}{\xi_x \sin(i')}, \tag{4.6}$$

where the radial component of the dimensionless parameter ξ is

$$\xi_x^2 = 2 - \frac{a_{\rm tar}}{a} - \frac{p}{a_{\rm tar}}\sqrt{2 - \frac{p}{a}}. \tag{4.7}$$

These equations are used to calculate the impact velocity distributions for comets originating from three potential source regions: Uranus-Netpune planetesimals (UNPs), Kuiper Belt objects (KBOs) and Oort Cloud objects (OCOs), which are assumed to have semi-major axes of $a = 25$, 50 and 20000 au respectively. The pericentre distributions span $0.1 - 5.1$ au for the Jovian moons (Europa, Ganymede and Callisto), $5.3 - 9.4$ au for Saturn's moon Titan and $19.3 - 29.9$ au for Netpune's moon Triton. The isotropic inclination distribution is assumed to have $i_{\rm max} = 10$ deg for the UNPs and KBOs, and 180 deg for the OCOs.

The calculated impact velocity distributions are shown in Fig. 4.1, which shows that the KBOs and UNPs show very similar distributions, while the OCOs are typically faster. This results from the higher orbital inclinations of the OCOs. The KBOs are expected to dominate the delivery of material to the outer moons and so are used as the nominal distribution of

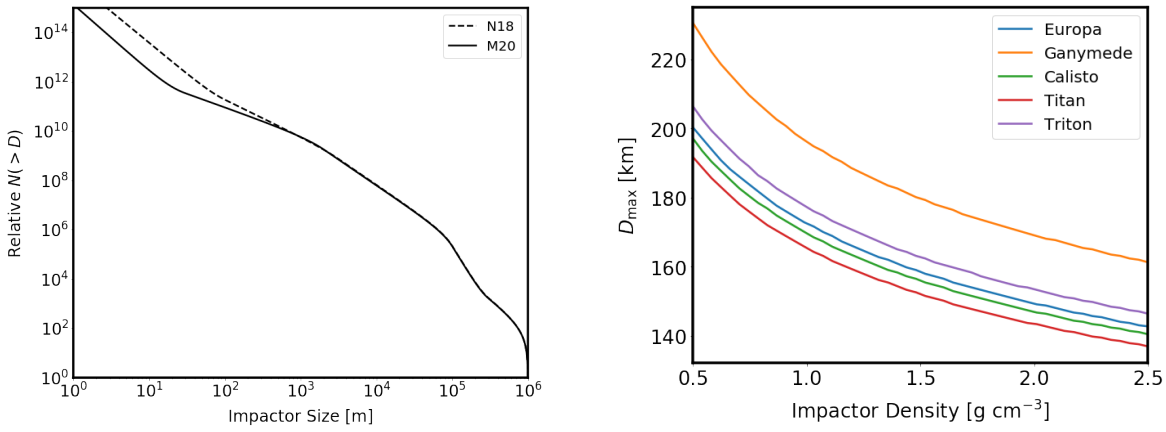

(a) (b)

Figure 4.2: Panel (a) shows the cumulative size distribution normalised such that there is one object with $D \geqslant 1000$ km in the size distribution. The nominal (Morbidelli et al., 2020) size distribution is shown as a solid line with the (Nesvorný et al., 2018) size distribution that is used for investigating the sensitivity of the results to the assumed size distribution shown as a dashed line. Panel (b) shows the maximum sampled impactor size as a function of impactor density for each of the moons. These have been calculated assuming the impact rate as described in §4.2.3.

impactor velocities. The difference in predicted atmosphere outcomes resulting from the alternative source regions is investigated in §4.5.4.

4.2.3 Size distribution

Slope of the distribution

The observed trans-Netpunian object SFD from Morbidelli et al. (2020) is used as the nominal case, and is illustrated in the top panel of Fig. 4.2a. It similar to an $\alpha = 3.1$ differential power-law SFD, but with fewer large impactors and a slope more similar to $\alpha = 3.5$ for the smallest impactors. An alternative distribution from Nesvorný et al. (2018) (also illustrated in Fig. 4.2a) is considered in §4.5.3 to investigate the sensitivity of my results to the assumed size distribution.

Size limits

The dependence of the predicted stalling masses on the limits of the impactor size distribution can also be investigated. The choice for the lower size limit is not a physical limit, since collisions will populate the distribution to arbitrarily low sizes. At small enough values of the erosional efficiency parameter (η) the effect of the impactor on the atmosphere becomes negligible, however η also depends on atmosphere mass and thus the size below which impacts can be neglected decreases as the atmosphere mass decreases. Based on convergence

testing using a realistic range of impactor and target properties impactors smaller than 0.01 m are found to typically have no impact on the atmosphere behaviour for atmosphere masses above the fluid limit (approximately 10^{-20} $M_\oplus$, see §2.1.4) and thus a conservative lower limit of 100 μ m is adopted.

The upper size limit is more complicated, since it is set by the combination of the slope of the size distribution and the assumed impact flux. The current impact flux to the outer moons is normalised to impacts with size $D > 1.5$ km, within impactors sampled from a parent distribution spanning 100 μm to 1000 km. The largest impactor sizes are unlikely to be sampled over the age of the Solar system given the total masses considered, i.e. $N(> D) \leqslant 1$ for a size D below the upper limit of the parent distribution, and thus including their effect in the analytic prediction will lead to inaccurate predictions. In the numerical code, the maximum impactor size is set by the stochastic sampling of the impactors and so this complication is accounted for. However, in the analytic approximation, it must be directly specified to avoid including a significant contribution to atmosphere erosion or volatile delivery by a fraction of an impactor. To do this, the cumulative impactor numbers $N(> D)$ are calculated and the nominal maximum impactor size for each impactor population is defined as the size at which $N(> D_{\rm max}) = 1$ over the age of the Solar system. This value depends on the assumed impactor density and varies between outer satellites, as shown in Fig. 4.2b, however it is typically of the order $D_{\rm max} \sim 100$ km. This effect is explored in more detail in §4.3.2.

4.2.4 Impact rates and total impacting mass

The impact fluxes, which give the total number of impacts of all velocities onto the outer satellites as a function of time, are important when considering the absolute time evolution of the atmosphere. The analytically predicted stalling mass is not dependent on the impact flux, however the time taken to reach this stalling mass is. I estimate the impact fluxes and total impacting mass using the (present day) ratio of impacts at all velocities by ecliptic comets onto the outer moons relative to Jupiter, taken from the Monte Carlo calculations carried out in Zahnle et al. (2003). Taking the current rate of impactors with $D > 1.5$ km onto Jupiter to be $\dot{N}(D > 1.5{\rm km}) \approx 0.005\,{\rm yr}^{-1}$ from the same work, the corresponding rate onto each moon is calculated. These imply a total mass impacting the outer moons over the last Gyr of $(1.4 - 3) \times 10^{-8}$ $M_\oplus$.

This current rate of bombardment is likely significantly lower than that experienced in the early history of the Solar system, and to correct for this I estimate a decay in impact flux, using

a model fit to calculated comet impacts onto Mars from data based on the simulations of Nesvorný et al. (2017b) over the first Gyr after Solar system formation (described in Chapter 5). This results in a total impacting mass over the age of the Solar system 650 times more massive than the estimate of the last Gyr.

Given the inherent uncertainty in this approximation, and the insensitivity of the final atmospheres to the absolute times at which the impacts arrive this decay is not included in the numerical evolution. Instead the total mass of impactors for each outer moon is distributed in a uniform impact rate. Most mass is contained in the largest impactors, and thus the total impacting mass sets the size of the largest impactor expected to be sampled. The analytic stalling mass prediction is sensitive to this largest impactor size, and therefore depends on the time scale over which the evolution of the atmosphere is considered. This phenomenon is explored in detail in §4.3.2, where I demonstrate that while the impact flux influences the degree of stochasticity expected from the numerical results, the predictions for the atmosphere stalling masses are unchanged.

4.3 Analytic predictions

The analytic stalling mass described in §2.3.1 can now be calculated, for all five outer moons, focusing on Titan when detail is needed, assuming the nominal impactor population described above. I first consider the maximum impactor size set by the estimated total impacting mass, as described in §4.2.3, before discussing how the timescale over which the impactors are sampled can affect the predicted stalling mass for the atmosphere.

4.3.1 Nominal stalling mass predictions

The first step is calculating f_{v} as a function of impact velocity, impactor density and atmosphere mass for each of the five moons, using equation 2.33. This requires summing over the impactor size distribution up to the maximum size, defined by $N(> D_{\mathrm{max}}) = 1$ as discussed in §4.2.3, over a timescale of 4.5 Gyr to consider the long-term evolution of the atmospheres. An example of the kind of $f_{\mathrm{v}}(m_{\mathrm{atm}})$ profiles produced for impacts with a range of velocities onto Titan are shown in Fig. 4.3a. Where these lines cross one on the y-axis (if they do so) gives the atmosphere stalling masses, as described in §2.3.1.

However, considering the effect of a single impact velocity in isolation is nonphysical, since impacts occur with a range of velocities. The effect of a realistic velocity distribution can be

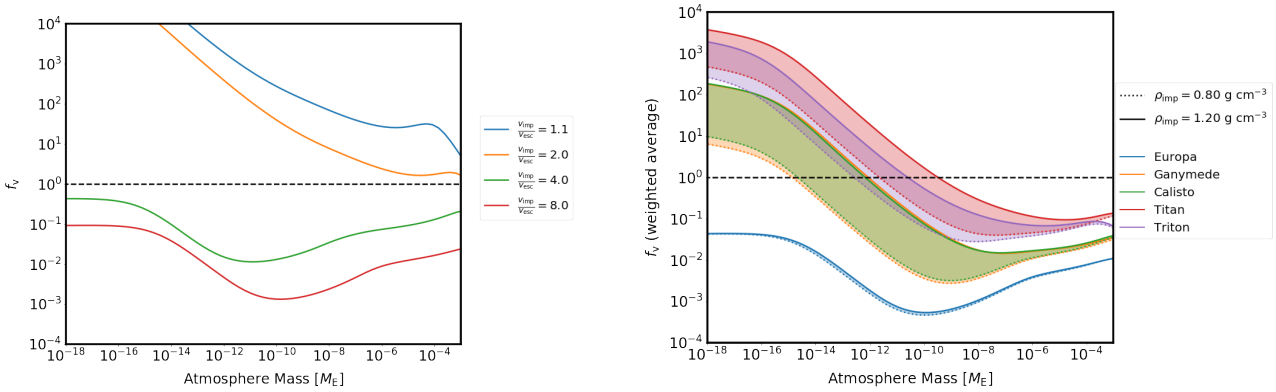

(a) (b)

Figure 4.3: Panel (a) shows the calculated values of the ratio of atmosphere mass gain to mass loss (f_v) as a function of atmosphere mass for a representative range of impact velocities. These results are shown for a single representative impactor density (1 g cm^{-3}) and for impacts onto Titan, with the line colour illustrating the impact velocity. In panel (b) the calculated values of f_v are shown summed over a realistic distribution of impact velocities. These results are shown for a range of impactor densities illustrated by the line style given in the caption, with the range between these densities shown as a shaded region. Each moon is shown by a different line and shading colour.

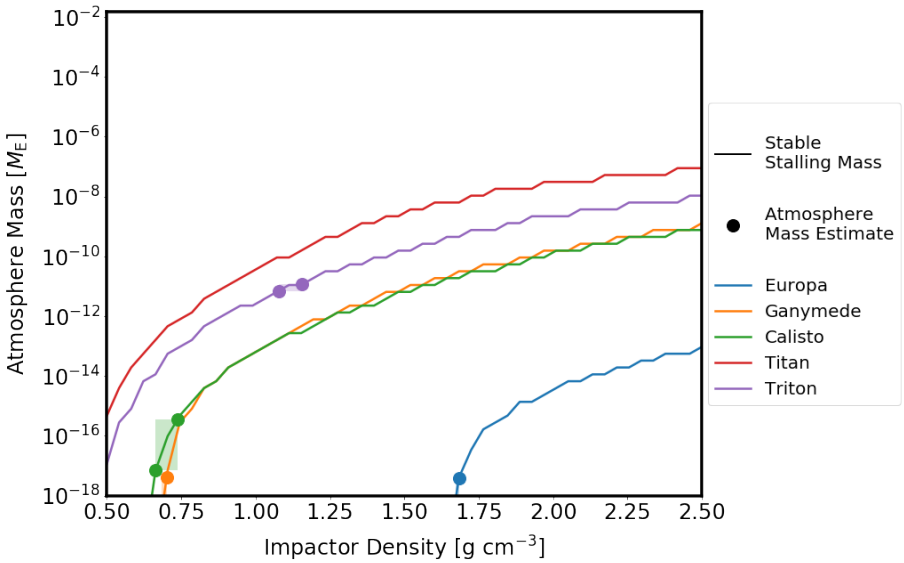

Figure 4.4: The stalling masses predicted for each of the moons summing the contributions to f_v using a realistic velocity distribution. The results for each of the different moons is shown by a different line colour, with a shaded rectangle between two markers indicating the region of parameter space in which the predicted stalling mass is in agreement with the estimated atmosphere mass limits given in Table. 4.1.

seen by calculating the weighted average of $f_{\rm v}$ over all velocities using the probabilities calculated in §4.2.2. These averaged profiles are shown for a representative span of impactor densities in Fig. 4.3b. The atmosphere mass at which $f_{\rm v} = 1$ is highest for Titan, followed by Triton, then Callisto and Ganymede (which are almost indistinguishable). Europa has a value of $f_{\rm v} < 1$ at all atmosphere masses, suggesting that impacts are never capable of growing an atmosphere on this moon. Lower density impactors result in lower stalling masses for all moons. Fig. 4.3b also illustrates the necessity of averaging $f_{\rm v}$ over a distribution of velocities, rather than approximating a single representative velocity, since these resultant curves are not well represented by any of the lines from Fig. 4.3a.

The stalling masses, calculated as a function of impactor density by locating the atmosphere mass at which $f_{\rm v} = 1$ for each of the five moons, are shown in Fig. 4.4. For Europa (which has essentially no atmosphere) runaway atmosphere depletion is predicted for all but the highest density impactors. The pattern of increasing atmosphere masses from Ganymede to Callisto to Triton is matched by my results, although no single impactor density results in simultaneous matching of all the observed masses. For example, an assumed impactor density of $1\ \mathrm{g\ cm^{-3}}$ is reasonable for Europa and Triton but overestimates the observed atmosphere masses of Callisto and Ganymede by more than an order of magnitude. While a higher atmosphere stalling mass is predicted for Titan than the other moons at all impactor densities ($2.85 \times 10^{-11}\ \mathrm{M_\oplus}$ for $\rho_{\rm imp} = 1\ \mathrm{g\ cm^{-3}}$), the actual atmosphere mass ($\sim 1.5 \times 10^{-6}\ \mathrm{M_\oplus}$) is six orders of magnitude higher than the predicted value. The potential solution to this discrepancy, impact-triggered outgassing, is discussed in §4.6.

4.3.2 Timescales

The analytic prediction for the stalling mass is a useful quantity when considering the long-term evolution of a small body's atmosphere. However, it does not address the feasibility of reaching the predicted stalling mass within the age of the Solar system.

The adopted size distribution and mass accretion rates described in §4.2.3 and §4.2.4 together determine the size of the largest impactor, $D_{\rm lim}$, sampled over a given timescale, $\tau_{\rm sample}$, i.e. the impactor size at which one impactor of this size or larger is expected to arrive in this time period. These two quantities are related through

$$\int_0^{\tau_{\rm sample}(D_{\rm lim})} \dot{N}(> D_{\rm lim})\ \mathrm{d}t = 1. \tag{4.8}$$

This relationship is illustrated for each of the five outer moons in the top panel of Fig. 4.5.

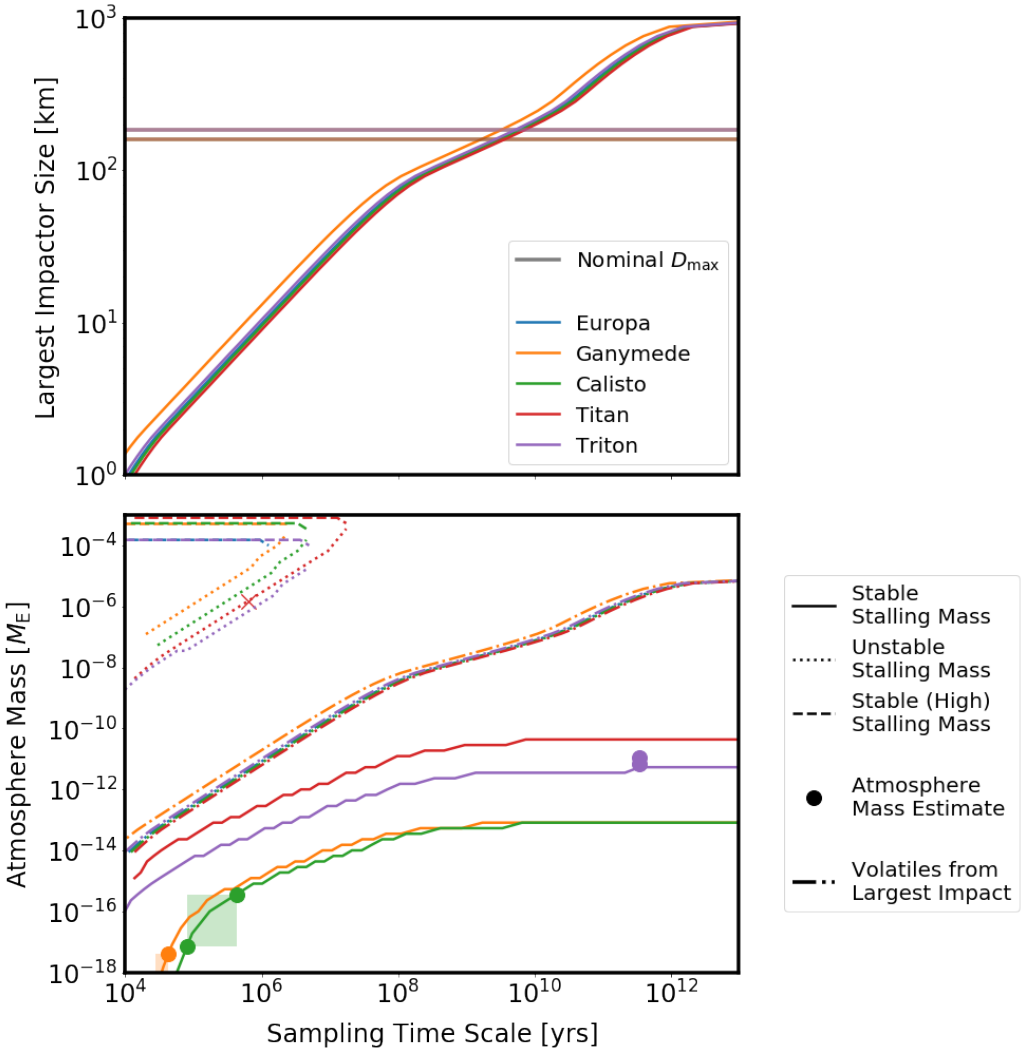

Figure 4.5: The top panel shows the dependence of the largest impactor size ($D_{\rm lim}$) on the timescale over which evolution of the atmosphere is considered, calculated from the impact fluxes as described in the text. The atmosphere stalling masses calculated for these largest impactor sizes are shown in the bottom panel as a function of the timescale. The lower stable stalling mass is shown by a solid line, the larger stable stalling mass by a dashed line, and the unstable equilibrium mass that separates the two by a dotted line, with the line colour illustrating the moon for which the values are calculated. The location on the lines of stalling mass that are in agreement with the estimated range of observed atmosphere masses from Table 4.1 are shown by shaded rectangles between two markers, with the colour again illustrating the moon. The mass of volatiles contained in the largest impactor expected to be sampled in the timescale is shown by a dash-dotted line in the same colour. The entire time period of the simulations ($\tau_{\rm sample} = 4.5$ Gyr) is shown by vertical black lines on both panels, from which the maximum impactor size (described in §4.2.3) and nominal stalling mass predictions (described in §4.3.1) can be inferred.

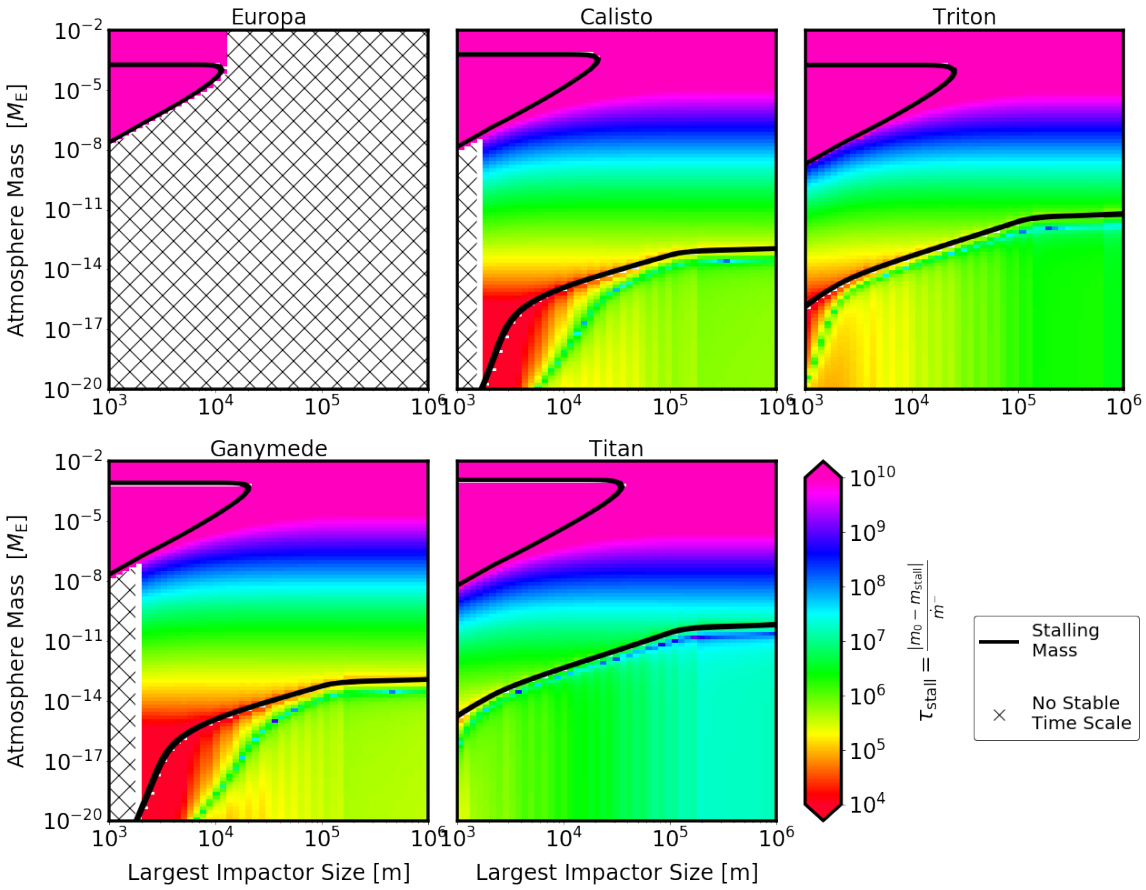

Figure 4.6: The value of the evolution timescale τ_{evolve} (defined in equation 4.9) as a function of maximum impactor size and atmosphere mass. The locations of the atmosphere stalling mass are shown by thick black lines. Where the plots are marked by black hatching there is no accessible stable stalling mass and the atmosphere is expected to undergo runaway depletion.

Over the longest time span considered, 4.5 Gyr, once the moons have undergone the expected total bombardment, this largest impactor size is equal to the maximum impactor size discussed in §4.2.3 (i.e. $D_{\rm lim}(\tau_{\rm sample} = 4.5{\rm Gyr}) = D_{\rm max} \approx 170$ km). On shorter timescales the size of the largest sampled impactor decreases, and considering the effect of this truncated size distribution on the atmosphere, keeping all other impactor and moon properties constant, results in a lower predicted stalling mass, $m_{\rm stall}(D_{\rm lim})$. This behaviour is shown for each of the five outer moons in the bottom panel of Fig. 4.5, from which it can be seen that decreasing the size of the largest impactor through considering a shorter timescale decreases the predicted stalling mass.

At small maximum impactor sizes (below $\sim$ 10 km) a new phenomenon emerges, that of multiple equilibrium atmosphere masses. This manifests as a stable (low) stalling mass, but an unstable equilibrium point at some higher atmosphere mass. An atmosphere mass below this unstable equilibrium should undergo erosion to the stable atmosphere mass, however if some stochastic event were to increase the atmosphere mass above this unstable equilibrium, the atmosphere should grow until it reaches the stable (high) stalling mass. This is interesting, but the high atmosphere stalling mass stalling is never accessible as a result of impacts. This would require the occurrence of a single stochastic event that can deliver enough atmosphere mass to jump from the bottom stable atmosphere mass to above the unstable equilibrium, which requires the delivery of 10^{-8} $\rm M_{\oplus}$ in volatiles in a single event, which assuming the nominal impactor properties corresponds to the volatiles contained in a single 110 km diameter object. This size of object is expected to impact the outer moons, however the accretion efficiency of these large bodies is low, and so either a substantially more massive impactor (which would be very rare) or an extremely slow impact (which is also rare) is required to deliver this mass in a single event. For this reason, in the following only the lower stable atmosphere stalling masses are considered.

To understand whether the predicted atmosphere stalling mass is a realistic prediction for the actual atmosphere behaviour it is necessary to consider first whether the impactors can erode or grow an initial atmosphere to the final stalling mass. In order to answer this first question, an atmosphere evolution timescale,

$$\tau_{\rm evolve} = \frac{|m_0 - m_{\rm stall}(D_{\rm lim})|}{\dot{m}(m_0, D_{\rm lim})}, \tag{4.9}$$

is defined, where m_0 is the initial atmosphere mass and $\dot{m}(m_0, D_{\rm lim})$ is the initial rate of atmosphere mass change. This timescale represents the time taken for an atmosphere to evolve from its initial mass to the stalling mass $m_{\rm stall}(D_{\rm lim})$, ignoring the fact that $\dot{m}$ depends

on the atmosphere mass and so changes as the atmosphere evolves.

The dependence of the evolution timescale on the atmosphere mass and the largest impactor size is illustrated in Fig. 4.6. These timescales imply that initially bare moons can grow to the stalling mass over the full time span of the simulation (once they have undergone the bombardment expected over the age of the Solar system), and suggest that initial atmosphere masses of $< 10^{-7}$ $M_\oplus$ can be eroded to the stalling mass within this time period. This upper atmosphere mass limit is lowest for Titan, which has the longest evolution timescales, followed by Triton and then the Jovian moons. Larger initial atmosphere masses take a significantly longer time to deplete to the stable stalling mass, suggesting that impacts alone are incapable of eroding massive primordial atmospheres to the current observed levels on these moons.

The second question is whether the atmosphere behaviour at the stalling mass is expected to be smooth or dominated by stochasticity. To address this question, it is necessary to consider the relationship between the evolution timescale defined in equation 4.9 and the stalling mass. This is considered using Titan and Ganymede as examples.

For Titan, Fig. 4.6 demonstrates that, provided the initial atmosphere mass is not so massive that it cannot be eroded, stalling masses are typically reached in around $1 - 10$ Myr, with this time largely insensitive to the size of the largest impactor. Fig. 4.5 shows that in this timescale objects around $10 - 20$ km are expected to be accreted, predicted a stalling mass of $\sim 10^{-12}$ $M_\oplus$. This is lower than the 2.85×10^{-11} $M_\oplus$ value predicted for the full distribution up to $D_{\max} = 170$ km expected over the entire time span considered. However, larger objects between 10 and 170 km in size are also impacting the moon in a stochastic fashion. These impacts deliver substantial volatile masses resulting in atmospheric growth, but this is rapidly followed by depletion back to $\sim 10^{-12}$ $M_\oplus$ over a timescale of $1 - 10$ Myr due to the continuous accretion of smaller objects. Over the full 4.5 Gyr time span of the simulation the atmosphere is therefore expected to vary stochastically between 10^{-12} $M_\oplus$ and a few $\times 10^{-9}$ $M_\oplus$ (the volatile mass delivered by the largest body).[2]

As a comparison, consider Ganymede, which is predicted to have a lower atmosphere stalling mass than Titan. In this case Fig. 4.6 shows that the stalling mass is typically reached on a shorter timescale, $\sim 0.1 - 1$ Myr, which from Fig. 4.5 can be seen to correspond to the accretion of $\sim 2 - 5$ km-sized objects and thus a predicted atmosphere stalling mass of

[2] Assuming an accretion efficiency of 10% for a $D = 170$ km comet, which contains $\sim 3 \times 10^{-8} M_\oplus$ in volatiles.

$\sim 10^{-17}$ $M_\oplus$. The atmosphere mass would therefore be expected to vary stochastically between this value and a few $\times 10^{-9}$ $M_\oplus$. This is substantially more stochastic variation than predicted for Titan, suggesting that lower predicted atmosphere stalling masses would be expected to show more stochastic variation in the numerical code results. These predictions are compared to the results of the numerical code in §4.4.3.

The discussion above cannot directly be applied to the present day evolution of the atmospheres of the moons, as I am assuming the constant average impact rate calculated in §4.2.4. For this reason the absolute times given are not directly able to be translated into real times. However the general arguments made regarding the comparison of the two timescales are applicable regardless of the impact rate, since for a constant value of $D_{\rm lim}$, both timescales scale with the impact rate in the same way. The true impact rate at the current time is lower than my assumed average rate, by a factor of ~ 145, equivalent to shifting the lines on the top panel of Fig. 4.5 to the right by the same factor, meaning that in a given timescale the largest impactor will be smaller. The specific factor by which the largest impactor size decreases depends on the slope of the size distribution, which is not constant, but in general is between 1 and 10. Since the stalling mass is dependent only on the size of this largest impactor, not the impact rate, this will also shift the lines in the bottom panel of Fig. 4.5 to the right by a factor of 145, decreasing the predicted stalling mass for a given timescale. When considering the evolution timescale shown in Fig. 4.6, the current impact rate gives timescales that are also a factor of 145 higher. Titan can be used as an example to consider how this influences the predicted atmosphere stalling mass and stochastic behaviour.

Fig. 4.6 implies that the stalling mass is currently expected to be reached in $0.1-1$ Gyr. However because the sampling timescale has increased by the same factor, the stalling mass to which the atmosphere evolves towards is still determined by the accretion of objects up to the same size as before, $10-20$ km, and thus is unchanged. As discussed above, the atmosphere is perturbed away from this equilibrium by the stochastic accretion of objects larger than $10-20$ km, and therefore the lower bombardment rate results in decreasing frequency of those impacts. This means that the maximum impactor size expected to arrive over 4.5 Gyr (if bombardment was constant at the current rate throughout) would be reduced from 170 km to 43 km. This means that the stochastic variation in the atmosphere mass is no longer likely to peak at a few 10^{-9} $M_\oplus$ but instead at approximately 10^{-10} $M_\oplus$, the mass of volatiles that could be delivered by this largest impactor.

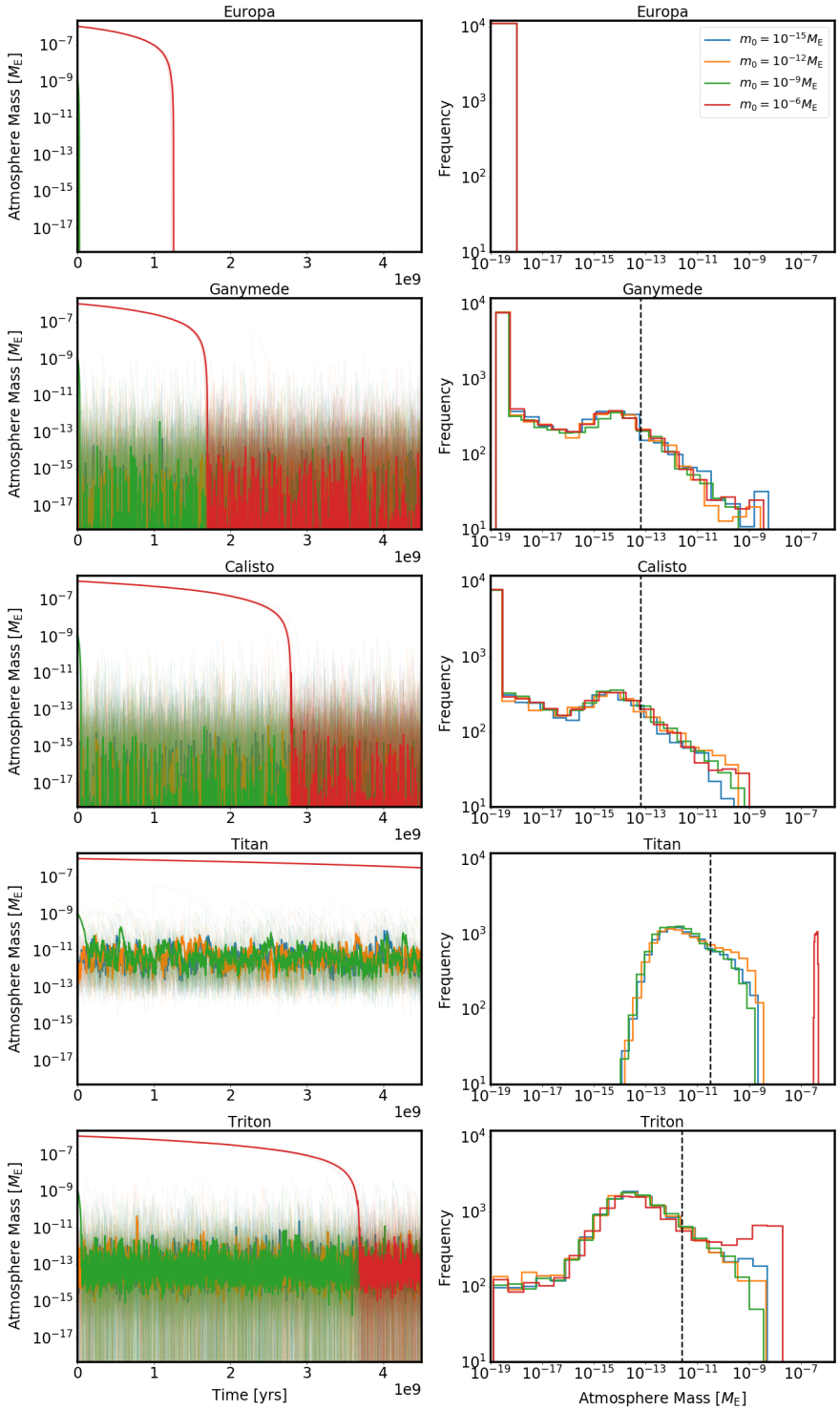

Figure 4.7: The results of numerical simulations of atmosphere evolution on the five outer moons. The left column illustrates the atmosphere mass through time for a range of initial atmosphere masses shown by different line colours. Thin transparent lines show the ten individual results, and the thick line shows the median mass. The right column shows a histogram of atmosphere masses sampled in the final Gyr over all ten simulations. The lower atmosphere limit (10^{-19} $M_\oplus$) implemented in the code results in an artificial spike in the distribution of observed atmosphere masses, which can be seen in the histograms for Ganymede and Callisto and is the only atmosphere mass recorded for Europa after the initial depletion. The analytic prediction discussed in the text is shown in the right panels by a vertical dashed black line.

4.4 Numerical results

4.4.1 Titan in detail

I first consider the evolution of Titan's atmosphere under bombardment by the nominal impactor population, using the numerical code described in §2.2, without including impact-triggered outgassing. This allows investigation of the effects of stochasticity in detail, and the evolution of different initial atmosphere masses. The code is run ten times for four different initial atmosphere masses spanning $10^{-15} - 10^{-6}$ $M_{\oplus}$, adopting the nominal impactor properties described in §4.2. Impactors are sampled stochastically from the size distribution described in §4.2.3, which given the assumed total impacting masses gives a typical largest sampled impactor size for Titan of ~ 170 km. As discussed in §4.2.4 I adopt a time-independent impact flux and thus the time shown in these results is not a real time.

The resulting atmosphere mass evolution is illustrated in the left-hand panel in the fourth row in Fig. 4.7. The evolution of the atmosphere mass shows two main features. Firstly, there exists a significant amount of stochastic variation within the each run at different times, as predicted in §4.3.2. Secondly, there is a tendency for the atmospheres with initial masses $\leqslant 10^{-7}$ $M_{\oplus}$ to converge to the same (stochastic) behaviour at later times. The atmosphere that starts with an initial mass similar to the current value depletes slightly but is too massive for the assumed total mass of impactors to erode a significant fraction of its initial mass.

The stochastically varying atmosphere masses recorded in the numerical results can be compared to the stalling mass predicted by the analytic arguments by considering the median and mean atmosphere masses recorded over a suitably long time period. The right-hand panel in the fourth row in Fig. 4.7 shows the histogram of atmosphere masses sampled at approximately 1100 evenly spaced time intervals in the final Gyr of each simulation. A comparison of these results to the analytically predicted stalling masses is discussed in §4.4.3.

4.4.2 Other moons

The numerical atmosphere evolution results for the other four moons are shown in the left-hand column in Fig. 4.7. Unlike on Titan, a 10^{-6} $M_{\oplus}$ initial mass atmosphere cannot be maintained for the full span of the simulations on any other moon. The atmospheres rapidly forget their initial masses and show significant stochastic variation. Europa is never recorded with an atmosphere mass higher than the lower atmosphere mass limit implemented in the code after the initial atmosphere is eroded.

The distributions of sampled atmosphere masses over the final Gyr of each simulation are shown in the right-hand column of Fig. 4.7. These results show similar convergence of the atmosphere mass in the later times, however the median final atmosphere mass varies between the different moons. Triton shows the highest median final atmosphere mass after Titan, with Ganymede and Callisto showing similar, lower mass, distributions of final atmosphere masses. In all cases there is an artificial peak in the distribution at the atmosphere mass bin corresponding to the lower limit implemented in the numerical code. The time spent at this lower limit is highest for Europa (it is always completely eroded), followed by Ganymede and Callisto. Titan and Triton spend almost no time at this limit.

4.4.3 Comparison to the analytic results

The results from the code are now compared to the analytic stalling mass predictions from §4.3.1 and stochasticity predictions from §4.3.2. The complete erosion of initial atmosphere masses of 10^{-6} $M_\oplus$ on all moons except Titan is in agreement with the timescales predicted in §4.3.2. From Fig. 4.6 it can be seen that the evolution timescale for an atmosphere with this mass is greater than the entire time span considered in the simulations for Titan, but not for the other four moons. Furthermore, this timescale is longest for Titan, followed by Triton, then Callisto, Ganymede and finally Europa in agreement with the results shown in Fig. 4.7.

Considering the median (± 1 standard deviation) atmosphere masses observed in the numerical results, for Titan this is $10^{(-11.4 \pm 1.1)}$ $M_\oplus$, lower than the analytic prediction of $10^{-10.5}$ $M_\oplus$ made in §4.3.1, which is shown by the vertical line in the right-hand panel of Fig. 4.7. The mean atmosphere mass is $10^{-10.1}$ $M_\oplus$, higher than the analytic prediction. As was discussed in §4.3.2, the timescale over which the atmosphere evolves determines both the stalling mass predicted for the atmosphere and the degree of stochastic variation expected. The atmosphere is expected to evolve due to small impacts faster than the largest impactors are sampled, meaning a smaller atmosphere stalling mass is predicted in comparison to the original analytic prediction. For Titan specifically, the atmosphere was predicted to tend towards the stalling mass predicted for a largest impactor size of $10 - 20$ km, a few 10^{-12} $M_\oplus$.

Stochastic variation due to the random accretion of larger objects was also predicted and is seen in the numerical results. The upper limit to the atmosphere mass distributions seen for all moons, with the exception of Europa, is approximately 10^{-9} $M_\oplus$. In §4.3.2 this limit was predicted to be set by the mass of volatiles that could be delivered to the atmosphere mass by

a single impact, and for Titan this was calculated to be approximately a few 10^{-9} $M_{\oplus}$. The value of this upper limit is slightly lower for the other moons due to lower impactor accretion efficiency on these bodies in comparison to Titan.

The same agreement between the numerical results and the stalling masses predicted by the analytic arguments are recreated for the other four moons, including the complete atmosphere erosion on Europa. Ganymede and Callisto show similar results, with median atmosphere masses (± 1 standard deviation) of $10^{(-18\pm2)}$ $M_{\oplus}$ for both. The mean atmosphere masses for these moons are $10^{-11.3}$ $M_{\oplus}$ and $10^{-12.0}$ $M_{\oplus}$ respectively. These values lie either side of the stalling masses of $(10^{-15} - 10^{-16})$ $M_{\oplus}$ predicted by the analytic method in §4.3.1. In §4.3.2, the timescale for evolution of Ganymede's atmosphere was used to argue for a lower predicted stalling mass (set by accretion of $2 - 5$ km objects) of $\sim 10^{-17} M_{\oplus}$, which agrees with the observed numerical results. Finally for Triton, the results give a final median atmosphere mass of $10^{(-13.3\pm1.8)}$ $M_{\oplus}$, again lower compared to the analytic prediction of $10^{-11.6}$ $M_{\oplus}$ from §4.3.1. This is however in good agreement with the lower stalling mass prediction of approximately a few 10^{-14} $M_{\oplus}$ made using the timescale arguments outlined in §4.3.2.

These comparisons support the use of the analytic stalling mass prediction, however there is a large degree of stochastic variation that is not captured by the analytic value. The median atmosphere mass recorded in the numerical results is determined by the accretion of small objects that arrive frequently, and determine the quiescent atmosphere level. The mean atmosphere mass is heavily influenced by the stochastic arrival of larger objects that perturb the atmosphere mass to higher values, after which it returns to the quiescent level on a timescale determined by the assumed impact flux. The stochastic nature of the results presented in this chapter mean that a large degree of variation between the different moons is dependent on the time since the last such large impact occurred. Therefore it is possible that the random arrival (or non-arrival) of a particularly significant impact has left an observable imprint on the atmosphere masses and compositions of the outer satellites today. The true nature of impacts onto the outer moons is unlikely to be perfectly represented by the nominal population I consider here, and so in §4.5 the effect on the atmosphere stalling mass prediction of variation in the impactor composition, size and velocity distributions is quantified. This allows consideration of how robust my predicted results are to this kind of potential variation.

4.5 Sensitivity to impactor properties

The analytic prediction from §4.3 can now be applied with the knowledge that it is capable of recreating the long-term trends in atmosphere mass (with the caveats discussed in §4.3.2) to investigate the sensitivity of the stalling mass to the assumed impactor properties. As in the previous section, these results neglect impact-triggered outgassing. Unless otherwise specified, the nominal impactor population described in §4.2 is used in the following. As shown in §4.3.2, the largest impactor size assumed in the calculation plays a significant role in determining the atmosphere stalling mass and so the maximum impactor size is again calculated through setting the sampling timescale in equation 4.8 to the age of the Solar system, 4.5 Gyr.

4.5.1 Density

The previous nominal results have been shown for a variety of impactor densities, but the dependence of the predicted atmosphere stalling mass on this parameter has not yet been discussed. Typically, an increase in the assumed impactor density results in a higher predicted stalling mass. This increase is sharpest at whichever density corresponds to the lowest predicted stalling mass, and in some cases there exists a critical density below which runaway atmospheric depletion is predicted. This critical density is highest for Europa, where impactors would need to have extremely high densities (for a comet) for any amount of atmospheric growth to occur. The other four moons do have stable predicted stalling masses for comet-like densities. For densities between $0.75 - 1.25$ g cm^{-3} the predicted stalling mass can vary by a few orders of magnitude, and so is not negligible given the uncertainty in this value. Slight variations in the density of impactors onto the different moons as a result of the stochastic nature of impacts could contribute to the variation in their observed atmosphere masses, but is not sufficient to explain the difference between Titan and the other moons.

4.5.2 Composition

The nominal results considered only one impactor volatile fraction ($x_{\mathrm{v}} = 10\%$), and so I investigate the effect of different values. The atmosphere mass delivered by an impactor is linearly dependent on the volatile fraction, and thus f_{v} and the predicted stalling mass are affected by variation in this parameter. Increasing the volatile content of the impactor population has no effect on the shape of $f_{\mathrm{v}}(m_{\mathrm{atm}})$ shown for the nominal case in Fig. 4.3b, but shifts the entire curve upwards increasing the atmosphere mass at which the curve crosses

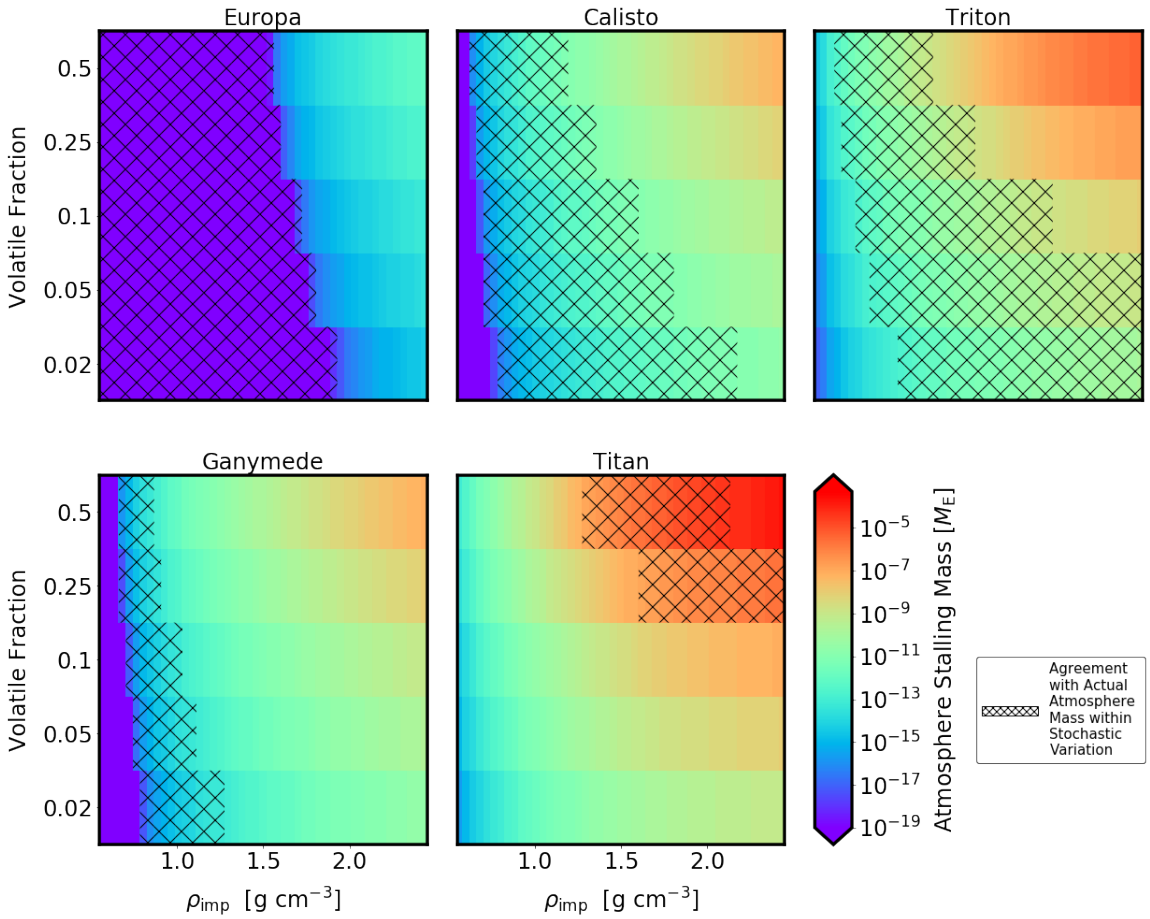

Figure 4.8: The stalling mass (atmosphere mass at which $f_v = 1$) calculated for the nominal impactor population, as a function of impactor density and impactor volatile fraction for each of the five outer moons. Note that the y axis scale is not linear, and shows results for five values of x_v only. The diagonal hatching shows the region of parameter space in which the predicted stalling mass, plus or minus an amount representative of the stochastic variation observed in the numerical results (calculated as described in the text) for each moon, is in in agreement with the estimated atmosphere masses from Table 4.1.

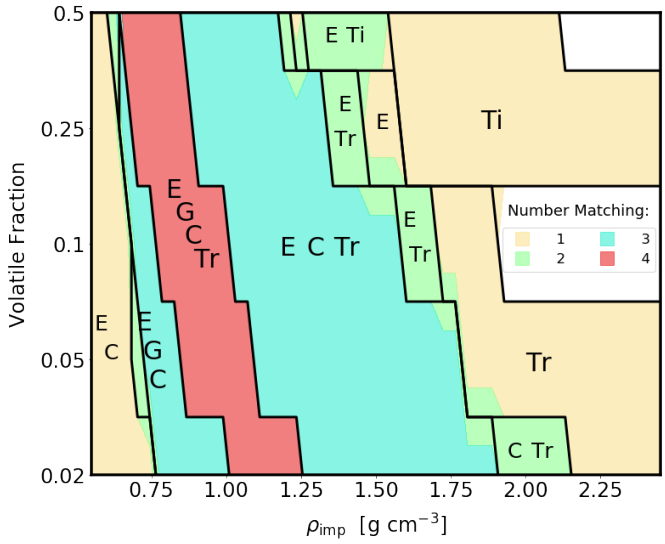

Figure 4.9: An illustration of number of moons for which the predicted atmosphere stalling mass is in agreement with the estimated atmosphere masses, within representative stochastic variation, as a function of impactor density and impactor volatile fraction, calculated from the results of Fig. 4.8. The specific moons for which the atmosphere mass is matched are indicated by text annotations on the plot as E (Europa), C (Callisto), G (Ganymede), Ti (Titan) and Tr (Triton). The solid black lines show the boundaries in parameter space of this agreement, and the colour of the filled are illustrates the number of moons for which the atmosphere mass is matched. The region of parameter space in which four of these regions overlap, for all the moons except Titan, can be seen to include the nominal impactor composition for cometary impactors.

one, leading to a higher predicted stalling mass.

The predicted atmosphere stalling masses for a range of potential impactor densities and volatile fractions are shown in Fig. 4.8. Increasing the impactor volatile fraction increases the stalling mass predicted for a given impactor density, but more weakly than changes in the density. The range of atmosphere masses that might be expected for a single impactor population as a result of the inherently stochastic atmosphere behaviour can be considered. Based on the numerical results shown in Fig. 4.7 I calculate the range of $\log_{10}(m_{\mathrm{atm}})$ covering 75% of the recorded atmosphere masses for each moon (i.e. the 12.5-th and 87.5-th percentiles of the distributions). This is used to indicate in Fig. 4.8 the range of parameter space in which the predicted stalling mass (plus and minus these intervals) are in agreement with the observed atmosphere mass estimates from Table 4.1.

While no impactor population simultaneously matches all moons, there is a region of parameter space that agrees within these 75% intervals for four moons with the exception of Titan. In Fig. 4.9 the boundaries of the hatched regions of parameter space for all five moons are shown, and the number of moons for which there is agreement between the predicted atmosphere stalling mass and the observed atmosphere mass estimates within the stochastic

limits is shown as a function of impactor density and volatile fraction. The red region in which there is agreement between the greatest number of moons (all except Titan) includes impactors with the nominal density of 1 g cm^{-3} and nominal volatile content of 10%. Given that the impactor population is expected to have the same composition for all outer moons this agreement indicates a composition within this constrained range, with stochastic variation in the current atmosphere mass introduced by differences among the moons in the time since the most recent large impact. None of these impactor compositions can recreate the observed atmosphere mass on Titan, which requires a significant increase in the assumed impactor density for even the most volatile-rich impactors, however as discussed in §4.6 this is not necessarily expected without including impact-triggered outgassing.

4.5.3 Size distribution

The size distribution for the nominal impactor population assumes a piece-wise power-law distribution based on that of the objects in the trans-Netpunian disk (Morbidelli et al., 2020). The effect of variation in this distribution can be investigated by adopting an alternative size distribution from (Nesvorný et al., 2018), keeping all other parameters the same as the nominal impactor population from §4.2.

The calculated predictions for $f_{\rm v}$ as a function of atmosphere masses are shown in the top panel of Fig. 4.10, suggesting that the two size distributions produce similar results at higher atmospheres masses, above approximately 10^{-12} M$_\oplus$. At smaller atmosphere masses the Nesvorný et al. (2018) distribution, which contains relatively more of the smallest <km-sized impactors, results in lower values of $f_{\rm v}$ for a given atmosphere mass. The impactor size below which comet-like impactors begin to deliver volatiles rather than erode the atmosphere decreases as the atmosphere mass decreases. For a small atmosphere mass, even km-sized impactors are generally erosive, and thus their relatively larger numbers in the Nesvorný et al. (2018) size distribution result in lower values of $f_{\rm v}$.

The corresponding predicted stalling masses are illustrated in the bottom panel of Fig. 4.10 as a function of impactor density, showing that despite the change in $f_{\rm v}$ at small atmosphere masses, there is very little difference in the predicted stalling masses between the two distributions. This implies that my results are robust to small changes in the slope of the size distribution assumed for the impactors, particularly in comparison to the dependence of the predicted atmosphere mass on the size of the largest impactor.

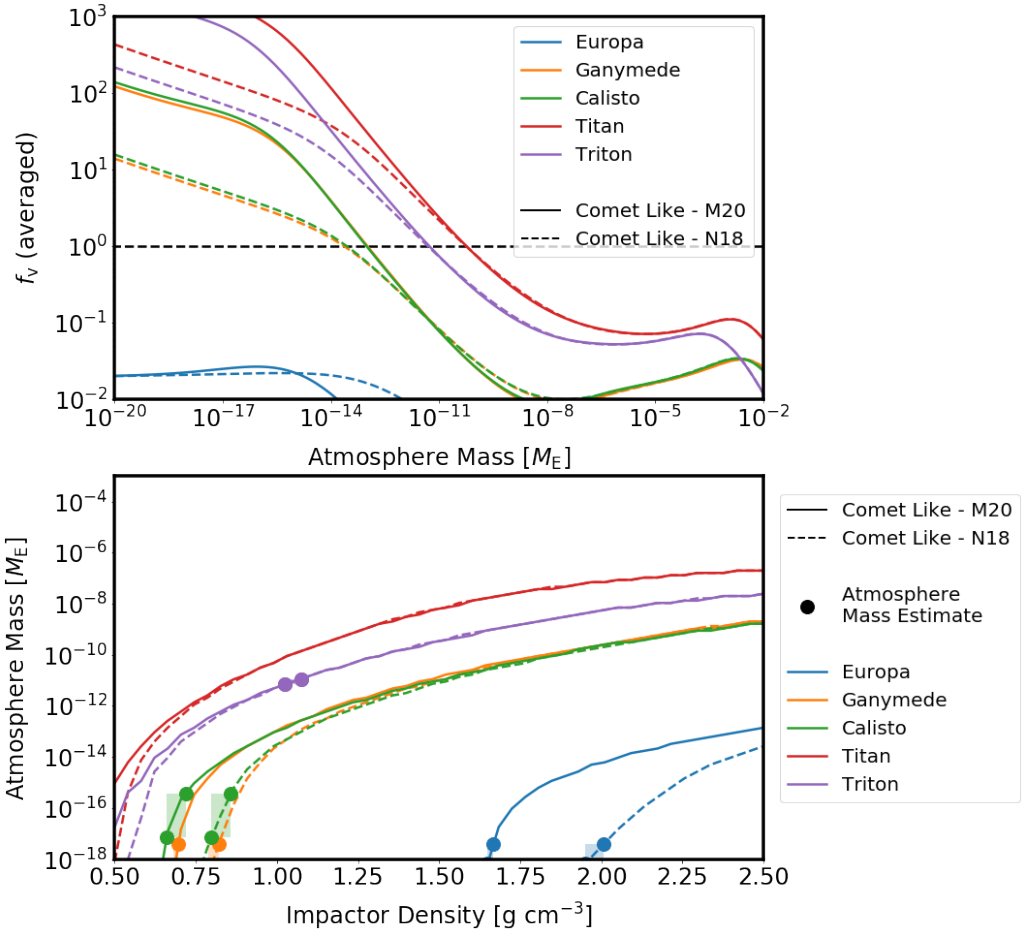

Figure 4.10: The top panel illustrates a comparison of the behaviour of f_v as a function of atmosphere mass varying the size distribution of the impacting population. The corresponding stalling mass estimates calculated are shown in the bottom panel as a function of impactor density. Each outer satellite is shown by a line of a different colour, while the line style illustrates the size distribution. The region of parameter space in which the predicted stalling mass matches the estimated atmosphere masses for each outer moon from Table 4.1 are shown by a rectangular shaded area and circular markers.

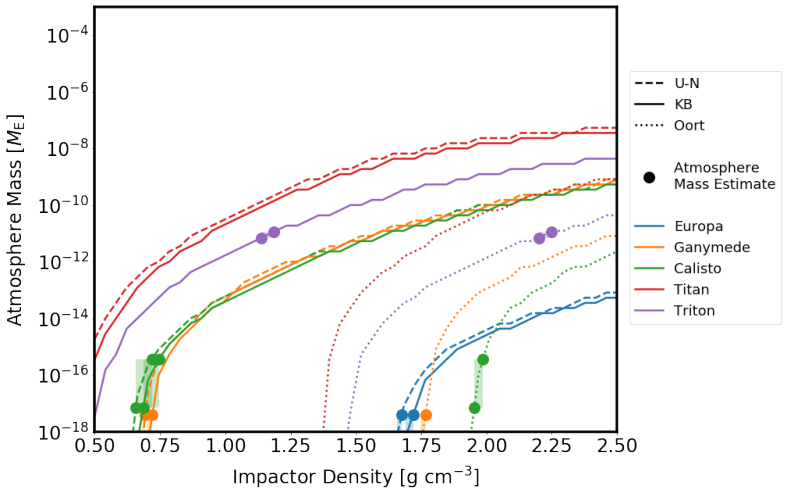

Figure 4.11: The stalling mass calculated for each of the five moons as a function of impactor density. The different source regions for the impactor populations (and thus the velocity distributions) used to calculate the weighted average of f_v are illustrated by different line styles.

4.5.4 Velocity distribution

Calculation of the stalling mass requires averaging the values of f_v over a distribution of impactor velocities. In the nominal case I have adopted a velocity distribution based on impacts from KBOs following the method of Zahnle et al. (1992), however this is not the only potential source region for impacts onto the outer satellites.

Three different populations of impactors onto the outer satellites can be considered: the UNPs, KBOs, and OCOs as discussed in §4.2.2. The predicted stalling masses predicted are shown as a function of impactor density in Fig. 4.11. As a result of their typically higher impact velocities, the OCOs result in substantially lower stalling masses for a given impactor density and outer satellite compared to the KBOs and UNPs (which are similar). Triton has no stalling mass for the UNPs, because the calculation of the impact velocity distributions fails when the satellite is located exterior to the impactor semi-major axis (the term inside the square root in equation 4.7 is negative).

The predicted stalling masses are relatively insensitive to small changes in the assumed impactor velocity distributions. However if the impacts were substantially faster than predicted for the KBOs or UNPs then the stalling mass predictions could be several orders of magnitude lower. Slower impactors typically result in higher atmosphere stalling masses, since impactor accretion is higher and atmospheric erosion is lower. The effect of a potentially slower distribution, that of planetocentric rather than heliocentric impactors, is discussed in §4.7.

4.5.5 Atmospheric temperature assumptions

The results shown in §4.3 were calculated assuming that the atmosphere temperature on the outer satellites can be calculated assuming radiative equilibrium at the distance of the host planet's orbit, $T = 278 L_* a_{\rm tar}^{-0.5}$. In reality, the surface temperature of the satellite is influenced a number of processes, including tidal heating, incident radiation and shading by the planet. As the values in Table 4.1 show, my estimated temperatures do not agree with the observed values from the literature. I investigate the sensitivity of my results to the assumptions made about the atmosphere temperature, by recalculating the atmosphere stalling masses using the observed temperatures. The predicted stalling masses are relatively insensitive to the atmosphere temperature, changing at most by a factor of two over the range of impactor densities. Since the dependence of the erosional efficiency on atmosphere temperature enters the prediction of the stalling solely in the calculation of the atmospheric scale height, it can also be concluded that the atmosphere MMW (a parameter that is also present only in the calculation of the scale height) is also relatively unimportant.

4.6 Impact-triggered outgassing results

While my results thus far are successful at reproducing the observed atmosphere masses of the Jovian moons and Triton, the observed atmosphere mass on Titan is significantly higher than my predictions. Titan is not only unique among the moons in the outer Solar system for having a massive atmosphere, but also potentially for the volatile-rich composition of its outer layers (Zahnle, 2010). As discussed in §2.1.5, a reservoir of volatile species (e.g. in clathrates) trapped in the surface of a body can be released by impact-triggered outgassing. This effect is considered separately from the nominal results due to the large uncertainties in many of the relevant parameters. For completeness, I consider the results for all five moons, although the assumptions made regarding the volatile content of the moons available for outgassing is likely a significant overestimate for all but Titan.

4.6.1 Analytic predictions

Using the prescription for the mass of outgassed volatiles from §2.1.5, I calculate the ratio of atmosphere mass gain to mass loss using equation 2.34. This can be compared to the previous value of $f_{\rm v}$ to understand the influence of impact-triggered outgassing.

This is illustrated in the top panel of Fig. 4.12, which shows three versions of $f_{\rm v}$ as a function of atmosphere mass for Titan only, as the same qualitative behaviour is observed for all the

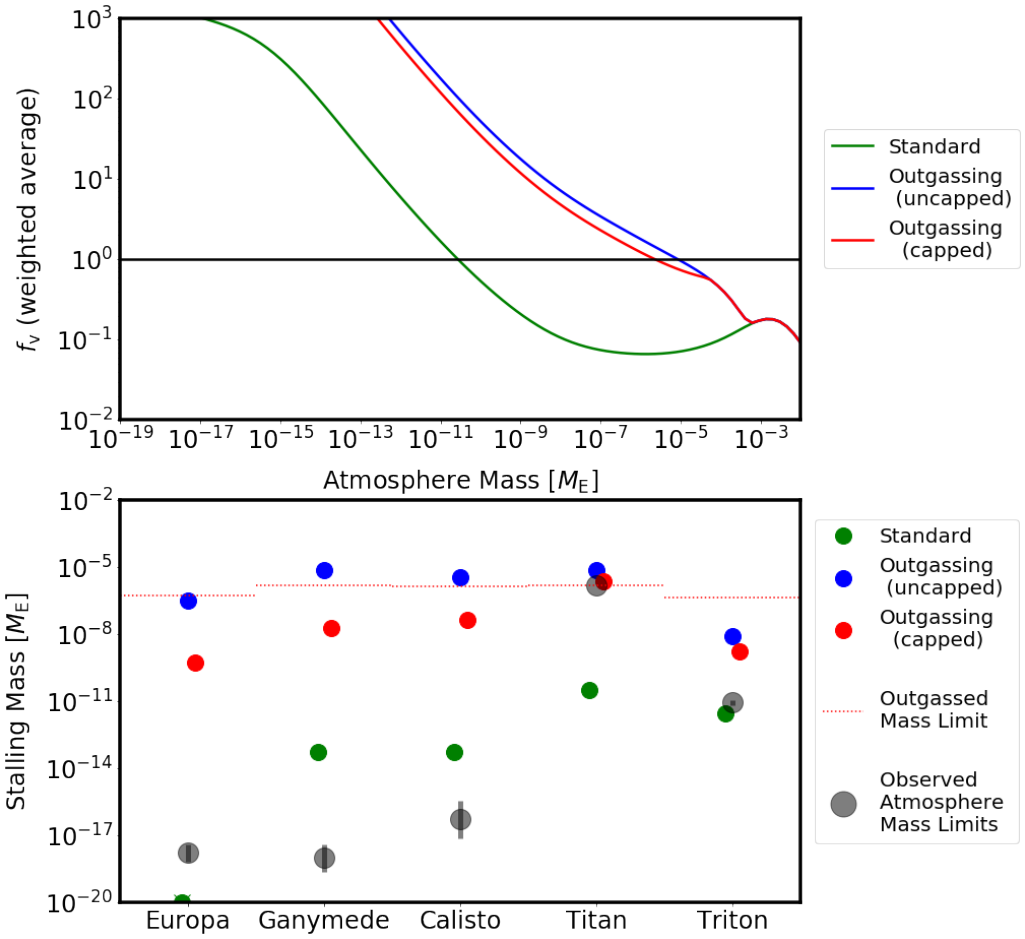

Figure 4.12: The ratio of atmosphere mass gain to mass loss as a function of atmosphere mass is shown in the top panel for Titan. The solid green line shows the previous calculation of f_v, which did not include any impact-triggered outgassing. The dotted blue line illustrates the values calculated including impact-triggered outgassing, and the dashed red line shows the same including both the volatile content crust limit and the single impact outgassing limit. The predicted atmosphere stalling masses (where $f_v = 1$) calculated for each of the outer moons are shown in the bottom panel. The marker colour represents which f_v curve was used to calculate the stalling mass (green for no outgassing, blue for uncapped outgassing and red for outgassing calculated including both the single and total limits described in the text). The volatile content crust limit calculated for each moon is shown as a dotted red line. The observed atmosphere mass limits for each of the outer moons are shown by large black markers and their associated error bars.

moons. The behaviour of f_v when neglecting impact-triggered outgassing can be compared to the behaviour including impact-triggered outgassing with no overall limit on the total mass of outgassed volatiles. This value is not necessarily physical, as it can predict more volatiles released than are estimated to be present in the crust. Therefore a third version is also plotted which caps the total contribution to the outgassed volatile mass at the estimated volatile content of the crust described in §2.1.5.

From this plot it can be seen that at very high atmosphere masses, impact-triggered outgassing has no effect on the atmosphere behaviour, because all impactors are slowed sufficiently whilst passing through the atmosphere to cause no outgassing. However at lower atmosphere masses the additional volatile contribution due to impact-triggered outgassing results in a higher value of f_v for a given atmosphere mass.

The predicted atmosphere stalling masses for these three cases are shown in the bottom panel of Fig. 4.12. This shows that the stalling mass is highest for the uncapped outgassing prediction and lowest when no impact-triggered outgassing is included, with orders of magnitude variation between the three cases. The capped prediction is in good agreement with the current atmosphere mass on Titan, however significantly over-predicts the atmosphere masses for the other four moons.

The methane component of Titan's atmosphere is estimated to have a total mass of 2.8×10^{20} g $\approx 5 \times 10^{-8}$ $M_\oplus$ (Lunine & Stevenson, 1987; Choukroun et al., 2010) and should rapidly undergo photolysis and be irreversibly lost from the atmosphere on a timescale of $10 - 100$ Myr (Yung et al., 1984; Toublanc et al., 1995; Lunine & Atreya, 2008). There must therefore be a continuing source of methane (Owen, 2004). Exogenous delivery by cometary impacts is unlikely due to the lack of simultaneous detection of CO in the atmosphere (which should be delivered by comets) (Choukroun et al., 2010). Episodic outgassing from clathrate hydrates in the crust has been proposed as a potential explanation for this phenomenon (Tobie et al., 2006; Stofan et al., 2007). Below I discuss two ways that impact-triggered outgassing could contribute the $\sim 5 \times 10^{-8}$ $M_\oplus$ budget of CH_4 to Titan's atmosphere within the last $10 - 100$ Myr.

Firstly, the continued accretion of small objects over the last $10 - 100$ Myr could cumulatively result in outgassing of the observed methane. The *current* impact rate onto Titan is approximately 1.4×10^{-11} $M_\oplus$/Myr, which over $10 - 100$ Myr results in the accretion of an approximate impactor mass of $(1.4 - 14) \times 10^{-10}$ $M_\oplus$, corresponding to objects up to roughly

10 km in size as discussed in §4.3.2. Assuming the nominal velocity distribution and accounting for atmospheric drag assuming the current atmosphere mass on Titan, equations 2.14 to 2.16 imply that these objects have an outgassing efficiency of ~ 0.01, meaning that at most $\sim 10^{-9}$ $M_\oplus$ CH_4 is able to be outgassed over this time period. This is lower than the estimated methane budget in Titan's atmosphere, and so continued outgassing from Titan's surface as a result of the current level of bombardment is unlikely to fully replenish the atmospheric methane.

Alternatively, a single stochastic impact could cause the catastrophic outgassing of this mass of CH_4 in a single event. Based on my prescription for impact-triggered outgassing, a single impact onto Titan could release this mass of methane (assuming a surface volatile fraction of $x_{\mathrm{v,targ}} = 1\%$ and that the outgassed material is 50% CH_4) if it had a mass of $\sim 3 \times 10^{-7}$ $M_\oplus$, corresponding to a comet-like impactor size of 158 km. This impactor size is larger than the largest size expected to be sampled at the *current* impact rate as discussed in in §4.3.2, however the stochastic sampling of larger objects is to be expected, and so it is not impossible that a recent large impact triggered the outgassing of the current budget of methane in Titan's atmosphere.

4.6.2 Numerical results

The discrepancy in time periods over which impact-triggered outgassing and impact volatile delivery contribute to the atmosphere mass can be addressed using the numerical code. To do this the contribution to the atmosphere as a result of impact-triggered outgassing as an extra contribution to the atmosphere mass gain resulting from each impactor in equation 2.26 is incorporated. The outgassing cap mass, from equation 2.17, is implemented as a limit on the outgassed mass contributed by each individual impact. The remaining volatile budget in the crust is updated after every time step to account for the removal by previous impacts, meaning that outgassing ceases to contribute once the total volatile budget has been exhausted. To improve computational speed, and since the effect of atmospheric drag on the outgassed mass is insignificant for atmosphere masses below 10^{-4} $M_\oplus$ this effect is not included in the numerical code.

The results for Titan are shown in Fig. 4.13 for ten iterations of the numerical code at each initial atmosphere mass. I do not include numerical results for the other four moons since, as discussed in §4.6.3, the assumptions about the available reservoir of volatiles available to be outgassed are likely to be applicable only to Titan.

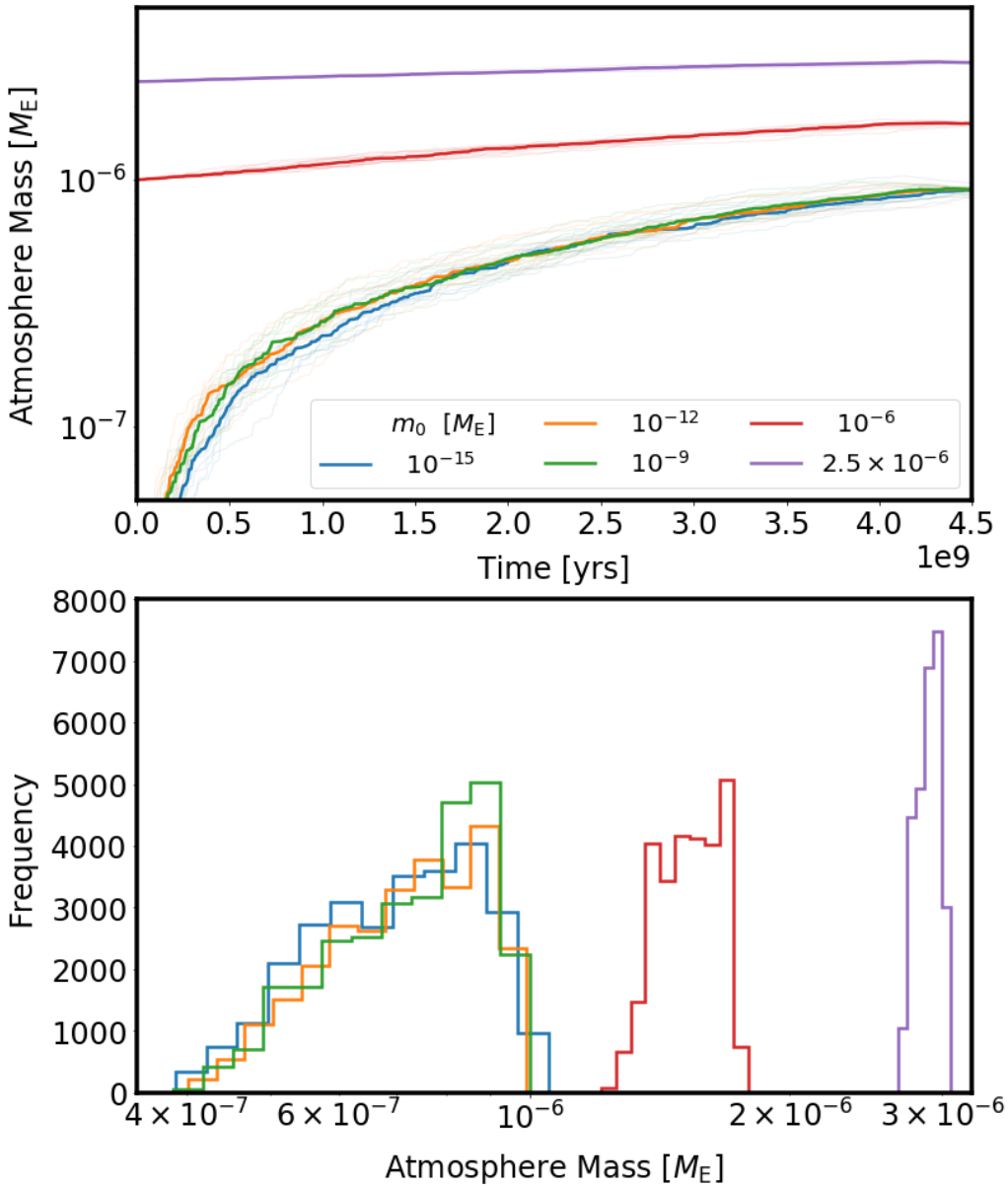

Figure 4.13: The top panel shows the atmosphere mass evolution over time calculated using the numerical code. Each initial atmosphere mass is represented by lines of a different colour, with the thin transparent lines showing individual runs and the thicker opaque line showing the median atmosphere mass values for all ten iterations at each initial mass. The bottom panel shows a histogram of the atmosphere masses in the final Gyr. This corresponds to around 1100 evenly spaced atmosphere mass values for each of the ten runs for each initial atmosphere mass. The line colour indicates the initial atmosphere mass.

The atmosphere mass profiles in Fig. 4.13 show that the atmosphere mass now grows over the simulation as the volatile budget of the crust is depleted (noting that the constant impact flux means the times shown are not the same as real time). The initial atmosphere mass is rapidly forgotten if it is less than the mass of volatiles in the crust available to be outgassed, converging at around 8×10^{-7} $\mathrm{M}_{\oplus}$ for initial atmosphere masses $m_0 \leqslant 10^{-7}$ $\mathrm{M}_{\oplus}$. An initially more massive atmosphere, $m_0 = 10^{-6}$ $\mathrm{M}_{\oplus}$ ends at 1.6×10^{-6} $\mathrm{M}_{\oplus}$, similar to the current atmosphere mass of Titan. For $m_0 = 10^{-5}$ $\mathrm{M}_{\oplus}$ the final atmosphere mass is approximately unchanged, with a mass equal to the mass of all the outgassed volatiles removed by impacts.

4.6.3 Volatile budget effects

The capped stalling mass for Titan from §4.6.1, shown in Fig. 4.12, is closer to the numerical result for $m_0 = 10^{-6}$ $\mathrm{M}_{\oplus}$ than the other initial atmosphere masses. For the other initial atmosphere masses, the final atmosphere mass is predicted to be slightly less than the mass of volatiles contained in the crust. This difference is due to all the available volatiles in the crust being released due to impacts with simultaneously acting to erode the atmosphere mass towards the impact only stalling mass of $\sim 10^{-11}$ $\mathrm{M}_{\oplus}$. As a result of this, it is important to consider how accurate the estimate for the total mass of volatiles contained in the crust is.

The assumptions of a depth of 20 km and a volatile fraction of 1% for all moons is likely too simplistic. The observed crust depths for each moon could be adopted as a plausible depth, however this is not the best approach, as volatiles deep in the crust may not be reached by the impactors that are expected to arrive at the outer moons. To conform that 20 km is reasonable, I use the equations describing the radius (R_{core}) and depth (D_{core}) of the isobaric core from Kraus et al. (2011). These suggest that the largest, $D = 100$ km, impactors can penetrate to a depth of ~ 200 km, deeper than the size of the typical crust. Subsurface oceans were discovered on Europa and Titan by Voyager I and Cassini (Carr et al., 1998; Kivelson et al., 2000; Iess et al., 2012). There is also tentative evidence for oceans on Ganymede and Callisto from the Galileo mission, something that will be studied further by the JUICE mission (Kivelson et al., 2002; Zimmer et al., 2000). This raises the question of what happens if the melt penetrates into the subsurface ocean, but consideration of this effect is left for future study. To estimate a depth to use in calculating the mass limit I consider instead the size of impactor expected to arrive in enough numbers to give good coverage of the entire surface of the moon. A few hundred impactors with size ~ 10 km are expected to arrive over the entire time period of the simulation, and penetrate to a depth of $17 - 19$ km, not dissimilar to the 20 km estimate.

For the volatile content, a range of $1 - 5\%$ is reasonable for the material that makes up Titan, based on measurements of ammonia in the plumes from Enceladus (Waite et al., 2009) and models of the Saturnian nebula from which Titan formed (Alibert & Mousis, 2007). However Titan may be unique among the moons considered in this paper in its volatile-rich composition (Zahnle, 2010). For Triton, there is evidence for N_2 ice on the surface, as well as in the atmosphere, implying that N_2 vaporised by impacts might precipitate out of the atmosphere on a relatively short timescale, making impact-triggered outgassing less significant than on the slightly warmer Titan, where the N_2 on the surface is trapped inside the ice and is therefore likely to remain in the atmosphere after release. Clathrate structures can form on the Jovian moons as well, but unlike Titan are believed to form only a very thin surface layer (Hand et al., 2006)..

4.7 Discussion

I have found that my nominal predicted stalling masses match the atmosphere masses on Triton, Callisto and Ganymede and recreate the depletion of Europa's atmosphere for a reasonable estimated impactor density. By including impact-triggered outgassing on Titan I can reproduce the observation of a thick atmosphere on this moon. I have also found that stochastic effects, both over time for the same moon and between the moons is a significant source of variation in the predicted atmosphere masses. While my results suggest that the inevitable impacts onto these moons have shaped their atmospheric evolution I have neglected several other processes that can alter the atmosphere: thermal (Jeans) escape, XUV driven escape, magnetospheric effects (atmosphere drag and ion delivery), and continuing outgassing. The magnitude of these effects will vary between the moons, due to their different masses, environments and atmospheres.

Triton: My results suggest that impacts by comets from the Kuiper Belt result in the atmosphere of Triton tending towards a median final mass comparable to the estimated current atmosphere mass. It is however possible that, unlike as I have assumed, a non-negligible fraction of the impacts onto Triton may arise from disrupted objects that have been captured by Netpune. Triton's cratering record is sparse, but has been interpreted by some to suggest a differential SFD with a slope of -4, compared to -3 on the prograde moon Miranda. This could imply that the impactors are primarily due to objects on planetocentric orbits (Strom & Croft, 1993), however more recent work suggests that the crater distributions are best produced by at most 30% planetocentric impactors (Mah & Brasser, 2019). These planetocentric impactors would have different orbits and therefore produce a different velocity distribution than I have used.

From Bell (2020), the planetocentric impact velocities

$$v_{\rm imp,pl}^2 = \frac{2GM_m}{R_m} + \frac{3(e_m^2 + e^2)GM_{pl}}{5a_m}, \tag{4.10}$$

are suggested to be slower than the heliocentric impact velocities

$$v_{\rm imp,hel}^2 = v_{\rm imp,pl}^2 + \frac{3GM_{pl}}{a_m}\left(1 - \frac{e^2}{5}\right) + \frac{3(e_{pl}^2 + e^2)GM_\odot}{5a_{pl}}. \tag{4.11}$$

Given the tendency for slower impacts to be less erosive, if there were a fraction of impacts resulting from planetocentric bodies then they may result in larger stalling mass estimates. As observed in §4.5.4, my results for the predicted analytic stalling mass depend more strongly on the assumed impactor density than the source region. However, there remains a possibility that substantially slower impacts arising from debris on planetocentric orbits may have affected one or more moons.

A higher stalling mass for Triton than is predicted with the heliocentric impactor populations would be above the observed atmosphere mass limits adopted. My results could therefore suggest that planetocentric impactors do not dominate the impactor population at Triton, with the caveat that other atmosphere loss processes could be acting to reduce the atmosphere mass.

Another potential discrepancy is the fact that the atmospheric pressure on Triton appears to be increasing over the period of time for which there are observations (Tyler et al., 1989; Lellouch et al., 2010). This has been explained as the result of increasing vapour pressure for N_2 as the atmosphere temperature increases (Grundy & Stansberry, 2000), either as a result of changing heat flux from the Sun or internal sources, or altered surface properties (Cruikshank, 2005). This approximate doubling in surface pressure, and thus atmosphere mass, is still within the range of atmosphere masses seen in my numerical results. The general agreement of my predicted stalling mass with the observed atmosphere mass on Triton supports the hypothesis that impacts shaped its early atmospheric evolution.

Titan: The planetocentric impactor argument was used in Farinella et al. (1997) to propose a potential origin for Titan's thick atmosphere, using material accreted after the disruption of a hypothetical "proto-Hyperion". These impacts were assumed to be significantly slower (< 4 km s^{-1}) and thus material was accreted efficiently, growing a thick atmosphere. However, there are other explanations proposed for the origin and evolution of Titan's

atmosphere, a topic which has long been debated (Niemann et al., 2010). The atmospheric D-H ratio, as well as the excess CH_4 compared to CO, both disfavour cometary material as the direct source of Titan's atmosphere (Coustenis, 2005), but do not exclude the possibility that impacts could trigger outgassing of volatiles contained within Titan. While slower planetocentric impactors would be more efficient at directly delivering volatiles they would be less efficient at triggering outgassing from the surface.

The most probable source of atmospheric N_2 is either ammonia which can later be decomposed through photolysis (Atreya et al., 1978) or impact-mediated chemistry (Sekine et al., 2011), or N_2 directly outgassed through thermal decomposition of chondritic insoluble organic material in the interior (Miller et al., 2019). The enrichment of ^{15}N relative to ^{14}N in the atmosphere compared to the terrestrial atmosphere cannot be achieved by conversion of NH_3 to N_2 alone. If the original source of N_2 in both Titan and Earth is the same, then this discrepancy (as well as other heavy isotope anomalies) might imply significant loss of N_2 from Titan's atmosphere early in its history, when the Solar XUV flux was higher, (Penz et al., 2005; Waite et al., 2005; Coustenis, 2005; Lammer et al., 2008). This is not necessarily in disagreement with my conclusions. As discussed in §4.6.3, the mass of volatiles that can be outgassed into the atmosphere is sensitive to the upper limit assumed for volatiles in the crust. A higher value for this limit could result in a much more massive early atmosphere that could then be lost through hydrodynamic escape as suggested in Lammer et al. (2008).

Ganymede: I have neglected magnetic effects in my model, which are likely to be important in particular on Ganymede, the only moon that possesses a permanent intrinsic magnetic dipole, as well as an induced dipole arising from Jupiter's magnetosphere (Kivelson et al., 2002). While this is dominated by Jupiter's own magnetic field the intrinsic field is believed to be the source of the asymmetric molecular oxygen air glow (caused by electron dissociation of O_2 on the surface) observed by HST (Hall et al., 1998).

Magnetospheric effects have been proposed as both a source of atmosphere material and as a loss mechanism. The magnetosphere on Ganymede is too weak to protect the surface from energetic particles in the Jovian magnetic field, resulting in release of oxygen ions from the surface by plasma sputtering (Carnielli et al., 2020). Ion pickup can accelerate atmospheric material to above the escape velocity, resulting in atmospheric loss (Luhmann & Kozyra, 1991; Lundin et al., 2007). The intrinsic and extrinsic magnetic fields undergo complex interactions, and the interactions between them and the atmosphere are not trivial, meaning it is challenging to predict what effect their inclusion may have on my stalling mass predictions. However my prediction for the atmosphere mass is likely relevant for the early atmosphere of

Ganymede, when impact rates were high and the effect of impacts would be expected to dominate. Since that time, impacts continue to erode the atmosphere and deliver material, a contribution that should be factored into a model that considers the evolution of the atmosphere due to magnetospheric effects.

Callisto: The CO_2 component of Callisto's current atmosphere was previously believed to be so tenuous that it should be lost almost immediately as a result of photoionisation and magnetic effects and so must be being constantly replenished, potentially by sublimation of CO_2 ice from the surface (Carlson, 1999). However the much more massive O_2 component inferred from the ionosphere is not expected to be lost on such a short timescale. These effects are not easily parameterised and so not included in my model, but an extra sink term acting to remove atmosphere mass could shift the predicted atmosphere mass from my predicted value downwards. Since CO_2 is an expected product when the CO present in comets is shocked in the presence of H_2O during an impact (Ishimaru et al., 2011), the potential role of comet impacts in supplying CO_2 ice to Callisto's surface is worth future study. I find that impacts by the nominal comet population can deliver a mass of $10^{17} - 10^{18}$ kg in solid material to the surface of Callisto (and a similar mass to the other moons) which is likely to contain a substantial mass of CO and CO_2, alongside water-ice and other material. Spectra of the surface of Callisto show similar signatures to interstellar ice grains, hinting at the possibility that these grains have been delivered by cometary material (Johnson, 2014).

Europa: The origin of Europa's atmosphere is believed to be radiative dissociation of water molecules on the surface into oxygen and hydrogen, which are then adsorbed and sputtered into the atmosphere. The hydrogen escapes rapidly, and any water is rapidly frozen back onto the surface, leaving oxygen to make up the bulk of the tenuous atmosphere (Ip et al., 1998; Lucchetti et al., 2016; Li et al., 2020). Escaped gas molecules form a torus of H_2 and O distributed around Europa's orbit which has been detected by Cassini and Galileo (Smyth & Marconi, 2006). I have demonstrated that impacts are not capable of growing a substantial atmosphere on Europa, however the potential for comets to deliver some portion of the water that subsequently dissociated to form the surface of the moon has not been explored. The estimated non-volatile mass delivered by comets in my model will contain water-ice, which may contribute to this atmosphere source reservoir.

4.8 Conclusions

In this Chapter I have investigated the effect of impacts on the atmospheres of Ganymede, Callisto, Europa, Triton and Titan. Using my numerical code I modelled the evolution of these atmospheres under bombardment by a impactor population similar to comets from the Kuiper Belt. For this nominal population I constructed size and velocity distributions from which impactors were sampled.

The code was used to predict the atmospheric evolution for a range of initial atmosphere masses. I found that the predicted atmosphere masses vary by orders of magnitude within single iterations due to the inherently stochastic nature of impacts onto the outer moons. I also applied the analytic approximation for the "stalling mass" described in §2.3.1 to show that over sufficiently long timescales, the median atmosphere mass from the numerical code is successfully predicted by the analytic method. This analytic stalling mass for the nominal impactor population is moderately successful at predicting the observed atmosphere masses of Ganymede, Callisto, Europa and Triton, however significantly underestimates the atmosphere mass of Titan.

The impactor volatile content can alter the predicted stalling mass by a factor of ~ 100 over the range $x_{\rm v} = 2 - 50\%$. The impactor density can have a significantly larger effect on the stalling mass, increasing it by several orders of magnitude between $\rho_{\rm imp} = 0.5 - 2.0$ g cm^{-3}. The slope of the size distribution has a relatively small effect on the predicted stalling mass, however the size of the largest impactor used in the calculation, determined by the timescale over which impactors are sampled from the parent population and thus over which the atmosphere evolves, is significant. On longer timescales, the largest sampled impactor size increases and this acts to increase the predicted atmosphere stalling mass. This dependence is stronger on short timescales as the nominal size distribution contains relatively few of the larger impactors. Finally, the stalling mass is reduced if the impactors originate in the Oort cloud, since this results in significantly faster (more erosive) impactors. Slower planetocentric impactors resulting from disrupted objects captured by the host planet would result in higher atmosphere stalling masses.

When including the effect of impact-triggered outgassing in both a modified version of the analytic prediction and the code I predict an atmosphere stalling mass for Titan comparable to its current value. This level of outgassing requires the existence of a volatile-rich crust (potentially not true for the Jovian moons), and that volatiles in this crust are able to remain in the atmosphere after outgassing (potentially not true for Triton). Therefore these results are

applicable only to Titan.

More detailed observations of the atmospheres of the Jovian moons by JUICE and Titan's atmospheric composition by Dragonfly will help to constrain the potential sources and evolutionary processes of the atmospheres on these outer moons (Wurz et al., 2014), helping to further constrain the properties of the impacting populations and the initial atmosphere masses.

The key results to take from this chapter are:

- Impacts are very erosive of atmospheres on the moons of Jupiter but less damaging to Triton and Titan;
- Significant stochastic variation in the atmosphere mass occurs when the atmosphere evolves due to small impactors fast than larger impactors are sampled;
- Plausible ranges of impactor properties can introduce significant variation in the predicted atmosphere stalling masses.

5

Evolution of the atmospheres of Venus and Mars due to bombardment

Venus and Mars both possess CO_2 atmospheres, yet why Venus has a massive atmosphere while Mars a thin one is not definitatively answered. The bombardment history of Venus is poorly constrained by observations, however for Mars the HSE abundances and crater counts provide a method by which to reconstruct the impact chronology. These observations suggest that (like the Earth) a population of left-over planetesimals dominated the impacting mass, with smaller contributions from asteroids and comets. These impacts will have influenced the atmosphere evolution, and in this chapter the numerical code described in §2.2 is used to investigate the effect of impacts on potential past atmospheres on Venus and Mars. This combines the Shuvalov (2009) cratering impact prescription described in §2.1.1, the Schlichting et al. (2015) giant impact prescription described in §2.1.2 and the Shuvalov et al. (2014) aerial burst and impactor fragmentation prescription described in §2.1.6.

In §5.1.1 I calculate impact velocity distributions from the results of numerical simulations for the impacting populations (asteroids, comets and left-over planetesimals) and describe the choices made regarding their properties. The initial planet conditions investigated are described in §5.1.2. The results for impacts by asteroids and comets are presented in §5.3.1 and §5.3.2. The nominal, mid-temperature atmosphere case results for the left-over

planetesimal population are discussed in detail before I consider the influence of the impactor dynamics and initial atmosphere state in §5.3.3. In §5.4 I discuss my results compared to other studies and the results for the Earth from Chapter 3 and I present my conclusions in §5.5.

5.1 Impactor and planet properties

5.1.1 Impactor properties

To investigate the evolution of atmospheres on Venus and Mars, it is necessary to constrain the properties of the impactor populations. In this Chapter I consider the same three populations of impactors as used for the study of the Earth in Chapter 3: left-over planetesimals, comets and asteroids. In the following the choices made regarding these parameters are described.

Composition

The composition of the impactors is defined in the code by a bulk density, volatile fraction and MMW. I adopt the same nominal impactor composition for each population as applied to the Earth, described in §3.1.4. These parameters are detailed in table 3.1, in summary comets are low-density and volatile-rich ($\rho_{\rm imp} = 0.9$ g cm^{-3}, $x_{\rm v} = 0.2$, $\mu_{\rm imp} = 38$), C-type asteroids (carbonaceous chondrite-like) are rocky and volatile-rich ($\rho_{\rm imp} = 2.0$ g cm^{-3}, $x_{\rm v} = 0.105$, $\mu_{\rm imp} = 39$) S-type asteroids (ordinary chondrite-like) are denser and less volatile-rich ($\rho_{\rm imp} = 3.4$ g cm^{-3}, $x_{\rm v} = 0.0046$, $\mu_{\rm imp} = 13$) and left-over planetesimals (enstatite chondrite-like) are the densest and most volatile-poor impactors ($\rho_{\rm imp} = 3.5$ g cm^{-3}, $x_{\rm v} = 0.00035$, $\mu_{\rm imp} = 15$).

In §3.2.1 I demonstrated that the method by which the asteroid sub-populations are distinguished based on their initial semi-major axes in the dynamical simulations has no effect on the resulting atmosphere behaviour. Therefore in the following only the simplified extrapolation of the DeMeo (2014) taxonomic distribution is considered, within which different proportions of S- and C-type material are assumed to populate three zones in the original asteroid belt, with $\sim 11.7\%$ of the total mass in S-type asteroids.

The alternative "wet" and "dry" impactor compositions are not considered here, as test simulations find they result in similar atmosphere evolution to the nominal composition. The adopted volatile fraction values $(x_{\rm v})$ do not include water (as it is liquid on the Earth's surface) which is inconsistent with some of the assumed atmosphere temperatures in this

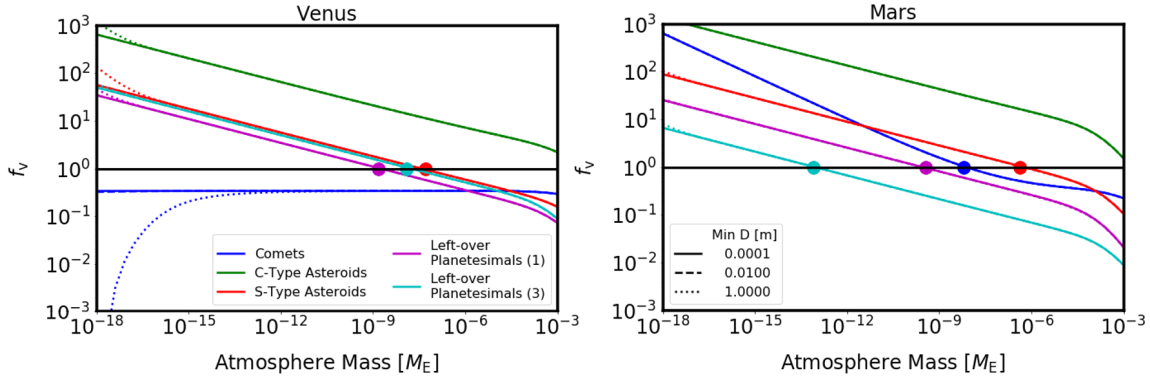

Figure 5.1: The behaviour of f_v as a function of atmosphere mass for the four impactor populations (shown by different line colours) onto Venus and Mars. The lower size limit used in the calculation is shown by the line style, although this is not noticeable as the lines are on top of each other.

chapter. Including a contribution to the outgassed material from water vapour would change not only x_v but also the volatile MMW, potentially altering the conclusions made. This is discussed in §5.4.6.

Size distribution

The size distribution of the asteroids and left-over planetesimals is assumed to follow the main belt asteroid distribution from Bottke et al. (2005). For the comets, I use a size distribution representing the primordial trans-Neptunian disk from Morbidelli et al. (2020). These size frequency distributions can be seen in Fig. 3.3 (for the left-over planetesimals and asteroids) and Fig. 4.2a (for the comets). While most of the mass in the asteroid and left-over planetesimal distributions is delivered by the largest objects the majority of the mass in the comet population is contained in ~ 100 km objects. There are a slightly larger number of the smallest ($D < 100$ m) objects in the updated comet size distribution compared to the Nesvorný et al. (2018) distribution used for the Earth, however these small objects have a negligible influence on the total population mass or the atmosphere behaviour. Therefore this change should not make comparison of the results in this chapter to those for the Earth challenging.

The upper and lower size limits ($D_{min} = 1$ m and $D_{max} = 1000$ km) are also kept unchanged from Chapter 3. This upper limit is set by the size of the largest object in the asteroid belt, but the lower size limit is not physically motivated as the distribution is expected to continue to arbitrarily small sizes. This lower limit becomes important to the predicted atmosphere behaviour at low atmosphere masses. In order to ensure that the choice of 1 m is appropriate for low atmosphere masses, I consider the behaviour of the analytic prediction for $f_v(m)$ for

the four impactor populations using three different values for the lower size limit ($D_{\min} = 1$ m, 0.01 m and 0.1 mm) the results of which are shown in Fig. 5.1. The lower size limit has a noticeable effect on the absolute value of $f_{\rm v}$ only at atmosphere masses below $\sim 10^{-17}$ $\rm M_{\oplus}$ for the asteroids and left-over planetesimals and below $\sim 10^{-13}$ $\rm M_{\oplus}$ for the comets. These are lower than the atmosphere stalling masses expected for these populations, and so to avoid the computational costs of including large numbers of small impactors the lower limit of 1 m is kept.

Velocity distribution and impact fluxes

The number of impactors at each velocity (150 bins log-spaced between $v_{\rm imp} = (1 - 12.5)v_{\rm esc}$ as described in §2.5.3) at each time for Venus and Mars are calculated from the results of N-body dynamical simulations, based on the Nice model and Grand Tack framework described in §1.2. These simulations are described in detail in §3.1.1, but in summary the asteroid data comes from CASE1B in Nesvorný et al. (2017a), the comet data from CASE2 in Nesvorný et al. (2017b) and the left-over planetesimal data from Morbidelli et al. (2018). The left-over planetesimal data covers only a limited time period, 500 Myr after the Moon-forming impact (which is assumed to occur at 50 Myr), unlike the asteroid and comet data, which spans the lifetime of the Solar system, from prior to the giant planet instability to the present day. While impacts undoubtedly continued onto Venus and Mars after 550 Myr, the decaying impact flux means the relative importance of impacts on the atmosphere compared to other processes decreases. Since the purpose of this dissertation is to consider the effect of impacts, and other atmospheric processes are not included in my model, I consider evolution only up to $t = 550$ Myr.

The time of the Moon-forming impact is not an obvious choice for the start time of simulations of the atmospheres of Venus and Mars (unlike was the case for the Earth). The simulations should begin after the final core-disrupting giant impact, however given the uncertainty in the past climates of both planets there is a degree of degeneracy between this start time and the choice of initial atmospheric conditions. This can be exploited to avoid introducing unnecessary uncertainties (by extrapolating the planetesimal data backwards in time to reconstruct the bombardment expected for Venus and Mars in the time prior to $t = 50$ Myr), instead considering a range of initial conditions for the atmospheres of Venus and Mars at $t = 50$ Myr. Furthermore, an extrapolated bombardment flux would contain more mass and thus the choice of giant impact prescriptions, which was shown in §2.7 to be important, becomes significant. Therefore I consider a range of potential initial atmosphere conditions,

described in §5.1.2. In 5.1.1 I do describe the method through which an extrapolated planetesimal impact flux (beginning 20 Myr earlier) can be constructed. The effect of bombardment over this extended time is discussed in §5.4.2, but a full study of this effect is left for future study.

To calculate the impact flux distributions from the simulation data described above I isolate the particles on planet-crossing orbits (interpolating the planet locations in the Nesvorný et al. (2017a) simulations to determine their locations in the Nesvorný et al. (2017b) simulations, as the terrestrial planets were not included at each time-step. The orbital elements for each particle and the planet are then used to calculate the number of impacts at each time in each velocity bin, using the process described in §3.1.1, based on the method from Wyatt et al. (2010). Later time-steps are combined to ensure there are always a minimum of $N_{\rm min} = 50$ particles used to calculate each velocity distribution, to avoid biasing the distributions through sampling only a small number of particles. The resulting distributions are shown as mass accretion rates, normalised by the total impacting mass estimates described in §5.1.1 in Fig. 5.2, illustrating the complex shapes of the impact velocity distributions. The corresponding values of the total impact flux and the velocity distribution (summed over velocity and time respectively) for the different impactor populations onto Venus and Mars are shown in Fig. 5.3.

The left-over planetesimals are typically slower than the other populations, while the comets have a more extended high-velocity tail than the asteroids. There are fewer very slow comets compared to the other two populations, and the distribution for asteroid impacts onto Venus shows the same double-peaked structure as was seen for the Earth. The velocities of impacts onto Mars relative to the planet escape velocity are higher than onto Venus. The different dynamical cases for the left-over planetesimal populations[1], are labelled as case 1 to case 7 in the same manner as the Earth. The extrapolated portion of the data results in a smooth decay in mass accretion rate prior to 50 Myr. A spike in impact probability occurs at around 180 Myr in case 6 on Venus. Inspecting the low-velocity tail of the mass accretion rate also reveals that this case has a significantly higher impact probability for the lowest velocity impacts. This is the result of a single particle which appears only once in the original dynamical simulation, briefly passing very close to Venus' orbit and thus giving a very high collision probability for a narrow range of very low impact velocities. A similar but less extreme single particle event occurs at around 210 Myr in case 5 in the data for Mars. These are potentially not realistic scenarios, but as the single particles are not trapped in any resonance I do not remove them arbitrarily. The effect of these distributions are investigated in §5.3.3.

[1] representing different initial conditions in the Morbidelli et al. (2018) simulations, described in detail in §3.1.1

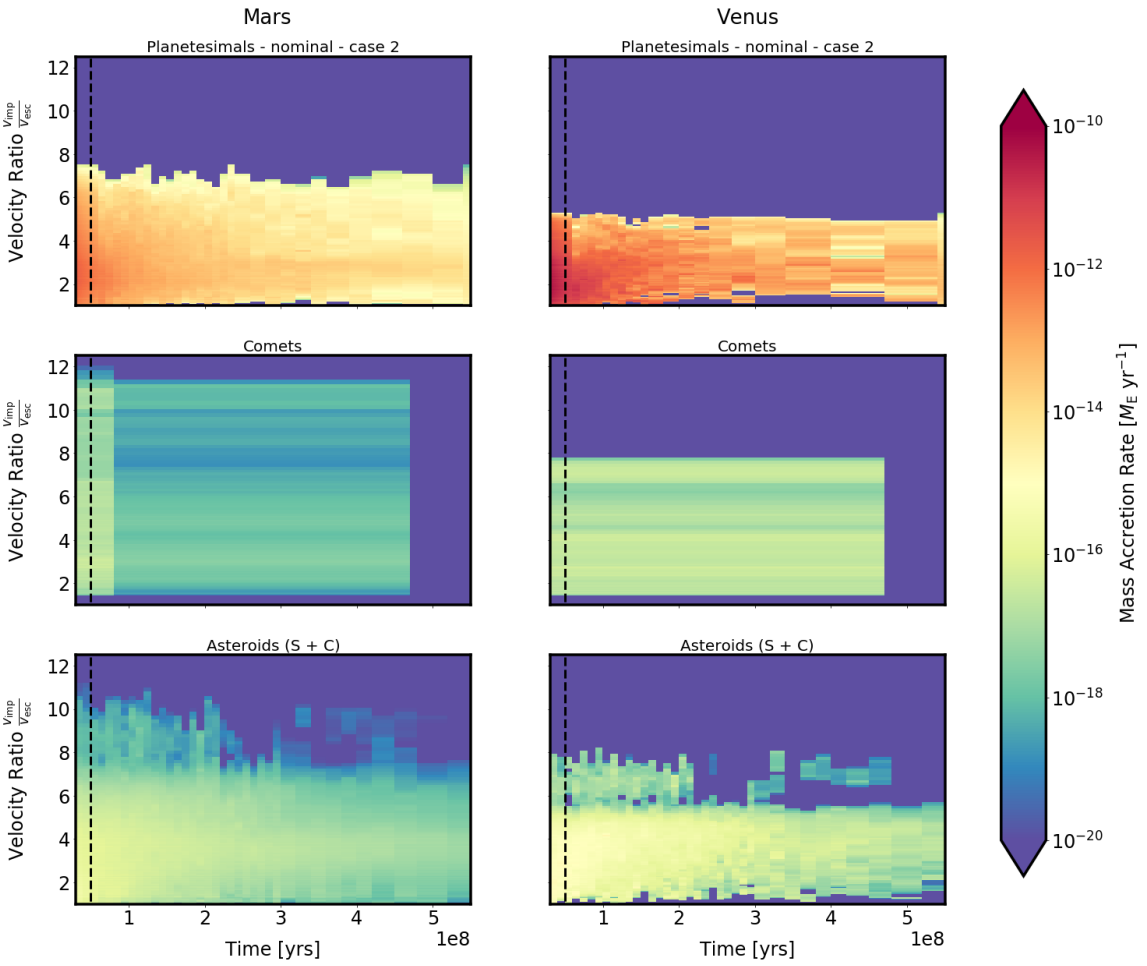

Figure 5.2: The distribution of mass accretion rate as a function of time and velocity ($\frac{R_k(t)}{\int R_k(t)\mathrm{d}t} f_{\mathrm{v}j,k}(t) M_{\mathrm{tot}\ k}$) for each of the three impactor populations: left-over planetesimals (top), comets (middle) and asteroids (bottom). The asteroid data has been combined (S- and C-types) and the planetesimal data shows the data for the chosen nominal dynamical case. The black vertical dashed line illustrates the time of the Moon-forming impact, with the planetesimal data extrapolated back in time shown. The data for Mars is shown in the left-hand column and for Venus in the right-hand column. These plots show the distribution after multiple time-steps have been combined (if necessary).

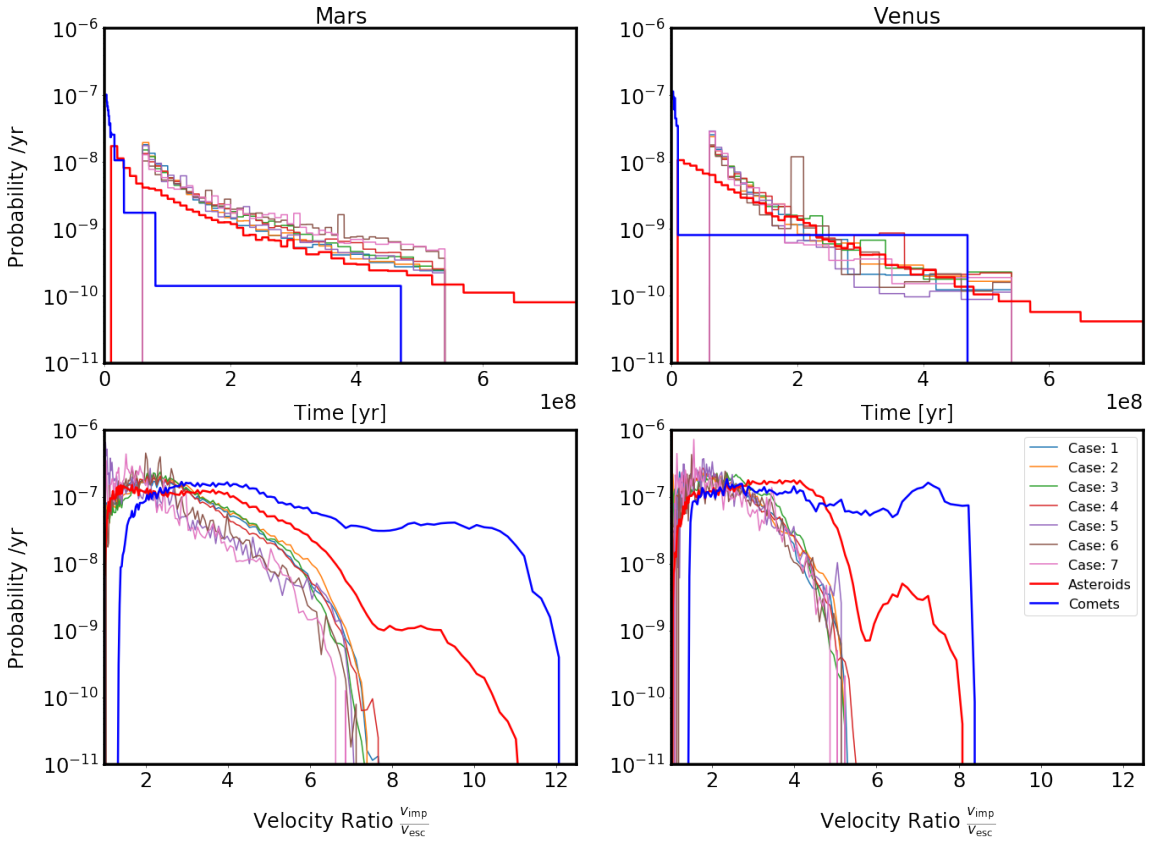

Figure 5.3: The mass accretion rate $(\frac{R_k(t)}{\int R_k(t)\mathrm{d}t} M_{\mathrm{tot}\ k})$ and impact fraction as a function of velocity $(f_{\mathrm{v},j,k})$ calculated for the different impactor populations onto Venus and Mars. The data for Mars is shown in the left-hand column and Venus in the right-hand column, with the mass accretion rates shown in the top panels and impact velocity fractions shown in the bottom panels.

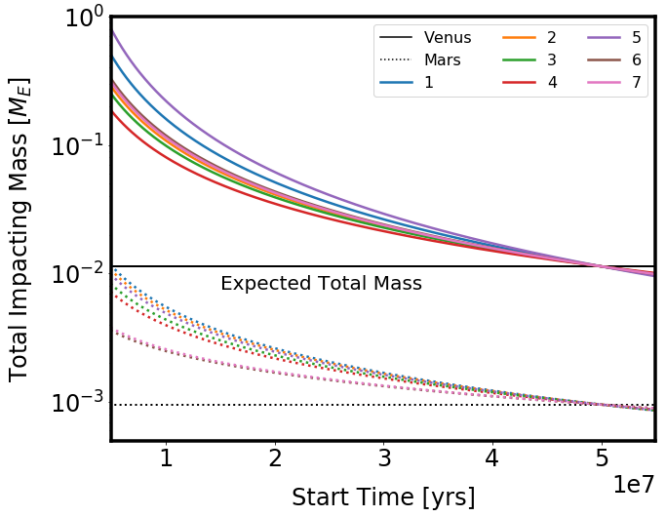

Figure 5.4: The calculated total impacting mass for planetesimals onto Venus and Mars as a function of when the accretion is assumed to begin. The horizontal lines show the nominal population masses calculated for the original distributions (with no extrapolation).

Extrapolating the planetesimal impact fluxes

Extrapolating the left-over planetesimal data requires making assumptions about both how the impact flux and the velocity distribution have evolved in time. For the velocity distribution, I assume that the impact velocities in the first 5 Myr of the data is representative of impacts prior to the start of the dynamical simulations. To model the time-dependence I fit a power-law decay to each dynamical case, of the form $R_k \propto t^{-\beta}$, where $-2.8 < \beta < -2.2$ for Venus and $-2 < \beta < 1.5$ for Mars. These extrapolated distributions are shown as mass accretion rates $\frac{R_k(t)}{\int R_k(t) \mathrm{d}t} M_{\mathrm{tot}\ k}$ in Fig. 5.3, normalised by the population masses described in §5.1.1 over the time period $50 - 550$ Myr. The dependence of the estimated total impacting mass on the start time is illustrated in Fig. 5.4.

Extrapolating arbitrarily far back in time cannot be justified, as early in the process of planet growth the orbits of the left-over planetesimal population are less excited and thus the impact fluxes are not expected to be as high as suggested by Fig. 5.4. Furthermore, while Mars likely reached its current mass very early, Venus and Earth may not have fully formed until later. The assumption made in the numerical code that the planet mass remains constant is only valid for changes in the total planet mass of less than $\sim 5\%$ and so cannot be applied if the planet accretes a significant portion of its mass during the simulation. In the following, I therefore consider a single start time, $t_{\mathrm{start}} = 50$ Myr, and discuss what effect considering this extended distribution may have in §5.4.2. The difference in the velocity distributions for the asteroid and comet populations assuming these two different start times can be seen from Fig. 5.3 to be small, further motivating the 50 Myr start time choice.

Total impacting mass

The total number of impactors from each population, summed over all velocity and size bins, is normalised by the total *impacting* mass,

$$M_{\mathrm{tot},k} \equiv \int \sum_{i}^{N_{\mathrm{size}}} \sum_{j}^{N_{\mathrm{vel}}} R_k(t) f_{\mathrm{N},i,k}(t) f_{\mathrm{v},j,k}(t) \frac{\pi}{6} \rho_k D_i^3 \, \mathrm{d}t. \tag{5.1}$$

This is not necessarily equal to the total *accreted* mass as the fraction of the impacting mass accreted by the planet depends on the atmosphere mass and composition and cannot be predicted in advance. The total impacting masses for the different populations are calculated as described below.

Asteroids: For the asteroid population, the total mass impacting the Earth between the nominal time span of the simulations ($50 - 550$ Myr) was calculated in Chapter 3 from the exponential fit to asteroid impact data fin Nesvorný et al. (2017a). This gave $M_{\mathrm{E\ tot,\ ast}} = 3.94 \times 10^{-6}$ $\mathrm{M}_{\oplus}$, assuming a weighted average density of the two asteroid sub-populations (11.7% S-type, 88.3 % C(+B)-type). The same method cannot be directly applied to Venus and Mars as the corresponding decay functions, and total number of impacts are not given for these planets in Nesvorný et al. (2017a). Instead, to calculate the total impacting mass of asteroids impacting Venus and Mars, I scale the Earth value using the ratio of intrinsic collision probabilities, through

$$M_{\mathrm{tot,\ V/M}} = \frac{P_{\mathrm{tot,\ V/M}}}{P_{\mathrm{tot,\ E}}} M_{\mathrm{tot,\ E}}, \tag{5.2}$$

where

$$P_{\mathrm{tot}} = \int_{t_0}^{t_{\mathrm{max}}} \sum_{v_j} P(t, v_j) \, \mathrm{d}t. \tag{5.3}$$

This gives a total impacting asteroid mass $M_{\mathrm{V\ tot,\ ast}} = 6.36 \times 10^{-6}$ $\mathrm{M}_{\oplus}$ for Venus, and $M_{\mathrm{M\ tot,\ ast}} = 1.47 \times 10^{-6}$ $\mathrm{M}_{\oplus}$ for Mars, which I adopt as the nominal values. If considering the earlier start time of 30 Myr, these total mass estimates would increase by approximately 25% to $M_{\mathrm{V\ tot,a}} = 8.05 \times 10^{-6}$ $\mathrm{M}_{\oplus}$ and $M_{\mathrm{M\ tot,a}} = 1.86 \times 10^{-6}$ $\mathrm{M}_{\oplus}$.

Comets: For the comet population, I compare the capture fraction of the Jupiter Trojans from the simulations of Nesvorný et al. (2013), $f_{\mathrm{capt}} = 5 \times 10^{-7}$ (Nesvorný et al., 2018), to my calculated intrinsic collision probabilities. These give the total probability per comet initially in the disk (for the standard time period) of $P_{\mathrm{M\ tot,c}} = 8.3 \times 10^{-8}$ for impacts onto Venus and $P_{\mathrm{V\ tot,c}} = 3.2 \times 10^{-8}$ for impacts onto Mars. The ratio of these numbers, $n_{\mathrm{V/M}} = \frac{P_{V/M\ \mathrm{tot,c}}}{f_{\mathrm{capt}}}$, gives the expected ratio between the comet total impacting mass and the estimated Jupiter

Trojan mass, $M_{\rm Trojans} = (0.3 \pm 0.19) \times 10^{-10}$ $\rm M_\odot$ and thus nominal values of $M_{\rm V\ tot,c} = 1.66 \times 10^{-6}$ $\rm M_\oplus$ for Venus and $M_{\rm M\ tot,c} = 0.642 \times 10^{-6}$ $\rm M_\oplus$ for Mars. Compared to the value for the Earth used in Chapter 3, $M_{\rm E\ tot,c} = 2.2 \times 10^{-6}$ $\rm M_\oplus$, comets contribute smaller masses to both Venus and Mars than to Earth. If considering the earlier start time, these estimates would become $M_{\rm V\ tot,c} = 2.55 \times 10^{-6}$ $\rm M_\oplus$ and $M_{\rm M\ tot,c} = 0.980 \times 10^{-6}$ $\rm M_\oplus$.

Left-over planetesimals: The total impacting masses of the left-over planetesimal populations are normalised through comparison of the total intrinsic collision probabilities and the estimated total impacting mass onto the Earth calculated in Chapter 3. The normalisation for the Earth was calculated such that the typical total accreted mass matched the Late Veneer mass, (0.005 ± 0.002) $\rm M_\oplus$ (Warren et al., 1999; Walker, 2009). Isotopic constraints imply that the majority of this mass was delivered by left-over planetesimals rather than asteroids and comets (Morbidelli et al., 2018). The conversion of this evidence for the total *accreted* mass into an estimate for the total *impacting* mass was an iterative process, resulting in a total mass estimate of $M_{\rm E,tot,plan} = 0.0075$ $\rm M_\oplus$, as described in §3.1.3.

The ratio of the median total impact probabilities onto Venus and Mars relative to the Earth are 1.5 and 0.13 respectively, in agreement with the values in Brasser et al. (2020). Comparison of the impact probabilities gives total impacting mass estimates of $M_{\rm V\ tot,plan} = 0.01136$ $\rm M_\oplus$ and $M_{\rm M\ tot,plan} = 0.000955$ $\rm M_\oplus$. If the accretional efficiency for impacts is comparable between the three terrestrial planets this should result in corresponding accreted masses of ~ 0.008 $\rm M_\oplus$ on Venus and ~ 0.0006 $\rm M_\oplus$ on Mars. These are similar to the Venusian Late Veneer estimate of 0.8% wt. from Gillmann et al. (2020) and within the range of Martian Late Veneer estimates, from 0.25% wt. (Marchi, 2020) to 1.4% wt (Brasser et al., 2016), based on measured HSE excesses.

When considering the earlier start time (30 Myr), the impact flux must be extrapolated. This would result in an addition to the total impacting masses of 30 Myr, of $\Delta M_{\rm V\ tot,plan} = 0.0110$ $\rm M_\oplus$ for Venus and $\Delta M_{\rm M\ tot,plan} = 0.000626$ $\rm M_\oplus$ for Mars. I discuss the potential impact of considering the earlier start time with correspondingly higher total mass estimates in §5.4.2.

Table 5.1: The initial atmosphere conditions (mass, temperature and MMW) assumed for the three representative starting conditions for Venus and Mars ("hot", "mid" and "cool").

Case	Atmosphere Mass [$M_\oplus$]	Venus Temperature [K]	Mars Temperature [K]	Mean Molecular Weight
Hot and Massive	10^{-4}	700	400	44
Mid (Earth-like)	10^{-6}	500	300	44
Cool and Thin	10^{-9}	300	200	44

5.1.2 Planet properties

The initial conditions (mass, temperature and MMW) of the atmosphere and bulk properties of the planet are also important determinants of the resulting atmosphere behaviour.

Bulk properties

Venus and Mars have bulk densities of $\rho_{\rm V,pl} = 5.24$ g cm^{-3} and $\rho_{\rm M,pl} = 3.93$ g cm^{-3}. As was discussed in §2.6.1 the change in planet mass has negligible effect on the predicted atmosphere mass evolution provided it is within $\pm 5\%$ of the initial value. This allows the assumption within the updated code described in §2.6 that the planet mass is constant. I therefore adopt the current masses of Venus and Mars as their initial masses, $0.815\ M_\oplus$ and $0.1075\ M_\oplus$ respectively. The accreted mass is still tracked for comparison to the Late Veneer estimates, discussed in §5.4.5. A summary of the values describing the planet bulk properties are shown compared to those for the Earth in table 2.1.

Initial atmospheric conditions

The varied potential atmospheric conditions on early Venus and Mars were discussed in §1.5.2. I do not attempt to pick one hypothesis in preference to the alternatives in this chapter, and instead investigate the evolution of three potential initial atmospheres for Venus and Mars, spanning a range of proposed early atmosphere states:

- "Hot", high-temperature and massive;
- "Mid", intermediate-temperature and Earth-like mass;
- "Cool", low-temperature and thin.

The initial atmosphere masses for these three cases are the same for both planets but the temperatures differ, as shown in Table 5.1. Venus' present day atmosphere is most similar to

the "hot" case, while Mars is currently most similar to the "cool" case. The initial atmosphere MMW is assumed to be $\mu_0 = 44$, representative of the CO_2-dominated atmospheres seen today on Venus and Mars. An SO_2-dominated atmosphere, which could be produced by volcanic outgassing on Mars would have a higher MMW however a steam (H_2O/CO_2) or a reduced outgassed (CO/H_2) atmosphere would have a lower MMW.

The assumption made in my model that the atmospheres of Venus and Mars are isothermal is a simplification, however it is a necessary assumption in order to make use of the Shuvalov (2009) prescription. In §2.1.6 I established that the isothermal assumption in combination with my modified aerial burst and fragmentation prescriptions is capable of recreating the Shuvalov et al. (2014) simulation results for hot atmospheres. Consideration of a non-isothermal atmosphere is left for a future study.

5.2 The analytic predicted stalling mass

Before running the full numerical simulations, I can make predictions for the expected atmosphere behaviour using the analytic model described in §2.3.1, using the distribution of impactor sizes and velocities described above for each population to calculate the weighted average value of f_v. The MMW is assumed to be representative of the original (CO_2-dominated) atmosphere for the asteroids and comets but equal to the material delivered by the impactors for the left-over planetesimals, as this population is massive enough to totally replace the atmosphere. The effects of aerial bursts and giant impacts are included, with the atmosphere temperature assumed to be 500 K for Venus and 300 K for Mars (the "mid" case discussed in §5.1.2). In addition, the results for the left-over planetesimals are calculated assuming a slower impactor velocity distribution and for the "hot" and "cool" atmosphere cases.

The resulting profiles of $f_v(m)$ are shown in Fig. 5.5. For asteroids, the C-type population results in growth of all but the most massive atmospheres on both Venus and Mars, but the S-type population have predicted stable stalling masses of 2.0×10^{-5} $M_\oplus$ on Mars and 3.6×10^{-5} $M_\oplus$ on Venus. The C-type populations are more massive than the S-types, therefore the atmosphere behaviour is likely to be determined by this population. However the atmosphere is not expected to reach the high stalling masses predicted because the assumed total impacting masses are too low to deliver sufficient mass in volatiles. The predicted stalling mass for impacts by comets is 6.3×10^{-11} $M_\oplus$ for Mars, and non-existent for Venus, since comets erode atmospheres of all masses.

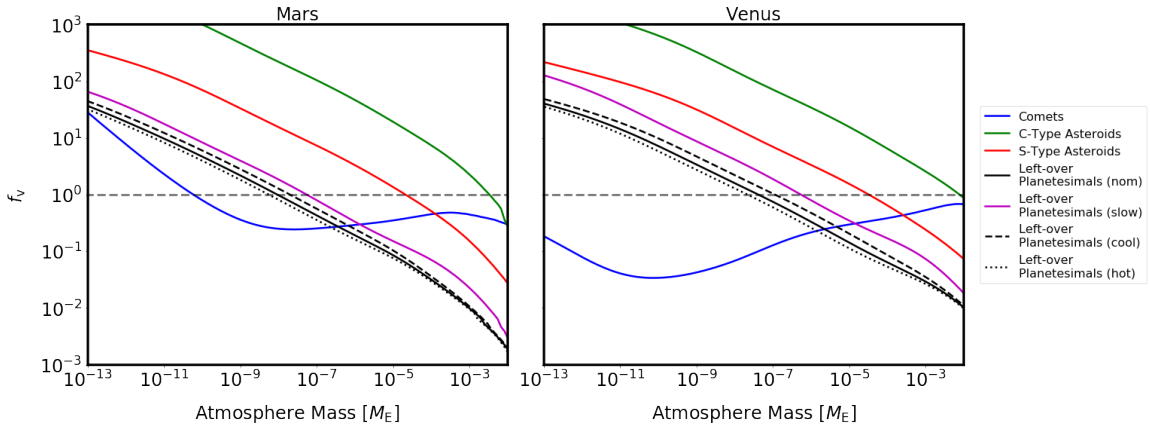

Figure 5.5: The analytically predicted behaviour of f_v as a function of atmosphere mass, calculating using the method described in §2.3.1, including the effect of aerial bursts and the giant impact prescription. The results are shown for the nominal impactor properties, assuming that the atmospheres are the "mid" case described in the text. For the asteroids and comets the atmosphere is assumed to have $\mu = 44$, but for the left-over planetesimals is is assumed to have $\mu = \mu_{\rm imp} = 15$ as these populations replace the bulk of the atmosphere mass. An alternative slow left-over planetesimal case is also shown, as is the predicted behaviour for the "hot" and "cool" cases assuming the nominal impactor dynamics.

For the populations of left-over planetesimals the stalling mass predicted for the nominal dynamics and "mid" atmosphere temperature is 9.5×10^{-9} M$_\oplus$ for Mars and 3.9×10^{-8} M$_\oplus$ for Venus. The strong dependence of the atmosphere stalling mass on the impact velocity can be seen from the results in Fig. 5.5 considering alternative planetesimal dynamics. Case 5 for Mars and case 6 for Venus are representative of "slow" impact velocity distributions, as discussed in §5.1.1. For Mars, this distribution results in a predicted stalling mass of 5.8×10^{-8} M$_\oplus$, and for Venus, which has a more heavily skewed velocity distribution, this difference is more extreme, with a predicted stalling mass of 5.3×10^{-7} M$_\oplus$, three orders of magnitude higher than the nominal case. This motivates the investigation into the different planetesimal dynamics presented in §5.3.3. Considering the "cool" atmosphere temperatures, the predicted stalling masses roughly double to 2.1×10^{-8} M$_\oplus$ on Mars and 1.1×10^{-7} M$_\oplus$ on Venus. Conversely, the "hot" atmospheres have lower predicted stalling masses of 5.2×10^{-9} M$_\oplus$ and 2.1×10^{-8} M$_\oplus$ respectively, a decrease of approximately a factor of 2.

Case		Atmosphere Mass			Atmosphere Impactor Fraction		
		Median [$M_\oplus$]	**Minimum** [$M_\oplus$]	**Maximum** [$M_\oplus$]	**Median** [%]	**Minimum** [%]	**Maximum** [%]
A	Mid	9.99×10^{-7}	9.94×10^{-7}	1.21×10^{-6}	$(0.332, 9.83 \times 10^{-4})$	$(0.0987, 3.48 \times 10^{-4})$	$(18, 0.381)$
A	Cool	4.60×10^{-9}	1.19×10^{-9}	1.27×10^{-6}	$(80.6, 0.173)$	$(17.4, 3.10 \times 10^{-4})$	$(99.9, 57.5)$
A	Hot	1.00×10^{-4}	1.00×10^{-4}	1.00×10^{-4}	$(4.76 \times 10^{-3}, 1.21 \times 10^{-5})$	$(1.94 \times 10^{-3}, 4.22 \times 10^{-6})$	$(0.425, 5.74 \times 10^{-4})$
C	Mid	9.97×10^{-7}	9.95×10^{-7}	9.98×10^{-7}	0.0320	0.0291	0.0358
C	Cool	8.22×10^{-10}	8.16×10^{-10}	8.57×10^{-10}	0.553	0.461	4.82
C	Hot	1.00×10^{-4}	1.00×10^{-4}	1.00×10^{-4}	2.06×10^{-3}	1.32×10^{-3}	3.94×10^{-3}
Pn*	Mid	4.64×10^{-13}	$< 10^{-19}$	5.13×10^{-8}	100	100	100
Pn*	Cool	9.39×10^{-12}	$< 10^{-19}$	5.65×10^{-8}	100	100	100
Pn	Hot	8.68×10^{-5}	8.48×10^{-5}	8.94×10^{-5}	0.26	0.14	0.38
Ps*	Mid	2.21×10^{-7}	1.40×10^{-7}	3.47×10^{-7}	38.1	19.4	53.6

Table 5.2: The results for impacts onto Mars (current atmosphere mass $\sim 4.2 \times 10^{-9}$ $M_\oplus$). The case describes whether the impacts are by asteroids (A), comets (C) or left-over planetesimals (P) For the non-stochastic results (all asteroids, comets and left-over planetesimals on hot initial atmospheres) these are given as the median, minimum and maximum values of the total final atmosphere mass and fraction of the final delivered by the impactors. For the stochastic results (left-over planetesimal impacts onto the mid and cool atmospheres these results are shown as the median, minimum and maximum values for the atmosphere masses recorded over the final 300 Myr of the simulations and marked by an asterisk ($*$). The number of simulations run for each population is described in the text. For the asteroids, the impactor fractions are shown as $(f_{\mathrm{S-type}}, f_{\mathrm{C-type}})$.

Case		Atmosphere Mass			Atmosphere Impactor Fraction		
		Median [$M_\oplus$]	**Minimum** [$M_\oplus$]	**Maximum** [$M_\oplus$]	**Median** [%]	**Minimum** [%]	**Maximum** [%]
A	Mid	9.99×10^{-7}	9.92×10^{-7}	1.06×10^{-6}	$(0.827, 5.24 \times 10^{-3})$	$(0.212, 1.81 \times 10^{-3})$	$(6.41, 0.639)$
A	Cool	8.98×10^{-9}	1.93×10^{-9}	3.40×10^{-7}	$(88.6, 0.571)$	$(53.8, 6.29 \times 10^{-3})$	$(99.8, 26.8)$
A	Hot	1.00×10^{-4}	9.99×10^{-5}	1.00×10^{-4}	$(0.0157, 8.56 \times 10^{-5})$	$(6.01 \times 10^{-3}, 2.98 \times 10^{-5})$	$(0.346, 0.0110)$
C	Mid	9.88×10^{-7}	9.87×10^{-7}	9.89×10^{-7}	0.109	0.107	0.112
C	Cool	5.95×10^{-10}	5.92×10^{-10}	6.01×10^{-10}	1.07	1.06	1.08
C	Hot	9.99×10^{-5}	9.99×10^{-5}	1.00×10^{-4}	9.27×10^{-3}	8.43×10^{-3}	9.69×10^{-3}
Pn*	Mid	6.78×10^{-10}	$< 10^{-19}$	8.45×10^{-8}	100	100	100
Pn*	Cool	1.72×10^{-9}	$< 10^{-19}$	8.38×10^{-8}	100	100	100
Pn	Hot	4.81×10^{-5}	4.60×10^{-5}	5.16×10^{-5}	4.1	3.7	5.1
Ps*	Mid	2.04×10^{-9}	$< 10^{-19}$	3.54×10^{-7}	100	100	100

Table 5.3: As for table 5.2 but for impacts onto Venus (current atmosphere mass $\sim 8.0 \times 10^{-5}$ $M_\oplus$).

5.3 Results

In the following the results produced by applying the numerical code described in §2.5.3 to Venus and Mars with the inputs described above are presented, considering variation in the impactor properties and initial atmosphere conditions for each population in isolation. The number of simulations that must be run for each population to get an accurate representation of the expected atmosphere evolution depends on whether stochastic rare events (sampling an extreme impactor size or velocity) are expected to have significant effects on the atmosphere evolution. As I showed for the Earth in Chapter 3, it is typically only asteroids and comets that are capable of causing significant stochastic changes to the atmosphere mass. This is because they are volatile-rich (so a single large object contains a significant mass in volatiles) and their total population mass is small (so impacts by the largest objects are rare). For this reason, the code is run 50 times for the nominal asteroid and comet populations and 30 times for the other asteroid and comet populations. The planetesimal populations are run 15 times for the nominal, "mid" case, and 10 times to consider different initial conditions and left-over planetesimal dynamics. The results of the 530 simulations run are summarised in table 5.2 for Mars and table 5.3 for Venus, and discussed in detail below.

5.3.1 Asteroids

The evolution of the "hot", "mid" and "cool" atmospheres under bombardment by asteroids are shown in Fig. 5.6a, from which it can be seen that these populations result in inherently stochastic atmosphere evolution. The current atmosphere mass of Mars is $\sim 4.2 \times 10^{-9}$ $\mathrm{M}_{\oplus}$, similar to the "cool" initial mass, and of Venus is $\sim 8.0 \times 10^{-5}$ $\mathrm{M}_{\oplus}$, similar to the "hot" initial mass. The distribution of the final atmosphere masses for each of the five cases is shown in Fig. 5.6b, and the average (median) value and range for both the final atmosphere mass and fraction of the atmosphere delivered by the two asteroid sub-populations are summarised in table 5.2 for Mars and table 5.3 for Venus.

The relatively small total impacting mass of the asteroid population ($\sim 10^{-6}$ $\mathrm{M}_{\oplus}$) results in negligible evolution of the most massive "hot" ($m_0 = 10^{-4}$ $\mathrm{M}_{\oplus}$) atmospheres. The "mid" and "cool" initial atmospheres both grow as a result of asteroid impacts, similar to the evolution of Earth's atmosphere presented in Chapter 3. The final atmosphere masses for the "cool" case span more than two orders of magnitude, $10^{-9} - 10^{-7}$ $\mathrm{M}_{\oplus}$. The jumps in atmosphere masses that can be seen in some runs are the result of the stochastic arrival of asteroids that deliver a substantial portion of their mass in volatiles to the atmosphere. Instantaneous increases in the atmosphere mass of $\sim 10^{-8}$ $\mathrm{M}_{\oplus}$ occur in all runs, with jumps of $\sim 10^{-7} - 10^{-6}$ $\mathrm{M}_{\oplus}$ in a few

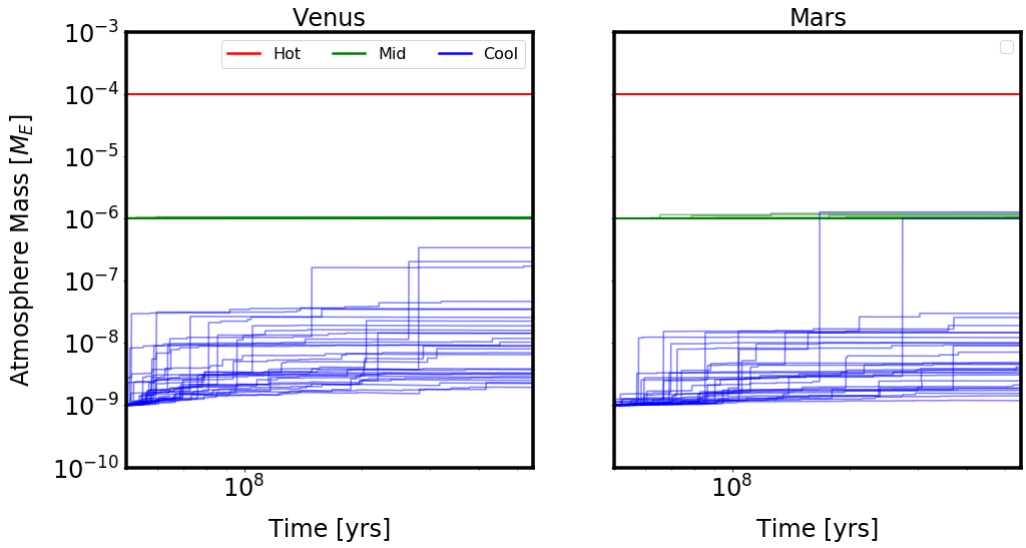

(a)

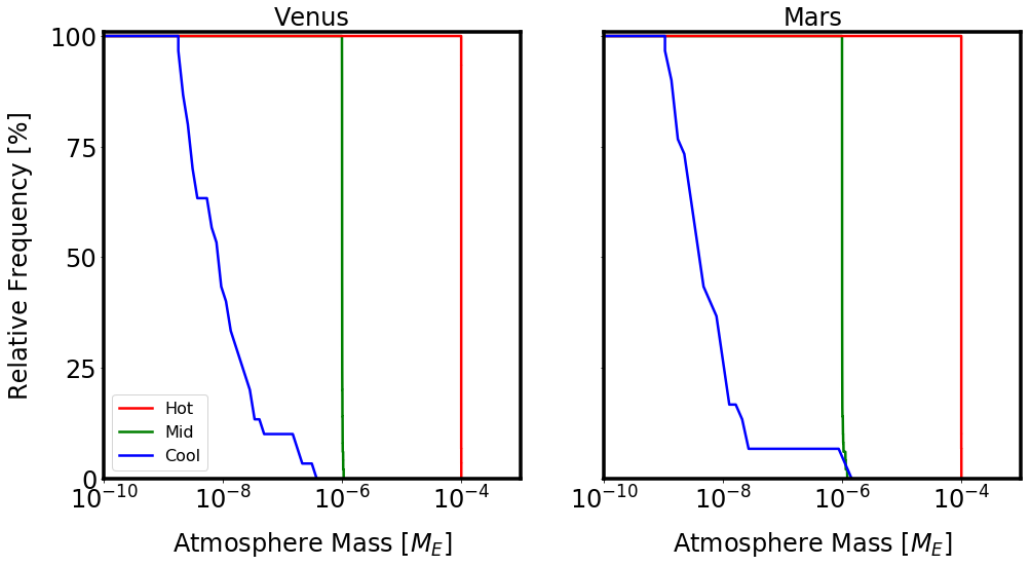

(b)

Figure 5.6: The results considering the evolution of Venus and Mars under bombardment by asteroids. The top panels (a) show the total atmosphere mass as a function of time, with Venus shown in the left panel and Mars in the right panel. The bottom panels (b) show the relative frequency distribution (percentage of atmospheres with masses greater than the x-axis value) of final atmosphere masses. These results are produced by running the numerical code 30 (50 for the "mid" atmosphere case) times each, considering three potential initial atmosphere conditions ("hot", "mid" and "cool", shown by different line colours)

cases. The maximum mass of volatiles that can be delivered by a single impactor is given by equation 3.2, which is approximately 10^{-6} $M_{\oplus}$ for the largest asteroids here. These impacts are rare, there are $\sim$ 0.08 asteroids larger than 500 km for Venus and only 0.02 for Mars in the nominal populations, meaning impacts by these objects are expected to occur for only a few percent of runs, as observed. This delivery occurs in the initially massive atmospheres also, but is negligible compared to the total atmosphere mass and so cannot be seen.

These results can be compared to the analytically predicted stalling masses discussed in §5.2. However the low total impacting mass for asteroidal impactors onto both Venus and Mars must be properly accounted for. The populations of asteroids are effectively truncated at a smaller maximum impactor sizes than was assumed in the naive calculation of the analytic stalling masses. As discussed in Chapter 4, the stalling mass decreases as the size of the largest impactor decreases. For the total asteroid population masses considered here, the large impactors required to grow the atmosphere towards the high predicted stalling mass are sampled only rarely, while the smaller impactors that are sampled result in less growth, or in some cases erosion of more massive initial atmospheres, as is seen.

The final composition of the initially massive atmospheres is dominated by primordial material, with less than 1% of the final atmosphere mass comprised of material delivered by the asteroid populations. The "mid" atmospheres on Venus and Mars typically end with a $\sim$ 1% level contribution to their atmospheres by C-type asteroid material, but this can be an order of magnitude higher or dominated by S-type material when stochastic large impacts occur. Initially low-mass atmospheres end with the bulk of their atmosphere mass delivered by asteroidal material, usually the more massive C-type population.

5.3.2 Comets

The effect of impacts by comets is considered in a similar manner to the asteroids, with the results shown in Fig. 5.7. The atmosphere mass stops evolving at 500 Myr as the impact flux onto both planets is zero after this time. In general, very little change in any of the atmospheres considered is seen. This is to be expected because the comet population is small, and furthermore the larger impactors have little effect on the atmosphere as they have very low accretion and erosional efficiencies due to their low density, as illustrated in Fig. 2.1. This also means that the results show little stochastic variation between iterations of the code, as the large impactors (which are stochastically sampled), have no noticeable effect on the atmosphere mass evolution.

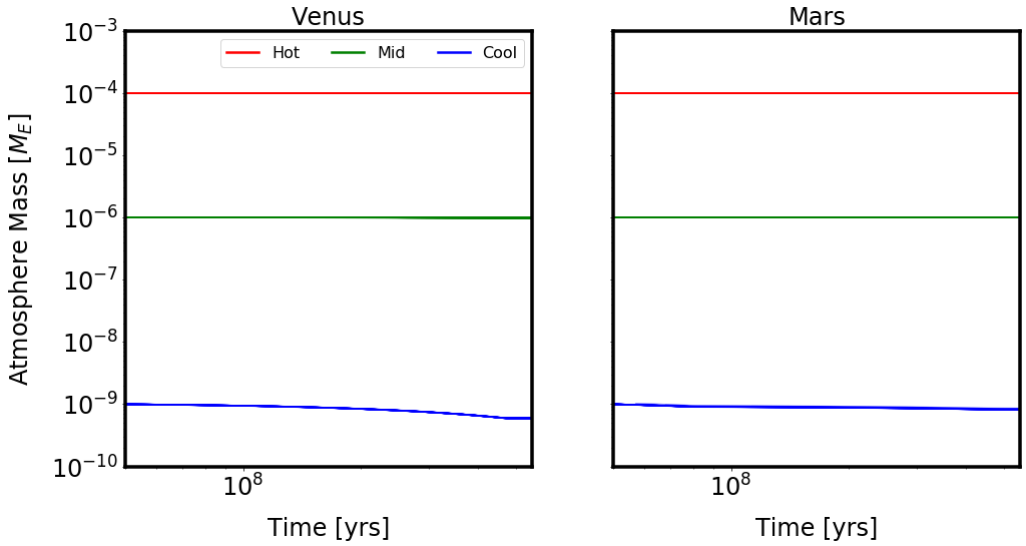

Figure 5.7: The total atmosphere mass as a function of time considering the evolution of Venus and Mars under bombardment by comets. The results for Venus are shown in the left panel and Mars in the right panel. These results are produced by running the numerical code 30 (50 for the nominal mid combination) times each, and show very little difference between individual simulations. The three initial atmosphere conditions ("hot", "mid" and "cool") are shown by different line colours

The atmosphere MMW is relatively unchanged for all atmospheres, since the bulk of the final atmosphere is made up of residual primary atmosphere material. At most $\sim 5\%$ of the initially lowest atmosphere masses ends up composed of delivered cometary material, and more typically $< 1\%$ of the final atmosphere by mass is made up cometary volatiles. Compared to the analytic predictions made in §5.2 these results agree with the predicted atmospheric erosion.

5.3.3 Planetesimals

The results for the dominant impactor population, the left-over planetesimals, are more complex than those for the asteroids and comets. For this reason I consider first the specific case of the "nominal" impactor population (dynamical case 2) impacting the "mid" atmosphere case on both Venus and Mars, in detail. Then the influence of the planetesimal dynamics on the resulting evolution is considered before finally the evolution of different initial atmospheres is investigated.

The nominal "mid" case in detail

The results of 15 runs of the numerical code considering the evolution of a mid-temperature ($T = 300$ K and 500 K on Mars and Venus respectively) intermediate mass ($m_0 = 10^{-6}$ M$_\oplus$)

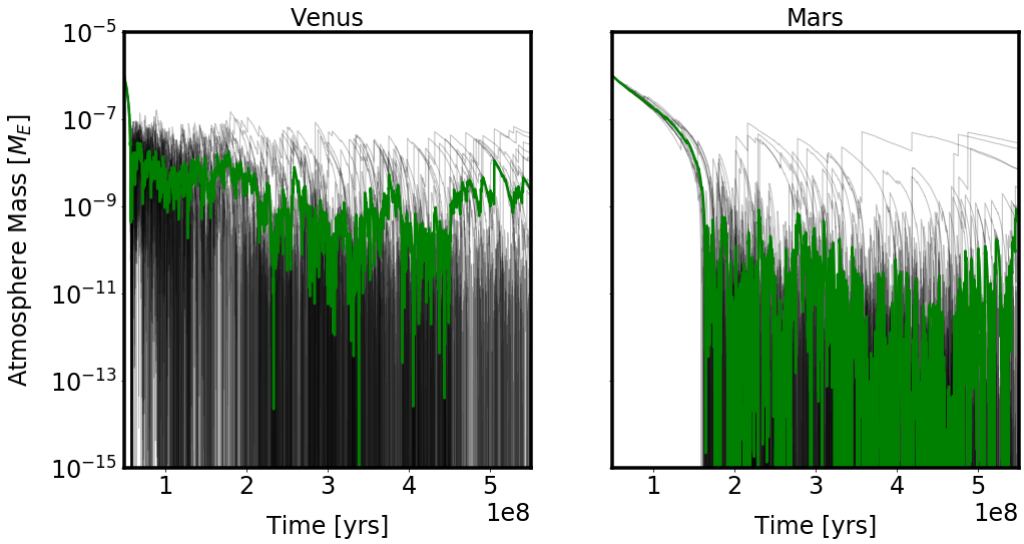

Figure 5.8: The results considering the evolution of Venus and Mars (the "mid" atmosphere case only) under bombardment by the nominal population of left-over planetesimals. The total atmosphere mass as a function of time is shown for Venus in the left panel and Mars in the right panel. The individual atmosphere mass profiles are shown by thin transparent lines with the median atmosphere evolution shown as a thick green line on each panel.

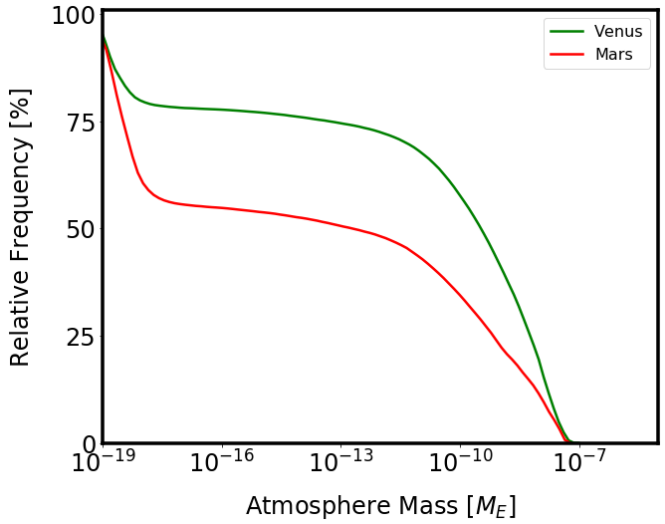

Figure 5.9: The relative frequency distribution of atmosphere masses recorded over the final 300 Myr of the numerical simulations, for the atmosphere mass profiles shown for Venus and Mars in Fig. 5.8. Venus is shown in green and Mars in red.

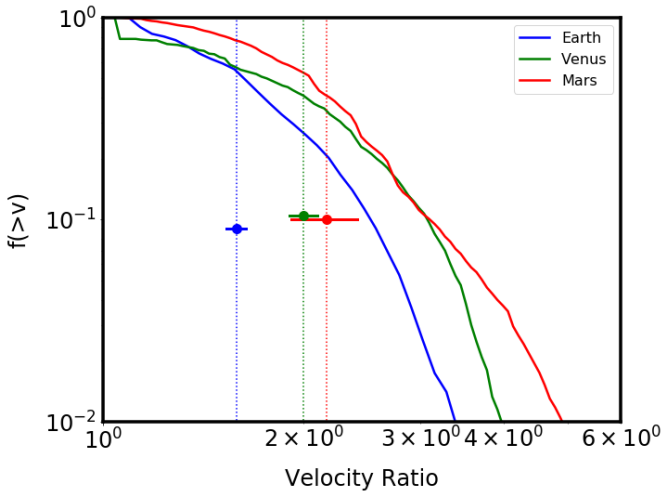

Figure 5.10: The velocity distributions for the nominal planetesimal dynamics (case 2), shown for Venus, the Earth and Mars. The solid lines show the fraction of impactors with velocity ratio greater than the x-axis value. The dashed vertical lines show the weighted average velocity for each planet and the marker and associated lines show the typical variation in this median value. This plot demonstrates the slower relative velocity distributions for impacts onto the Earth compared to Venus and Mars.

atmosphere due to bombardment by the nominal left-over planetesimal population is shown in Fig. 5.8. The relative frequency distributions of atmosphere masses recorded by the code in the final 300 Myr of the simulations (once the initial atmosphere mass is forgotten) are shown in Fig. 5.9. Several observations can be made regarding these results. Firstly, the atmosphere mass evolution is very stochastic, very different to that seen for the Earth in Chapter 3. The median atmosphere masses recorded are lower than the analytically predicted stalling masses, and while the upper and lower limits of the atmosphere mass distributions are similar Venus spends more time at higher atmosphere masses than Mars and so this discrepancy is greater for Mars. Furthermore, Mars shows more variation between the results for individual simulations. The median atmosphere mass for Venus can be seen to evolve over time, increasing over the final $\sim$ 100 Myr of the simulation. Finally, the distribution of atmosphere masses appear to be bi-modal, with a low-mass and a high-mass peak shown for both planets. The explanations for these effects are described in turn below.

Stochasticity To understand why the evolution of the atmospheres on Venus and Mars is stochastic it is necessary to consider the timescale over which the atmosphere evolves towards the analytically predicted stalling mass, how this depends on the size of the largest impactor, and the timescale on which this largest impactor is expected to be sampled by the code. As was discussed in Chapter 4, the stalling mass is strongly dependent on the size of the largest expected impactor. The size distribution and mass accretion rates described in §5.1.1 and

§5.1.1 together set the largest impactor, $D_{\rm lim}$, sampled over a given timescale, $\tau_{\rm sample}(D_{\rm lim})$, through equation 4.8. On short timescales the size of the largest impactor is not necessarily the maximum possible impactor size ($D_{\rm max} = 1000$ km, which was used to calculate the analytic stalling mass prediction), and so the atmosphere evolves under bombardment by a truncated size distribution, towards a lower stalling mass than predicted for the full size distribution.

Whether the atmosphere will evolve smoothly towards the stalling mass predicted for the full size distribution or undergo depletion and stochastic replenishment depends on the relative values of the sampling timescale and the atmosphere evolution timescale ($\tau_{\rm evolve}(D_{\rm lim}, m_0)$, defined by equation 4.9). A full discussion of this effect is given in §4.3.2, but in summary if the atmosphere evolves due to impacts smaller than the largest impactor more rapidly than these impactors are expected to be sampled (i.e. $\tau_{\rm sample}(D_{\rm lim}) > \tau_{\rm evolve}(D_{\rm lim})$) then the atmosphere will undergo cycles of rapid depletion to the stalling mass expected for impactors smaller than $D_{\rm lim}$ followed by stochastic accretion of larger impactors, resulting in stochastic evolution. Smaller impacts are more erosive, according to my adopted impact prescriptions, when they are less volatile-rich and when they are faster relative to the target body escape velocity. Atmospheres undergoing bombardment by a population of impactors dominated by dry left-over planetesimals (as is assumed for the terrestrial planets in this dissertation) are therefore more susceptible to experiencing this kind of stochastic evolution than would be expected for more volatile-rich impactors.

Comparison to the Earth For the nominal size distribution and total impacting mass described in §5.1.1, there are ~ 50 objects with $D > 500$ km (capable of delivering a volatile mass of $\sim 10^{-8}$ M$_\oplus$) expected to impact Venus in each simulation, and ~ 5 expected to impact Mars. However the number of such objects expected to impact the Earth in the simulations performed in Chapter 3 is similar to that for Venus, so it is reasonable to ask why the Earth did not undergo stochastic evolution. While the impactor sampling timescales are similar for Venus and the Earth (and only marginally longer for Mars), the atmosphere evolution timescale for the atmospheres on Venus are Mars are both shorter than for the Earth. A small contribution to this arises from the hotter atmosphere temperature assumed on Venus (500 K) however as discussed in §5.3.3 even "cool" Venus undergoes stochastic evolution, and this effect does not apply to the "mid" Mars case.

The dominant factor causing more rapid atmosphere erosion on Venus and Mars is the increase in the impact velocities. Assuming a characteristic value of $\xi = \frac{v_{\rm rel}}{v_{\rm pl}}$ for each population means that the relative velocity of the planetesimal population with respect to the

planet increases as the semi-major axis of the planet decreases, and thus the velocity ratio distribution for impacts onto Venus (which has a similar escape velocity to the Earth) is higher than onto the Earth. Mars, while experiencing slower absolute impact velocities, has a significantly smaller escape velocity than Venus or the Earth and thus the velocity ratio is also higher than for the Earth. This can be seen from the impact velocity distributions for the nominal left-over planetesimals shown in Fig. 5.10. Impacts onto Venus and Mars are therefore more erosive than onto the Earth, and so these planets have shorter atmosphere evolution timescales and so the atmospheres evolve stochastically. These faster impacts also explain the lower predicted atmosphere stalling masses for these planets relative to the Earth.

Comparison to the analytic stalling mass Stochastic evolution results in the atmosphere tending towards a quiescent level lower than the analytically predicted stalling mass, with the stochastic delivery of the volatiles in larger impactors causing stochastic deviations. The stochasticity seen in Fig. 5.8 is reflected in the median atmosphere mass sampled in the final 300 Myr of the simulations, which are 6.78×10^{-10} $M_\oplus$ for Venus and 4.64×10^{-13} $M_\oplus$ for Mars, lower than the predicted stalling masses of 3.9×10^{-8} $M_\oplus$ and 9.5×10^{-9} $M_\oplus$ respectively from §5.2. The distribution of atmosphere masses shown in Fig. 5.9 include the predicted stalling masses, but span from the lower atmosphere mass limit to values as high as 10^{-7} $M_\oplus$ (the maximum mass in volatiles that can be delivered by a single large left-over planetesimal), in agreement with the qualitative stochasticity predictions.

Despite the similar analytically predicted stalling masses for Venus and Mars, the results in Fig. 5.8 show differences between the two planets: Mars evolves more slowly than Venus initially, but once the initial atmosphere mass has been eroded it is more variable. The shorter sampling timescale for Venus relative to Mars means that the limiting impactor size at which $\tau_{\rm evolve} = \tau_{\rm sample}$ is larger on Venus than Mars, and thus the quiescent atmosphere mass towards which the atmosphere mass evolves is higher and the magnitude of stochastic variation is less.

Additionally, individual simulations of Mars' atmosphere show substantially more variation (with median-sampled atmosphere masses varying between $\sim 10^{-18} - 10^{-8}$ $M_\oplus$) compared to individual simulations of Venus. If sufficient mass is delivered by a single large, slow impactor, the atmosphere evolution timescale can become longer than the remaining simulation time and thus the atmosphere will not transition into the stochastic regime. Due to the lower impact flux onto Mars than Venus the evolution timescale is longer on Mars, and so this effect is more common, resulting in the variation between simulations on Mars.

Time-dependent evolution A further feature observed in the evolution of both atmospheres is the time-dependence of the median atmosphere mass, which is used to demonstrate general trends in the results of multiple simulations. For Venus, this can be seen as a tendency for the atmosphere to decrease between $200 - 400$ Myr before growing in the final 150 Myr of the simulations. This phenomenon arises from the time-dependence of the impactor velocity distribution. Fig. 5.2 shows that the nominal population of left-over planetesimals contain none of the very slowest impactors between $200 - 400$ Myr, which results in higher rates of atmosphere erosion. This is potentially due to the small number of particles in the original N-body dynamical simulations, motivating the consideration of an alternative distribution in §5.3.3. Atmosphere survival is more likely at late times not only due to the relative increase in impacts by slower objects but also as a result of the general decay in impact flux rates. This can be seen in the individual atmosphere mass profiles shown in Fig. 5.8, at early times the delivery of $\sim 10^{-7}$ $\mathrm{M}_{\oplus}$ in volatiles is eroded in approximately 0.1 Myr, by the end of the simulation this can take as long as 50 Myr. The impact flux decay, and thus the increase in the atmosphere evolution timescale, can also result in the transition of the atmosphere on Mars from stochastic to non-stochastic evolution at late times, as discussed above. These observations highlight the importance of considering the time-dependence of the impact velocity distribution and the overall decay in impact flux over time.

The bi-modal atmosphere mass distribution A final observation from Fig. 5.9 is the bi-modal distribution of recorded atmosphere masses. The fraction of atmospheres with masses below $\sim 10^{-17}$ $\mathrm{M}_{\oplus}$ is approximately 20% for Venus in the final 300 Myr, and almost 50% for Mars. This apparent peak in the atmosphere mass distribution is an artefact due to the accretion of a finite mass of volatiles during the smallest time-step implemented in the code. This should more accurately be considered an upper limit on the atmosphere mass, determined by the combination of mass flux and minimum time-step, $\Delta t_{\mathrm{min}} = 1$ yr,

$$m_{\mathrm{limit}} = \Delta t_{\mathrm{min}} \times \dot{m}^{+}_{\mathrm{imp}}(t).$$

While accretion efficiency decreases as the atmosphere mass decreases it is still non-zero for the left-over planetesimals at very low atmosphere masses, and so some fraction of the impacting material arriving in this minimum time-step will be accreted, and contribute a mass $m_{\mathrm{limit}} f_{\mathrm{acc}} x_{\mathrm{v}}$ to the atmosphere.

Impactor dynamics

I now investigate the sensitivity of the results to the assumed dynamics of the left-over planetesimal populations. While the distributions of the seven dynamical cases discussed in §5.1.1 and shown in Fig. 5.3 appear similar they are not identical. A key factor influencing the atmosphere evolution is the relative number of impacts by the slowest objects, as they deliver more volatiles to the atmosphere and cause lower atmosphere erosion than faster impactors. As discussed in §3.2.4 there exists a critical impact velocity ratio below which impacts of a given composition result in net atmosphere growth and above which they erode the atmosphere. For the nominal left-over planetesimal properties, this value is $v_{\rm imp} \approx 1.12\ v_{\rm esc}$ for the Venus "mid" atmosphere case, and $v_{\rm imp} \approx 1.04\ v_{\rm esc}$ for Mars.

While the behaviour of the realistic impactor populations constructed in §5.1.1 is more complicated than the toy model used to calculate these critical impact velocities, sampling from distributions with relatively more slow impactors should result in higher atmosphere masses. The nominal (case 2) used previously in the results presented above contains an intermediate fraction of impactors with the slowest impact velocities ($f_{\rm V,crit} = 0.075$ and $f_{\rm M,crit} = 0.018$ for Venus and Mars respectively). Cases 5 and 6 represent "slow" distributions for Mars and Venus respectively ($f_{\rm V,crit} = 0.23$ and $f_{\rm M,crit} = 0.065$), as the result of the inclusion of single high-probability particles in the distribution, as discussed in §5.1.1. Running the code 10 times for these cases, assuming the nominal impactor composition and "mid" atmosphere conditions, produces the mass evolution and distribution of final atmosphere masses sampled in the final 300 Myr of the simulations shown in Fig. 5.11.

Considering first Mars, the "slow" case results in some atmosphere depletion, but does not tip over into the stochastic regime, with atmosphere masses in the final 300 Myr ranging between $(3.5 - 1.4) \times 10^{-7}$ $\rm M_\oplus$. The analytically predicted stalling mass for the "slow" case (5.8×10^{-8} $\rm M_\oplus$) is lower than these values, however the numerical atmospheres in this case are still evolving and so would not be expected to have reached the predicted stalling mass. For Venus, the atmospheres do evolve stochastically, but the "slow" case results in a higher median atmosphere mass of 2.04×10^{-9} $\rm M_\oplus$, than the nominal case, as can be seen in the distributions shown in Fig. 5.11. The analytic prediction (1.7×10^{-8} $\rm M_\oplus$) is again higher than the numerical results due to the stochastic effects described above.

These simulations demonstrate the importance of considering the time evolution of the impactor velocity distribution. In this case, the slowest (atmosphere-growing) impactors are not distributed evenly throughout the simulation time period. From Fig. 5.3 it can be seen that

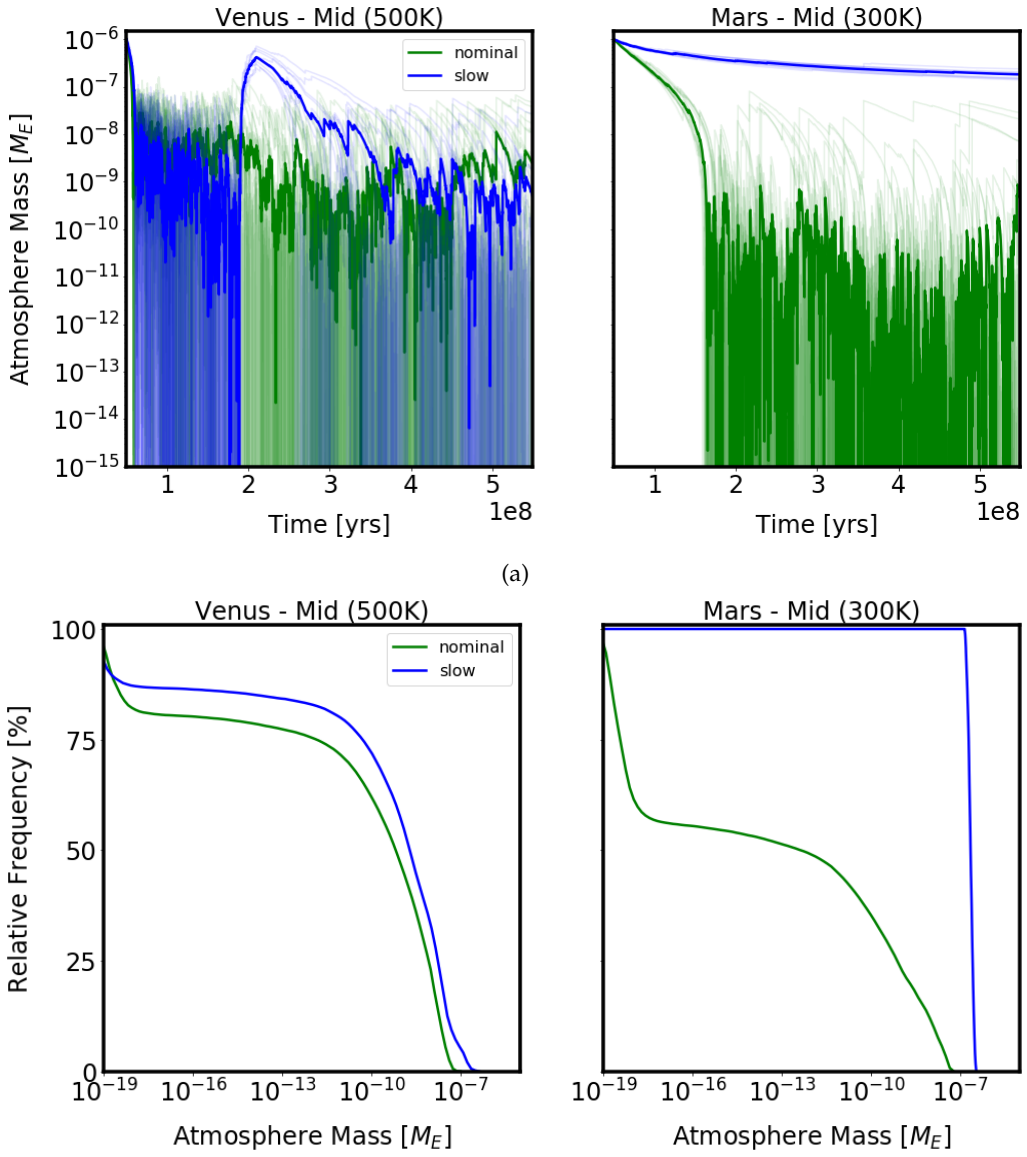

Figure 5.11: The results considering the evolution of Venus and Mars (the "mid" atmosphere case only) under bombardment by the nominal population of left-over planetesimals, showing three alternate dynamical cases. The top panels (a) show the total atmosphere mass as a function of time, with Venus shown in the left panel and Mars in the right panel. The individual atmosphere mass profiles are shown by thin transparent lines with the median atmosphere evolution shown as a thick line, with the colour indicating the dynamical case. The bottom panels (b) show the distribution of atmosphere masses recorded over the final 300 Myr of the numerical simulations. These results are produced by running the numerical code 5 times each. Individual results are shown by thin transparent lines with the distribution for all atmosphere masses shown as a thick line on each panel.

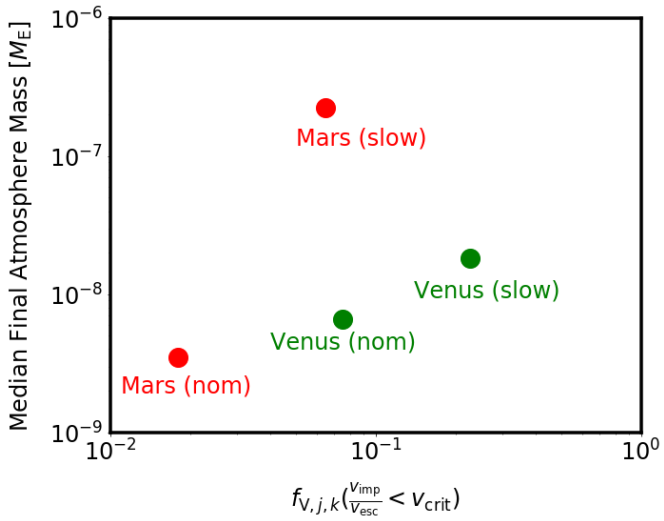

Figure 5.12: The relationship between the final recorded atmosphere mass shown in Fig. 5.11b and the fraction of impactors in the velocity distribution with velocities below the critical impact velocity described in the text (predicted to grow a 10^{-6} $M_\oplus$ mass atmosphere on both Venus and Mars. The different cases are shown by different colour markers with the results shown as for Mars and Venus shown as crosses and filled circles respectively.

the time-step in which the anomalously slow single particle was present coincides with a sudden increase in the atmosphere mass by orders of magnitude in all the simulation runs seen in Fig. 5.11. At later times, after $\sim$ 450 Myr, the atmosphere masses are typically lower than those seen in the nominal case, as the impactors at this time are faster. The analytically predicted stalling mass is calculated assuming a single velocity distribution, and hence does not capture this variation.

The influence of the impactor dynamics are summarised in Fig. 5.12, which shows the median atmosphere mass sampled in the final 300 Myr of the simulations as a function of the fraction of impactors below the critical impact velocity. A positive relationship between the average atmosphere mass and $f_{\mathrm{V/M,crit}}$ can be seen for each planet, demonstrating that the dynamics of the left-over planetesimals is critical in determining the effect of impactors on the atmosphere. These results should be interpreted with caution, as the slow distributions have been skewed by the inclusion of single low-velocity, high-probability particles and so may not be realistic. They do indicate how the atmosphere evolution may be influenced by a slower distribution of impactors, regardless of the physical motivation behind such a distribution. Further work remains to be done to fully quantify the variation introduced by the full range of potential dynamics for the left-over planetesimal population.

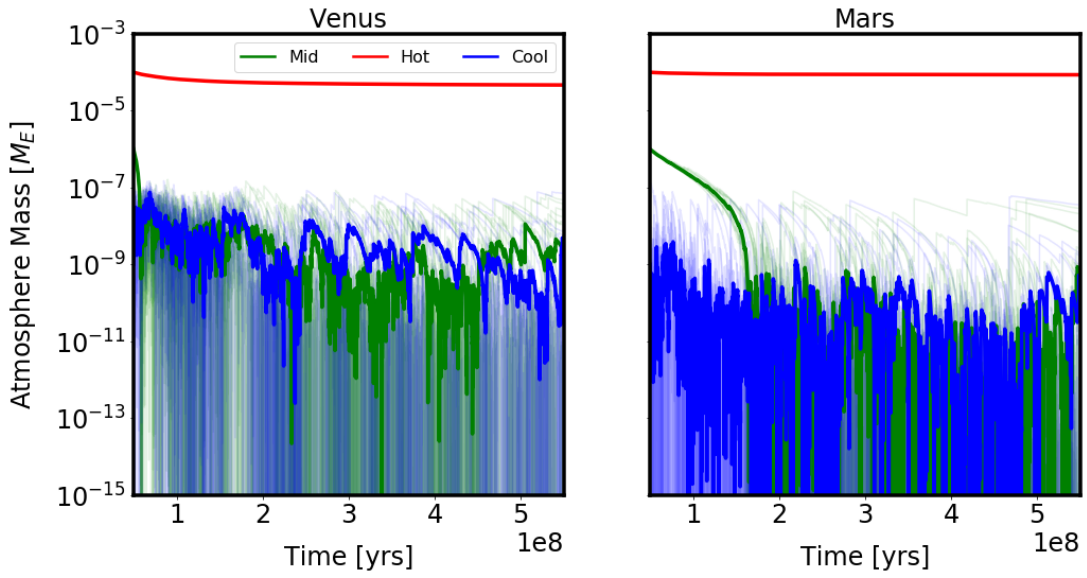

(a)

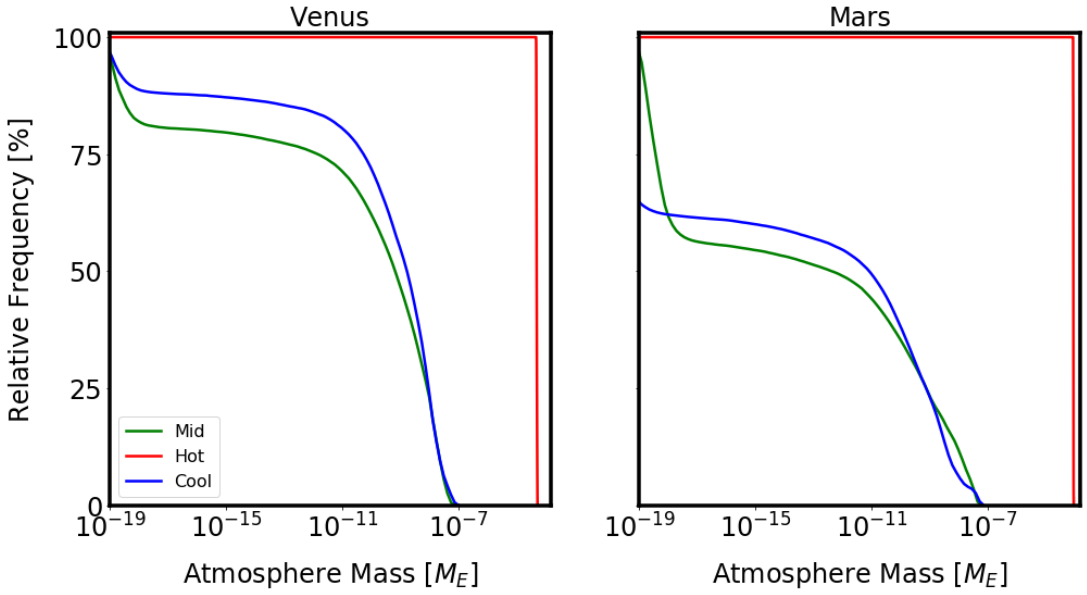

(b)

Figure 5.13: The results considering the evolution of Venus and Mars under bombardment by the nominal population of left-over planetesimals, showing three different initial atmosphere conditions. The top panels (a) show the total atmosphere mass as a function of time, with Venus shown in the left panel and Mars in the right panel. The individual atmosphere mass profiles are shown by thin transparent lines with the median atmosphere evolution shown as a thick black line on each panel. The bottom panels (b) show the distribution of atmosphere masses recorded over the final 300 Myr of the numerical simulations. The individual distributions are shown by thin transparent lines with the results for all runs shown as a thick black line on each panel. These results are produced by running the numerical code 10 times each.

Initial conditions

Finally, I consider how alternative initial atmospheres ("hot", "mid" and "cool", as described in §5.1.2) may evolve as a result of bombardment by the nominal population of left-over planetesimals. The code is run 10 times for each case, with the results shown in Fig. 5.13. The atmosphere mass evolution is shown in the top panels with distributions of the atmosphere masses recorded by the numerical code in the final 300 Myr of evolution shown in the bottom panels. From these plots it can be seen than an initially massive ($m_0 = 10^{-4}$ $\mathrm{M}_\oplus$) atmosphere cannot be completely eroded on either planet by the impacts considered here over the course of the simulation, even when the atmospheric temperature is as hot as 700 K on Venus. The atmosphere mass is reduced by around a factor of a half on Venus, and by approximately 14 $\%$ on Mars, with the final atmosphere made up of ~ 5 $\%$ and ~ 0.2 $\%$ material delivered by the left-over planetesimals respectively (with the remainder consisting of the initial atmosphere material). The total mass of impacting material assumed for the nominal population is not sufficient to erode this massive an initial atmosphere on either planet. The impacts are still erosive, and so a more massive population of impactors might be capable of removing the entire atmosphere mass. This potential is discussed in §5.4.2.

The "mid" and "cool" cases both evolve stochastically on Venus and Mars once the initial atmosphere mass has been forgotten. On Venus, the two cases appear very similar, however considering the distribution of atmosphere masses in Fig. 5.13b the "cool" atmosphere spends more time at slightly higher atmosphere masses, despite starting with an initially smaller atmosphere. This is also seen in the median atmosphere masses shown in table 5.3, which is a factor of ~ 2.5 higher compared to the "mid" atmosphere results, in agreement with the approximate doubling of the predicted atmosphere stalling mass calculated in §5.2. This difference is a result of the dependence of the atmosphere scale height on temperature, cooler atmospheres are more contracted and thus harder to remove as a result of impacts. A similar difference is seen between the "mid" and "cool" atmospheres on Mars, with the median atmosphere masses shown in table 5.2 differing by a factor of ~ 20. In addition to the general increase in atmosphere mass, the "cool" Mars case (which is most similar to the present-day Martian atmosphere) also appears less stochastic than the "mid" case, particularly towards the end of the simulations when the impact flux decreases.

5.4 Discussion

5.4.1 Variation in the impactor population parameters

I can consider how changing the assumed impactor properties may alter my results. The results of §5.3.1 have shown that the atmosphere evolution resulting from bombardment by asteroids is determined by the volatile content of the largest impactors. A more volatile-rich population of asteroids (for example if the proportion of C-type material was higher than previously assumed) would therefore be expected to result in greater atmosphere growth. It should be noted that impacts by these large asteroids are not expected to be common occurrences unless the total impacting mass of asteroids was significantly higher.

The effect of the comet population on the atmosphere is only likely to become significant if the total impacting mass was increased significantly, which is not physically likely. However a more volatile-rich population would result in higher predicted stalling masses and thus potentially result in growth of the initially smallest atmospheres.

The atmosphere evolution expected for the population of left-over planetesimals is very sensitive to the assumed dynamics of the impacting population. If the impactors were slower for any reason, for example with a distribution comparable to that calculated for the Earth in Chapter 3, then the evolution of atmospheres on Venus and Mars may not be stochastic, instead resulting in steady depletion to a lesser degree than observed in §5.3.3. Conversely, a faster distribution would result in higher rates of atmosphere erosion leading to lower median atmosphere masses and also more stochastic behaviour. If the volatile content of the left-over planetesimals was increased, then the stochastic delivery of volatiles by single impactors would be expected to be higher, with the opposite expected if they were more volatile-poor. A combination of a slower and more volatile-rich impacting population may even result in atmospheric growth on Venus and Mars, if the initial atmosphere mass was sufficiently low.

Considering the effect of all impactor populations combined would result in predictions similar to those made in Chapter 3 for the Earth, with the majority of simulations producing results similar to those found for the left-over planetesimal population alone (due to their dominant mass). In a few % of runs however, a stochastic large asteroid impact may occur, and if this delivered sufficient mass for the resulting atmosphere to survive the remainder of the simulation without being eroded back into the stochastic regime the final atmosphere would be massive and dominated by material delivered by the asteroid.

5.4.2 An earlier start time

It is possible to consider how the atmosphere evolution may change if an earlier start time was used for the simulations, using the extended impactor populations considered in §5.1.1. These populations had similar velocity distributions to the nominal time period considered in the rest of this chapter, but extending the period of bombardment considered would result in an increased total impacting mass for all three populations. The analytically predicted atmosphere stalling mass is independent of the total mass of impacting material, but the timescale on which the atmosphere evolves is not. It is therefore expected that atmospheres that reach their predicted stalling masses in the results presented above (noting that this could manifest as stochastic evolution) will not show quantitatively different evolution if the start time for the simulation was to be extended backwards. However, the initially hot and massive atmospheres considered in §5.3.3 never reached a steady state, and so significantly increasing the mass of impacting material by extending the start time backwards could deliver enough material to tip these atmospheres into the stochastic regime that is seen for the other initial atmospheres. The asteroid and comet populations also failed to reach a steady state, but even considering an extremely early start time of $t_0 = 15$ Myr would not increase their total population masses sufficiently to be comparable to the mass of left-over planetesimals, and so the influence of these populations on the final atmosphere masses is still likely to be minor. Numerical simulations of this effect are left for future study.

5.4.3 Comparison with other studies

My conclusions regarding Venus and Mars can be compared to those of Pham et al. (2011), de Niem et al. (2012), Sakuraba et al. (2019) and Wyatt et al. (2019), which made use of different impact prescriptions, and assumed different impactor properties. Combined with the different methods of calculating the atmospheric evolution these result in different predictions for the evolution of Mars and Venus' atmospheres. The methods adopted by Pham et al. (2011) and de Niem et al. (2012) are described in §3.3.4, and so are not repeated here.

Pham et al. (2011)

Pham et al. (2011) modelled the atmospheres of the Earth, Venus and Mars due to impacts, using an analytic model that assumes a fixed fraction of the impactors have velocities high enough to cause the loss of the polar cap mass. They consider only asteroids and comets, and calibrate the impact fluxes using the Lunar crater record. The initial atmospheric conditions assumed differ from my model, with a higher initial pressures, however the initial

temperatures are comparable to my "cool" states. This paper found that impacts remove atmosphere on Mars but not Venus and the Earth, consistent with my results for asteroids and comets. However the significantly less volatile-rich left-over planetesimal population that is now believed to make up the majority of the Late Veneer mass was not considered in Pham et al. (2011). I have shown both that this population can cause significant erosion resulting in stochastic atmosphere evolution, and that the impactor dynamics can have a significant effect on the final atmosphere mass, making the difference between growth or loss, an effect that was not accounted for in Pham et al. (2011).

de Niem et al. (2012)

The results from de Niem et al. (2012) allow me to consider how advances in the understanding of the dynamical history of the Solar system affect the predicted atmosphere evolution. This is because de Niem et al. (2012) used a similar (although not identical) approach to my model for simulating atmosphere evolution, stochastically sampling from impactor size and velocity distributions to consider the atmosphere evolution of Mars and the Earth undergoing impacts by asteroids and comets. The velocity distributions used for these impactors are calculated from simulations of the first Nice model (Gomes et al., 2005; Morbidelli et al., 2010), and while the values for Mars are not shown those for the Earth appear similar to those I calculated for the left-over planetesimals in §3.1.1.

I can compare my results for asteroids and comets to those from de Niem et al. (2012). While I predict atmosphere erosion resulting from comet impacts in all cases, they result in the greatest atmosphere growth in de Niem et al. (2012). This is in part due to the denser and less volatile-rich comet composition assumed in de Niem et al. (2012) (which would alter my prediction for no accretion of the largest comets) and in part due to the higher velocities sampled by my distributions. For the asteroids, my results predict growth of initially small atmospheres, but erosion of more massive atmospheres due to the lack of large impacts. The effect of stochastically sampled large impactors was also noted as significant in de Niem et al. (2012).

Importantly, the influence of the left-over planetesimals (now considered to dominate during this period of bombardment) in my model results in significantly different overall conclusions due to the slower impact velocities and very volatile-poor composition of this population. This is in agreement with the result from de Niem et al. (2012) that decreasing the impactor volatile fraction to < 0.2 % results in atmosphere erosion. These differences reinforce the

importance of reconsidering the evolution of the terrestrial planet atmospheres in light of the advances in the understanding of the bombardment history of the Solar system.

Sakuraba et al. (2019)

In Sakuraba et al. (2019) a model for element partitioning during atmosphere evolution, specifically considering reservoirs for nitrogen, carbon dioxide and water was presented. They considered atmosphere temperatures similar to my "cool" Mars, "hot" Venus and nominal Earth, finding growth of an initially 0.1 bar ideal atmosphere for impactors with volatile content between $0.1 - 1$ %. Erosion occurs only if the volatile content is reduced to 0.01 %, in agreement with my findings of erosion by dry left-over planetesimals but growth by volatile-rich asteroids. Sakuraba et al. (2019) also investigated an extensive range of initial atmosphere pressures for Venus ($50 - 1000$ bar) finding that while massive atmospheres do experience significant erosion as a result of impacts with 0.1 % volatile content, a sufficiently massive initial atmosphere could survive to the end of the expected period of bombardment with a significant mass of N_2 remaining. If Venus retained a significant fraction of a primordial atmosphere but the Earth and Mars did not, potentially through the mechanisms discussed in §1.5.2, then the enrichment of Venus' noble gases by approximately two orders of magnitude compared to the Earth can be explained (Sakuraba et al., 2019).

5.4.4 Other atmospheric processes

I have not included in my model any atmospheric processes besides impacts. This is a reasonable approximation during the period of time when the impact flux is high and thus the effect of impacts dominate atmospheric evolution, motivating the $t = 550$ Myr end time in the simulations. Considering three initial atmosphere conditions on each planet allows me to account for some of the uncertainties in the prior atmospheric evolution, which is very poorly constrained. This is preferable to extrapolating the left-over planetesimal flux back in time, as the EUV flux from the young Sun is believed to have been high and thus could drive atmosphere loss through hydrodynamic escape (described in §1.3.3), which is not accounted for in my model.

Furthermore, extrapolating backwards in time would require more detailed consideration of the effect of giant impacts, which was shown in §2.7 to be sensitive to the choice of impact prescription. These impacts could result not only in significant atmosphere and planet erosion, but also cause global magma oceans which could exchange volatiles with the

atmosphere (Elkins-Tanton, 2012). Impact-triggered outgassing was shown to potentially contribute substantial masses of volatiles to the atmosphere of Earth in §3.3.5, in a non-trivial manner that is not currently accounted for in my model.

The atmospheres predicted in this Chapter are unlikely to be stable, and so should continue to evolve in the period of time following the simulations. Photo-dissociation will act on various timescales to destroy some delivered species, while volcanoes can outgas new material, influencing the atmosphere composition. For this reason, the discrepancies between the final atmosphere compositions predicted above and those observed on Venus and Mars today are not necessarily a reason to discount my results.

5.4.5 Possible observational signatures

As discussed in §1.2.5, Venus is predicted to accrete 0.8% wt. mainly in enstatite-like left-over planetesimals (Gillmann et al., 2020). For the nominal "mid" planetesimal case on Venus, the planet mass increases by $0.8 - 1.1$ % wt. between the different runs, consistent with this observation. The observational evidence on Mars suggests the accretion of between $0.25 - 1.4\%$ wt (Brasser et al., 2016; Marchi, 2020) in a volatile-poor Late Veneer. My nominal "mid" planetesimal results show an increase in the planet mass of $0.3 - 1$ % wt., consistent with these observations.

Considering the earlier start time, as described in §5.4.2, the associated increase in total impacting mass could result in a corresponding increase in the accreted mass of material. The upper range of observed Late Veneer masses would permit this on Mars, but only up to approximately 1.5 times the adopted estimate, less than the addition of ~ 1.7 assumed for a 30 Myr start time discussed in §5.1.1. This potential conflict highlights the uncertainties involved in extrapolating this data backwards in time, supporting the decision to instead consider a range of initial atmosphere conditions.

An initially massive atmosphere on Venus cannot be eroded as a result of impacts during accretion of the Late Veneer in my model. It has been proposed that the Noble gas budget discrepancy between Venus and the Earth could be explained by the survival of a primordial component of the atmosphere on Venus but not Earth. It is therefore possible that the scenario discussed in §1.5.2 in which Venus sustains an early large atmosphere while the Earth and Mars do not could be reconciled with evolution during the accretion of the Late Veneer. However such a massive initial atmosphere mass on Mars cannot have existed unless an

alternative mechanism through which it could be lost before the present day was acting.

5.4.6 Water delivery

The potential for the impactor populations to deliver water to Venus and Mars can be inferred from my results. Adopting the same water fractions (H_2O $\mathrm{wt.\%}$) as used for the Earth in §3.3.3 for the nominal populations of comets, asteroids (weighted average of C- and S-types), and left-over planetesimals of 50% (Mumma & Charnley, 2011), 10% and 0.01% respectively (Barnes et al., 2016) allows comparison of the results for the three planets.

The asteroid populations typically result in delivery of less than 10^{-4} $\mathrm{M_{ocean}}$ in water to both Venus and Mars, however in the rare cases in which a large asteroid impacts either planet up to 0.5% of an ocean of water ($M_{\mathrm{ocean}} = 2.3 \times 10^{-4}$ $\mathrm{M_\oplus}$) can be delivered in a single event. Due to the low accretion efficiency of comets combined with their small population masses, these populations deliver negligible masses of water to Venus and Mars ($< 5 \times 10^{-5}$ $\mathrm{M_{ocean}}$, despite their high water content.

The largest contribution to water delivery on Venus and Mars comes from the left-over planetesimals, which deliver around 0.4 $\%$ of an ocean mass of water to Venus, but less than 0.1% of an ocean mass to Mars. These predicted masses of delivered water are insensitive to the assumed initial atmosphere state and to the dynamics of the left-over planetesimals. If the composition of the left-over planetesimals contained more water by weight then this population could deliver at least an ocean mass of water to both planets. The total current water content of Venus is believed to be low, but estimates for Mars are uncertain and so it is challenging to compare these predictions to observations.

This water was expected to be in the liquid phase on Earth, and this is likely to be the case for the "cool" Venus and "cool" and "mid" Mars cases, but should be vapourised in the atmosphere for the hotter cases. The total mass in water delivered by left-over planetesimals to Venus and Mars over the entire simulation is less than 10^{-6} $\mathrm{M_\oplus}$, which when present as the initial atmosphere mass is rapidly removed by impacts on both planets. This suggests that including this contribution to x_{v} would not change the qualitative conclusions regarding stochastic atmosphere evolution, however the precise effect it may have on the quantitative results of the numerical simulations is left for future study.

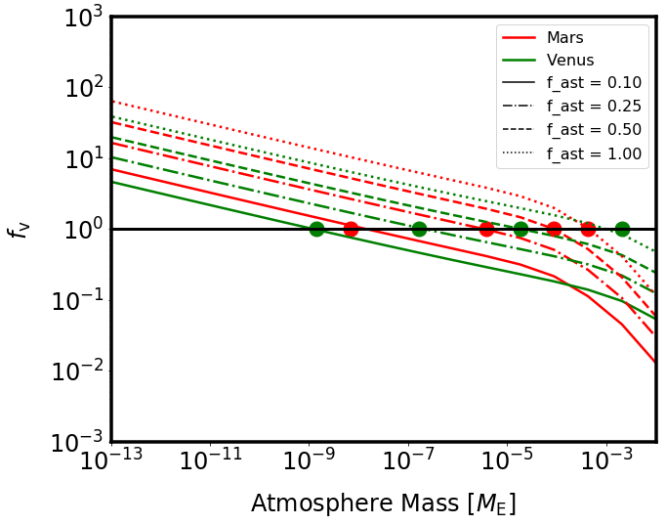

Figure 5.14: The ratio of atmosphere mass gain to mass loss as a function of atmosphere mass for Venus (green lines) and Mars (red lines). The comets are assumed to contribute zero mass, and the asteroids are equal S- and C- type with fraction as shown by the line style. The remaining contribution is made up of equal contributions from the two left-over planetesimal dynamics considered.

5.4.7 Is the current Martian atmosphere stable?

Mars currently has a low-mass, cool atmosphere ($m \approx 10^{-9}$ M$_\oplus$) comprised predominantly of CO_2. Data from the Martian Insight mission suggests a current cratering rate of approximately 1.65×10^{-6} km^{-2} yr^{-1} with $D_{\rm eff} > 4$ m (Daubar et al., 2013). This corresponds to an approximate impact mass flux of $\sim 10^{-15}$ M$_\oplus$ yr^{-1}, assuming an average impactor density of 2.5 g cm^{-3}. This is low, but not zero, and so it is possible to ask whether this atmosphere is currently undergoing erosion or growth as a result of this continued bombardment.

Considering the velocity distribution I calculated in §5.1.1 for Mars at the latest times in the original simulation data, the resulting predicted stalling masses are lower than those calculated using the velocity distribution over the entire time period of the simulations. This is the result of a small increase in the typical impact velocity ratio onto Mars over time. If these impacts are still dominated by dry left-over planetesimal impactors then this would imply that the current atmosphere is unstable to erosion by impacts. However, the relative contribution from the different populations will change over time. There are no cometary impacts in my model after 500 Myr, so given this population's very low current impact it rate it can be neglected in the following. At early times the left-over planetesimals dominate by around $1000\times$ in mass, but the ratio of asteroid to planetesimal impacts increases over time as the decay in impact flux is more rapid for the left-over planetesimals than the asteroids.

Considering the values of $f_{\rm v}$ calculated as a function of impactor mass for the combined effect of asteroids and left-over planetesimals using a range of different asteroid fractions as shown in Fig. 5.14 it can be seen that bombardment of this nature could result in depletion of the present day atmosphere ($\sim 10^{-9}$ M$_{\oplus}$) if asteroids were to make up less than $\sim 10\%$ of the overall impactor distribution by mass. However if asteroidal material dominates the current distribution of impactors the net result on the atmosphere is growth. Any such atmosphere growth is limited by the total mass of impacting material, which is not large enough to deliver sufficient impactor material to grow the atmosphere to the stalling masses predicted in Fig. 5.14. The current atmosphere on Mars may therefore be removed or added to by current impacts, but the present day impact flux is so lows that this atmosphere evolution is minor in comparison to other processes.

5.5 Conclusions

In this chapter I have investigated the evolution of potential atmospheres on Venus and Mars due to impacts during the final stages of accretion. To do this I have calculated distribution of impact velocities and fluxes from the results of dynamical simulations of the Solar system for asteroids, comets and left-over planetesimals (Nesvorný et al., 2017a, 2013; Morbidelli et al., 2018). I apply these distributions in my numerical code and analytic model for the stable stalling mass, making appropriate assumptions regarding the impactor and planet properties.

Asteroids cause stochastic growth of initially low-temperature thin atmospheres on Venus and Mars, however the low total mass of the asteroid populations means that the size distribution of impacting objects is truncated at sizes of the order of ~ 100 km and this results in depletion of initially more massive atmospheres. The exception to this is the rare case (a few $\%$ of runs) when a larger impactor is sampled and can result in significant atmosphere growth. The comet populations result in minor atmosphere depletion in all cases, due to the low total population mass and low accretion efficiency of the nominal comet population.

The dominant population of left-over planetesimals results in stochastic atmosphere evolution on both Venus and Mars. This results from the efficient rate of atmospheric erosion caused by fast impacts (relative to the planet escape velocity), relative to the rate at which large (atmosphere replenishing) impactors are expected to impact the planets. The analytically predicted stalling masses are similar for both planets, $\sim 10^{-8}$ M$_{\oplus}$, but the results from the numerical code show lower median atmospheres on Venus (6.78×10^{-10} M$_{\oplus}$) and Mars (4.64×10^{-13} M$_{\oplus}$). The lower masses seen in the numerical results for Mars than Venus are

due to the lower total impacting population mass onto Mars, which combined with the efficient atmosphere erosion caused by smaller left-over planetesimals results in the atmosphere spending more time at lower atmosphere masses.

Considering the potential variation in the impactor dynamics, it is possible for an initially Earth-like atmosphere on Mars to survive with only moderate erosion, or be tipped into the stochastic regime depending on the fraction of impactors with velocity ratios below a critical value. For Venus, the effect of this variation is less extreme, but can still result in noticeable variation in the median atmosphere mass by a factor of ~ 10.

Initially cool and thin atmospheres on both Venus and Mars rapidly forget their initial state, and show resulting atmosphere evolution that is similar to warmer initially intermediate mass atmospheres. The cool case results in slightly higher median atmosphere masses than the intermediate case due to the lower temperatures making them harder to erode. However, initially hot and massive atmospheres (similar to the current atmosphere on Venus) can survive bombardment during the accretion of the Late Veneer without significant mass loss. These results imply that if Venus, the Earth and Mars all had atmospheres similar to their present day masses early in their history then bombardment by a population of enstatite-like left-over planetesimals would result in little change.

Unlike the Earth the atmospheres of Venus and Mars are very stochastic, varying by orders of magnitude over the time period of the simulation, suggesting that the survival of an Earth-like (and therefore potentially habitable) atmosphere over this period of bombardment may be challenging. The composition of the final atmospheres on both Venus and Mars is dominated by primordial material in the case of initially hot, massive atmospheres but dominated by the material delivered by left-over planetesimals for the initially Earth-like or thin, cool atmospheres.

The total accreted solid mass is in agreement with estimates for the Late Veneer mass on both Venus and Mars, with the observational constraints for Mars implying that at most 1.5 times more impactor material could be accreted. This is potentially in conflict with the increased total impacting mass calculated by extrapolating the planetesimal flux backwards in time by 20 Myr.

Further work needs to be done to better understand the influence of the impactor properties not considered in this chapter (for example the composition) on the conclusions made. In

addition, the isotopic signatures of the different atmosphere evolution histories presented in this chapter may provide a useful constrain through comparison to observational evidence.

The key conclusions from the work described in this chapter are:

- Impacts onto Venus and Mars are more erosive than onto the Earth, and can transition into a stochastic evolution regime if the impacts are sufficiently fast;
- The current atmospheres of Venus and Mars would survive the period of bombardment with their total masses relatively unchanged, but it is not possible for a potentially habitable (Earth-like) atmosphere on either to avoid erosion.

6

Minor projects and future work

The following section brings together a number of minor projects that were begun during the writing of this dissertation, based on the results presented in the previous chapters. While this dissertation has focused on the role impacts have played in shaping atmospheres on bodies within our Solar system, there are a large and ever increasing number potentially habitable planets in other planetary systems. Impacts in these systems are likely to occur given their apparent similarity to our own, and thus investigation into the habitability of these planets should include a consideration of how impacts in these systems may shape their atmospheres. In §6.1 the analytic model from §2.3.1 is extended to investigate the potential effect of impacts on exoplanet atmospheres. This is further extended to consider the stability of atmospheres on hypothetical exomoons in §6.2.

In §6.3 I extend the prescriptions for giant impacts, discussed in §2.1.2 and §2.7, to include the potential for significantly larger impacts to cause global melting of a planet's surface resulting in a magma ocean phase. The subsequent cooling of the surface depends on the atmosphere mass, and so I investigate the potential for impact erosion by smaller objects to result in faster magma ocean solidification.

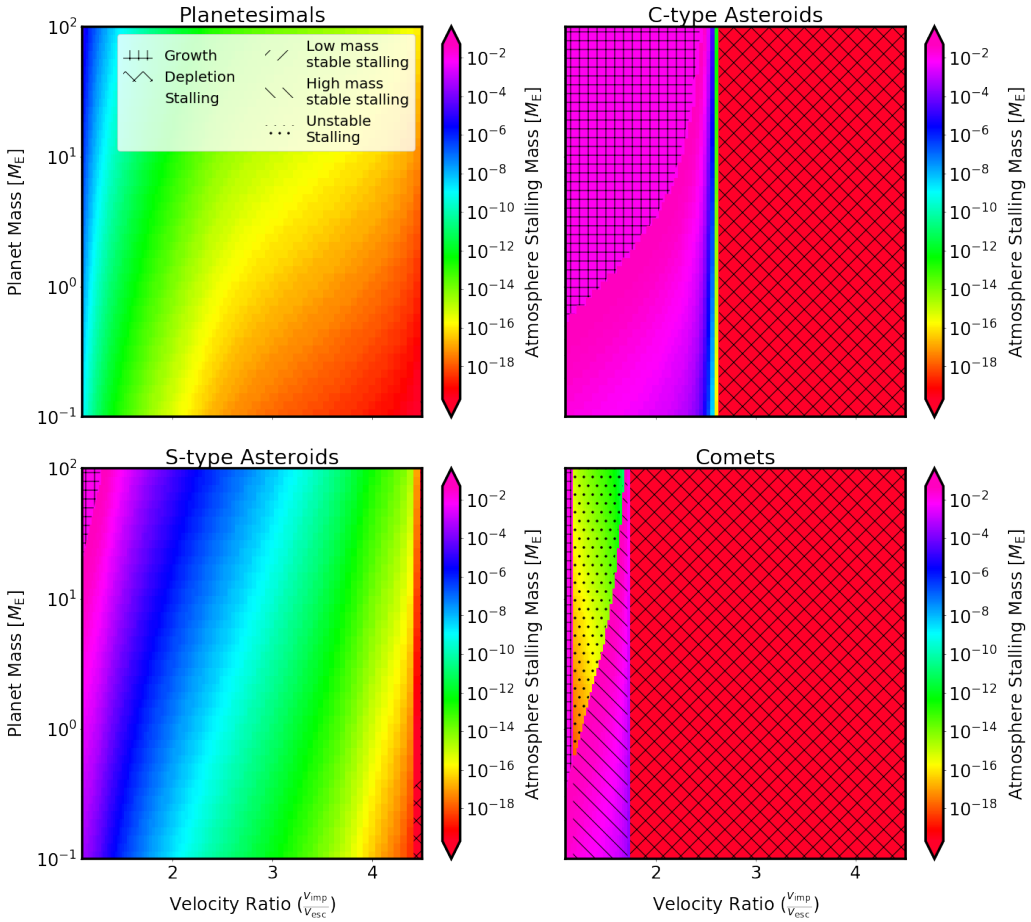

Figure 6.1: The stalling mass (and qualitative atmosphere behaviour regime) as a function of the ratio of impact velocity to planet escape velocity and the planet mass for a rocky ($\rho_{\rm pl} = 5.5$ g cm^{-3}) planet orbiting a Sun-like star at 1 au.

6.1 Exoplanet predictions

6.1.1 A simple single impact velocity model

The method by which $f_{\rm v}$, the ratio of atmosphere mass gain to mass loss rates, can be calculated as a function of atmosphere mass for an assumed target and impactor population was described in §2.3.1. The behaviour of $f_{\rm v}$ as a function of atmosphere mass can be broadly grouped into five qualitative categories of behaviour (growth, depletion, stable stalling, unstable equilibria, and conditional stalling) as illustrated in Fig. 2.4. Which of these profiles occurs depends on both the impactor and planet properties, when considering the evolution of the terrestrial planets in Chapters 3 and 5 typically only the stable stalling mass and runaway atmosphere growth or depletion regimes were observed. In Chapter 4, when investigating the behaviour of the atmospheres of the outer moons, more extreme types of atmosphere behaviour were encountered, with multiple stalling masses and unstable equilibria seen.

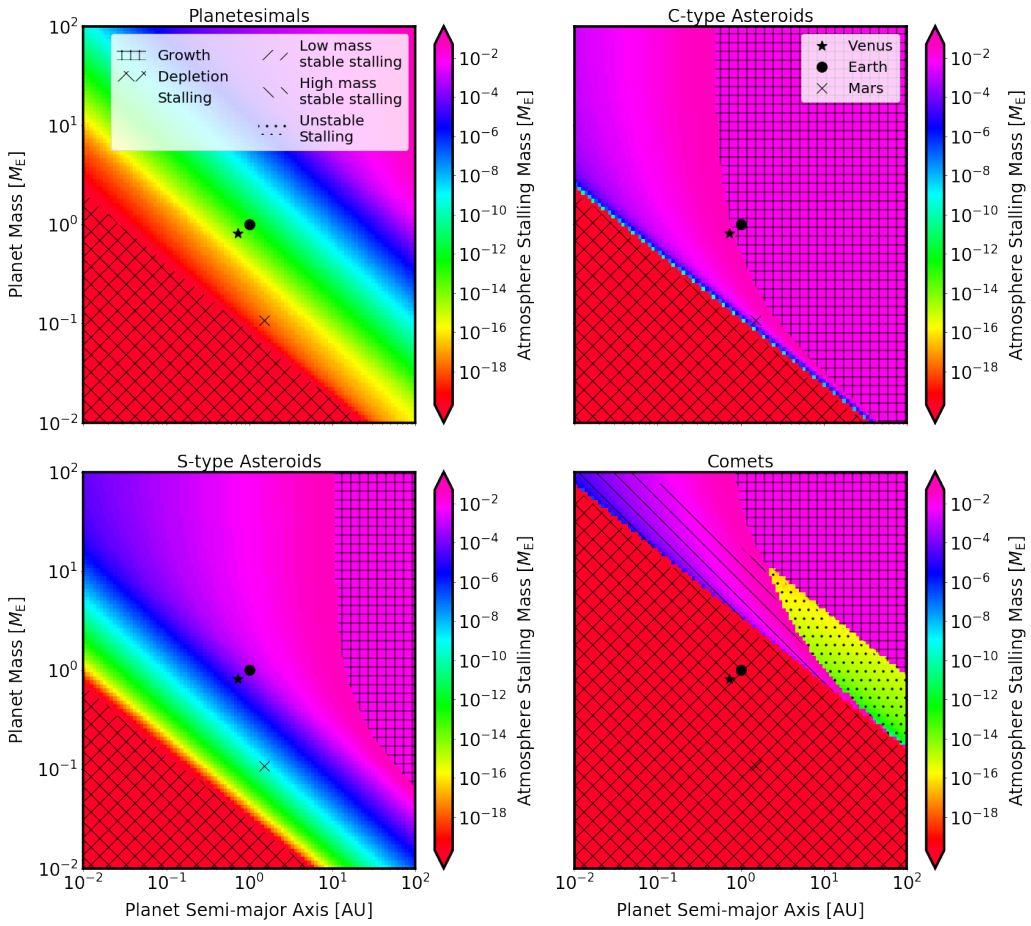

Figure 6.2: The stalling mass (and qualitative atmosphere behaviour regime) as a function of the planet semi-major axis and mass for a rocky planet planet orbiting a Sun-like star, assuming radiative equilibrium atmosphere temperature and a single value for the ratio of impact velocity to planet escape velocity calculated as described in the text.

The work presented so far in this dissertation has investigated the evolution of atmospheres on specific Solar system bodies as a result of impacts by populations of smaller objects with relatively well-constrained properties. There are many more planets than those in our own Solar system, and the numbers continue to increase (Defrère et al., 2018). These exoplanet systems show a wide range of planet types and orbital architectures, but also have many features in common with our own Solar system. These include observations of debris disks, and evidence for exo-asteroids and exo-comets, suggesting the existence of potential impactor populations (Beust & Morbidelli, 1996; Wyatt, 2008; Krivov, 2010; Anglada-Escudé et al., 2016; Kennedy, 2018). It is therefore reasonable to assume that impacts also play a role in the evolution of exoplanet atmospheres.

Applying the analytic model described in §2.3.1 in principle allows the calculation of the stalling mass (if it exists), and the prediction for whether an initial atmosphere is expected to undergo growth or depletion as a result of bombardment. This is complicated by the fact that this stalling mass depends strongly on the fine structure in the distribution of impact velocities which can vary significantly based on the assumptions made regarding the dynamical history of a planetary system. However, it is possible to firstly find out how the stalling mass (and qualitative atmosphere behaviour) depends on impact velocity in different situations, and secondly make some assumptions about the impact velocity and estimate the stalling mass as a function of other system parameters. The process by which this is achieved is described in the following section.

To apply my model, described in §2.3.1, to a wider range of planets without introducing a large number of new free parameters, I make a number of simplifying assumptions. In this preliminary investigation, all planets are assumed to be rock and thus have a density of $\rho_{\rm pl} = 5.5$ g cm^{-3} and to orbit a Sun-like star ($M_* = M_\odot$, $L_* = L_\odot$). The atmospheres are assumed to be Earth-like with a MMW of $\mu_{\rm atm} = 29$, and temperature of 278 K. I further assume that the smaller bodies impacting these planets can be represented by the four nominal impactor populations considered to impact the Earth, Venus and Mars in Chapters 3 and 5. These are comets (icy, low density objects scattered inwards from an exterior belt), asteroids (higher density objects scattered from an intermediate location) and left-over planetesimals (extremely dry, high density objects left over after close-in planet formation is completed); the properties of these populations are summarised in Table 3.1.

To first investigate the dependence of the predicted atmosphere behaviour on the planet mass,

the stalling mass is calculated for a range of planet masses (covering $0.1 - 100$ $M_\oplus$) and a range of values of the ratio of impact velocity to planet escape velocity (spanning $1 - 4.5$), considering the nominal density and volatile fraction for each of the four impactor populations. These results are illustrated in Fig. 6.1 for each of the four populations.

From this plot it can be seen that the stalling mass depends strongly on both the velocity ratio and planet mass, as well as varying significantly between different impactor populations for the same planet mass and impactor velocity. Considering first the results for the left-over planetesimals and asteroids, it can be seen that the stalling mass decreases as impactor velocity increases, because faster impactors tend to be more erosive and also less efficient at delivering volatiles to the planet, as discussed in §2.1.3. As the planet mass is increased, the stalling mass, if it exists, tends to increase. This results from the dependence of the erosional efficiency parameter on $M_{\rm pl}$ and $\delta = \frac{m_{\rm atm}}{M_{\rm pl}}$, giving overall $\eta \propto M_{\rm pl}^{-2/3}$. Larger planet masses therefore have smaller values of η for the same impactor properties. From equation 2.10, this can be seen directly to result in more efficient impactor accretion. While the effect on atmosphere mass loss is more complex it is generally less sensitive to shifts in η than impactor accretion, and so the net effect is a higher value of $f_{\rm v}$ at a given atmosphere mass for each impactor population, and therefore a higher predicted stalling mass.

In general the denser (and less volatile-rich) S-type asteroids and left-over planetesimals result in predictions for the simple stalling behaviour (a single stable equilibrium atmosphere mass, below which atmospheres grow and above which they deplete) for most combinations of impact velocity and planet mass, with the predicted atmosphere stalling masses lower for the left-over planetesimals (the most volatile-poor population considered). C-type asteroids, which are less dense and more volatile-rich show the same trends in behaviour, but faster impacts now result in total atmosphere depletion (as a result of their low accretional efficiency) and slow impacts onto massive planets result in runaway atmosphere growth.

The predicted atmosphere behaviour for comets is more complex. At all planet masses, impacts faster than approximately $1.75\times$ the planet escape velocity result in runaway atmosphere depletion, as a result of the low accretion of these objects discussed in §2.1.4. Extremely slow impacts result in runaway atmosphere mass growth. In between these velocities the atmosphere is unstable to growth. At higher planet masses and slower impact velocities there exists a relatively low mass single unstable equilibrium ($10^{-18} - 10^{-12}$ $M_\oplus$). At lower planet masses and faster impact velocities the atmosphere undergoes conditional (high mass) stalling, which results from the existence of an unstable equilibrium at low atmosphere masses (not shown by the colour scheme) and a stable stalling mass at high

atmosphere masses. In both cases this means that atmospheres that begin below the unstable equilibrium value will experience runaway depletion and those that start above it will experience runaway accretion or accretion up to the stable high atmosphere mass.

Next, if some assumptions can be made regarding the most likely value of the velocity ratio $\frac{v_{\rm imp}}{v_{\rm esc}}$ it is possible to extend the predictions for the atmosphere stalling mass to include the dependence on the planet semi-major axis. The temperature of a planet in thermodynamic equilibrium with the host star with luminosity L_* is given by equation 2.2. Assuming all planets are orbiting a Sun-like star, this equilibrium temperature scales as

$$T_{\rm atm} = 278\ a_{\rm pl}^{-0.5}. \tag{6.1}$$

If each impactor population is then assumed to have a typical impact velocity, characterised by $\xi = \frac{v_{\rm rel}}{v_{\rm pl}}$, the ratio of the relative velocity of the impactor (the velocity of the impactor relative to the planet at infinity) to the Keplerian velocity of the planet, the typical impact velocity can be calculated as

$$\frac{v_{\rm imp}}{v_{\rm esc}} = \sqrt{1 + \left(\xi \frac{v_{\rm pl}}{v_{\rm esc}}\right)^2}, \tag{6.2}$$

where

$$\frac{v_{\rm pl}}{v_{\rm esc}} = 3.4 M_*^{0.5} a_{\rm pl}^{-0.5} M_{\rm pl}^{-1/3} \rho_{\rm pl}^{1/6}. \tag{6.3}$$

For the assumptions made here, this gives

$$\frac{v_{\rm imp}}{v_{\rm esc}} = \sqrt{1 + \left(4.5 \xi a_{\rm pl}^{-0.5} M_{\rm pl}^{-1/3}\right)^2}, \tag{6.4}$$

and so impacts are faster relative to the planet escape velocity for less massive planets at orbital distances closer to their host stars. The assumed values of ξ for each impactor population considered here are shown in Table 2.3, with comets as the fastest impactors ($\xi = 1$), followed by left-over planetesimals ($\xi = 0.5$) and then asteroids as the slowest ($\xi = 0.3$) (Wyatt et al., 2019).

The stalling masses predicted for each of the four populations, with the assumptions described above, are shown in Fig. 6.2. From this plot it can be seen that for all four impactor populations, close-in low mass exoplanets are predicted to experience runaway atmosphere depletion, and the predicted stalling mass increases with increasing planet mass and increasing semi-major axis. This is because increasing either of these parameters decreases the value of the ratio of impact velocity to escape velocity calculated above, and thus makes

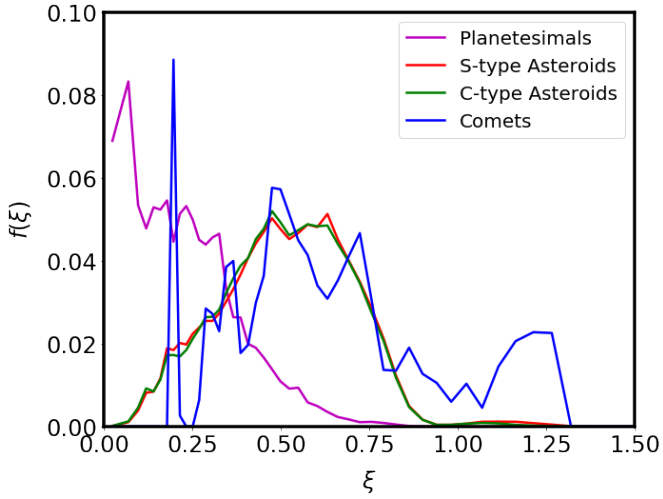

Figure 6.3: The distribution of ξ (the ratio of the relative velocity to the planet velocity) for each of the four nominal impactor populations, calculated from the Earth impact velocity distributions according to equation 6.5. The line colour indicates the impactor population.

impacts less erosive and more efficient at delivering volatiles. As was seen in Fig. 6.1 the region of parameter space with a stable stalling mass is large for left-over planetesimals and S-type asteroids, and smaller for C-type asteroids. Comets display regions of unstable equilibria and conditional (high mass atmosphere stalling). Overall, these results suggest that the planet parameter space for comet impacts is sharply divided between atmospheres that will typically undergo runaway depletion and those that will typically undergo runaway accretion.

6.1.2 Incorporation of a velocity distribution

The approach in the previous section is useful for investigating general trends in the atmosphere stalling mass with planet properties, however assuming a single impact velocity for a population of impactors gives an inaccurate stalling mass estimate. This is obvious when looking at the prediction for Earth undergoing impacts by the left-over planetesimals, which gives a stalling mass of $\sim 10^{-12}$ $M_\oplus$, when the full numerical simulations presented in §3.2 find that the atmosphere stalls at $\sim 10^{-7}$ $M_\oplus$. This difference arises from the fact that the simple calculation of f_v assumes a single impact velocity is typical for the entire population, when in reality the final atmosphere mass is sensitive to the details of the full distribution of impactor velocities. As was discussed in §3.3.2 using a calculation of f_v that weights the contribution from each impact velocity (as described by equation 2.33) in the distribution can much more accurately predict the stalling mass. It therefore makes sense to extend this calculation to the planet properties considered above, calculating the average f_v over a distribution of impact velocities.

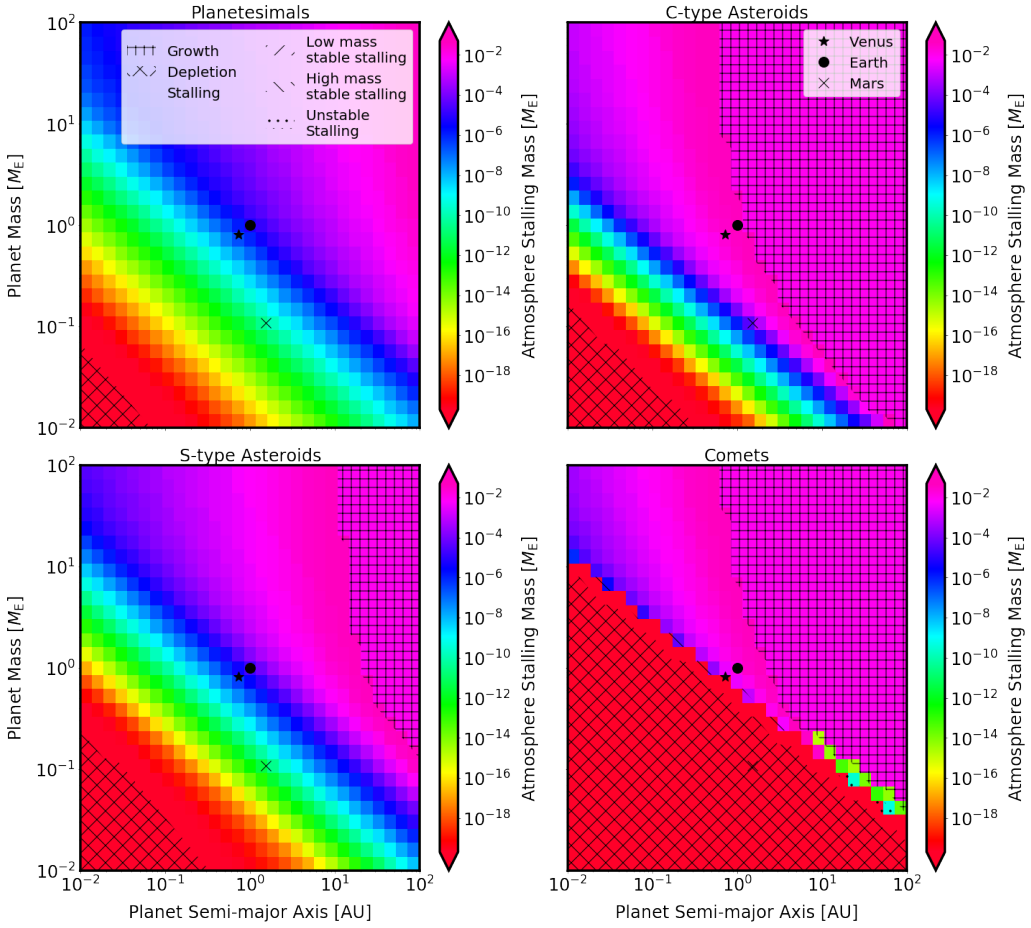

Figure 6.4: The stalling mass as a function of the planet semi-major axis and mass for a rocky planet planet orbiting a Sun-like star, assuming radiative equilibrium atmosphere temperature. The distribution of impact velocities for each population and system is scaled from the impact velocity distribution calculated for each population onto Earth as described in the text. The qualitative atmosphere behaviour regime is illustrated by the hatching superposed according to the legend.

To do this, it is necessary to know what this distribution of impact velocities should be. Previously, it was assumed that each impactor population had a characteristic value of $\xi = \frac{v_{\rm rel}}{v_{\rm pl}}$ such that the impact velocity can be calculated through equations 6.2 and 6.3. If it is instead assumed that each planet is impacted by populations of objects are similar to the Solar system populations of comets, asteroids and left-over planetesimals in velocity distributions as well as composition, then it is possible to use the individual velocity distributions calculated for these objects onto the Earth (described in §3.1.1) and invert them to calculate the unique distribution of ξ for each of the four impactor types, through

$$\begin{aligned} \xi &= 0.39 a_{\rm pl}^{1/2} M_{\rm pl}^{1/3} \sqrt{\left(\frac{v_{\rm imp}}{v_{\rm esc}}\right)^2 - 1} \\ &= 0.39 \sqrt{\left(\frac{v_{\rm imp,\oplus}}{v_{\rm esc,\oplus}}\right)^2 - 1}. \end{aligned} \tag{6.5}$$

These distributions, calculated for the four impactor populations, are shown in Fig. 6.3, and can be seen to be complex shapes that are not well-represented by a single average value. The distributions of ξ can then be used to calculate the distribution of $\frac{v_{\rm imp}}{v_{\rm esc}}$ for each system and each impactor population. This is an oversimplification, since these distributions are calculated for a planet at 1 au, so would likely differ for a planet at 0.1 or 100 au, and furthermore are based on the specific dynamical history of the Solar system, but it provides a more realistic distribution of impact velocities than choosing an arbitrary single impact velocity. Applying this new velocity distribution to the calculation of $f_{\rm v}$ as a function of atmosphere mass for the same range of planet masses and semi-major axes shown in Fig. 6.2 gives the results shown in Fig. 6.4.

From this figure it can be seen that the general trends in stalling mass with planet mass and planet semi-major axis are unchanged, with low mass planets at small semi-major axes showing the lowest stalling masses and high mass planets on wide orbits showing the highest stalling masses. However in comparison to the results shown in Fig. 6.2 the regions of parameter space that result in a prediction of either runaway atmosphere depletion or runaway growth are much smaller. This results in a larger region of parameter space predicted to result in a stable stalling mass for all four impactor populations. This change is a result of summing the contributions to atmosphere growth and erosion over a full velocity distribution. Furthermore, the weighted average values of ξ using these distributions are not the same as the values assumed in table 2.3. For the left-over planetesimals the weighted average value of $\xi = 0.23$ in comparison to the value of 0.5 assumed in the previous calculation. These typically slower impactors are less erosive and so result in higher stalling

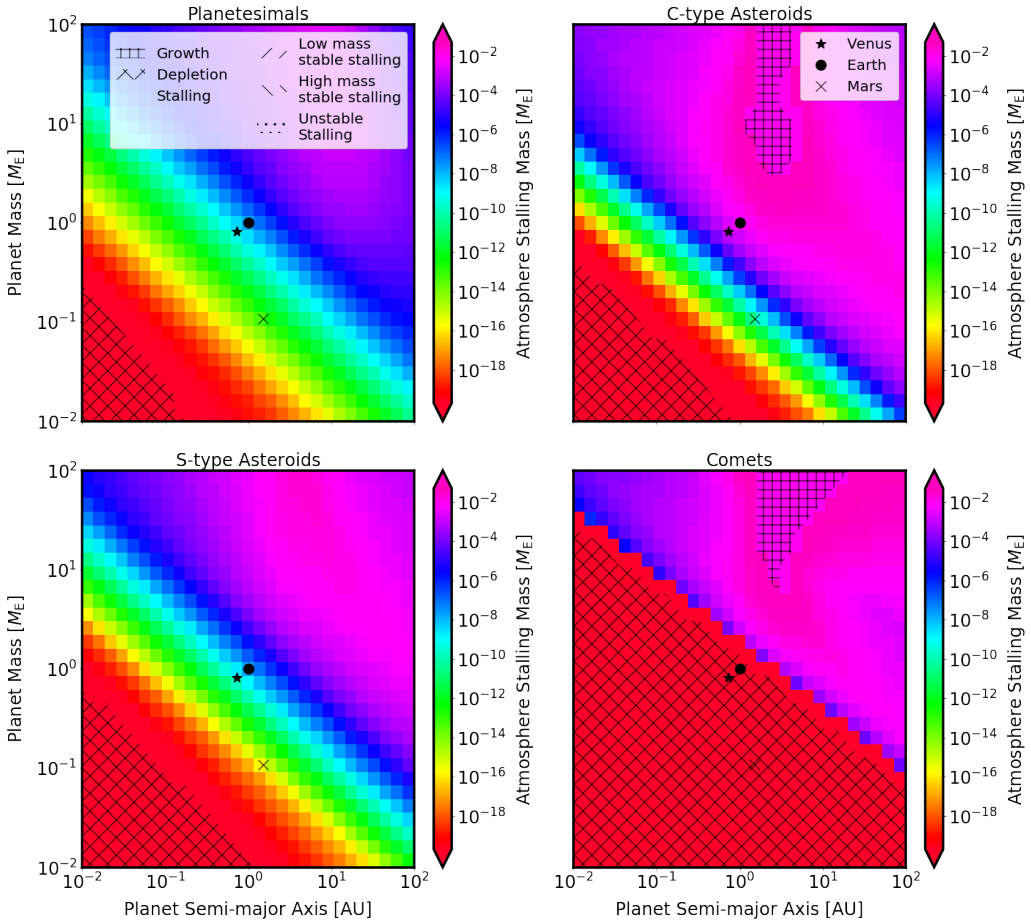

Figure 6.5: The stalling mass (and qualitative atmosphere behaviour regime) as a function of planet semi-major axis and mass for a rocky planet planet orbiting a Sun-like star, assuming radiative equilibrium atmosphere temperature. The increased atmospheric mass loss due to aerial bursts and fragmentation of the impactors is included, resulting in slightly lower stalling masses than observed in Fig. 6.4.

mass predictions. It is worth noting that while this approach does now match the full numerical results found for the Earth in Chapter 3, the predictions for Venus and Mars are slightly too high compared to the numerical results presented in Chapter 5, highlighting the inaccuracies introduced by this simple approach. For the C–type asteroid populations, the inclusion of a full distribution of velocities results in a larger region of parameter space with a stable stalling mass, and a smaller region of space undergoing runaway accretion. The weighted average value of $\xi = 0.5$ is higher than the value of 0.3 assumed in the earlier calculation, and thus the faster impactors result in more atmosphere erosion and thus lower stalling mass predictions. For comets, the previous value of $\xi = 1$ is higher than the weighted average value of 0.6. This reduction in the average impact velocity explains the reduction in parameter space undergoing runaway depletion and increase in parameter space that undergoes runaway accretion.

The above calculations have assumed cratering atmosphere mass loss, using the Shuvalov (2009) cratering prescription and the Schlichting et al. (2015) giant impact prescription only. This is realistic for cool atmospheres, such as the Earth, but at low semi-major axes when the atmosphere is hot then the fragmentation of impactors high in the atmosphere will increase the atmosphere mass loss and decrease the estimated atmosphere stalling mass. We can repeat the above calculation of $f_{\rm v}$ including the atmosphere mass loss due to aerial bursts using the Shuvalov et al. (2014) prescription , the result of which are shown in Fig 6.5.

These results are qualitatively similar to those in Fig. 6.4, but show lower stalling masses, in particular when the previously calculated stalling mass was high. The obvious difference is that far fewer atmospheres undergo runaway growth, which would be expected as it is the highest mass atmospheres that are most influenced by the fragmentation of the impactors. The results for the Earth, Venus and Mars are unchanged, apart from the change from unconstrained growth to stalling at an extremely high mass for the C-type asteroid impactors.

This section has presented an initial parameter space survey into the role impacts may play in shaping exoplanet atmospheres, building on the work presented in Wyatt et al. (2019). I have extended the model for predicted whether an atmosphere would grow or deplete under impacts by either comets or asteroids presented in Fig. 5 and 8 of Wyatt et al. (2019) to predict the characteristic stalling mass at which the atmosphere will grow or deplete to as a result of impacts. I also include a population of left-over planetesimals, which are believed to have been the dominant impacting population in our Solar system. The inclusion of a realistic distribution of impactor velocities for each population, based on dynamical simulations of impactors in the Solar system, has been shown throughout this dissertation to have a significant effect on the predicted atmosphere behaviour. Future work remains to be done in both extending this study to consider planets orbiting stars unlike our own, and better constraining the properties of potential impactor properties in exoplanetary systems. It may also be an interesting avenue of research to consider specific systems in detail. This approach has been applied to the TRAPPIST-1 system in Kral et al. (2018) already, and allows the specific dynamics of the individual system to be used to inform the distribution of impactor velocities.

6.2 Exomoon habitability constraints

Exomoons, despite the lack of any definitive detections to date, remain a promising possibility when considering habitable environments outside out own Solar system (Lammer et al., 2014). For this reason it is important to understand the processes that will influence their atmospheres and thus their potential to host life. Much like exoplanets, their atmospheres are likely to be influenced by impacts. In this section I investigate the role that these impacts may play in the evolution of exomoon atmospheres using an extension of the calculations performed for the Solar system moons in Chapter 4.

To do this several simplifying assumptions must be made, first assuming that the atmosphere temperature on the exomoon is set by radiative equilibrium with a Sun-like star. The impactor population is assumed to be the nominal comet-like composition (described in §4.2.1) with a maximum impactor size of 1000 km, and impact-triggered outgassing from an icy surface is neglected. Four host planet cases are considered, with masses 10 and 100 $\mathrm{M}_{\oplus}$ and semi-major axes 0.1 and 1 au. For each case the distribution of impactor velocities for a grid of moon masses (M_{moon}) and orbital radii (a_{moon}) is calculated using the process as described by equations 4.2 to 4.7 in §4.2.2, following Zahnle et al. (1992) and Shoemaker & Wolfe (1982), and assuming an exterior icy planetesimal belt located at 100 au. These properties are then used to calculate the ratio of expected atmosphere mass gain to mass loss rates, f_{v}, as a function of atmosphere mass and thus the predicted stalling mass and quantitative atmosphere behaviour regime, as described in §2.3.1.

From the predicted atmosphere stalling masses illustrated in Fig. 6.6, it can be seen that stable atmosphere stalling masses are accessible only to a small region of the $(M_{\mathrm{moon}}) - (a_{\mathrm{moon}})$ parameter space. The orbital stability limit is also shown in these plots, and is assumed to be $0.4R_{\mathrm{hill,pl}}$ based on the work of Rosario-Franco et al. (2020), where the Hill radius of a planet with mass M_{pl} orbiting a star of mass M_* at a semi-major axis of a_{pl} is defined to be

$$R_{\mathrm{hill,pl}} = a_{\mathrm{pl}} \left(\frac{M_{\mathrm{pl}}}{3M_*} \right)^{1/3}.$$

The region of parameter space in which the moon mass is greater than the planet mass (and thus the moon-planet designation become meaningless) is also shown by a hatched region in each panel.

For each of the panels, increasing the mass of the moon increases the atmosphere stalling mass, because the escape velocity increases and thus it is easier to retain an atmosphere. The region

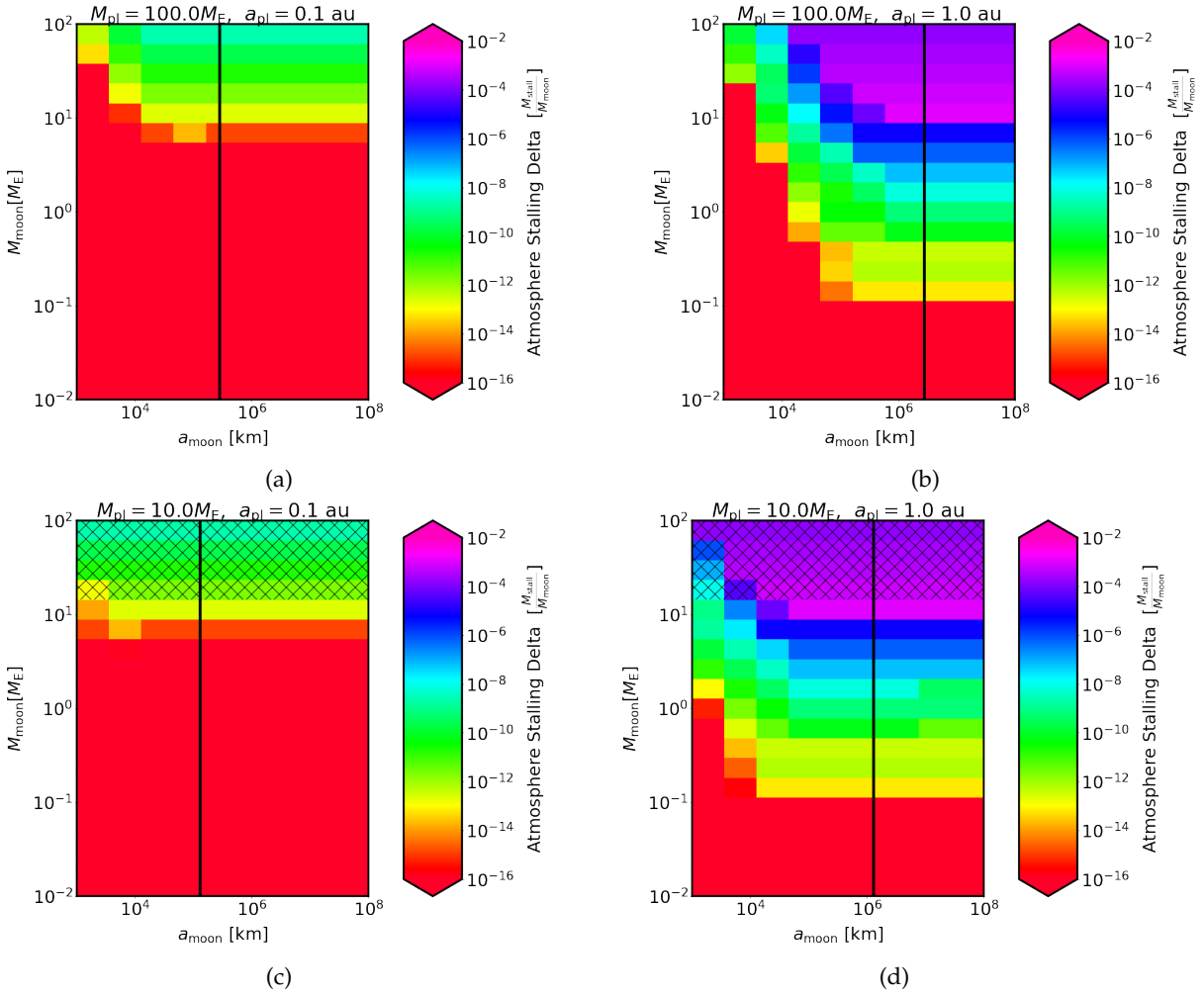

Figure 6.6: The predicted atmosphere stalling mass as a function of moon mass and moon orbital radius for four representative giant exoplanets. The 100 $M_\oplus$ cases are shown in the top panels, and the 10 $M_\oplus$ cases shown in the bottom panels. The hot ($a = 0.1$ au) cases are shown on the left and the cool ($a = 1$ au) cases on the right, as described by the text above the plots. The orbital stability limit ($0.4R_{\rm hill}$) discussed in the text is shown by a thick black line, and hatching shows the forbidden regions of parameter space where the moon mass is greater than the planet mass.

of parameter space in which an atmosphere is predicted to be unstable to XUV induced mass loss, $M_{\rm moon} < 0.25$ $M_\oplus$ according to Lammer et al. (2014), corresponds to a region where the predicted atmospheres are also unstable to atmosphere erosion by impacts, in particular for the close in planets. These results are shown as the ratio of the stalling mass to the moon mass ($\delta = \frac{m_{\rm atm}}{M_{\rm moon}}$), which shows a decrease at very high moon masses for planets located at 1 au as the increase in atmosphere stalling mass is smaller than the increase in moon mass. In general increasing the orbital separation of the moon increases the stable atmosphere stalling mass (as the impacts are relatively slower and thus less erosive). Increasing the planet mass decreases the stable stalling atmosphere mass, as does decreasing the semi-major axis of the planet.

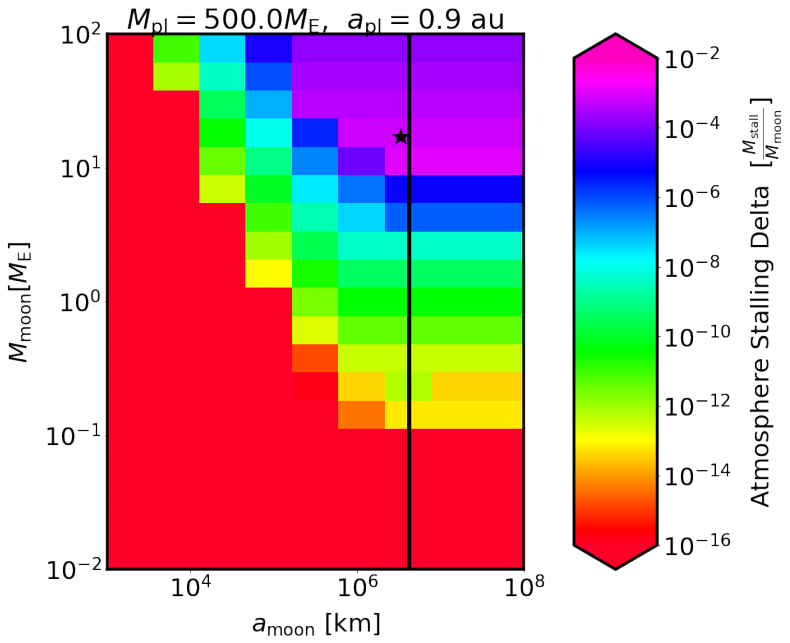

Figure 6.7: The predicted atmosphere stalling mass as a function of moon mass and moon orbital radius for the specific case of the exoplanet K1625b. The details of the assumptions made regarding the planet and moon parameters are discussed in the text. The orbital stability limit ($0.4R_{\rm hill}$) is shown by a thick black line. The location of the hypothetical Neptune mass exomoon is shown by a black marker.

I also consider the specific case of Kepler 1625b-i, the most promising exomoon candidate. Kepler 1625 is a $M_* = 0.96 M_\odot$ mass, $R_* = 0.94 R_\odot$ radius G-type star, with effective temperature $T_{\rm eff} = 5677$ K. The properties of the planet and moon are not certain, with estimates for the planet mass ranging from $0.4 - 112 {\rm M_J}$ (see Heller, 2018, for a full discussion). For the purposes of this very preliminary exploration I adopt a planet radius of 1.18 $\rm R_J$, planet mass of 500 $\rm M_\oplus = 1.5$ $\rm M_J$ and planet semi major axis of 0.87 au. The resulting atmosphere stalling mass values as a function of moon mass and moon orbital radius are illustrated in Fig. 6.7.

From this figure it can be seen that a range of dynamically stable moon orbits can host atmospheres resistant to erosion by impacts. The proposed location of the exomoon candidate Kepler 1625b-i ($M_{\rm moon} = M_{\rm Nept} = 17.15$ $\rm M_\oplus$, $a_{\rm moon} = 40 R_{\rm pl} = 3.3 \times 10^6$ km) is shown as a black marker. At this location the atmosphere is predicted to undergo accretion to a stalling mass of $\sim 10^{-3}$ $\rm M_\oplus$ as a result of impacts, which in reality means I expect an atmosphere mass limited by the mass of volatiles that could be delivered by the hypothetical impactor population.

This approach has many associated caveats, including ignoring any other atmospheric effects

such as hydrodynamic escape, impact-triggered outgassing, and atmospheric chemistry. Furthermore I do not consider yet whether the impact rates required to reach the predicted stalling masses are plausible within the age of the system, and the assumption of an exterior planetesimal belt at 100 au used to calculate the distribution of impact velocities is somewhat arbitrary. Despite these caveats, there are potentially regions of exomoon parameter space that may be detectable in the near future, and that may appear habitable based on the planet location but that are predicted to experience significant atmospheric erosion due to impacts. Impacts should therefore be taken into account in holistic view of exomoon habitability, in particular if the system architecture can be constrained and thus more accurate predictions about the impacting populations can be made.

6.3 Magma ocean production

Magma oceans (MOs) are an inevitable consequence of the largest, most energetic, impacts (Elkins-Tanton, 2012). These kinds of impacts are expected to occur during the latter stages of planet formation, as discussed in §1.1. In the following section I investigate the potential to extend my impact atmosphere evolution model to include the production and subsequent evolution of a MO after a large impact.

6.3.1 A toy model for magma ocean evolution

Here I present a very simplified toy model to investigate the role that atmosphere erosion due to impacts may play in the time taken for a global MO to cool and solidify. This model includes an initial planet with an atmosphere, and a distribution of impactors, and evolves the planet and atmosphere mass through time using my model presented in Chapter 2. I furthermore include the potential for impacts to create a MO if they are sufficiently energetic. This impact energy threshold is assumed to be

$$Q_{\rm MO} = 0.3 \times 10^6 {\rm J/kg}. \tag{6.6}$$

For simplicity the planet surface is allowed to exist in only two states, either a hot MO or a cool solid surface. This is a valid approximation, since the MO is believed to undergo a rheological transition at 40% melt fraction, at which point it switches from behaving like a liquid to a solid (Bonati et al., 2019). The temperature of the MO immediately post impact is $T_{\rm MO,0} \approx 1800$ K.

The rate at which the MO cools from the hot state ($T_{\rm MO,0}$) depends on the size of the MO and the emissivity (how efficiently the atmosphere radiates heat from the planet surface into space) of the atmosphere. The emissivity (ϵ) itself is dependent on the mass and composition

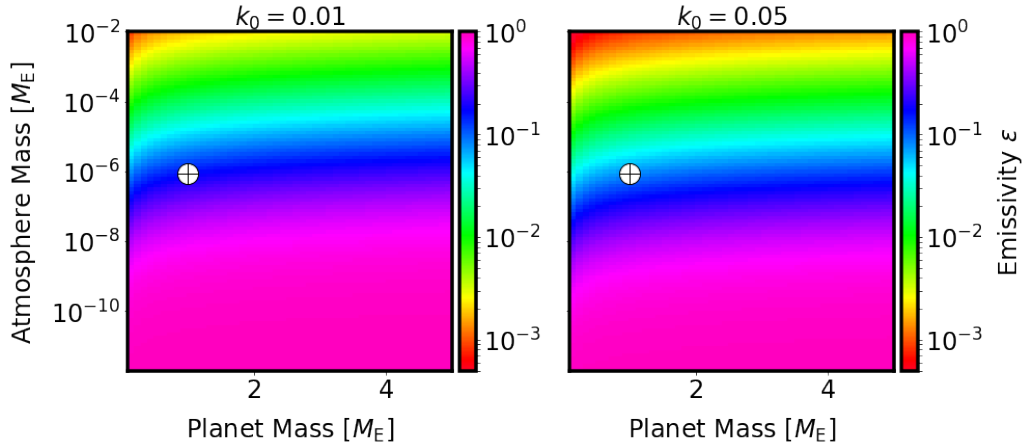

Figure 6.8: The emissivity for steam (left panel) and carbon dioxide (right panel) atmospheres of calculated for a range of atmosphere and planet masses.

of the atmosphere. An emissivity of 0 equates to no emission, while a value of 1 corresponds to black-body radiation. A hot steam atmosphere has a much lower emissivity ($\epsilon \approx 0.001$) than a cooler 10^{20} kg H_2O or CO_2 atmosphere ($\epsilon \approx 0.01$) (Bonati et al., 2019). In order to parameterise the emissivity in terms of the atmosphere mass, temperature and MMW I assume a grey atmosphere, such that ϵ is the same for all wavelengths of light. The heat flux (F) from the atmosphere to space is therefore approximated by

$$F = \sigma_{SB}\left(T_{\rm MO}^4 - T_{\rm eq}^4\right), \tag{6.7}$$

where σ_{SB} is the Stefan-Boltzmann constant and $T_{\rm eq}$ is the equilibrium temperature of the atmosphere.

For a single gas species, the optical depth can be expressed as

$$\tau^* = \frac{3m_{\rm atm}}{8\pi R_{\rm pl}^2}\sqrt{\frac{k_0 g}{3P_0}}, \tag{6.8}$$

where g is the gravitational acceleration and P_0 is the atmospheric pressure at the surface of the planet. k_0 is the atmospheric absorbtion coefficient of the species in question. For H_2O it is 0.01 m ^{2}/kg while for CO_2 it is 0.05 m ^{2}/kg (Elkins-Tanton, 2008). This can be used to calculate the emissivity through

$$\epsilon = \frac{2}{2+\tau^*}. \tag{6.9}$$

In this model, the planet is assumed to be rocky, with constant density $\rho_{\rm pl} = 5.5$ g cm^{-3}, and therefore the planet mass scales with radius as $M_{\rm pl} \propto R_{\rm pl}^3$. The atmospheres are also assumed to be isothermal, ideal and thin such that the surface pressure scales with atmosphere mass and

planet mass according to equation 2.4. Normalising such that an Earth-like planet has a 1 bar atmosphere this results in

$$\begin{aligned} P_0 &= \frac{kT\rho_0}{\mu m_{\rm H}} \\ P_0 &\propto M_{\rm pl}^{-1/3} m_{\rm atm}. \end{aligned} \tag{6.10}$$

From this equation, the emissivity for a single species (either pure carbon dioxide or pure steam) atmosphere can be calculated. These emissivities are illustrated in Fig. 6.8 for a range of atmosphere and planet masses.

The assumption of an isothermal atmosphere is obviously inaccurate, but a necessary simplification for this very basic model. In the following toy model, the atmosphere is assumed to be hot when the MO is molten, at a bulk average temperature

$$T_{\rm hot} = 0.5\big(T_{\rm MO} + T_{\rm eq}\big), \tag{6.11}$$

and cool at a temperature of

$$T_{\rm cool} = T_{\rm eq} \tag{6.12}$$

when the surface has solidified, where $T_{\rm eq}$ is the equilibrium temperature for an atmosphere in radiative equilibrium given by equation 2.2.

To parameterise the MO cooling rate I make use of the results presented in Bonati et al. (2019). From their figure it can be inferred that temperature decreases linearly with time for a range of planet radii and atmosphere emissivities. The cooling time is calculated to be the time taken for the MO temperature to decrease from the initial MO temperature $T_0 = 1800$ K to a transition temperature $T_{\rm RT} = 1120$ K, estimated for each of the lines in the Bonati et al. (2019) figure to reconstruct a 2D fit. This approach implies that the MO lifetime scales as

$$\tau_{\rm MO} \approx 6310 R_{\rm pl} \epsilon^{-0.9} \text{ yrs}. \tag{6.13}$$

Converting this into a linear cooling rate gives

$$\dot{T}_{\rm MO} \approx 0.108 R_{\rm pl}^{-1} \epsilon^{0.9}, \tag{6.14}$$

where the emissivity is a function of the parameters described above, $\epsilon(m_{\rm atm}, M_{\rm pl}, k_0)$.

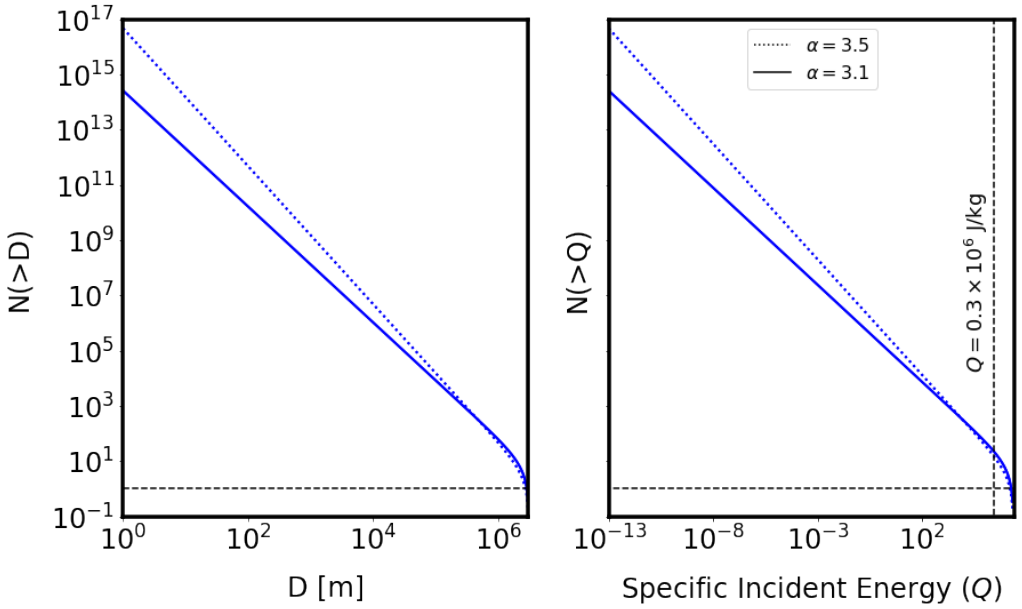

Figure 6.9: The impactor size distributions described in the text, shown as number of impacts greater than a given size (left panel) or with specific incident energy greater than a given value (right panel). Only a few impactors have energy greater than the critical energy required to cause a global MO (shown by a vertical dashed line). The different values of the power-law index for the differential size distribution (α) are shown by different line colours.

6.3.2 Numerical magma ocean evolution

This toy model can now be incorporated into the numerical code described in Chapter 2, including the effects of aerial bursts and impactor fragmentation, which are relevant for the hot atmosphere states. The MO states are included in the code by implementing a check every time step (after the impactors have been randomly sampled from the size distribution) to determine whether any sampled impactors have specific incident energy above the threshold adopted ($Q > Q_{\rm MO} = 0.3 \times 10^6$J/kg as given by equation 6.6) and so can cause a MO.

If this is the case, the planet is assumed to be in a MO state with the MO at temperature $T_0 = 1800$ K and the atmosphere in the hot state ($T_{\rm hot}$). At this point, the cooling function switches on and the impacts continue to grow or erode the atmosphere while the MO and atmosphere cool. The cooling function calculates the cooling rate in terms of the planet and atmosphere properties at that time. The cooling is assumed to stop when the MO temperature reaches the equilibrium temperature, at which point the timing and length of the MO phase is recorded. Once the MO has cooled, the system returns to the equilibrium temperature state and continues to evolve under the influence of impacts. If a MO causing impact arrives during the MO state it resets the MO temperature to 1800 K.

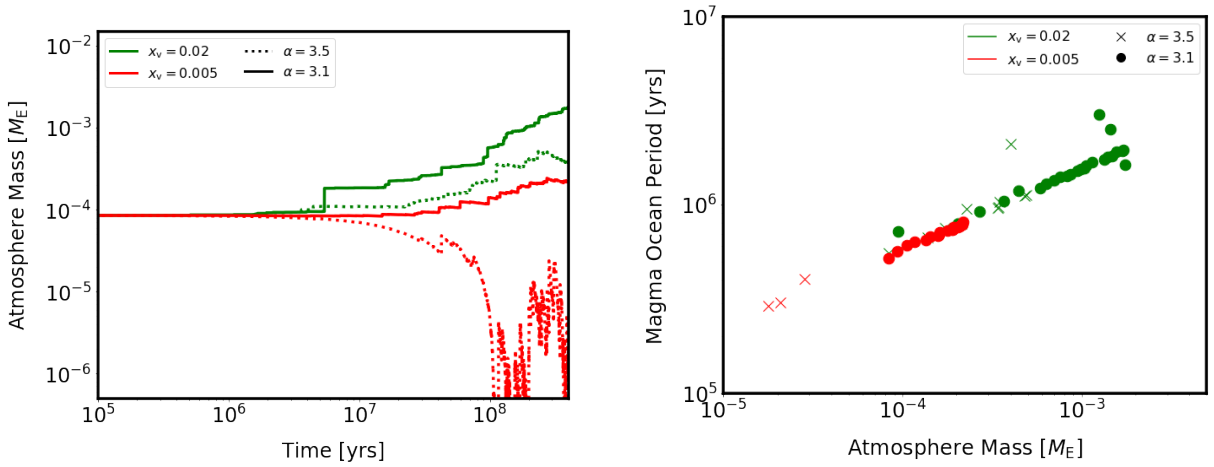

(a) (b)

Figure 6.10: The time evolution of the atmosphere mass as a function of time for the four cases described in the text is shown in panel (a), while the corresponding length of the MO phases as a function of atmosphere mass at the time which they began is shown in panel (b). The different size distributions are shown by different line or marker styles and the different volatile fractions are shown by different colours.

The impactor population is parameterised by a single impact velocity, constant impact rate and a power-law size distribution, to minimise the complexity introduced by variation in these parameters, and is assumed to be a fast, asteroid-like impactor with $\rho_{\rm imp} = 2.8$ g cm^{-3}, $\xi = 0.9$. Two volatile fractions are considered, $x_{\rm v} = 0.02$ and 0.005, to investigate the behaviour of an atmosphere that typically grows and one that typically depletes. For each of these compositions, two different differential power-law indices ($\alpha = 3.5$ and $\alpha = 3.1$) are considered, for a maximum impactor size $D_{\rm max} = 3000$ km (Mars-sized), and total impacting mass $M_{\rm tot} = 0.1$ M$_\oplus$. The number of impactors in each size bin for each of these distribution, as well as the number of impactors as a function of their specific incident energy are shown in Fig. 6.9. From this it can be seen that for there to be any impacts massive enough to cause a global MO the maximum impactor size must be larger than $D_{\rm max} = 1000$ km, the limit adopted previously in this dissertation. There should be ~ 14 such impacts for the $\alpha = 3.5$ power-law size distribution, and ~ 21 for the $\alpha = 3.1$ distribution.

The results of running the modified code a single time for each population are shown as the atmosphere mass as a function of time in Fig. 6.10a. While care should be taken when interpreting these results due to the fact that a single iteration of the code may be influenced by the inherent stochasticity of the results, these results do provide a clue as to whether the role of impacts will alter the MO cooling rate. The MO causing events are uniformly distributed over time (due to the constant impact rate), but differ in frequency between the two α values. As predicted, there are more MO causing impacts in the two $\alpha = 3.1$ size

distributions (25 and 19 in comparison to 11 and 14).

The prescriptions adopted for MO cooling imply that MOs under thick atmospheres will cool more slowly than when the atmosphere is depleted. From Fig. 6.10a it can be seen that the volatile-rich impactors generally result in atmosphere growth while the volatile-poor impactors deplete the atmosphere (although this depletion stalls and the atmosphere behaviour becomes stochastic at later times). The effect of the different atmosphere masses can be seen in Fig. 6.10b, which shows the length of each MO phase as a function of the atmosphere mass at the time of MO creation. The average length of the MO phase is longest for the volatile-rich shallow size distribution (~ 1.5 Myr), followed by the volatile-rich $\alpha = 3.5$ distribution (~ 1.0 Myr), then the volatile-poor $\alpha = 3.1$ distribution (~ 0.7 Myr) and finally the volatile-poor $\alpha = 3.5$ distribution (~ 0.2 Myr). Similar trends are observed in the total length of time spent in a MO phase summed over the entire simulation.

The results presented in this section suggest that the time a planet spends with a molten surface may depend on whether the MO causing impacts are statistically unlikely events sampled rarely from a distribution of impactors or are the high-mass end of a continuous distribution. In the latter case the simultaneous bombardment by all the smaller objects in the size distribution will erode the massive insulating atmosphere and cause more rapid cooling of the MO. Further work remains to be done, to extend this model to more accurately represent the cooling of a MO under a realistic atmosphere (for example by incorporating a prescription for outgassing from the MO and including an adiabatic atmosphere temperature profile) and to extend the range of impactor populations considered. Additionally, the potential for more volatile-rich or slower populations of impactors to grow the massive insulating atmosphere, prolonging the MO phase should be considered.

In summary, the key points from this chapter are:

- The effect of impacts on the atmospheres of exoplanets and exomoons can be significant, and should be considered in a holistic view of their potential habitability;
- The potential for smaller impacts to influence the evolution of a magma ocean caused by a giant impact by eroding the massive insulating steam atmosphere is a potential avenue for future study.

7

Summary

This thesis has studied the effect of bombardment by small bodies on the evolution of terrestrial planet and moon atmospheres, using analytic and numeric methods. In the following I summarise my main conclusions.

7.1 Chapter 2: A statistical code of stochastic bombardment to model the evolution of an atmosphere

I presented prescriptions parameterising the effect of an impact on an atmosphere, covering a range of impact regimes (cratering impacts, aerial bursts and fragmentation, giant impacts, and impacts onto planets without atmospheres), modifying them when required to apply them to the impact regimes considered in this dissertation. I derived an analytic framework that can be used to predict the qualitative behaviour of an atmosphere undergoing impacts by a population of objects and calculate the characteristic atmosphere mass at which the volatile delivery and atmosphere erosion balance and the atmosphere stalls. I also presented a new numerical code for stochastic bombardment of an atmosphere, which incorporates any combination of impact prescriptions, calculating the cumulative effect of impactors sampled stochastically from time-dependent size, velocity and composition distributions. This code includes an adaptive time step and tracks the total atmosphere mass, bulk MMW, accreted

solid mass and fraction of the atmosphere that has been delivered by each population and was validated against the analytical model for atmosphere evolution from Wyatt et al. (2019). It can be used to study atmosphere evolution in detail, capturing the often stochastic nature of the largest impacts, which while rare can have significant influence on the final atmosphere state.

7.2 Chapter 3: The evolution of Earth's atmosphere

I considered the evolution of Earth's atmosphere after the Moon-forming impact, constructing three populations of impactors: comets, asteroids and left-over planetesimals. I calculated the distribution of impact velocities and fluxes from the results of dynamical simulations of the Solar system. Considering each population individually, I found that comets cause atmosphere depletion, and this loss is greater for more massive or lower density impactors. Higher density comets can occasionally result in growth due to the stochastic arrival of large, slow impactors. In contrast, asteroids cause atmospheric growth, and the final atmosphere mass in general increases as the assumed volatile content or total impacting mass is increased. The left-over planetesimals cause atmospheric erosion, with the final atmosphere mass decreasing as the impactor volatile content is decreased, with the entire atmosphere stripped for sufficiently "dry" impactors. Considering plausible variation in the impactor dynamics I found that this can cause typical atmosphere mass loss to vary between -72 % and -96 %.

Investigating the combined effect of all three populations, my results emphasise the importance of considering stochastic events, as the relatively rare arrival of a single large impactor can have significant effects on the atmosphere. For identical initial conditions a wide range of outcomes is possible, with variation introduced through the uncertainty in the impactor dynamics and compositions. The results from the nominal case show modest atmospheric loss, with a median final atmosphere mass of 0.24×10^{-6} $M_\oplus$. I found that the final atmosphere is in general dominated by material delivered by the population of left-over planetesimals, with the cometary fraction (< 1 %) is consistent with observational constraints. None of the populations considered are capable of delivering a significant mass of water, implying that the water budget of the Earth predates this period of bombardment.

The initial mass and composition assumed for the Earth's atmosphere makes relatively little difference to the final outcome, however an initial atmosphere mass significantly greater than the present mass cannot be entirely eroded by the mass delivered, unless the initial atmosphere is primordial.

7.3 Chapter 4: The role of impacts on the atmospheres on the moons of outer giants

I investigated the effect that impacts by objects similar to comets from the Kuiper Belt have on the atmospheres of five satellites of the giant planets, Ganymede, Callisto, Europa, Triton and Titan using the numerical code described in Chapter 2.

The code was used to predict the atmospheric evolution for a range of initial conditions, finding that the atmosphere masses vary by orders of magnitude both between and within single iterations of the code due to the inherently stochastic nature of impacts onto the outer moons. I also used the analytic prediction for the stalling mass presented in Chapter 2 to show that over long timescales, the median atmosphere mass from the numerical results successfully reproduces the analytic value. This analytic stalling mass for the nominal population of impactors is moderately successful at predicting the observed atmosphere masses of Ganymede, Callisto, Europa and Triton, however it significantly underestimates the atmosphere mass of Titan.

When considering the sensitivity of my predicted stalling masses to the properties of the impactor population I found that the volatile content and size distribution are less important than the impactor density, but still capable of altering the predicted stalling mass by a factor of ~ 100. The size of the largest impactor used in the calculation is determined by the timescale over which impacts are sampled from the parent population and thus over which the atmosphere evolves, and is extremely important in determining the predicted atmosphere stalling mass. On longer timescales, the largest sampled impactor size increases and this acts to increase the predicted atmosphere stalling mass. Finally, the stalling mass is significantly reduced when impactors originate in the Oort cloud, since this results in faster (more erosive) impactors.

When including the effect of impact-triggered outgassing I predicted an atmosphere stalling mass for Titan comparable to its current observed atmosphere mass, using both a modified version of the analytic prediction and the code. This level of outgassing requires the existence of a volatile-rich crust, and that the volatiles remain in the atmosphere after outgassing. Therefore these results are applicable only to Titan.

7.4 Chapter 5: Evolution of the atmospheres of Venus and Mars due to bombardment

I considered the evolution of potential atmospheres on Venus and Mars as a result of impacts by comets, asteroids and left-over planetesimals. The distribution of impact velocities and impact fluxes for these populations were calculated from the results of dynamical simulations of the Solar system, consistent with the results for the Earth, and the assumed impactor properties justified. I considered three initial atmosphere states for each planet (hot and massive, mid-temperature and Earth-like, and cool and thin). I found that asteroids cause stochastic growth of initially low-mass, low-temperature atmospheres, however their low total impacting mass results in a truncated impactor size distribution that causes depletion of initially massive atmospheres. In a few cases a large rare impactor can be sampled by the code, resulting in delivery of up to 10^{-6} $M_{\oplus}$ in a single event. Comets in general cause little evolution of the atmosphere on either planet regardless of the initial atmosphere conditions, due to the small total population mass and low accretion efficiency of the largest objects.

The left-over planetesimals, which are expected to dominate the mass of impacting material, result in depletion of initially massive atmospheres, but are not capable of depleting the atmosphere mass by more than a few $\%$ over the course of the simulations. In contrast, initially lower-mass atmospheres are rapidly eroded into a stochastic evolution regime, where the atmosphere mass varies by orders of magnitude on short timescales. This results from the rapid erosion of the atmosphere due to a constant background flux of small impactors, with stochastic sampling of larger objects delivering significant amounts of volatiles in a single instance, replenishing the atmosphere. This stochastic variation in greater on Mars than Venus due to the lower impact flux experienced by the smaller planet. The behaviour for Venus and Mars differs from the steady evolution observed for the Earth due to the faster impact velocity relative to the planet escape velocity on both planets. The analytically predicted stalling masses over-predict the median atmosphere masses recorded in the code, due to the stochastic nature of the atmosphere evolution on these planets.

Variation in the potential dynamics of the left-over planetesimals can cause significant variation in the atmosphere mass evolution for both planets. On Mars, this results in the transition from non-stochastic survival of the atmosphere (which loses $\sim 78\%$ of its initial mass) into stochastic erosion. Cooler initial atmospheres result in higher median atmosphere masses after bombardment due to their smaller atmosphere scale heights. An atmosphere similar to Venus' today would survive the expected bombardment, as does an similarly hot and massive initial atmosphere on Mars. This is unlikely to be a realistic possibility for Mars,

but is plausible for Venus and additionally may be able to explain the observed noble gas discrepancies between the terrestrial planets. The final atmospheres are dominated by primordial material if the initial atmosphere is hot and massive, but are dominated by material delivered by left-over planetesimals if they are initially Earth-like or thin and cool.

7.5 Chapter 6: Minor projects and future work

I described a series of minor projects begun during this dissertation, which represent potential future directions for research. I considered the potential evolution of exoplanet atmospheres, assuming impacts by populations of objects comparable to those in our own Solar system. These results suggested that impacts are capable of both growing and depleting atmospheres on Earth-like terrestrial exoplanets, depending on the specific impactor and planet properties. I extended the analytic stalling mass prediction to consider the evolution of atmospheres on exomoons. My findings suggest that it is challenging to sustain an atmosphere because of the high expected impact velocities due to their proximity to a host planet. For the proposed exomoon Kepler 1625b-i runaway accretion is predicted as a result of impacts, which in reality means an atmosphere mass limited by the mass of volatiles that could be delivered by the hypothetical impactor population.

I also presented a simple model to consider the effect of atmosphere evolution due to impacts on magma ocean cooling. Planets undergoing bombardment at high enough fluxes for giant impacts to be common are also expected to undergo impacts by smaller objects, which can erode a massive steam atmosphere, reducing the insulation experienced by the magma ocean and speeding up its cooling process.

Bibliography

Agnor, C. B., & Lin, D. N. C. 2012, ApJ, 745, 143

Ahrens, T. J. 1989, Nature, 342, 122

—. 1993, Annual Review of Earth and Planetary Sciences, 21, 525

Alibert, Y., & Mousis, O. 2007, A&A, 465, 1051

Anderson, J. D., Jacobson, R. A., McElrath, T. P., et al. 2001, Icarus, 153, 157

Anglada-Escudé, G., Amado, P. J., Barnes, J., et al. 2016, Nature, 536, 437

Artemieva, N., & Lunine, J. I. 2005, Icarus, 175, 522

Asphaug, E., & Reufer, A. 2014, Nature Geoscience, 7, 564

Atreya, S. K., Donahue, T. M., & Kuhn, W. R. 1978, Science, 201, 611

Awiphan, S., & Kerins, E. 2013, MNRAS, 432, 2549

Bahcall, J. N., Pinsonneault, M. H., & Basu, S. 2001, ApJ, 555, 990

Barnes, J. J., Kring, D. A., Tartèse, R., et al. 2016, Nature Communications, 7, 11684

Barnhart, C. J., Howard, A. D., & Moore, J. M. 2009, Journal of Geophysical Research (Planets), 114, E01003

Basilevsky, A. T., & Head, J. W. 2000, J. Geophys. Res., 105, 24583

Bekker, A., Holland, H. D., Wang, P. L., et al. 2004, Nature, 427, 117

Bell, S. W. 2020, Journal of Geophysical Research (Planets), 125, e06392

Bennett, D. P., Ranc, C., & Fernandes, R. B. 2021, arXiv e-prints, arXiv:2104.05713

Bertaux, J.-L., Vandaele, A.-C., Korablev, O., et al. 2007, Nature, 450, 646

Beust, H., & Morbidelli, A. 1996, Icarus, 120, 358

Birnstiel, T., Dullemond, C. P., & Brauer, F. 2010, A&A, 513, A79

Blum, J. 2018, Space Sci. Rev., 214, 52

Blum, J., & Wurm, G. 2008, ARA&A, 46, 21

Boatwright, B. D., & Head, J. W. 2021, arXiv e-prints, arXiv:2103.01098

Boley, A. C. 2009, ApJ, 695, L53

Bolfan-Casanova, N., Keppler, H., & Rubie, D. C. 2003, Geophysical Research Letters, 30

Bonati, I., Lichtenberg, T., Bower, D. J., Timpe, M. L., & Quanz, S. P. 2019, A&A, 621, A125

Borucki, W. J. 2016, Reports on Progress in Physics, 79, 036901

Boss, A. P. 1997, Science, 276, 1836

Bottke, W. F. 2015, in IAU General Assembly, Vol. 29, 2248900

Bottke, W. F., Durda, D. D., Nesvorný, D., et al. 2005, Icarus, 175, 111

Bottke, W. F., Walker, R. J., Day, J. M. D., Nesvorny, D., & Elkins-Tanton, L. 2010, Science, 330, 1527

Bowler, B. P. 2016, PASP, 128, 102001

Brandon, A. D., Puchtel, I. S., Walker, R. J., et al. 2012, Geochim. Cosmochim. Acta, 76, 206

Brasser, R., Mojzsis, S. J., Werner, S. C., Matsumura, S., & Ida, S. 2016, Earth and Planetary Science Letters, 455, 85

Brasser, R., Morbidelli, A., Gomes, R., Tsiganis, K., & Levison, H. F. 2009, A&A, 507, 1053

Brasser, R., Werner, S. C., & Mojzsis, S. J. 2020, Icarus, 338, 113514

Broadfoot, A. L., Sandel, B. R., Shemansky, D. E., et al. 1981, J. Geophys. Res., 86, 8259

Budde, G., Burkhardt, C., & Kleine, T. 2019, Nature Astronomy, 3, 736

Canup, R. M. 2004, Icarus, 168, 433

—. 2012, Science, 338, 1052

Carlson, R. W. 1999, Science, 283, 820

Carnielli, G., Galand, M., Leblanc, F., et al. 2020, Icarus, 351, 113918

Carr, M. H., Belton, M. J. S., Chapman, C. R., et al. 1998, Nature, 391, 363

Carrera, D., Gorti, U., Johansen, A., & Davies, M. B. 2017, ApJ, 839, 16

Carry, B. 2012, Planet. Space Sci., 73, 98

Cataldi, G., Brandeker, A., Thébault, P., et al. 2017, Astrobiology, 17, 721

Catling, D. C., & Kasting, J. F. 2017, Atmospheric Evolution on Inhabited and Lifeless Worlds (Cambridge University Press)

Chambers, J. 2021, arXiv e-prints, arXiv:2104.10704

Chambers, J. E. 2001, Icarus, 152, 205

Chambers, J. E., & Lissauer, J. J. 2002, in Lunar and Planetary Science Conference, Lunar and Planetary Science Conference, 1093

Chambers, J. E., & Wetherill, G. W. 1998, Icarus, 136, 304

Choukroun, M., Grasset, O., Tobie, G., & Sotin, C. 2010, Icarus, 205, 581

Chyba, C. F. 1990, Nature, 343, 129

Clement, M. S., Kaib, N. A., Raymond, S. N., Chambers, J. E., & Walsh, K. J. 2019, Icarus, 321, 778

Clement, M. S., Kaib, N. A., Raymond, S. N., & Walsh, K. J. 2018, Icarus, 311, 340

Coltice, N., Moreira, M., Hernlund, J., & Labrosse, S. 2011, Earth and Planetary Science Letters, 308, 193

Coustenis, A. 2005, Space Sci. Rev., 116, 171

Cruikshank, D. P. 2005, Space Sci. Rev., 116, 421

Ćuk, M., Hamilton, D. P., Lock, S. J., & Stewart, S. T. 2016, Nature, 539, 402

Cunningham, N. J., Spencer, J. R., Feldman, P. D., et al. 2015, Icarus, 254, 178

Daubar, I. J., McEwen, A. S., Byrne, S., Kennedy, M. R., & Ivanov, B. 2013, Icarus, 225, 506
Dauphas, N. 2003, Icarus, 165, 326
Dauphas, N., Robert, F., & Marty, B. 2000, Icarus, 148, 508
Day, J. M. D., Brandon, A. D., & Walker, R. J. 2016, Reviews in Mineralogy and Geochemistry, 81, 161
Day, J. M. D., Pearson, D. G., & Taylor, L. A. 2007, Science, 315, 217
Day, J. M. D., & Walker, R. J. 2015, Earth and Planetary Science Letters, 423, 114
de Niem, D., Kührt, E., Morbidelli, A., & Motschmann, U. 2012, Icarus, 221, 495
de Sousa, R. R., Morbidelli, A., Raymond, S. N., et al. 2020, Icarus, 339, 113605
de Wit, J., Wakeford, H. R., Lewis, N. K., et al. 2018, Nature Astronomy, 2, 214
Defrère, D., Léger, A., Absil, O., et al. 2018, Experimental Astronomy, 46, 543
Deienno, R., Morbidelli, A., Gomes, R. S., & Nesvorný, D. 2017, AJ, 153, 153
DeMeo, F. E. 2014, Nature, 505, 629
Denman, T. R., Leinhardt, Z. M., Carter, P. J., & Mordasini, C. 2020, MNRAS, 496, 1166
Dohnanyi, J. S. 1969, J. Geophys. Res., 74, 2531
Dominik, M. 2010, General Relativity and Gravitation, 42, 2075
Drake, M. J., & Campins, H. 2006, in IAU Symposium, Vol. 229, Asteroids, Comets, Meteors, ed. D. Lazzaro, S. Ferraz-Mello, & J. A. Fernández, 381–394
Elkins-Tanton, L. T. 2008, Earth and Planetary Science Letters, 271, 181
—. 2012, Annual Review of Earth and Planetary Sciences, 40, 113
Elkins-Tanton, L. T., Burgess, S., & Yin, Q.-Z. 2011, Earth and Planetary Science Letters, 304, 326
Ercolano, B., & Pascucci, I. 2017, Royal Society Open Science, 4, 170114
Erickson, T. M., Kirkland, C. L., Timms, N. E., Cavosie, A. J., & Davison, T. M. 2020, Nature Communications, 11, 300
Farinella, P., Marzari, F., & Matteoli, S. 1997, AJ, 113, 2312
Fastook, J. L., & Head, J. W. 2015, Planet. Space Sci., 106, 82
Feldman, P. D., McGrath, M. A., Strobel, D. F., et al. 2000, ApJ, 535, 1085
Festou, M. C., Keller, H. U., & Weaver, H. A. 2004, Comets II ( )
Fischer, D. A., Anglada-Escude, G., Arriagada, P., et al. 2016, PASP, 128, 066001
Fox, C., & Wiegert, P. 2021, MNRAS, 501, 2378
Gaudi, B. S. 2012, ARA&A, 50, 411
Genda, H., & Abe, Y. 2003, Icarus, 164, 149
Genda, H., Brasser, R., & Mojzsis, S. J. 2017, Earth and Planetary Science Letters, 480, 25
Gillmann, C., Chassefière, E., & Lognonné, P. 2009, Earth and Planetary Science Letters, 286, 503
Gillmann, C., Golabek, G. J., Raymond, S. N., et al. 2020, Nature Geoscience, 13, 265
Gillon, M., Jehin, E., Lederer, S. M., et al. 2016, Nature, 533, 221
Gomes, R., Levison, H. F., Tsiganis, K., & Morbidelli, A. 2005, Nature, 435, 466

Griffith, C. A., & Zahnle, K. 1995, J. Geophys. Res., 100, 16907

Gronoff, G., Arras, P., Baraka, S., et al. 2020, Journal of Geophysical Research (Space Physics), 125, e27639

Grundy, W. M., & Stansberry, J. A. 2000, Icarus, 148, 340

Hall, D. T., Feldman, P. D., McGrath, M. A., & Strobel, D. F. 1998, ApJ, 499, 475

Hall, D. T., Strobel, D. F., Feldman, P. D., McGrath, M. A., & Weaver, H. A. 1995, Nature, 373, 677

Halliday, A. N. 2013, Geochim. Cosmochim. Acta, 105, 146

Hamano, K., Abe, Y., & Genda, H. 2013, Nature, 497, 607

Hand, K. P., Chyba, C. F., Carlson, R. W., & Cooper, J. F. 2006, Astrobiology, 6, 463

Harper, Jr., C. L., & Jacobsen, S. B. 1996, Science, 273, 1814

Hartmann, W., Ryder, G., Dones, L., et al. 2000, The University of Arizona Press, Tucson and Lunar Planetary Institute, Houston

Hayashi, C., Nakazawa, K., & Mizuno, H. 1979, Earth and Planetary Science Letters, 43, 22

Heller, R. 2018, A&A, 610, A39

Heller, R., Hippke, M., Placek, B., Angerhausen, D., & Agol, E. 2016, A&A, 591, A67

Hoke, M. R. T., Hynek, B. M., & Tucker, G. E. 2011, Earth and Planetary Science Letters, 312, 1

Holland, G., Cassidy, M., & Ballentine, C. J. 2009, Science, 326, 1522

Honda, M., & McDougall, I. 1998, Geophys. Res. Lett., 25, 1951

Hopp, T., B., B., & T., K. 2020, Earth and Planetary Science Letters, 534, 116065

Housen, K. R., & Holsapple, K. A. 2011, Icarus, 211, 856

Hsu, D. C., Ford, E. B., Ragozzine, D., & Ashby, K. 2019, AJ, 158, 109

Hsu, D. C., Ford, E. B., & Terrien, R. 2020, MNRAS, 498, 2249

Hughes, A. M., Duchêne, G., & Matthews, B. C. 2018, ARA&A, 56, 541

Ida, S., & Makino, J. 1993, Icarus, 106, 210

Iess, L., Jacobson, R. A., Ducci, M., et al. 2012, Science, 337, 457

Ikoma, M., & Genda, H. 2006, ApJ, 648, 696

Ingersoll, A. P. 1990, Nature, 344, 315

Ip, W. H., Williams, D. J., McEntire, R. W., & Mauk, B. H. 1998, Geophys. Res. Lett., 25, 829

Ishimaru, R., Sekine, Y., Matsui, T., & Mousis, O. 2011, ApJ, 741, L10

Jacquet, E., Balbus, S., & Latter, H. 2011, MNRAS, 415, 3591

Jambon, A., & Zimmermann, J. L. 1990, Earth and Planetary Science Letters, 101, 323

Johansen, A., & Lacerda, P. 2010, MNRAS, 404, 475

Johansen, A., Oishi, J. S., Mac Low, M.-M., et al. 2007, Nature, 448, 1022

Johnson, R. E., Leblanc, F., Yakshinskiy, B. V., & Madey, T. E. 2002, Icarus, 156, 136

Johnson, T. 2014, in Treatise on Geochemistry (Second Edition), second edition edn., ed. H. D. Holland & K. K. Turekian, 313–334

Kaib, N. A., & Chambers, J. E. 2016, MNRAS, 455, 3561

Kaltenegger, L., & Traub, W. A. 2009, ApJ, 698, 519
Kasting, J. F. 1993, Science, 259, 920
Kasting, J. F., & Harman, C. E. 2013, Nature, 504, 221
Kegerreis, J. A., Eke, V. R., Catling, D. C., et al. 2020a, ApJ, 901, L31
Kegerreis, J. A., Eke, V. R., Massey, R. J., & Teodoro, L. F. A. 2020b, ApJ, 897, 161
Kennedy, G. M. 2018, MNRAS, 479, 1997
Kipping, D. 2020, ApJ, 900, L44
Kipping, D. M. 2009, MNRAS, 392, 181
Kivelson, M. G., Khurana, K. K., Russell, C. T., et al. 2000, Science, 289, 1340
Kivelson, M. G., Khurana, K. K., & Volwerk, M. 2002, Icarus, 157, 507
Kopparapu, R. K., Hébrard, E., Belikov, R., et al. 2018, ApJ, 856, 122
Korycansky, D., & Zahnle, K. 2005, Planetary and Space Science, 53, 695
Kral, Q., Wyatt, M. C., Triaud, A. H. M. J., et al. 2018, MNRAS, 479, 2649
Kraus, R. G., Senft, L. E., & Stewart, S. T. 2011, Icarus, 214, 724
Krijt, S., Ormel, C. W., Dominik, C., & Tielens, A. G. G. M. 2016, A&A, 586, A20
Krivov, A. V. 2010, Research in Astronomy and Astrophysics, 10, 383
Lammer, H., Kasting, J. F., Chassefière, E., et al. 2008, Space Sci. Rev., 139, 399
Lammer, H., Schiefer, S.-C., Juvan, I., et al. 2014, Origins of Life and Evolution of the Biosphere, 44, 239
Lammer, H., Zerkle, A. L., Gebauer, S., et al. 2018, A&A Rev., 26, 2
Laskar, J. 1996, Celestial Mechanics and Dynamical Astronomy, 64, 115
Leinhardt, Z. M., & Stewart, S. T. 2012, ApJ, 745, 79
Lellouch, E., de Bergh, C., Sicardy, B., Ferron, S., & Käufl, H. U. 2010, A&A, 512, L8
Levison, H. F., Dones, L., Chapman, C. R., et al. 2001, Icarus, 151, 286
Levison, H. F., Thommes, E., & Duncan, M. J. 2010, AJ, 139, 1297
Li, J., Gudipati, M. S., & Yung, Y. L. 2020, Icarus, 352, 113999
Liang, M.-C., Lane, B. F., Pappalardo, R. T., Allen, M., & Yung, Y. L. 2005, Journal of Geophysical Research: Planets, 110
Lichtenegger, H. I. M., Kislyakova, K. G., Odert, P., et al. 2016, Journal of Geophysical Research (Space Physics), 121, 4718
Lin, D. N. C., & Papaloizou, J. 1986, ApJ, 309, 846
Lissauer, J. J., Dawson, R. I., & Tremaine, S. 2014, Nature, 513, 336
Lock, S. J., Stewart, S. T., Petaev, M. I., et al. 2018, Journal of Geophysical Research (Planets), 123, 910
Lucchetti, A., Plainaki, C., Cremonese, G., et al. 2016, Planet. Space Sci., 130, 14
Luhmann, J. G., & Kozyra, J. U. 1991, J. Geophys. Res., 96, 5457
Lundin, R., Lammer, H., & Ribas, I. 2007, Space Sci. Rev., 129, 245
Lunine, J., & Atreya, S. 2008, Nature Geoscience, 1, 335

Lunine, J. I., & Stevenson, D. J. 1987, Icarus, 70, 61

Lyons, T. W., Reinhard, C. T., & Planavsky, N. J. 2014, Nature, 506, 307

Mah, J., & Brasser, R. 2019, MNRAS, 486, 836

Mahaffy, P. R., Webster, C. R., Atreya, S. K., et al. 2013, Science, 341, 263

Mangold, N., Quantin, C., Ansan, V., Delacourt, C., & Allemand, P. 2004, Science, 305, 78

Marchi, S. 2020, in AAS/Division for Planetary Sciences Meeting Abstracts, Vol. 52, AAS/Division for Planetary Sciences Meeting Abstracts, 311.01

Marinova, M. M., Aharonson, O., & Asphaug, E. 2008, Nature, 453, 1216

Marounina, N., Tobie, G., Carpy, S., et al. 2015, Icarus, 257, 324

Marty, B. 2012, Earth and Planetary Science Letters, 313, 56

Marty, B., Altwegg, K., Balsiger, H., et al. 2017, Science, 356, 1069

Marty, B., Avice, G., Sano, Y., et al. 2016, Earth and Planetary Science Letters, 441, 91

Marty, B., Zimmermann, L., Pujol, M., Burgess, R., & Philippot, P. 2013, Science, 342, 101

Massol, H., Hamano, K., Tian, F., et al. 2016, Space Sci. Rev., 205, 153

Mayor, M., Marmier, M., Lovis, C., et al. 2011, arXiv e-prints, arXiv:1109.2497

Mayor, M., & Queloz, D. 1995, Nature, 378, 355

McKinnon, W. B., & Kirk, R. L. 2014, in Encyclopedia of the Solar System (Third Edition), third edition edn., ed. T. Spohn, D. Breuer, & T. V. Johnson, 861 – 881

Melosh, H. J., & Vickery, A. M. 1989, Nature, 338, 487

Miller, K. E., Glein, C. R., & Waite, J. Hunter, J. 2019, ApJ, 871, 59

Moraes, R. A., & Vieira Neto, E. 2020, MNRAS, 495, 3763

Morbidelli, A., Brasser, R., Gomes, R., Levison, H. F., & Tsiganis, K. 2010, AJ, 140, 1391

Morbidelli, A., Brasser, R., Tsiganis, K., Gomes, R., & Levison, H. F. 2009, A&A, 507, 1041

Morbidelli, A., & Crida, A. 2007, Icarus, 191, 158

Morbidelli, A., Levison, H. F., Tsiganis, K., & Gomes, R. 2005, Nature, 435, 462

Morbidelli, A., Marchi, S., Bottke, W. F., & Kring, D. A. 2012, Earth and Planetary Science Letters, 355, 144

Morbidelli, A., Nesvorny, D., Bottke, W. F., & Marchi, S. 2020, arXiv e-prints, arXiv:2012.03823

Morbidelli, A., Nesvorny, D., Laurenz, V., et al. 2018, Icarus, 305, 262

Morbidelli, A., Petit, J.-M., Gladman, B., & Chambers, J. 2001, Meteoritics and Planetary Science, 36, 371

Mumma, M. J., & Charnley, S. B. 2011, ARA&A, 49, 471

Nesvorný, D. 2018, ARA&A, 56, 137

Nesvorný, D., Li, R., Youdin, A. N., Simon, J. B., & Grundy, W. M. 2019, Nature Astronomy, 3, 808

Nesvorný, D., & Morbidelli, A. 2012, AJ, 144, 117

Nesvorný, D., Roig, F., & Bottke, W. F. 2017a, AJ, 153, 103

Nesvorný, D., Vokrouhlický, D., Bottke, W. F., & Levison, H. F. 2018, Nature Astronomy, 2, 878

Nesvorný, D., Vokrouhlický, D., Dones, L., et al. 2017b, ApJ, 845, 27
Nesvorný, D., Vokrouhlický, D., & Morbidelli, A. 2007, AJ, 133, 1962
—. 2013, AJ, 768, 45
Niemann, H. B., Atreya, S. K., Demick, J. E., et al. 2010, Journal of Geophysical Research (Planets), 115, E12006
Niles, P. B., Catling, D. C., Berger, G., et al. 2013, Space Sci. Rev., 174, 301
Noack, L., Breuer, D., & Spohn, T. 2012, Icarus, 217, 484
Okuzumi, S., Tanaka, H., Kobayashi, H., & Wada, K. 2012, ApJ, 752, 106
O'Neill, C., Jellinek, A. M., & Lenardic, A. 2007, Earth and Planetary Science Letters, 261, 20
Owen, T. C. 2004, in AGU Fall Meeting Abstracts, Vol. 2004, P42A–01
Ozima, M., & Podosek, F. A. 2002, Noble gas geochemistry (Cambridge University Press)
Palumbo, A. M., Head, J. W., & Wordsworth, R. D. 2018, Icarus, 300, 261
Penny, M. T., Gaudi, B. S., Kerins, E., et al. 2019, ApJS, 241, 3
Penz, T., Lammer, H., Kulikov, Y., & Biernat, H. 2005, Advances in Space Research, 36, 241 , space Life Sciences: Astrobiology: Steps toward Origin of Life and Titan before Cassini
Pepin, R. O. 1991, Icarus, 92, 2
Pham, L. B. S., Karatekin, Ö., & Dehant, V. 2011, Planet. Space Sci., 59, 1087
Pierens, A., & Nelson, R. P. 2008, A&A, 478, 939
Pierens, A., & Raymond, S. N. 2011, A&A, 533, A131
Pollack, J. B., Hubickyj, O., Bodenheimer, P., et al. 1996, Icarus, 124, 62
Pollack, J. B., Kasting, J. F., Richardson, S. M., & Poliakoff, K. 1987, Icarus, 71, 203
Porcelli, D., Woolum, D., & Cassen, P. 2001, Earth and Planetary Science Letters, 193, 237
Rafikov, R. R. 2004, AJ, 128, 1348
Rauer, H., Catala, C., Aerts, C., et al. 2014, Experimental Astronomy, 38, 249
Reese, C. C., & Solomatov, V. S. 2006, Icarus, 184, 102
Rice, W. K. M., Lodato, G., Pringle, J. E., Armitage, P. J., & Bonnell, I. A. 2004, MNRAS, 355, 543
Righter, K., Danielson, L. R., Pando, K. M., et al. 2015, Meteoritics and Planetary Science, 50, 604
Rodenbeck, K., Heller, R., & Gizon, L. 2020, A&A, 638, A43
Rosario-Franco, M., Quarles, B., Musielak, Z. E., & Cuntz, M. 2020, AJ, 159, 260
Rubie, D. C., Laurenz, V., Jacobson, S. A., et al. 2016, Science, 353, 1141
Rubin, M., Altwegg, K., Balsiger, H., et al. 2019, MNRAS, 489, 594
Ruiz, J. 2003, Icarus, 166, 436
Sakuraba, H., Kurokawa, H., & Genda, H. 2019, Icarus, 317, 48
Salvador, A., Massol, H., Davaille, A., et al. 2017, Journal of Geophysical Research (Planets), 122, 1458
Schaefer, L., & Fegley, B. 2010, Icarus, 208, 438
Schlichting, H. E., Elkins-Tanton, L. T., Black, B., & Marchi, S. 2017, in Lunar and Planetary

Science Conference, Lunar and Planetary Science Conference, 2405
Schlichting, H. E., & Mukhopadhyay, S. 2018, Space Sci. Rev., 214, 34
Schlichting, H. E., Sari, R., & Yalinewich, A. 2015, Icarus, 247, 81
Schlichting, H. E., Warren, P. H., & Yin, Q.-Z. 2012, ApJ, 752, 8
Seager, S. 2014, Proceedings of the National Academy of Science, 111, 12634
Sekine, Y., Genda, H., Sugita, S., Kadono, T., & Matsui, T. 2011, Nature Geoscience, 4, 359
Sephton, M. A. 2002, Natural product reports, 19, 292
Sharp, Z. D., & Draper, D. S. 2013, Earth and Planetary Science Letters, 369, 71
Shoemaker, E. M., & Wolfe, R. F. 1982, in Satellites of Jupiter, 277–339
Shuvalov, V. 2009, Meteoritics and Planetary Science, 44, 1095
Shuvalov, V., Kührt, E., de Niem, D., & Wünnemann, K. 2014, Planet. Space Sci., 98, 120
Shuvalov, V. V., Svetsov, V. V., & Trubetskaya, I. A. 2013, Solar System Research, 47, 260
Shuvalov, V. V., & Trubetskaya, I. A. 2007, Solar System Research, 41, 220
Sindoni, G., Formisano, V., & Geminale, A. 2011, Planet. Space Sci., 59, 149
Smyth, W. H., & Marconi, M. L. 2006, Icarus, 181, 510
Sohl, F., Spohn, T., Breuer, D., & Nagel, K. 2002, Icarus, 157, 104
Solomatov, V. S. 2004, Journal of Geophysical Research (Solid Earth), 109, B01412
Stofan, E. R., Elachi, C., Lunine, J. I., et al. 2007, Nature, 445, 61
Stone, J. M., Skemer, A. J., Hinz, P. M., et al. 2018, AJ, 156, 286
Strobel, D. F. 1982, Planet. Space Sci., 30, 839
Strom, R. G., & Croft, S. K. 1993, in Lunar and Planetary Science Conference, Lunar and Planetary Science Conference, 1373
Strom, R. G., Malhotra, R., Ito, T., Yoshida, F., & Kring, D. A. 2005, Science, 309, 1847
Suzuki, D., Bennett, D. P., Ida, S., et al. 2018, ApJ, 869, L34
Svedhem, H., Titov, D. V., Taylor, F. W., & Witasse, O. 2007, Nature, 450, 629
Svetsov, V. 2010, in European Planetary Science Congress 2010, 192
Svetsov, V. V. 2000, Solar System Research, 34, 398
—. 2007, Solar System Research, 41, 28
Taylor, G. J. 2013, Chemie der Erde / Geochemistry, 73, 401
Teachey, A., & Kipping, D. M. 2018, Science Advances, 4, eaav1784
Thébault, P., & Augereau, J.-C. 2007, A&A, 472, 169
Thompson, M. A., Telus, M., Schaefer, L., et al. 2021, arXiv e-prints, arXiv:2104.08360
Tinetti, G., Drossart, P., Eccleston, P., et al. 2018, Experimental Astronomy, 46, 135
Tobie, G., Lunine, J. I., & Sotin, C. 2006, Nature, 440, 61
Toublanc, D., Parisot, J. P., Brillet, J., et al. 1995, Icarus, 113, 2
Touboul, M., Puchtel, I. S., & Walker, R. J. 2015, Nature, 520, 530
Trainer, M. G., Wong, M. H., McConnochie, T. H., et al. 2019, Journal of Geophysical Research (Planets), 124, 3000

Tsiganis, K., Gomes, R., Morbidelli, A., & Levison, H. F. 2005, Nature, 435, 459

Tucker, J. M., & Mukhopadhyay, S. 2014, Earth and Planetary Science Letters, 393, 254

Tyler, G. L., Sweetnam, D. N., Anderson, J. D., et al. 1989, Science, 246, 1466

Vickery, A. M., & Melosh, H. J. 1990, Atmospheric erosion and impactor retention in large impacts, with application to mass extinctions, Vol. 247 (LPSC), 289–300

Volkov, A. N., Johnson, R. E., Tucker, O. J., & Erwin, J. T. 2011, ApJ, 729, L24

Waite, J. H., J., Lewis, W. S., Magee, B. A., et al. 2009, Nature, 460, 1164

Waite, J. H., Niemann, H., Yelle, R. V., et al. 2005, Science, 308, 982

Walker, J. C. G., Hays, P. B., & Kasting, J. F. 1981, J. Geophys. Res., 86, 9776

Walker, R. J. 2009, Chemie der Erde / Geochemistry, 69, 101

Walsh, K. J., Morbidelli, A., Raymond, S. N., O'Brien, D. P., & Mandell, A. M. 2011, Nature, 475, 206

Warren, P. H., Kallemeyn, G. W., & Kyte, F. T. 1999, Geochim. Cosmochim. Acta, 63, 2105

Way, M., Del Genio, A., Kiang, N., et al. 2016, in AAS/Division for Planetary Sciences Meeting Abstracts #48, AAS/Division for Planetary Sciences Meeting Abstracts, 122.14

Way, M. J., & Del Genio, A. D. 2020, Journal of Geophysical Research: Planets, 125, e2019JE006276, e2019JE006276 10.1029/2019JE006276

Weidenschilling, S. J. 1977, Ap&SS, 51, 153

Wiechert, U., Halliday, A. N., Lee, D. C., et al. 2001, Science, 294, 345

Willbold, M., Mojzsis, S. J., Chen, H.-W., & Elliott, T. 2015, Earth and Planetary Science Letters, 419, 168

Williams, J. P., & Cieza, L. A. 2011, ARA&A, 49, 67

Williams, R. M. E., Dietrich, W. E., Grotzinger, J. P., et al. 2013, in Lunar and Planetary Science Conference, Lunar and Planetary Science Conference, 1617

Winn, J. N., & Fabrycky, D. C. 2015, ARA&A, 53, 409

Wolf, R., & Anders, E. 1980, Geochim. Cosmochim. Acta, 44, 2111

Wordsworth, R., Knoll, A. H., Hurowitz, J., et al. 2021, arXiv e-prints, arXiv:2103.06736

Wordsworth, R. D., Kerber, L., Pierrehumbert, R. T., Forget, F., & Head, J. W. 2015, Journal of Geophysical Research (Planets), 120, 1201

Wu, J., Desch, S. J., Schaefer, L., et al. 2018, Journal of Geophysical Research: Planets, 123, 2691

Wurz, P., Vorburger, A., Galli, A., et al. 2014, in European Planetary Science Congress, Vol. 9, EPSC2014–504

Wyatt, M. C. 2008, ARA&A, 46, 339

Wyatt, M. C., Booth, M., Payne, M. J., & Churcher, L. J. 2010, MNRAS, 402, 657

Wyatt, M. C., Kral, Q., & Sinclair, C. A. 2019, arXiv e-prints, arXiv:1910.10731

Yalinewich, A., & Schlichting, H. 2019, Monthly Notices of the Royal Astronomical Society, 486, 2780

Yokochi, R., & Marty, B. 2004, Earth and Planetary Science Letters, 225, 77

Youdin, A. N., & Goodman, J. 2005, ApJ, 620, 459

Young, E. D., Kohl, I. E., Warren, P. H., et al. 2016, Science, 351, 493

Yung, Y. L., Allen, M., & Pinto, J. P. 1984, ApJS, 55, 465

Zahnle, K. 2010, in Through Time; A Workshop On Titan's Past, Present and Future, ed. V. Cottini, C. Nixon, & R. Lorenz, 25

Zahnle, K., Arndt, N., Cockell, C., et al. 2007, Space Sci. Rev., 129, 35

Zahnle, K., Pollack, J. B., Grinspoon, D., & Dones, L. 1992, Icarus, 95, 1

Zahnle, K., Schenk, P., Levison, H., & Dones, L. 2003, Icarus, 163, 263

Zahnle, K. J., Lupu, R., Catling, D. C., & Wogan, N. 2020, The Planetary Science Journal, 1, 11

Zel'dovich, Y. B., & Raizer, Y. P. 1967, Physics of shock waves and high-temperature hydrodynamic phenomena (Ney York: Academic Press)

Zhu, M., Artemieva, N., Morbidelli, A., et al. 2019, Nature, 571, 2226

Zhu, Z., Hartmann, L., Nelson, R. P., & Gammie, C. F. 2012, ApJ, 746, 110

Zimmer, C., Khurana, K. K., & Kivelson, M. G. 2000, Icarus, 147, 329

Zsom, A., Ormel, C. W., Güttler, C., Blum, J., & Dullemond, C. P. 2010, A&A, 513, A57